University of Alberta

An open-source two-phase non-isothermal mathematical model of a polymer electrolyte membrane fuel cell

by

Madhur Bhaiya

A thesis submitted to the Faculty of Graduate Studies and Research in partial fulfillment of the requirements for the degree of

Master of Science

Department of Mechanical Engineering

Spring 2014
Edmonton, Alberta

To Mummy, Papa, Vishu and the Almighty

Abstract

A comprehensive open-source two-phase non-isothermal MEA model including the microporous layer and accounting for multi-step reaction kinetics for the ORR and HOR is developed for the first time. The model is integrated into openFCST, an open-source FEM based fuel cell simulation framework. All the significant non-isothermal effects such as anisotropic heat transport, irreversible and reversible heating due to electrochemical reactions, ohmic heating, heat of sorption and thermal osmosis are accounted for in the model. Accurate experimental data for capillary pressure-saturation relationships are reformulated and incorporated into a liquid water saturation transport equation. The model showed, for the first time, that thermal osmosis effects account for up to 15% water-crossover in membrane, and the heat of sorption can be as large as protonic ohmic heating. The model could accurately predict the performance drops corresponding to mass transport limitations due to presence of liquid water and ohmic losses due to membrane dry-out.

Keywords: polymer electrolyte fuel cells, finite element method, non-isothermal, two-phase, open-source, simulation, membrane electrode assembly

Acknowledgements

I would like to thank my supervisor Dr. Marc Secanell for providing me the opportunity to pursue research under his guidance. He has been a great source of inspiration and learning for me. Whenever stumbled upon by a problem, be it modelling issues, or understanding a phenomena, he helped me out effectively by providing necessary information and guidance. His zeal for programming has kept me motivated towards coding for the past two years. I have learned a lot from him about developing science; had intense discussions on politics and various other aspects of the life. It was a thoroughly enriching and unforgettable experience.

I would like to thank my mummy for her love and affection, my papa who taught me first about mathematics and life, and my younger brother Vishu who has always backed up for me. Without the constant encouragement and emotional support from my family, I would not have reached this far.

I would like to thank all my colleagues at ESDL group for making the research experience comfortable. I would like to thank Lalit (a good old friend from undergraduate days) for he introduced me to Dr. Secanell and helped me get accustomed to a new environment; Valentin for enriching chats on science and coding; and Shantanu and Prafful for discussions on the fuel cells and politics over a coffee.

I would like to acknowledge the financial support from Automotive Fuel Cell Cooperation (AFCC). Last but not the least, I bow to the omnipresent.

Table of Contents

List of Tables

List of Figures

Nomenclature

English Letters

$\bar{C}_p$	Molar specific heat, $[J \cdot mol^{-1} \cdot K^{-1}]$
$\bar{G}$	Molar Gibbs free energy, $[J \cdot mol^{-1}]$
$\bar{H}$	Molar enthalpy, $[J \cdot mol^{-1}]$
$\bar{H}_{lv}$	Molar latent heat of vaporization of water, $[J \cdot mol^{-1}]$
$\bar{S}$	Molar entropy, $[J \cdot mol^{-1} \cdot K^{-1}]$
$\dot{W}$	Rate of work done by the system, $[W \cdot cm^{-3}]$
$\hat{C}_p$	Specific heat, $[J \cdot g^{-1} \cdot K^{-1}]$
$\hat{h}$	Specific enthalpy, $[J \cdot g^{-1}]$
$\hat{s}$	Effective saturation
$\hat{u}$	Specific internal energy, $[J \cdot g^{-1}]$
$\vec{N}$	Molar flux of the species, $[mol \cdot cm^{-2} \cdot s^{-1}]$
$\vec{N}$	Molar flux, $[mol \cdot cm^{-2} \cdot s^{-1}]$
$\vec{q}$	Molecular heat flux, $[W \cdot cm^{-2} \cdot K^{-1}]$
$\vec{v}$	Velocity, $[cm \cdot s^{-1}]$
A	Area, $[cm^2]$
A_v	Active area, $[cm^2 \cdot cm^{-3}]$
a_{lv}	Interfacial liquid-vapour surface area per unit volume, $[cm^2 \cdot cm^{-3}]$
Bo	Bond number

C Compaction pressure, [MPa]

c Molar concentration of the gaseous species, $[mol \cdot cm^{-3}]$

Ca Capillary number

D Diffusion coefficient, $[cm^2 \cdot s^{-1}]$

d Diameter, $[m]$

D_T Thermoosmotic diffusion coefficient, $[g \cdot cm^{-1} \cdot s^{-1} \cdot K^{-1}]$

E_{HOR} Equilibrium cell voltage for HOR, $[V]$

E_{ORR} Equilibrium cell voltage for ORR, $[V]$

E_{rev} Reversible cell potential, $[V]$

E_{tn} Thermo-neutral potential, $[V]$

EW Equivalent weight

F Faraday's Constant, 96485.3365 $[C \cdot mol^{-1}]$

h Convective heat transfer coefficient, $[W \cdot cm^{-2} \cdot K^{-1}]$

j Current density, $[A \cdot cm^{-3}]$

k Thermal conductivity, $[W \cdot cm^{-1} \cdot K^{-1}]$

k_t Time constant, $[s^{-1}]$

$K_{e/c}$ Evaporation/Condensation rate constant, $[molPa^{-1} \cdot cm^{-2} \cdot s^{-1}]$

L Characteristic length, $[cm]$

M Molar weight, $[g \cdot mol^{-1}]$

n_d Electro-osmotic drag coefficient

p Pressure, $[Pa]$

R Universal Gas Constant, 8.3144 $[J \cdot mol^{-1} \cdot K^{-1}]$

r Radius, $[m]$

Re Reynolds number

S Volumetric source term

s Liquid water saturation

S_{heat} Volumetric heat source, $[W \cdot cm^{-3}]$

s_{irr} Irreducible saturation

s_{TR} Compressive strain

T Temperature, $[K]$

t Thickness, $[cm]$

V_{Pt} Platinum mass loading per unit volume in the catalyst layer, $[g \cdot cm^{-3}]$

$w_{\%}$ Weight percent of the PTFE

We Weber number

x Molar fraction of the gaseous species

X_N Mass fraction of the electrolyte

V Volume, $[cm^3]$

Abbreviations

ACL Anode Catalyst Layer

AGDL Anode Gas Diffusion Layer

AMPL Anode Microporous Layer

APU Auxiliary Power Unit

BC Boundary Conditions

BPP Bi-polar Plates

CCL Cathode Catalyst Layer

CFD Computational Fluid Dynamics

CGDL Cathode Gas Diffusion Layer

CL Catalyst Layer

CMPL Cathode Microporous Layer

DOF Degrees of Freedom

FCS Fuel Cell Vehicles

FEM Finite Element Method

GDL Gas Diffusion Layer

HOR Hydrogen Oxidation Reaction

LTNE Local Thermal Non-Equilibrium

MEA Membrane Electrode Assembly

MIP Mercury Intrusion Porosimetry

ML Membrane Layer

MPL Microporous Layer

MSP Method of Standard Porosimetry

OCV Open Cell Voltage

ORR Oxygen Reduction Reaction

PEM Polymer Electrolyte Membrane

PEMFC Polymer Electrolyte Membrane Fuel Cell

PSD Pore Size Distribution

PTFE Polytetrafluoroethylene

REV Representative Elementary Volume

RH Relative humidity

SOFC Solid Oxide Fuel Cells

Greek Letters

$\bar{\bar{\tau}}$ Shear stress tensor

$\bar{\mu}$ Electrochemical potential, $[J \cdot mol^{-1}]$

ϵ	Porosity
ϵ^{th}	Percolation threshold
ϵ_c	Compressed porosity
ϵ_N	Electrolyte phase volume fraction
ϵ_S	Solid phase volume fraction
ϵ_V	Void phase volume fraction
η	Over-potential, $[V]$
γ	Surface tension, $[N \cdot m^{-1}]$
$\hat{\mu}$	Chemical potential, $[J \cdot mol^{-1}]$
κ	Permeability, $[cm^2]$
λ	Membrane water content
μ	Viscosity, $[g \cdot cm^{-1} \cdot s^{-1}]$
ν	Specific volume, $[cm^3 \cdot g^{-1}]$
ϕ	Electrical potential, $[V]$
Π	Peltier coefficient, $[V]$
ρ	Density, $[g \cdot cm^{-3}]$
ρ_{dry}	Dry membrane density, $[g \cdot cm^{-3}]$
σ	Ionic conductivity, $[S \cdot cm^{-1}]$
τ	Tortuosity
$H_{g,N}$	Henry's constant, $[Pa \cdot cm^3 \cdot mol^{-1}]$

Subscripts and Superscripts

0	Reference state
λ	Sorbed water in the membrane
c	Capillary

duf Dufour effect

e^- Electron

eff Effective value averaged over a representative elementary volume

eq Equilibrium value for vapour-equilibriated membrane

$f0$ Reference state of formation

g Gas mixture

GDL Gas diffusion layer (GDL) alone

H^+ Proton

H_2 Hydrogen gas

H_2O Water vapour

i Index of the species

l Liquid water

m Membrane (electrolyte) phase

MPL Microporous layer (MPL) alone

N_2 Nitrogen gas

O_2 Oxygen gas

ORR Oxygen reduction reaction

$overall$ Overall reaction

$pore$ Pore (void space)

rl Relative liquid

s Solid phase

$sample$ GDL with MPL sample

sat Saturation

tot Total mixture

v Water vapour

Chapter 1

Introduction

1.1 Motivation

Fuel cells have received increased attention in the last several decades, mainly because of global warming and depletion of fossil fuels. Fuel cells are highly efficient electrochemical energy conversion devices which are not limited by the Carnot efficiency for thermal systems. Efficiencies as high as 60% and 80% have been observed for electrical energy conversion and co-generation with thermal energy respectively [1]. Fuel cells promise a sustainable future because of low noise electricity production alongside very low emission levels of greenhouse gases, particulate matter and other pollutants. For instance, fuel cells powering various systems in an aircraft such as auxiliary power units (APU) and flight control systems are found to be feasible and numerous demonstrators have been developed [2].

Fuel cells can be categorized into various types depending on the type of electrolyte and reactants used. Out of numerous fuel cell types, polymer electrolyte membrane fuel cells (PEMFC) have emerged as the main alternative to replace internal combustion engines used in the transportation sector. Besides offering a positive impact on the environment, PEMFCs offer good transient characteristics and high power densities at low operating temperatures which can be easily scaled up. Due to these advantages, major automakers have developed and demonstrated fuel cell vehicles (FCV) solely based on PEMFCs, such as GM Hydrogen 1, Toyota FCHV and Honda FCX-V3 and have plans to start mass producing these vehicles by 2015-2017. PEMFCs also have advantages over batteries such as, faster refuelling capabilities and the ability to provide continuous power for as long as fuel is being supplied. They can also be scaled down without any loss of efficiencies, hence promising to be next generation power sources for portable and stationary applications. Commercial back-up power

units such as Plug Power GenSys® have been deployed in many locations by telecommunication companies and banks. PEMFCs are also looked upon as a replacement to batteries (due to short life of batteries) in modern-day electronic necessities like mobile phones and portable computers [3].

Numerous breakthroughs in the PEMFC technologies have been achieved in the past couple of decades. However further reduction in costs and improvements in durability are required to make PEMFCs a viable option for consumers. For instance, the estimated cost of PEMFC technologies on 2009 was \$61/kW, which is still much higher than the \$30/kW target set by the US Department of Energy by 2015 [4]. Experimental research in PEMFCs is marred by limitations such as high costs of manufacturing and testing, inability to precisely measure micro and nano scale transport processes inside the PEMFC and the time consuming nature of the experiments. None of these limitations however restrict numerical models, which can be effectively used to investigate the physics inside the PEMFC and further optimize the designs as well [5–7].

PEMFCs are complex multi-component, multi-phase systems involving numerous interconnected multiphysics phenomena such as electrochemistry, fluid transport, ion transport and heat transport. An optimal balance must be found between all of these individually complicated phenomena for efficient and durable operation of the PEMFC. At high current density operation, the closely coupled phenomena of water and thermal management are very critical for efficient and durable operation of the PEMFC. For instance, utilization of the expensive platinum catalyst can be improved by avoiding liquid water build-up in the catalyst layers, which is responsible for blocking reactant gas transport inside the fuel cell. Also polymer electrolyte membranes, a critical part of PEMFC, degrade significantly at high temperatures; thus efficient thermal management can improve durability. Weber and Newman [8] have presented an extensive review of PEMFC models available in the literature. The majority of them have ignored liquid water and heat transport inside the PEMFC.

The motivation of this project is to understand the liquid water and heat transport inside the membrane electrode assembly (MEA) of a PEMFC. Governing equations describing these transport phenomena inside the MEA are developed taking into account all the significant effects occurring inside the MEA. Impact of liquid water and heat transport onto the transport of other species is rigorously included in the model formulation. These are further incorporated into an open-source, finite ele-

ment method (FEM) based fuel cell simulation architecture developed in `C++`, namely openFCST [9, 10]. A two-phase, non-isothermal model employing accurate multi-step reaction kinetics for oxygen reduction reaction (ORR) and hydrogen oxidation reaction (HOR) is developed for the first time. This detailed model will be helpful in accurately and reliably assessing the PEMFC performance at high current densities. The model could avoid costly and time consuming experimentation and can be used to determine the impact of numerous parameters in PEMFC performance. Finally, the model could be used to perform optimization studies thus enabling rapid progress in the PEMFC design.

This thesis describes the development of an open-source, two-phase, non-isothermal PEMFC simulation architecture. Chapter 2 discusses a detailed single-phase, non-isothermal PEMFC model and its results. Chapter 3 further expands the model developed in Chapter 2 to include a two-phase, non-isothermal model and discusses the results. This chapter gives a basic background on PEMFC and then presents a literature review of non-isothermal and two-phase PEMFC models in different sections. Finally, the contributions of this research and the thesis outline are discussed in this chapter.

1.2 PEMFC Background

Hydrogen gas (fuel) electrochemically react with oxygen/air in a polymer electrolyte membrane fuel cell, producing usable electricity and water. A basic schematic of a PEMFC, also showing species transport is given in Figure 1.1. Like other electrochemical devices such as batteries, a PEMFC is composed of two electrodes, *viz.*, anode and cathode, where oxidation and reduction electrochemical reactions occur respectively. Hydrogen gas (H_2) is supplied as a fuel at the anode and air/oxygen gas (O_2) is supplied as the oxidizing agent at the cathode. Both the electrodes are separated by a polymer electrolyte membrane which acts as ionic conductor while blocking the gas transport. Hence the direct combustion reaction between hydrogen and oxygen is avoided.

At the anode half-cell, the fuel *i.e*, hydrogen gas (H_2) is oxidized into protons (H^+) and electrons (e^-). Once an external circuit is connected to the fuel cell, the produced electrons flow out of the electrode forming usable electric current. Protons conduct through the polymer electrolyte membrane in order to reach the cathodic reaction sites. The electrochemical reaction taking place at the anode is termed the

hydrogen oxidation reaction (HOR) and is given as:

$$H_2 \rightleftharpoons 2H^+ + 2e^- \tag{1.1}$$

Electrons are consumed in the reduction reaction taking place at the cathode half-cell. Oxygen gas (O_2) is reduced by the protons and electrons coming from the anode side, producing liquid water (H_2O). The electrochemical reaction taking place at the cathode is termed as oxygen reduction reaction (ORR) and is given as:

$$\frac{1}{2}O_2 + 2H^+ + 2e^- \rightleftharpoons H_2O \tag{1.2}$$

Thus the overall electrochemical reaction taking place inside a PEMFC can be expressed as:

$$H_2 + \frac{1}{2}O_2 \rightleftharpoons H_2O \tag{1.3}$$

The oxidation and reduction reactions given in equations (1.1) and (1.2) take place at the platinum (acting as a catalyst) sites in the fuel cell. It can proceed only when the protons and electrons travel from the anode side to the cathode side and reach the reaction sites. The reactant gases must also be able to reach the reactant sites at both the anode and cathode sides. Finally the product water, if in liquid phase, can block the gas transport and hence must be removed from the cathode reaction

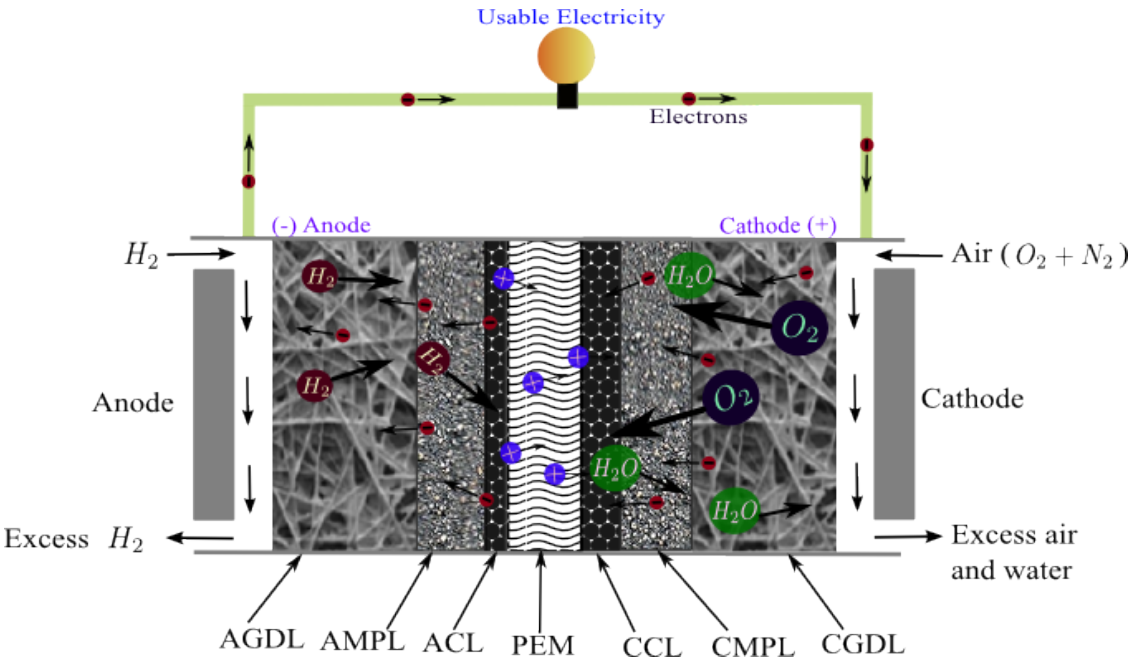

Figure 1.1 – Basic schematics and operation diagram of the polymer electrolyte membrane fuel cell (PEMFC).

sites. In order to satisfy these requirements, a PEMFC is composed of several layers as shown in Figure 1.1.

Platinum (catalyst) particles are located in the catalyst layers in each half of the cell, termed as anode catalyst layer (ACL) and cathode catalyst layer(CCL). The catalyst layer is generally fabricated by depositing an ink which contains platinum particles supported on carbon black and an electrolyte. The electrolyte typically used in a PEMFC is a perfluorosulfonated ionomer, known as Nafion® produced by DuPont. Due to agglomerate formation, it gives rise to the presence of three phases at the platinum sites facilitating the electrochemical reactions. These three phases include empty pore spaces through which gases can travel, electrolyte through which protons can travel and the carbon base through which electrons can reach the reaction sites [11]. The ACL is generally thinner than the CCL due to very fast nature (kinetics) of the hydrogen oxidation reaction.

Both the half-cell reactions (hence the catalyst layers) are separated by a polymer electrolyte membrane (typically Nafion®), which only acts as a conductor of protons. The reactant gases and electrons cannot cross through the membrane layer (ML). However at temperatures higher than 80 ℃, membrane degradation is observed due to hydrogen peroxide formation [12]. This leads to hydrogen fuel crossover causing a drop in the cell performance.

Electrons travel through the external circuit to reach the cathode site. They travel through two electronically conductive layers, *viz.*, microporous layer (MPL) and gas diffusion layer (GDL). The gas diffusion layers are porous media composed of a carbon matrix, which can be fibres, paper or cloth. The carbon matrix serves the purpose of an electronic conductor while the void spaces in the porous media transports the reactant gases to the catalyst layers. It also provides structural stability to the fuel cell. GDLs are generally impregnated with hydrophobic polytetrafluroethylene (PTFE), in order to prevent liquid water from blocking the gas path (void spaces). Sometimes it is also coated with an ink composed of carbon powder with high PTFE content, forming the microporous layer. MPLs serve as an interface between the GDL and the CL, minimizing the contact resistance. Due to the almost hydrophobic nature of the MPL, it also aids in liquid water management from the cathode catalyst layer. All of these layers which are present on both the sides of the membrane are collectively termed as the membrane electrode assembly (MEA).

The fuel cell is completed by pressing the MEA between two bi-polar plates (BPP), also termed current collectors. These are made up of materials like graphite or metals which are excellent conductors of electricity and heat. The complete route of electron transport forming the overall current circuit is shown in Figure 1.1. The channels, that carry the reactant gases to the MEA, are etched in the bi-polar plates in different configurations. The BPP forms the basic structural block of the fuel cell.

The performance of any electrochemical device is measured by plotting current density (A/cm^2) versus cell voltage (V). Fuel cells achieve their highest voltage under no load conditions (open circuit), known as open cell voltage (OCV). However when current is drawn, the cell voltage drops. This voltage drop is known as a cell polarization. Hence the current-voltage curves generally known as polarization curves. A typical polarization curve of the PEMFC is shown in Figure 1.2. Voltage losses can be characterized into three types, *viz.*, kinetics losses, ohmic losses and mass transport losses [13]. Kinetics (activation) losses are attributed to slowness of the reaction. Thus, a fraction of the voltage is lost in driving the reaction. Ohmic losses occur due to voltage losses associated with charge transport (mainly due to proton transport). Mass transport losses occur at higher current densities as the reactants are consumed at a faster rate than they can be supplied causing starvation in the fuel cell.

Fuel cell power output is a function of the cell voltage and the current produced. Due to mass transport limitations at high current densities, the power output of the fuel cell decreases drastically, as shown in Figure 1.2. At high current densities, liquid water produced during the reaction floods the pore spaces blocking the oxygen transport to the reaction sites. Moreover due to very high over-potential losses, lots of heat is generated at the reaction sites. Hence the temperature at the reaction sites is very high causing dry-out of the membrane which in turn leads to higher ohmic losses. This research is thus focused on developing accurate physical models to understand the physical phenomena occurring inside the PEMFC at high current densities. In the next section, the main non-isothermal and two-phase PEMFC models proposed in the literature are reviewed and their limitations discussed.

1.3 Literature Review

From the early 90's onwards, a lot of PEMFC mathematical modelling efforts have appeared in the literature. These models can be distinguished as empirical and physical/mechanistic models. Empirical models are generally used to assess the perfor-

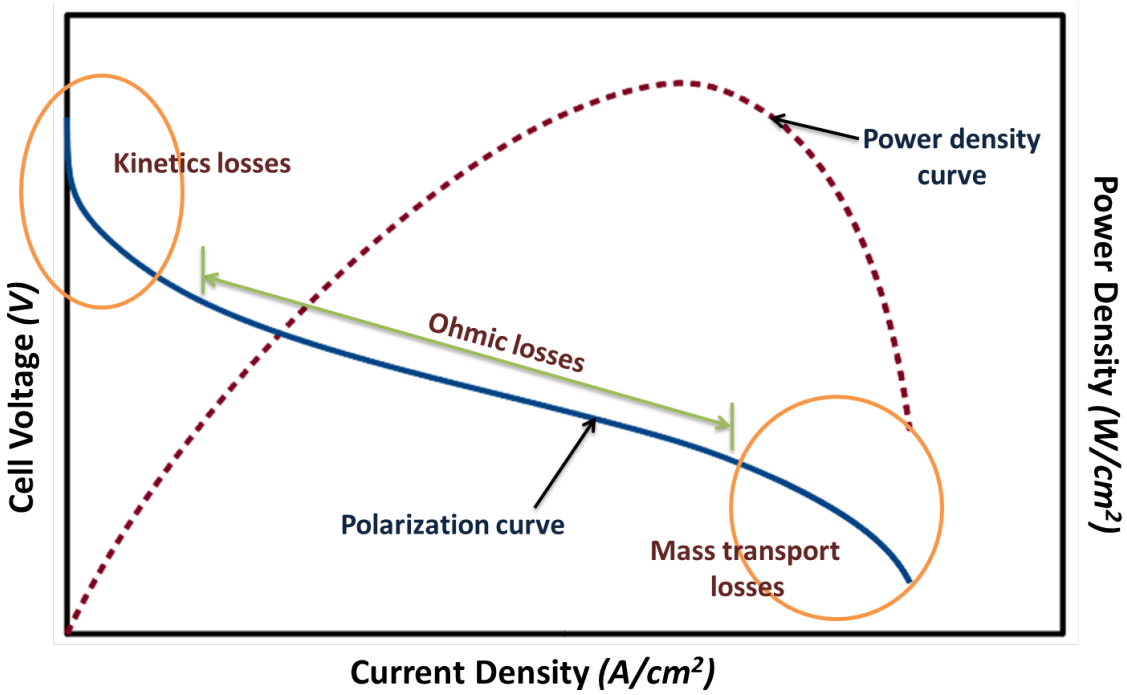

Figure 1.2 – Typical performance characteristics of a PEMFC.

mance of a fuel cell stack assembly as it is difficult and time-consuming to converge complicated physical models at the stack scale. Their models however are only suited to a particular fuel cell for which the empirical model was developed and cannot be used to predict generalized behaviour. Hence these models are not suitable for MEA design. Governing equations corresponding to transport of various species inside the PEMFC are solved in physical models. These models can be used to accurately predict and optimize the performance of a fuel cell.

Water saturation pressure fluctuates considerably in the PEMFC operating temperature range of 80-100 ℃, thus water and thermal management are closely coupled inside the PEMFC. Hence it is crucial to develop a non-isothermal model first before expanding it to a two-phase model. In order to develop a non-isothermal model, the energy balance inside the fuel cell is required to be analyzed in detail. Hence the thermodynamics of the PEMFC is reviewed in the next section. In the later sections, non-isothermal and then two-phase physical models presented in the PEMFC literature are reviewed and discussed separately.

1.3.1 Thermodynamics of PEMFCs

The overall cell reaction taking place inside the PEMFC is given in equation (1.3). During the reaction, exchange of heat, mass and work takes place with the surroundings. In any ideal electrochemical reaction (without any irreversibility), enthalpy changes due to the reaction do not completely transform into electrical work. By the principles of thermodynamics, the maximum electrical work obtainable from the electrochemical reaction at constant T and p, is related to the Gibbs free energy change of the reaction. This maximum electrical work can be determined by reversible cell voltage, E_{rev}, and its relation to the Gibbs free energy change, $\Delta\bar{G}$, is expressed as:

$$E_{rev} = -\frac{\Delta\bar{G}}{nF} \tag{1.4}$$

where n is the number of moles of electrons transferred per mole of fuel in the reaction and F is the universal Faraday's constant. Under standard temperature and pressure conditions, E_{rev} for the overall cell reaction is calculated to be 1.229 V.

The heat released in the overall reaction at constant pressure is determined by the overall enthalpy changes associated with the reaction. The thermo-neutral potential, E_{tn} is defined corresponding to the overall enthalpy change [14]:

$$E_{tn} = -\frac{\Delta\bar{H}}{nF} \tag{1.5}$$

At standard temperature and pressure, E_{tn} for the overall cell reaction is calculated to be 1.48 V. Hence there is always a reversible heat release associated with the overall reaction. The Gibbs free energy change, $\Delta\bar{G}$, associated with the overall reaction at a constant temperature, T, and pressure, p, is given as:

$$\Delta\bar{G} = \Delta\bar{H} - T\Delta\bar{S} \tag{1.6}$$

where $\Delta\bar{H}$ and $\Delta\bar{S}$ are the overall reaction enthalpy changes and entropy changes per mole of fuel (H_2) respectively. Thus the reversible heat release, Q_{rev}, associated with the overall reaction can be formulated as:

$$Q_{rev} = -T\Delta\bar{S} \tag{1.7}$$

The total entropy change associated to the overall reaction producing liquid water per unit mole of fuel (H_2) is very well known in the literature and is given as [15]:

$$\Delta\bar{S}_{overall} = (8(1 + lnT) - 92.84) \times 4.184 \quad [\text{J/(mol-K)}] \tag{1.8}$$

At $T = 353$ K (80 ℃), it results in a reversible heat release of 55.99 kJ/mol-H_2 inside the fuel cell. This heat is not evenly distributed amongst the anode and cathode reactions taking place simultaneously. The anodic and cathodic half cell reactions in a fuel cell can be written as follows:

$$\textbf{Anode (HOR):} \quad H_{2_{(gas)}} + 2H_2O_{(adsorbed)} \longrightarrow 2H_3O^+_{(adsorbed)} + 2e^- \tag{1.9}$$

$$\textbf{Cathode (ORR):} \quad \frac{1}{2}O_{2_{(gas)}} + 2H_3O^+_{(adsorbed)} + 2e^- \longrightarrow H_2O_{(liquid)} + 2H_2O_{(adsorbed)} \tag{1.10}$$

The single electrode reversible reaction heat (commonly known as Peltier heat) can be determined by temperature multiplied by the entropy change of the half-cell reaction. The Peltier effect is observed when reversible heat is released (or absorbed) at the junctions of a thermocouple as current is passed through the two different conductors forming the thermocouple. The heat released is given by the Peltier coefficient multiplied by the current. Similarly in an electrochemical cell, reversible heat is released at the individual electrodes when electric current is generated (passed) at the electrodes. On the basis of this analogy, the Peltier coefficient (Π) in an electrochemical reaction, can be approximated as [16]:

$$\Pi_{a/c} \approx \frac{T\Delta\bar{S}_{a/c}}{nF} \tag{1.11}$$

where the subscript a/c represents either the anode or cathode electrode.

Weber and Newman [17], based on a thorough literature review, reported an average value of Peltier coeffcient of HOR, $\Pi_{HOR} = -13$ mV at 25 ℃. On utilizing the knowledge of total entropy change of the reaction, the Peltier coefficient of the ORR, Π_{ORR}, is determined to be -240 mV. Based on these values, we find that $\Delta\bar{S}_{HOR} = -8.4$ J/(mol-K) and $\Delta\bar{S}_{ORR} = -155.4$ J/(mol-K). These values basically state that almost all of the reversible heat is produced inside the cathode electrode, which is commonly adopted by most of the non-isothermal models in the literature.

Efforts to determine the entropy changes in a single half cell reaction are marred with difficulties because of a lack of reliable knowledge for the entropy values of hydronium ions (H_3O^+) and electrons (e^-). Lampinen and Fomino [18] derived a relationship to determine the entropy of an electron in various states. By employing this relation, they calculated that the anodic entropy change is 0.104 J/(mol-K) while

the cathodic entropy change is -163.18 J/(mol-K) at standard operating conditions.

Ramousse et al. [19] presented a review of the values of the half cell reaction entropy change of the anodic reaction (HOR) reported in the literature. They observed a wide discrepancy in the data from -133.2 J/(mol-K) (Exothermic) to 84.7 J/(mol-K) (Endothermic) for the HOR. They observed that the values reported in the literature were calculated/measured for different conditions. They estimated the entropy change for the anodic half cell reaction by studying proton solvation in water. They calculated that $\Delta\bar{S}_{HOR} = -226$ J/(mol-K) (highly exothermic). By employing the known value for overall reaction entropy change, half cell entropy change due to cathodic reaction is calculated as, $\Delta\bar{S}_{ORR} = +62.8$ J/(mol-K) (endothermic). These values are opposite to the normally modelled values in the literature.

Burheim et al. [20] designed a special calorimeter cell which can measure heat fluxes separately coming out from the cathode and anode end of the fuel cell. They separately developed a one-dimensional non-isothermal model. The fractions of heat released due to various individual source that will pass through anode/cathode end of the fuel cell are determined using the thermal model. Fractions are observed to be only location-specific. Utilizing the model, they calculated that the entropy change in the cathode side is nearly -80 J/(mol-K) and nearly zero for anode side. It is also stressed that these values vary with membrane states hence these values are specific for catalyst coated Nafion® membranes using Solvicore® GDLs.

Kjelstrup et al. [21] performed experiments on a hydrogen-hydrogen cell using a Nafion® membrane as an electrolyte. The advantage of using this cell is that the irreversibility effect (due to ORR) becomes negligible and hence a direct measurement of the reversible heat due to HOR can be obtained. They reported that at 340 K, $\Delta\bar{S}_{HOR} = -66 \pm 5$ J/(K-mol) and $\Delta\bar{S}_{ORR} = -19 \pm 5$ J/(K-mol), under the Soret equilibrium conditions (no current is being generated in the cell). However, it is also concluded that as current is being generated in the cell (moving away from the Soret equilibrium), there can be a considerable enthalpy transport along with water and protons shifting the reversible heat production towards the cathode side.

Hence there is ambiguity in the literature for the reversible heat production distribution inside the cell. However there is clarity about the reversible heat generation for the overall reaction. A parametric study will be performed by employing different fractions for cathode/anode reactions, in order to assess the impact of reversible heat

distribution on the cell performance.

Due to ohmic and activation polarization in the electrochemical reactions, overpotentials[1] are observed in the fuel cell. So the amount of energy recovered from the fuel cell is lesser than thermodynamically predicted value. This lost energy is generated as waste heat due to irreversibilities in the cell. An additional irreversible heat source term is therefore considered in most of the thermal models in the literature [22]:

$$Q_{irrev} = j\eta = j \ (E_{eq} - V_{cell}) \tag{1.12}$$

where j is the volumetric current density, η is the overpotential, E_{eq} is the equilibrium cell potential and V_{cell} is the actual cell voltage.

1.3.2 Non-isothermal models

Thermal management is very important for PEMFCs. PEMFCs operate at temperatures much lower than other prominent fuel cell types such as solid oxide fuel cells (SOFC). Increase in temperature inside a PEMFC has various pros and cons. Reaction rates and species transport rates are increased at higher temperatures. However increased temperature reduces the theoretical cell potential, lowers the water content inside the membrane and increases the hydrogen (fuel) gas crossover through the membrane. Also the saturation pressure of water increases with temperature which leads to more dilution of gaseous mixtures by water vapour. This leads to reduced transport of the reactant gases affecting the cell performance. These issues are becoming more important at higher current densities as temperatures increase.

Membrane requires hydration ionic conductivity and maybe to increase solubility of reactant gas (so that it can reach the platinum sites). However flooding is caused by presence of excessive water leading to limited gas transport. Proton conduction through the polymer electrolyte membrane changes considerably with hydration levels in the electrolyte. A slight variation in temperature causes significant changes in membrane hydration levels hence affecting fuel cell performance. Also local hot spots cause pin holes and degeneration of the membrane, which significantly reduce fuel cell performance and durability. This happens normally during high power density operations.

[1]Overpotential is the potential difference between a half cell reaction's equilibrium potential and the cell voltage.

Conventionally PEMFC models in the literature are assumed to be isothermal because of small heat generation at low to medium current densities. Nguyen and White [23] presented one of the first non-isothermal model for a PEMFC. The governing equation for heat transport is only a coarse approximation as they assume an overall heat transfer coefficient for the PEMFC. Only latent heat of vaporization is considered in their model, neglecting major heat sources associated with the electrochemical reactions. Nevertheless, their model served as a good starting point despite a number of limiting assumptions. Since PEMFC layers are multiphase in nature, two major classes of models exist in the literature. Most of the models assume local thermal equilibrium, *i.e.*, local temperatures are the same for all phases. This reduces the problem to a single equation for the temperature. A few models however assume local thermal non-equilibrium and solve separate heat transport equations (temperatures) for the solid and fluid phases. Pore scale models [24] also exist in the literature; however, they are not discussed here since the main focus in this work is on developing a macro-homogeneous model in this work. Single equation and multi-equation macro-homogeneous models for the heat transport in the PEMFC literature are reviewed.

Shimpalee and Dutta [25] performed a non-isothermal, three-dimensional flow simulation of a straight channel using commercial solver FLUENT™. They observed a considerable temperature variation across the fuel cell. Cell performance is found to be on the lower side when compared with an isothermal model predictions. The model however had several drawbacks. Heat source terms were modelled as a global heat source rather than the location specific sources. Moreover, ohmic heat generation due to ion transport and irreversibility of electrochemical reactions are neglected in their work.

Rowe and Li [26] developed a one-dimensional, two-phase, non-isothermal model for the PEMFC in the through-membrane (through-plane) direction. Their model included various heat sources *viz.*, reversible and irreversible heats associated with the electrochemical reactions, ohmic heating due to proton transport and heat released/absorbed due to phase change of water. Significant drops in cell performance are observed if suitable hydration is not maintained in the anode electrodes. The model however simulated only CL and membrane and assumed them to be fully hydrated which negated the effects of increased ohmic losses with temperature. Thermophysical properties were approximated at an average cell temperature.

Ramousse et al. [27] performed a one-dimensional heat transfer simulation of the MEA. They included an additional heat source/sink term corresponding to sorption/desorption of water into the electrolyte taking place at the catalyst layers. However the heat transport is not coupled with other transport equations and temperature is assumed to be uniform in predicting cell performance. Weber and Newman [17] performed one-dimensional, two-phase, non-isothermal simulations on a PEMFC sandwich configuration. An interface catalyst layer model is used and their model is specifically focused on assessing temperature effects on two-phase transport. The heat pipe effect is observed where liquid water product evaporates inside the cathode catalyst layer and travels towards the GDL in vapour phase. Reactant transport is reduced by increased amounts of water vapour as well as due to pore blocking, when the water vapour is condensed back into liquid water inside the GDL.

Wang et al. [28] developed a comprehensive three-dimensional non-isothermal model and validated against experimental data by varying operating temperatures, pressures and humidification. Fuel cell performance is found to be increasing with operating temperatures under the conditions of sufficient humidification. However reversible heat of reaction and ohmic heating due to electron transport are not considered in their model. Mazumder and Cole [29] also developed a rigorous three-dimensional, non-isothermal model including viscous dissipation effects in the heat transport equation. It is observed that the 3-D model predictions differ significantly with 2-D model predictions at high current densities. However they also ignored the reversible heat release associated with the reaction taking place inside the catalyst layers.

Ju et al. [22] presented a rigorous three-dimensional, single-phase, non-isothermal model for a PEMFC. All three major mechanisms of heat generation are considered in their model, *viz.*, entropic heat, irreversible heat of reaction and ohmic heating. Location specific expressions for these heat source terms are used in their model. They further presented the application of this model on a 50 cm^2 segmented cell and validated their model predictions against experimental data by varying cell voltages and humidity conditions [30]. Model predictions are found to deviate with respect to experimental results due to liquid water flooding under low cell voltage operations. However reversible heat is formulated for liquid water product, over-predicting the heat generated in the cell. For a single phase model to be consistent, heat sink due to complete evaporation of water should be included in the model, which is ignored in their work. Ohmic heating due to electron current in the GDL is neglected in their

work. Wang and Wang [31] improved upon the model by incorporating two-phase effects and observed that the vapour diffusion process accounts for 15-18% of heat transfer. However the species transport in their models are based on multiphase mixture (M^2) theory, which is not considered in this work.

Pasaogullari et al. [32] presented a two-phase, non-isothermal model for a cathode GDL only, considering anisotropic heat transport. An anisotropic GDL is found to be more prone to flooding than an isotropic GDL. Temperature gradients of upto 5 ℃ are observed in comparison to the isotropic model. Bapat and Thynell [33] observed that anisotropic thermal conductivity of the membrane does not have significant bearing on the temperature distributions inside a single phase model. It is also observed that a higher in-plane thermal conductivity of the GDL is desirable for better heat management of the fuel cell. They however considered only conduction heat transport in their model. Birgersson et al. [34] included contact resistance effects between various layers in their two-phase, non-isothermal model. The catalyst layer is modelled as an interface, and convective heat transfer is neglected based on a scale analysis. It is observed that most of the temperature gradients occur at interfaces. Zamel and Li [35] observed highest temperatures in the catalyst layer in two-phase, non-isothermal model of the cathode electrode.

Non-equilibrium non-isothermal models solve solid and fluid phase temperatures as separate variables. Berning et al. [36] developed a comprehensive non-equilibrium non-isothermal three-dimensional model of the PEMFC. However the model assumed the catalyst layer as an interface and the membrane to be fully humidified, hence ohmic losses are neglected in their work. Phase change of water is also neglected in their work. Using the approach of local thermal non-equilibrium (LTNE), Hwang and Chen [37] implemented a two-equation approach for heat transfer in the porous regions. It is stressed that this approach is valid because of a significant difference between thermal conductivities of solid and fluid phases in the PEMFC. However the model assumed values of interstitial heat transfer coefficient and interstitial surface area value, in order to consider heat transfer between solid and fluid phases. Hwang et al. [38, 39] implemented this approach and presented simulation results for the cathode electrode. The catalyst layer is assumed to be a thin surface and effectively only the GDL is simulated. It is observed that the bulk of heat transfer takes place through conduction in the solid phase. In this work, a steady state model is being developed. Moreover porous media have very high interstitial surface area, hence it is fair to assume that local thermal equilibrium exist inside the PEMFC. Thus a single

equation (variable) approach is being considered.

Based on the literature review, it is observed that a detailed non-isothermal PEMFC model that accounts for all non-isothermal effects in the PEMFC does not exist. Kjelstrup and Røsjorde [40] developed a one-dimensional model which solved for entropy production and transport inside the cell. The model is based on the principles of non-equilibrium thermodynamics for heterogeneous systems. It allowed for consistent inclusion of all thermal effects which are normally neglected in other approaches. However this approach does not result in an explicit governing equation for determining temperature profiles inside the cell. A detailed thermal equation considering anisotropic heat transport and all heat sources, *viz.*, reversible, irreversible, ohmic heating, phase change, and sorption/desorption, will be developed in this work. The model will be implemented into an open-source comprehensive PEMFC model using multi-step reaction kinetics for ORR and HOR [41–43]. Further temperature dependent transport relations and kinetics parameters will be considered in this work.

Table 1.1 details the layer-specific thermal conductivity values used in the PEMFC modelling literature. Most of the thermal conductivity values used in the PEMFC modelling literature are assumed and hence a wide variation is observed. A number of experimental and modelling efforts for estimating the thermal conductivity values of the PEMFC layers have recently emerged in the literature. GDL thermal conductivity values are found to be significantly affected by various parameters such as cell compression [44, 45], temperature [46, 47] and liquid water presence [44]. It can also be seen that the models available in the literature do not account for MPL effects. However the MPL is found to have a significant effect in reducing the overall thermal conductivity of the gas diffusion electrodes [48, 49]. Moreover MPL thermal conductivity values are experimentally measured to be anisotropic in nature [45, 50]. Zamel and Li [51] have extensively reviewed the methods to determine effective transport properties for various fuel cell layers and compiled the experimentally measured thermal conductivity values. Based on the new available data, accurate thermal conductivity values (based on experimental observations) will be considered in this work. Nevertheless a parametric study will also be performed to assess the impact of the various thermal parameters on the fuel cell performance.

Table 1.1 – Thermal conductivity $\left[W \cdot cm^{-1} \cdot K^{-1}\right]$ values for different PEMFC layers used in the modelling literature.

References	GDL	MPL	CL	Membrane
Berning et al. [36]	0.75	–	–	0.0067
Rowe and Li [26]	0.016	–	0.015	0.0034
Ramousse et al. [27]	0.016	–	–	0.0034
Weber and Newman [17]	0.015	–	0.003	0.0025
Ju et al. [22, 30]	0.005 - 0.0294	–	–	0.0095
Wang and Wang [31]	0.003	–	0.003	0.0095
Pasaogullari et al. [32]	0.017 (through-plane) 0.21 (in-plane)	–	–	–
Birgersson et al. [34]	0.002	–	–	0.001
Zamel and Li [35]	0.013	–	0.008725	0.00445
Hwang et al. [38, 39]	0.017	–	–	0.005

1.3.3 Two-phase models

Water is produced inside the cathode catalyst layer during the fuel cell operation. Also, feed gas streams are normally humidified before entering the fuel cell. Depending on local temperature, pressure and water vapour mole fraction, the water will exist either in liquid or vapour form. Besides these two phases, water also exists as a third phase inside the polymer electrolyte membrane as sorbed phase. Thus water exists in three phases inside the PEMFC, *viz.*, gas, liquid and sorbed phase. This makes the transport phenomena inside the fuel cell a comprehensive multi-phase, multi-fluid system.

Water management is very crucial in PEMFC operation since it controls gas and proton transport [52]. It is critically linked to the thermal management [17, 53]. Current generation polymer electrolyte membranes, *e.g.*, Nafion®, Gore® membranes, depend on water content (hydration) inside the membrane for protonic electrical conductivity. Water content inside the membrane should be sufficiently high in order to maintain high levels of protonic conductivity, thus increasing the efficiency of the electrochemical reaction. If the membrane water content is very low, ohmic losses due to proton transport increase thereby reducing the overall cell performance. The dried membrane also degrades more rapidly due to pinhole formation at hot spots, reducing the durability of the fuel cell. Liquid water present inside the porous diffusion media,

viz. GDL and MPL, however blocks the reactant gas transport, reducing diffusivity and relative permeability of the reactant gas. This results in the reduction of the overall performance of the fuel cell due to mass transfer losses at the macroscopic level. Liquid water also affects mass transfer at the microscopic level by filling the catalyst agglomerates with liquid water inside the catalyst layer.

At high current densities, water is produced in large quantities inside the cathode catalyst layer. Water is also electroosmotically dragged from the anode to the cathode. These cause severe flooding resulting in a significant performance drop inside the fuel cell. For automotive applications, this phenomenon can even occur at low current densities during start-up. At start-up cells are at ambient conditions. At this temperature, water vapour saturation pressure is very low and condensation can occur. This severely affects the start-up and transient performance/characteristics of the fuel cell. Fuel cells also exhibit hysteresis in performance due to the presence of the liquid water. Thus there has to be an optimal balance between the flooding inside the fuel cell (mass transfer losses) and dehydration of the membrane (ohmic losses). A detailed review of all these issues regarding water balance and recent research efforts in this field is presented by Dai et al. [52].

Porous diffusion media, *viz.*, GDL and MPL, are made up of carbon which is hydrophilic in nature, but are rendered hydrophobic due to a treatment with PTFE. The GDL is highly anisotropic and due to defects generated during the manufacturing process, hydrophilic cracks are created inside the layer. MPLs are generally found to be almost completely hydrophobic in nature because of their homogeneous nature. Therefore, liquid water does not usually enter the layer and water removal from catalyst layers is in the vapour phase only [54, 55]. Liquid droplets formed during condensation are randomly dispersed inside the porous media due to mixed wettability[2]. Under the conditions of low saturation or low gas flow, these isolated water droplets cannot move hence block the reactant gas flow. This residual water is commonly known as immovable saturation[3]. It can be a source of ionic impurities thus causing degradation of the catalyst layer and dangerous for initial start-up, freeze thaw performance of the fuel cell.

Experimental efforts to understand the liquid transport inside the PEMFC have

[2]Wettability is defined as the degree by which fluid can stick to the solid surface by striking a balance between the adhesive and cohesive forces.

[3]Saturation is defined as the fraction of the volume occupied by the liquid out of the overall empty volume (void space) in the porous media.

been undertaken. However, they have been marred by various limitations such as the very small size of the MEA and the inability to visualize liquid water due to opaque layers unless very expensive equipments such as synchrotron facilities are used. Hence a large number of modelling efforts have been undertaken in the last few decades in order to characterize the water transport transport mechanisms inside the fuel cell. Due to the very small length scales inside the porous media and the anisotropic and mixed wettability nature of the PEMFC layer, liquid water transport inside the PEMFC layers is still not yet well understood.

The liquid water can be transported by means of various mechanisms *viz.*, viscous drag associated with flow of surrounding gas phase, capillary driven flow due to saturation gradients and other body forces, *e.g.*, gravity. Consequently, macro-homogeneous two phase models in the PEMFC literature can be divided on the basis of complexity, ranging from the most generalized models accounting for all modes of the liquid water transport (multi-fluid models) to the models considering stationary liquid water (porosity correction models) [56]. Recently a new class of models have emerged which use stochastic reconstructions along with: a) the Lattice-Boltzmann method (mesoscopic models) [57], b) full-morphology models [58], and c) pore network models [59, 60]. In this thesis, the main focus is on developing a macro-homogeneous MEA model, hence in subsequent paragraphs only macro-homogeneous modelling approaches are discussed in detail.

Some of the early models presented in the literature focused more on the water balance inside the fuel cell. Bernardi [61] performed water-balance calculations in the PEMFC, with the purpose of determining the humidification requirements of the reactant gas streams. The model was one-dimensional, isothermal with some simplifying assumptions, such as no liquid water inside the GDLs and insignificant electro-osmotic drag inside the membrane. One significant conclusion from the model is that at higher current densities, due to very large temperatures inside the fuel cell, water evaporation is very high. Thus anode gas stream should be humidified in preference to the cathode gas stream. Bernardi improved upon this model with Verbrugge [62] while studying the cathode gas diffusion electrode bonded to the polymer electrolyte membrane. Although the membrane is assumed to be fully hydrated, water transport inside the membrane was considered via convection and diffusion. It is observed that at high current densities, ohmic losses inside the membrane become very significant. They later extended their model to an overall one-dimensional isothermal MEA model [63]. It showed good agreement with the experimental results but a lot

of their simulation parameters were fitted to match experimental predictions. In later models, commonly known as **porosity correction models** [56], transport of liquid water is not solved for but the effect of its presence (*e.g.* flooding) is considered by assuming a constant saturation value inside the diffusion media [64]. Baschuk and Li [65] improved the approach further by accounting for the variation of saturation values across the cathode diffusion media. These values were obtained by fitting these saturation parameters to experimental data.

Multi-fluid models are more general liquid water transport mathematical models [56]. In these models, liquid water transport is solved considering all mechanisms *viz.*, viscous drag, capillary diffusion, and gravity. The corresponding transport equations for each of the fluids are solved separately, and are coupled to each other using various mass transfer terms. Pasaogullari and Wang [66] developed a set of linear equations on the basis of a simplistic water balance analysis on a one-dimensional model. These equations were employed to determined the threshold current density at which onset of two-phase flow appeared. The model also considered the blocking of reaction sites by using a saturation dependent reduction factor for the active area in the catalyst layer. Capillary driven flow is found to be the dominating factor in assisting water removal from the GDLs. Saturation levels up to 10% are observed inside the CL, even at zero saturation boundary condition at the gas channel-GDL interface.

Berning and Djilali [67] presented a three-dimensional, non-isothermal, multiphase model of a MEA. Both liquid and gas phase transport are coupled using relative permeabilities, which depend on the local saturation value. Constitutive equations defining the relationship between capillary pressure and saturation values inside the porous layers are determined using a standard Leverett approach [68, 69]. Relative permeability values are considered using a simple linear relationship with the saturation content. It is interestingly observed that for large permeability values in the anode GDL, very high saturation values (upto 20%) were observed in the anode side. In contrast to this, large permeability values in the cathode side GDL helped to push out liquid water produced during the reaction. The model however treated catalyst layers as a thin surface and the microporous layers are not considered in their model.

Acosta et al. [70] developed a transient two-phase non-isothermal two-dimensional cathode electrode model. The extended Darcy's law is used for modelling gas and liquid phase transport individually. The catalyst layer is modelled as a thin surface and a polarization equation is used to model the reaction kinetics. At the gas

channel-GDL boundary, zero value for liquid saturation is used as the boundary condition. The membrane is considered to be fully humidified. Using mercury intrusion porosimetry, various properties/relations needed to characterize two-phase flow, *viz.*, Leverett functions, relative permeability, and contact angles, are measured experimentally for the commercial double sided ELAT GDLs from E-TEK, Inc.

Wu et al. [71] developed a transient, non-isothermal, two-phase, three-dimensional MEA model considering a straight flow channel. However microporous layers are not considered in their model. Saturation boundary conditions at the flow inlet boundary are also assumed to be zero. Water produced during the ORR is considered to be formed in sorbed phase and then depending on the local temperature and water vapour saturation conditions, it is considered to be produced in the liquid or vapour form directly. Non-negligible differences are observed on comparing this approach with the model where water is produced in the liquid form directly. Model predictions using validated Leverett functions from Kumbur et al. [72–74] are compared against experimentally determined Leverett functions for GDL and CL by Ye and Van Nguyen [75]. The former resulted in uniform saturation drop from CL to GDL while the latter led to higher flooding in CL. A steep decrease in saturation is observed from GDL to CL in the latter case. A parametric study is performed on relative permeability values on the liquid water transport and interestingly they are found to have bigger impact than the capillary-pressure saturation relationships.

Another set of models, known as **moisture diffusion models** [56], are used in the case when viscous drag due to surrounding gas phase is negligible. In these models, a capillary pressure gradient is the only driving force behind the liquid water transport process. Hence the governing equations concerning liquid water transport are simplified and condensed to a single equation for a variable representing saturation [76]. Terms corresponding to the phase transfer and other physical properties such as relative permeability are modelled in the same way as the multi-fluid models. Nam and Kaviany [77] predicted effective diffusivity relationships using anisotropic pore network models as a function of porosity and saturation. These are incorporated into a one-dimensional moisture diffusion model and parametric studies are performed on parameters such as fibre diameter and porosity, assessing performance impacts. It is recommended to have a two-layer diffusion media (like GDL with MPL) for best performance. Optimal parameters are suggested.

Natarajan and Van Nguyen [78] presented an isothermal, two-phase, three dimen-

sional model using a conventional gas distribution plate. The immovable saturation value is arbitrarily assumed to be 0.1 inside the porous layers. This same value is used as a boundary condition at the gas inlet boundary. Certain effects such as reduction in oxygen concentration along the length of the gas channel are modelled using an iterative procedure. Performance predictions matched well with the experimental results in contrast to their previous two-dimensional model [79]. Liquid water transport is also observed to be the slowest and most critical factor in determining cathode performance.

Shah et al. [80] developed a transient, non-isothermal, two-phase, one-dimensional MEA model including agglomerate effects inside the cathode catalyst layer. Liquid water produced during the reaction is considered to be in sorbed form (because of hydrophilic ionomer sites). A phase transfer term is used to account for both condensation and evaporation. A modified Leverett approach [77] is used in modelling the liquid water transport inside the MEA. Convective enthalpy transport due to liquid water flux is also incorporated in the thermal equation. A zero liquid water removal boundary condition is used at the gas channel-GDL interface. The model could reproduce the hysteresis effects observed in experimental data.

Wang and Van Nguyen [81] performed a parametric study on various coefficients in the capillary-pressure curve determined by Ye and Van Nguyen [75]. According to them, since the CL is highly hydrophilic, capillary forces are required to be balanced at GDL-CL interface leading to a saturation jump, in contrast to the previous model [75]. Two different saturation variables for GDL and CL are solved, using a steady-state, one-dimensional isothermal cathode model with fully hydrated membrane. It is observed that water transport inside the catalyst layer is bound to the hydrophillic regions alone, because of saturation jump conditions at the GDL-CL interface. Zero capillary pressure boundary condition is used for fully saturated feed gas stream at gas channel-GDL interface, while for under-saturated feed gas stream, liquid water flux is set to zero. More hydrophobic GDLs are found to significantly improve the fuel cell performance.

Gerteisen et al. [82] developed a transient, non-isothermal, one-dimensional MEA model, which accounted for mixed wettability using a modified Leverett approach. Immobile saturation values of 0.2 are used inside the GDL, while a zero value is used inside the CL. An outflow boundary condition at the gas channel-GDL interface is used as a quadratic function of the difference between the local saturation value and

the immobile saturation, when the local saturation values are higher than the immobile saturation values. This condition ensured an effective water removal by the gas stream in the channel. A current versus voltage hysteresis loop is observed in the model predictions and compared well against the chronoamperometry experiments.

Based on the principles of mixture flow theory, a new model (**M^2 model**) for multi-component, multi-phase transport in porous media was developed by Wang and Cheng [83]. The model is developed without any approximations and is mathematically equivalent to the multi-fluid models [84]. Multiple field (transport) equations are amalgamated together, eventually reducing the computational efforts required. Individual phase velocities are obtained later in the post-processing stage of the model predictions. Wang et al. [85] combined this approach with CFD techniques in simulating a cathode model and observed that capillary diffusion transport phenomena is the most dominating mode in liquid water transport. Pasaogullari and Wang [86] employed a modified Leverett approach in conjunction with the mixture model. Ju et al. [87] further improved upon the model by employing empirical quartic functions of saturation for relative permeability of the liquid in the diffusion media. Blocking of active area sites in the CL is also modelled using quadratic functions of saturation. Model predictions for water distribution are found to be well within the range of results obtained in neutron radiography experiments. Koido et al. [88] experimentally measured capillary pressure-saturation relationships and relative permeability values of commercially available Toray TGP-H-060 GDL (5% PTFE content). These are later incorporated into a isothermal, multi-phase mixture model for GDL only.

Mixture models have the advantage over multi-fluid models that there is no need to account for the inter-phase transfer terms but a lot of mixture terms are required to be solved in the simulation. Convergence issues are also expected at high saturation values [56], hence they are suited to flows when either the gas phase is dominating or the capillary pressure is driving the liquid in the same direction as the invading gas phase [56]. The porosity correction models do not account for liquid water transport and are suited for very low saturation conditions (below immovable saturation values) [56], *e.g.*, low current densities. In a PEMFC, gas transport is mostly by diffusion due to low capillary numbers thus gas pressure gradients are generally negligible [17, 56]. Capillary driven transport is also observed to be the dominating mechanism in the model predictions [66, 85]. Thus a single transport equation for the saturation considering capillary diffusion should be sufficient in characterizing liquid water transport in the PEMFC and is considered in this work. A detailed multi-dimensional (2-D

or 3-D), two-phase, non-isothermal MEA model that does not treat catalyst layers as a thin surface, includes microporous layers, and incorporates multi-step reaction kinetics for ORR and HOR, is not available in the literature.

The physical properties/relationships characterizing liquid water transport used in the fuel cell literature are generally empirical in nature, and are based on the studies conducted in soil mechanics and petroleum reservoir engineering. Leverett [68] proposed a semi-empirical relationship for capillary pressure v/s saturation, based on a dimensional analysis performed on experimental results obtained for soil science. Udell [69] later presented empirical functions for packed soil beds based on Leverett's approach. The traditional Leverett approach is valid for highly hydrophilic and isotropic soil beds. Leverett's formulation is hence further improved in fuel cells by introducing a contact angle factor, in order to account for hydrophobic gas diffusion media of the PEMFC [77, 86]. The external contact angle values used in the literature however are not correct in characterizing the porous media [75]. Gurau et al. [89] has reported the internal contact angle values for numerous commercially available porous diffusion media used in the PEMFC. But since these contact angle values are generally statistically averaged over the porous media, this approach has been shown to be ineffective for mixed wettability, highly anisotropic, fibrous diffusion media of the PEMFC [90]. Kumbur et al. [90] showed that the saturation values inside the diffusion media are consistently over-predicted using Leverett's approach in comparison to experimentally obtained relationships [54]. It has also been shown that different capillary pressure v/s saturation curves are obtained when the liquid is being injected (imbibition) or being drained (drainage) into the porous media, hence hysteresis effects in the porous media are also not effectively accounted for by Leverett's approach [75, 91]. Recently a new approach using experimentally determined pore size distribution was proposed, accounting for mixed wettability effects. Weber et al. [92] derived analytical expressions for various physical properties of the diffusion medium, such as relative permeability, saturation and average Knudsen radius. Weber [93] and Sinha et al. [94] improved upon the model by using a uniform contact angle distribution and Cheung et al. [95] further improved upon that by employing a mix of the previous two approaches [92, 94]. Other noteworthy works in this field are Eikerling [96], Mulone and Karan [97] and Villanueva [98].

With the recent experimental advances in reporting capillary pressure v/s saturation relationships for commercially available PEMFC porous media [54, 70, 75, 88, 99], it is possible to characterize liquid water transport inside the PEMFC more accu-

rately. Kumbur et al. has presented a generalized Leverett function for commercially available Sigracet® GDLs, accounting for PTFE content [72], compression [73] and temperature [74] dependence. Details about these relationships alongside empirical relations for relative liquid permeability and effective diffusivity reported in the literature shall be discussed during the two-phase MEA model development in subsequent chapters. Henceforth appropriate relations will be chosen and integrated into the MEA model under development in this work.

1.4 Contributions

The main contributions to PEMFC modelling literature are:

1. Development of a thermal equation accounting for anisotropic heat transport inside the MEA due to conduction and diffusive enthalpy transport. All the relevant heat terms such as reversible and irreversible heating due to reactions, ohmic heating and heat of sorption and non-isothermal effects such as thermal osmosis are considered in the model.

2. Development of a saturation equation accounting for liquid water transport inside the MEA. Experimental correlations for capillary pressure - saturation relationships based on the data by Kumbur et al. are reformulated and separate correlations for the GDL and MPL are proposed and considered in the model.

3. Rigorous integration of the two equations into the existing isothermal 2D MEA model using accurate multi-step reaction kinetics, and analysis of the new model results against the existing model and the experimental data.

1.5 Thesis Outline

Chapter 1 presents a background on the thermodynamics of PEMFC and existing two-phase, non-isothermal models in the literature. Chapter 2 presents detailed derivations of the layer-specific thermal equations for the MEA model. The non-isothermal model predictions are assessed and the importance of considering various non-isothermal effects are highlighted. Chapter 3 presents the development of saturation transport equation and reformulation of accurate constitutive relations for the PEMFC layers. The impact of two-phase model on the cell performance is assessed. The conclusions of this research and the scope for future work are summarized in Chapter 4.

Chapter 2

Single-phase non-isothermal model

2.1 Introduction

In the previous chapter, a literature review of various non-isothermal models (single-phase and two-phase) was presented. Two types of thermal models are observed in the literature, *viz.*, single equation and two equation models. The former considers local thermal equilibrium between multiple phases inside the layer while the latter does not. There is large interstitial area of heat transfer between multiple phases in a porous medium. Hence at steady state, it is fair to assume that all the different phases will be at thermal equilibrium. As discussed in Section 1.3.2, it is also observed that there is a lack of detailed single-phase non-isothermal mathematical models in the literature, which account for all consistent and relevant thermal effects in a PEMFC, such as, reversible heat generation and heat of sorption/desorption.

In this chapter, a detailed single-phase thermal transport mathematical model is formulated for the membrane electrode assembly. It is later incorporated with various multiphysics phenomena occurring inside the PEMFC, accounting for multi-step reaction kinetics. These equations are implemented in an open-source fuel cell simulation framework, namely openFCST [9, 10]. Simulation results comparing isothermal and non-isothermal models are presented here, by varying operating conditions, *viz.*, pressure, temperature and humidification. Parametric studies on various thermal parameters, such as thermal conductivities, are also presented highlighting the need to characterize some of them for fuel cell materials. This chapter is divided into three sections. The first section will present the thermal transport equation and its formulation accounting for all consistent heat sources in the various MEA layers. The FEM formulation for implementing this non-linear equation will also be discussed in detail. Next section will describe the overall mathematical model detailing various transport

processes in a PEMFC. The final section will validate and discuss the simulation results.

2.2 Thermal Transport Equation

In a polymer electrolyte fuel cell, there are basically three phases in a porous media, *viz.*, solid, liquid and gas. For a single phase model, the gas phase is allowed to be in super-saturated form (higher than 100 % relative humidity (RH) values) and the liquid phase is assumed non-existent. GDL, MPL and CL have very high interstitial surface area between the fluid (gas) phase and the solid phase. There is basically convective heat transfer between these two phases and due to large convective heat transfer area, it can be assumed that the fluid phase and solid phase are in thermal equilibrium. This assumed can be assumed to be valid under a steady state model, after dying of initial transients.

The temperature profiles in a system can be deduced by solving an equation for the internal energy in the system. It can be written as follows [100]:

$$\begin{aligned}\begin{pmatrix}\textbf{rate of increase}\\ \textbf{of internal energy}\end{pmatrix} = &\begin{pmatrix}\textbf{rate of internal energy}\\ \textbf{addition by convection}\end{pmatrix}\\ &+\begin{pmatrix}\textbf{rate of internal energy}\\ \textbf{addition by molecular heat transport}\end{pmatrix}\\ &+\begin{pmatrix}\textbf{rate of reversible internal}\\ \textbf{energy addition by compression}\end{pmatrix}\\ &+\begin{pmatrix}\textbf{rate of irreversible internal}\\ \textbf{energy addition by viscous dissipation}\end{pmatrix}\\ &+\begin{pmatrix}\textbf{rate of increase}\\ \textbf{due to source terms}\end{pmatrix}\end{aligned} \tag{2.1}$$

For a multi-component mixture, in per unit volume terms, it is expressed as [100]:

$$\frac{\partial}{\partial t}\left(\rho_g \hat{u}_g\right) = -\vec{\nabla}\cdot\left(\rho_g \hat{u}_g\right)\vec{v}_g - \vec{\nabla}\cdot\vec{q} - p_g\left(\vec{\nabla}\cdot\vec{v}_g\right) - \left(\bar{\bar{\tau}}\cdot\vec{v}_g\right) + S_{heat} \tag{2.2}$$

where ρ_g, $\hat{u}_g$, $\vec{v}_g$ and p_g are density, specific internal energy, velocity and pressure of the gas mixture respectively, $\vec{q}$ is the molecular heat flux,$\bar{\bar{\tau}}$ is the shear stress tensor corresponding to the fluid (gas) flow, and S_{heat} is the volumetric heat source term.

In a multi-component mixture, molecular heat flux, $\vec{q}$, is comprised of three contributions, *viz.*, Fourier conduction, enthalpy transport due to inter-diffusion amongst

species and heat transfer associated with diffusion-thermo effect (Dufour effect) [100]. It can be written as follows:

$$\vec{q} = -k\vec{\nabla}T + \sum \bar{H}_i \vec{N}_i + \vec{q}_{duf} \tag{2.3}$$

where k is the thermal conductivity, $\bar{H}_i$ and $\vec{N}_i$ are the molar enthalpy and molar flux of gas i, and $\vec{q}_{duf}$ is the heat flux corresponding to the Dufour effect.

Now, using the concept of material derivative, $\frac{D()}{Dt}$, Equation (2.2) can be further simplified as follows [100]:

$$\rho_g \frac{D(\hat{u}_g)}{Dt} = -\vec{\nabla} \cdot \vec{q} - p_g \left(\vec{\nabla} \cdot \vec{v}_g\right) - (\bar{\bar{\tau}} \cdot \vec{v}_g) + S_{heat} \tag{2.4}$$

In a flow process, it is more convenient to deal with enthalpy rather than internal energy. Specific enthalpy of the gas mixture, $\hat{h}_g$, is expressed as:

$$\hat{h}_g = \hat{u}_g + p_g \nu_g \tag{2.5}$$

where ν_g is the specific volume of the gas mixture.

Using equation (2.5) into (2.4) [100]:

$$\rho_g \frac{D(\hat{h}_g)}{Dt} - \rho_g \nu_g \frac{D(p_g)}{Dt} - p_g \rho_g \frac{D(\nu_g)}{Dt} = -\vec{\nabla} \cdot \vec{q} - p_g \left(\vec{\nabla} \cdot \vec{v}_g\right) - (\bar{\bar{\tau}} \cdot \vec{v}_g) \tag{2.6}$$

Now since specific volume, ν_g, is basically inverse of the density, ρ_g, and also combining the last term on the left hand side with the second term on the right hand side (accounting for continuity principle):

$$\rho_g \frac{D(\hat{h}_g)}{Dt} = -\vec{\nabla} \cdot \vec{q} - (\bar{\bar{\tau}} \cdot \vec{v}_g) + \frac{D(p_g)}{Dt} + S_{heat} \tag{2.7}$$

Finally, expanding the material derivative, $\frac{D()}{Dt}$, and assuming ρ_g to be constant, equation (2.7) can be expressed as:

$$\frac{\partial(\rho_g \hat{h}_g)}{\partial t} = -\vec{\nabla} \cdot \left(\rho_g \hat{h}_g \vec{v}_g\right) - \vec{\nabla} \cdot \vec{q} - (\bar{\bar{\tau}} \cdot \vec{v}_g) + \frac{D(p_g)}{Dt} \tag{2.8}$$

Following assumptions are being considered:

1. Ideal gas mixtures exist inside the layers.

2. Steady state model, hence all time derivative terms would be zero.

3. Soret and Dufour effects are neglected since the thermo-diffusion effect is negligible at fuel cell operating temperatures [8].

4. Velocity gradients are generally negligible in a PEMFC, hence heat generation due to viscous dissipation is neglected (very low Brinkmann number).

5. Pressure gradients are negligible, hence material derivative of the gas mixture pressure, $\frac{D(p_g)}{Dt}$, is considered zero.

The thermal transport given as equation (2.8) is valid for continuum only. PEMFC layers are composite porous media which consist of at least two different species. So after performing average integration over a REV and considering the above stated assumptions, thermal transport equation valid over a PEMFC layer is obtained as:

$$\vec{\nabla} \cdot \left(\epsilon \rho_g \hat{h}_g \vec{v_g} \right) = \vec{\nabla} \cdot \left(k^{eff} \vec{\nabla} T \right) - \vec{\nabla} \cdot \left(\sum \bar{H}_i \vec{N}_i \right) + S_{heat} - \dot{W}_{electrical} \tag{2.9}$$

where ϵ is porosity, k^{eff} is the effective thermal conductivity, $\vec{N}_i$ is the effective molar flux of specie i, S_{heat} and $\dot{W}$ are volumetric rates of heat production and work done by the system respectively.

In Equation (2.9), the left hand side term corresponds to enthalpy transport due to convection of the mixture, first term on the right hand side corresponds to heat transport due to Fourier conduction, and second term corresponds to enthalpy transport due to inter-diffusion amongst various species. In a fuel cell, there are various other sources, such as, irreversible heat generation associated with the electro-chemical reaction. These additional heat source/sink terms are included in the third term on the right hand side of equation (2.9). Finally the last term on the right hand side of equation (2.9) considers the electrical work done by the fuel cell. Since, there are three modes of heat transport, namely, conduction, convection and diffusion, it would be worthwhile to perform an order of magnitude analysis on these individual heat transport modes. This is considered in the next section.

2.2.1 Order of magnitude analysis

There are various species transported inside a fuel cell, *viz.*, gases, electrons, protons, and sorbed water. It will be seen later that the diffusive enthalpy transport term

corresponding to ionic species can be transformed into heat sources, hence they are not considered in the order of magnitude analysis here. Also enthalpy transport due to sorbed water is not considered, since it is generally smaller than the enthalpy transport due to gas diffusion. Heat transport due to conduction, convection of the gas mixture and diffusion of individual gases, are compared in this analysis. In this thesis, infinitely dilute gaseous mixtures are assumed, hence gases diffuse according to Fick's law. The effective molar flux due to diffusion of the gas i, $\vec{N}_i$, can therefore be written as:

$$\vec{N}_i = -D_i^{eff} c_{tot} \vec{\nabla} x_i \tag{2.10}$$

where D_i^{eff} and x_i are the effective diffusion coefficient and the mole fraction of the gas i respectively, and c_{tot} is the molar concentration of the total gas mixture.

For a PEMFC, the order with which each of the following quantities scale is given as follows:

$$\begin{aligned}
\epsilon &\sim 10^{-1}, \\
T &\sim 10^{2} \ [K], \\
\vec{v}_g &\sim 10^{-4} \ \left[m \cdot s^{-1}\right] \quad \text{Ref. [17]}, \\
k^{eff} &\sim 10^{0} \ \left[W \cdot cm^{-1} \cdot K^{-1}\right] \quad \text{Ref. [30]}, \\
D_i^{eff} &\sim 10^{-5} \ \left[m^2 \cdot s^{-1}\right], \\
\rho_g &\sim 10^{0}, \ \left[kg \cdot m^{-3}\right], \\
\hat{C}_{p_g} &\sim 10^{4} \ \left[J \cdot kg^{-1} \cdot K^{-1}\right], \\
\bar{C}_{p_i} &\sim 10^{1}, \ \left[J \cdot mol^{-1} \cdot K^{-1}\right], \\
\hat{h}_g = \hat{C}_{p_g} T &\sim 10^{4} \times 10^{2} \sim 10^{6} \ \left[J \cdot kg^{-1}\right], \\
\bar{H}_i = \bar{C}_{p_i} T &\sim 10^{1} \times 10^{2} \sim 10^{3} \ \left[J \cdot mol^{-1}\right], \\
p_{tot} &\sim 10^{5} \ [Pa], \\
c_{tot} &\sim \frac{p_{tot}}{RT} \ \left[Pa \times J^{-1} \cdot mol \cdot K \times K^{-1}\right] \\
&\sim 10^{5} \times 10^{-1} \times 10^{-2} \\
&\sim 10^{2} \ \left[mol \cdot m^{-3}\right]
\end{aligned}$$

Convection enthalpy transport term is: $\vec{\nabla} \cdot \left(\epsilon \rho_g \hat{h}_g \vec{v}_g\right) \sim 10^1/L$.
Conduction heat transport term is: $\vec{\nabla} \cdot \left(k^{eff} \vec{\nabla} T\right) \sim 10^2/L^2$.
Diffusion enthalpy transport term is: $\vec{\nabla} \cdot \left(\bar{H}_i D_i^{eff} c_{tot} \vec{\nabla} x_i\right) \sim 10^0/L^2$.

In a PEMFC, the characteristic length scale, L, is of the order of 10^{-5} $[m]$. Hence it can be written:

$$\mathcal{O}(convection) : \mathcal{O}(diffusion) : \mathcal{O}(conduction) \sim 10^{-6} : 10^{-2} : 10^{0} \tag{2.11}$$

Clearly the convective enthalpy transport is negligible inside a PEMFC while the enthalpy transport due to diffusion is still significant even though it is two order of magnitude smaller than the heat transport due to Fourier conduction. On the basis of this analysis, the convection term in the Equation (2.9) can be neglected and the thermal transport equation can be rewritten as shown below:

$$\vec{\nabla} \cdot \left(k^{eff} \vec{\nabla} T \right) - \vec{\nabla} \cdot \left(\sum \bar{H}_i \vec{N}_i \right) + S_{heat} - \dot{W}_{electrical} = 0 \tag{2.12}$$

In various PEMFC layers, different species transport inside the layer. Also heat sources vary with the layer. For instance, electrochemical reactions take place only inside the catalyst layer, hence there is irreversible heat generation inside the catalyst layer only, but not in the porous transport layers (GDL or MPL) and the polymer electrolyte membrane. Hence it is necessary to detail the thermal transport equation (2.12) for various layers separately, which are described in the subsequent sections.

2.2.2 Thermal transport equation in porous diffusion media

This section covers both porous diffusion media inside the PEMFC, *viz.*, gas diffusion layer and microporous layer. Humidified air (consisting mainly oxygen, water vapour and nitrogen) is supplied to the cathode electrode. The mole fraction of nitrogen gas, x_{N_2}, can be determined as, $1 - x_{O_2} - x_{N_2}$. So nitrogen gas transport is not solved in the MEA model. In the cathode side of the PEMFC, four species, *viz.*, oxygen, water vapour, nitrogen and electrons are transported. The cathode gas mixture is assumed to be infinitely dilute with nitrogen gas as the solvent. Gases (oxygen and water vapour) diffuse in nitrogen, according to Fick's law. There is neither heat generation nor work done corresponding to the electrochemical reaction. Hence equation (2.12) can be expanded as follows:

$$\vec{\nabla} \cdot \left(k^{eff} \vec{\nabla} T \right) - \vec{\nabla} \cdot \left(\bar{H}_{O_2} \vec{N}_{O_2} \right) - \vec{\nabla} \cdot \left(\bar{H}_{H_2O} \vec{N}_{H_2O} \right) - \vec{\nabla} \cdot \left(\bar{H}_{N_2} \vec{N}_{N_2} \right) - \vec{\nabla} \cdot \left(\bar{H}_{e^-} \vec{N}_{e^-} \right) = 0 \tag{2.13}$$

The molar flux of the total gas mixture, N_g, can be expressed as:

$$\vec{N}_g = \vec{N}_{N_2} + \vec{N}_{O_2} + \vec{N}_{H_2O} = c_{tot} \ \vec{v}_g \tag{2.14}$$

where c_{tot} is concentration of the total gas mixture. Since the gas mixture velocity, $\vec{v}_g$, is assumed to be zero:

$$\vec{N}_g = \vec{N}_{N_2} + \vec{N}_{O_2} + \vec{N}_{H_2O} = 0 \tag{2.15}$$

$$\Rightarrow \vec{N}_{N_2} = -\vec{N}_{O_2} - \vec{N}_{H_2O} \tag{2.16}$$

The equation (2.13) can therefore be expressed as:

$$\vec{\nabla}\cdot\left(k^{eff}\vec{\nabla}T\right) - \vec{\nabla}\cdot\left((\bar{H}_{O_2} - \bar{H}_{N_2})\vec{N}_{O_2}\right) - \vec{\nabla}\cdot\left((\bar{H}_{H_2O} - \bar{H}_{N_2})\vec{N}_{H_2O}\right) - \vec{\nabla}\cdot\left(\bar{H}_{e^-}\vec{N}_{e^-}\right) = 0 \tag{2.17}$$

Now considering the enthalpy transport due to electron movement in the solid phase of the porous media:

$$-\vec{\nabla}\cdot\left(\vec{N}_{e^-}\bar{H}_{e^-}\right) = -\vec{N}_{e^-}\cdot\vec{\nabla}\bar{H}_{e^-} - \bar{H}_{e^-}\vec{\nabla}\cdot\vec{N}_{e^-} \tag{2.18}$$

In the porous diffusion media of the PEMFC, there is no production/consumption of electrons as no electrochemical reactions are taking place inside the layer. Hence:

$$\vec{\nabla}\cdot\vec{N}_{e^-} = 0 \tag{2.19}$$

Also the molar enthalpy of an electron, $\bar{H}_{e^-}$, can be simplified using electrochemical potentials [16, 101]. Since the reference chemical potential of electron, $\hat{\mu}^0_{e^-}$ is constant:

$$\begin{aligned}\vec{\nabla}\bar{H}_{e^-} &= \vec{\nabla}\bar{\mu}_{e^-} \\ &= \vec{\nabla}\hat{\mu}^0_{e^-} - F\vec{\nabla}\phi_s \\ &= -F\vec{\nabla}\phi_s\end{aligned} \tag{2.20}$$

Electron movement inside the porous layer is governed by Ohm's law:

$$\vec{N}_{e^-} = +\frac{\sigma_s^{eff}}{F}\vec{\nabla}\phi_s \tag{2.21}$$

where σ_s^{eff} is the effective electron conductivity, F is the universal Faraday's constant and ϕ_s is the solid phase potential. Thus by combining the results above, Equation (2.18) is simplified as follows:

$$-\vec{\nabla}\cdot\left(\vec{N}_{e^-}\bar{H}_{e^-}\right) = \sigma_s^{eff}\left(\vec{\nabla}\phi_s\cdot\vec{\nabla}\phi_s\right) \tag{2.22}$$

Hence diffusion enthalpy transport due to electron movement inside the layer is expressed as a heating source term due to the irreversibility associated with electron movement. This is popularly known as Ohmic heating or Joule heating inside the

conductive solid matrix of the porous layer.

There is no production/consumption of gaseous species inside these layers:

$$\nabla \cdot \vec{N}_{O_2} = 0 \tag{2.23}$$

$$\nabla \cdot \vec{N}_{H_2O} = 0 \tag{2.24}$$

Considering Fick's law of diffusion for species transport inside the layer (Equation (2.10)), thermal transport equation in the cathode GDL/MPL is expressed as follows:

$$\begin{aligned}\vec{\nabla} \cdot \left(k^{eff} \vec{\nabla} T\right) + D^{eff}_{O_2,N_2} c_{tot} \vec{\nabla} x_{O_2} \cdot (\vec{\nabla} \bar{H}_{O_2} - \vec{\nabla} \bar{H}_{N_2}) \\ + D^{eff}_{H_2O,N_2} c_{tot} \vec{\nabla} x_{H_2O} \cdot (\vec{\nabla} \bar{H}_{H_2O} - \vec{\nabla} \bar{H}_{N_2}) + \sigma_s^{eff} \left(\vec{\nabla} \phi_s \cdot \vec{\nabla} \phi_s\right) = 0\end{aligned} \tag{2.25}$$

Humidified hydrogen is supplied in the anode electrode of the PEMFC. Anode gas mixture is also assumed to be infinitely dilute, consisting mainly of hydrogen. Hydrogen mole fraction, x_{H_2}, can be determined as, $1 - x_{H_2O}$. So transport of the hydrogen gas is therefore not considered in the MEA model. In the anode side of the PEMFC, three species, *viz.*, hydrogen, water vapour and electrons are transported. Water vapour diffuse in hydrogen, according to Fick's law. The gas mixture velocity in the anode is also assumed to be zero. Thus the thermal transport equation in the anode GDL/MPL, can be written as follows:

$$\vec{\nabla} \cdot \left(k^{eff} \vec{\nabla} T\right) + D^{eff}_{H_2O,H_2} c_{tot} \vec{\nabla} x_{H_2O} \cdot (\vec{\nabla} \bar{H}_{H_2O} - \vec{\nabla} \bar{H}_{H_2}) + \sigma_s^{eff} \left(\vec{\nabla} \phi_s \cdot \vec{\nabla} \phi_s\right) = 0 \tag{2.26}$$

Now for an ideal gas, molar enthalpy, $\bar{H}$, is a function of temperature alone [102] and it can be expressed as:

$$\bar{H}_i = \bar{H}_i^{f0} + \bar{C}_{p_i}(T - T^{f0}) \tag{2.27}$$

where $\bar{C}_{p_i}$ is the molar specific heat of gas i, and can be expressed as empirical functions of temperature as [102]:

$$\bar{C}_{p_i} = \left[C_{0,i} + C_{1,i}\left(\frac{T}{1000}\right) + C_{2,i}\left(\frac{T}{1000}\right)^2 + C_{3,i}\left(\frac{T}{1000}\right)^3\right] M_i \tag{2.28}$$

where $C_{0,i}$, $C_{1,i}$, $C_{2,i}$, $C_{3,i}$ are empirical constants for gas i. Values for these constants for different gases are tabulated in Table 2.1.

Now since molar enthalpy of gaseous species is a function of temperature alone, the thermal transport equation for the cathode GDL/MPL can be written finally as:

$$\vec{\nabla}\cdot\left(k^{eff}\vec{\nabla}T\right)+D^{eff}_{O_2,N_2}c_{tot}\left(\frac{\partial\bar{H}_{O_2}}{\partial T}-\frac{\partial\bar{H}_{N_2}}{\partial T}\right)\vec{\nabla}T\cdot\vec{\nabla}x_{O_2} + D^{eff}_{H_2O,N_2}c_{tot}\left(\frac{\partial\bar{H}_{H_2O}}{\partial T}-\frac{\partial\bar{H}_{N_2}}{\partial T}\right)\vec{\nabla}T\cdot\vec{\nabla}x_{H_2O}+\sigma_s^{eff}\left(\vec{\nabla}\phi_s\cdot\vec{\nabla}\phi_s\right)=0 \tag{2.29}$$

Similarly for anode GDL/MPL, the thermal transport equation can be written as:

$$\vec{\nabla}\cdot\left(k^{eff}\vec{\nabla}T\right)+D^{eff}_{H_2O,H_2}c_{tot}\left(\frac{\partial\bar{H}_{H_2O}}{\partial T}-\frac{\partial\bar{H}_{H_2}}{\partial T}\right)\vec{\nabla}T\cdot\vec{\nabla}x_{H_2O}+\sigma_s^{eff}\left(\vec{\nabla}\phi_s\cdot\vec{\nabla}\phi_s\right)=0 \tag{2.30}$$

As discussed in the literature review, thermal conductivity of the GDL has been extensively measured in the literature [51]. However same is not true for other MEA layers, *viz.*, MPL, CL and membrane. So parametric study will be performed on thermal conductivity values of MEA layers (except GDL). A temperature-dependent empirical correlation is used for the thermal conductivity values in the GDL. Zamel et al. [46, 47] studied the temperature variation of through-plane and in-plane thermal conductivity values of Toray® TGP-H-120 carbon paper GDLs, from -50 to 120 ℃. The experimental setup used thermal capacitance (slug) calorimeter technique based on ASTM E2584-07. Effective thermal conductivity in through-plane direction is given as follows [47]:

$$k^{eff}_{\text{through}}=M\left(-7.166\times10^{-6}\;T^{\circ 3}+2.24\times10^{-3}\;T^{\circ 2}-0.237\;T^{\circ}+20.1\right)\;\;[\text{W/(m-K)}] \tag{2.31}$$

where T° is the temperature in degree-Celsius and M is the heat barrier resistance coefficient. M depends on inner micro-structure of the carbon fibres and cracks present in them. It is also dependent on the temperature and compaction pressure. Zamel et al. [47] has graphically presented the values of M under different operating conditions. It is observed that the through-plane thermal conductivity increases with temperature because carbon fibres expand thereby reducing the contact resistance. After fitting to the data by Zamel et al., following correlation is obtained:

$$M=-1.495\times10^{-11}\;T^{\circ 5}+2.601\times10^{-9}\;T^{\circ 4}-6.116\times10^{-8}\;T^{\circ 3}-9.829\times10^{-6}\;T^{\circ 2}+8.754\times10^{-4}\;T^{\circ}+0.0664 \tag{2.32}$$

Effective thermal conductivity in the in-plane direction is expressed as [46]:

$$k^{eff}_{\text{in-plane}}=-7.166\times10^{-6}\;T^{\circ 3}+2.24\times10^{-3}\;T^{\circ 2}-0.237\;T^{\circ}+20.1\;\;[\text{W/(m-K)}] \tag{2.33}$$

2.2.3 Thermal transport equation in the membrane layer

In the polymer electrolyte membrane, there are basically two moving species, *viz.*, sorbed water (λ) and protons (H^+). There is neither heat generation nor work done corresponding to the electrochemical reaction. Hence Equation (2.12) can be expanded as follows:

$$\vec{\nabla} \cdot \left(k^{eff} \vec{\nabla} T \right) - \vec{\nabla} \cdot \left(\bar{H}_{\lambda} \vec{N}_{\lambda} \right) - \vec{\nabla} \cdot \left(\bar{H}_{H^+} \vec{N}_{H^+} \right) = 0 \tag{2.34}$$

Proton transport inside the membrane (electrolyte phase) is modelled using Ohm's law, hence using the same derivation principle as in section 2.2.2, the second term in the left hand side of the Equation (2.34) can be written as:

$$- \vec{\nabla} \cdot \left(\vec{N}_{H^+} \bar{H}_{H^+} \right) = \sigma_m^{eff} \left(\vec{\nabla} \phi_m \cdot \vec{\nabla} \phi_m \right) \tag{2.35}$$

Hence proton transport inside the electrolyte phase results in irreversible heat generation known as Ohmic heating.

Since there is no sorption/desorption and production/consumption of water taking place inside this layer:

$$\nabla \cdot \vec{N}_{\lambda} = 0 \tag{2.36}$$

For considering sorbed water transport inside the membrane, Springer et al. [103] model is used here. Sorbed water inside the membrane is assumed to be equilibrating with water vapour only. In vapour equilibriated membranes, sorbed water transport occurs via two modes, *viz.*, electro-osmotic drag and water diffusion. Besides this, there is a third mode of water transport due to temperature gradient across the membrane, known as thermal osmosis [104–107]. Details of the sorbed water transport model will be discussed during the overall MEA model description (Section 2.3.3), but the molar flux of sorbed water can be expressed as follows:

$$\vec{N}_{\lambda} = -\frac{n_d \ \sigma_m^{eff}}{F} \vec{\nabla} \phi_m - \frac{\rho_{dry}}{EW} D_{\lambda}^{eff} \vec{\nabla} \lambda - \frac{1}{M_{H_2O}} D_T^{eff} \vec{\nabla} T \tag{2.37}$$

Table 2.1 – Empirical constants and reference state values for determining molar specific heat, $\bar{C}_p$, of various gaseous species [102].

Gas	C_0	C_1	C_2	C_3	$\bar{H}^{f0}$	T^{f0}	M
O_2	0.88	-0.0001	0.54	-0.33	0	298	31.999
H_2	13.46	4.6	-6.85	3.79	0	298	2.016
H_2O	1.79	0.107	0.586	-0.20	-241826	298	18.015

where the first term on the right hand side accounts for electro-osmotic drag, the second term for water diffusion and the last term for thermo-osmotic diffusion. Also molar enthalpy of sorbed water, $\bar{H}_\lambda$, can be defined as:

$$\bar{H}_\lambda = \bar{H}_{H2O} - \bar{H}_{sorption} \tag{2.38}$$

where $\bar{H}_{sorption}$ is molar enthalpy change (heat release) corresponding to sorption of water vapour into the electrolyte and $\bar{H}_{H2O}$ is molar enthalpy of the water vapour. Ramousse et al. [19] has tabulated the various values of enthalpy of sorption/desorption reported in the literature for various polymer electrolyte membranes and concluded that this term is similar to the enthalpy of vaporization of water. Ostrovskii and Gostev [108] has shown that the enthalpy of sorption decreased from $68\,[kJ \cdot mol^{-1}]$ (at $\lambda \simeq 0$) to nearly $45\,[kJ \cdot mol^{-1}]$ (at $\lambda \simeq 5$), but values below the latent heat of water vaporization are not reached. In this thesis, $\bar{H}_{sorption}$ value is taken to be constant at $45\,[kJ \cdot mol^{-1}]$ which roughly corresponds to the latent heat of vaporization of water at 80 °C. The molar enthalpy of water vapour, $\bar{H}_{H2O}$, is obtained from the expressions given in Equation (2.27), (2.28) and Table 2.1. Equation (2.34) can therefore be expressed as follows:

$$\begin{aligned}\vec{\nabla}\cdot\left(k^{eff}\vec{\nabla}T\right) + \frac{n_d\ \sigma_m^{eff}}{F}\vec{\nabla}\phi_m\cdot\vec{\nabla}\bar{H}_\lambda + \frac{\rho_{dry}}{EW}D_\lambda^{eff}\vec{\nabla}\lambda\cdot\vec{\nabla}\bar{H}_\lambda \\ + \frac{1}{M_{H_2O}}D_T^{eff}\vec{\nabla}T\cdot\vec{\nabla}\bar{H}_\lambda + \sigma_m^{eff}\left(\vec{\nabla}\phi_m\cdot\vec{\nabla}\phi_m\right) = 0\end{aligned} \tag{2.39}$$

Since molar enthalpy of sorbed water, $\bar{H}_\lambda$, is a function of temperature alone, the thermal transport equation in the membrane can finally be written as:

$$\begin{aligned}\vec{\nabla}\cdot\left(k^{eff}\vec{\nabla}T\right) + \frac{n_d\ \sigma_m^{eff}}{F}\frac{\partial\bar{H}_\lambda}{\partial T}\vec{\nabla}T\cdot\vec{\nabla}\phi_m + \frac{\rho_{dry}}{EW}D_\lambda^{eff}\frac{\partial\bar{H}_\lambda}{\partial T}\vec{\nabla}T\cdot\vec{\nabla}\lambda \\ + \frac{1}{M_{H_2O}}D_T^{eff}\frac{\partial\bar{H}_\lambda}{\partial T}\vec{\nabla}T\cdot\vec{\nabla}T + \sigma_m^{eff}\left(\vec{\nabla}\phi_m\cdot\vec{\nabla}\phi_m\right) = 0\end{aligned} \tag{2.40}$$

2.2.4 Thermal transport equation in the catalyst layer

Besides heat transport, there is heat generation associated with the electrochemical reaction (reversible and irreversible), taking place inside the catalyst layer. However it will be seen that the reversible heat release term is automatically considered when enthalpy transport due to species is included. So the additional heat source term is only due to irreversibility of the electrochemical reaction. Due to the reaction, electrochemical work is also done by the system. Thus the thermal transport equation is written as [109]:

$$\vec{\nabla}\cdot\left(k^{eff}\vec{\nabla}T\right) - \vec{\nabla}\cdot\left(\sum\vec{N}_i\bar{H}_i\right) + S_{irrev} - \dot{W}_{electrical} = 0 \tag{2.41}$$

The electrical work can be written as follows:

$$-\dot{W}_{electrical} = \frac{j}{nF}\Delta\bar{G}_{overall} = -\frac{j}{nF}\left(\Delta\bar{H}_{overall} - T\Delta\bar{S}_{overall}\right) \tag{2.42}$$

where, $\Delta\bar{G}_{overall}$, $\Delta\bar{H}_{overall}$, $\Delta\bar{S}_{overall}$ are molar Gibbs free energy change, enthalpy change and entropy change respectively for the overall reaction producing n moles of electrons per mole of fuel, and j is the volumetric current density. Value of n is 2 for the overall fuel cell reaction producing water per unit mole of hydrogen gas used.

In the cathode catalyst layer, the transporting species are oxygen, water vapour, nitrogen, electrons, protons and sorbed water. Enthalpy transport term corresponding to moving species inside the layer can be broken down as follows:

$$-\vec{\nabla}\cdot\left(\sum\vec{N}_i\bar{H}_i\right) = -\sum\left(\bar{H}_i\vec{\nabla}\cdot\vec{N}_i\right) - \sum\left(\vec{N}_i\cdot\vec{\nabla}\bar{H}_i\right) \tag{2.43}$$

On considering the first term on the right hand side of the equation (2.43) and doing summation over all gaseous and ionic species (ignoring λ for the moment):

$$\begin{aligned}-\sum\left(\bar{H}_i\vec{\nabla}\cdot\vec{N}_i\right) = &-\bar{H}_{O_2}\vec{\nabla}\cdot\vec{N}_{O_2} - \bar{H}_{H_2O}\vec{\nabla}\cdot\vec{N}_{H_2O} - \bar{H}_{N_2}\vec{\nabla}\cdot\vec{N}_{N_2}\\ &- \bar{H}_{e^-}\vec{\nabla}\cdot\vec{N}_{e^-} - \bar{H}_{H^+}\vec{\nabla}\cdot\vec{N}_{H^+}\end{aligned} \tag{2.44}$$

Inside the cathode catalyst layer, the half-cell reaction of the oxygen reduction takes place. It can be written as follows:

$$\frac{1}{2}O_{2_{(g)}} + 2H^+_{(aq)} + 2e^-_{(s)} \longrightarrow H_2O_{(l)} \tag{2.45}$$

For the cathode reaction (2.45), molar enthalpy change per one mole of fuel (H_2) corresponding to ORR, $\Delta\bar{H}_{ORR}$, is expressed as follows:

$$\Delta\bar{H}_{ORR} = \bar{H}_{H_2O} - \frac{1}{2}\bar{H}_{O_2} - 2\bar{H}_{H^+} - 2\bar{H}_{e^-} \tag{2.46}$$

Since a single-phase model is considered in this part of the thesis, water is considered to be produced in the vapour phase. Oxygen, electrons and protons are consumed during the ORR. There is also sorption/desorption of water taking place inside the catalyst layer, as discussed in Section 2.3.4.2. Nitrogen is neither consumed nor produced inside the cathode catalyst layer. So the source/sink terms for various species inside the cathode catalyst layer, can be written as follows:

$$\vec{\nabla}\cdot\vec{N}_{O_2} = -\frac{j}{4F} \tag{2.47}$$

$$\vec{\nabla} \cdot \vec{N}_{H_2O} = \frac{j}{2F} - \frac{k_t \rho_{dry}}{EW} (\lambda_{eq} - \lambda) \tag{2.48}$$

$$\vec{\nabla} \cdot \vec{N}_{e^-} = -\frac{j}{F} \tag{2.49}$$

$$\vec{\nabla} \cdot \vec{N}_{H^+} = -\frac{j}{F} \tag{2.50}$$

$$\vec{\nabla} \cdot \vec{N}_{N_2} = 0 \tag{2.51}$$

Using equations (2.47), (2.48), (2.49), (2.50) and (2.51) into (2.44):

$$\begin{aligned} -\sum \left(\bar{H}_i \vec{\nabla} \cdot \vec{N}_i \right) &= \frac{j}{2F} \left(\frac{1}{2} \bar{H}_{O_2} - \bar{H}_{H_2O} + 2\bar{H}_{e^-} + 2\bar{H}_{H^+} \right) + \frac{k_t \rho_{dry}}{EW} (\lambda_{eq} - \lambda) \bar{H}_{H_2O} \\ &= -\frac{j}{2F} \Delta \bar{H}_{ORR} + \frac{k_t \rho_{dry}}{EW} (\lambda_{eq} - \lambda) \bar{H}_{H_2O} \end{aligned} \tag{2.52}$$

Hence it can be seen that the term corresponding to enthalpy change of the reaction in Equation (2.42) is cancelled by the enthalpy change term in the Equation (2.52). Also on the similar principles discussed in the previous sections:

$$-\vec{N}_{H^+} \cdot \vec{\nabla} \bar{H}_{H^+} = \sigma_m^{eff} \left(\vec{\nabla} \phi_m \cdot \vec{\nabla} \phi_m \right) \tag{2.53}$$

$$-\vec{N}_{e^-} \cdot \vec{\nabla} \bar{H}_{e^-} = \sigma_s^{eff} \left(\vec{\nabla} \phi_s \cdot \vec{\nabla} \phi_s \right) \tag{2.54}$$

Based on the above discussed simplifications, and considering Fick's law for gaseous species diffusion, the thermal transport equation (2.41) can be simplified as follows:

$$\begin{aligned} &\vec{\nabla} \cdot \left(k^{eff} \vec{\nabla} T \right) - \vec{N}_{O_2} \cdot (\vec{\nabla} \bar{H}_{O_2} - \vec{\nabla} \bar{H}_{N_2}) - \vec{N}_{H_2O} \cdot (\vec{\nabla} \bar{H}_{H_2O} - \vec{\nabla} \bar{H}_{N_2}) - \vec{\nabla} \cdot \left(\vec{N}_\lambda \bar{H}_\lambda \right) \\ &+ \sigma_m^{eff} \left(\vec{\nabla} \phi_m \cdot \vec{\nabla} \phi_m \right) + \sigma_s^{eff} \left(\vec{\nabla} \phi_s \cdot \vec{\nabla} \phi_s \right) + S_{irrev} + \frac{j}{2F} \left(-T \Delta \bar{S}_{ORR} \right) \\ &+ \frac{k_t \rho_{dry}}{EW} (\lambda_{eq} - \lambda) \bar{H}_{H_2O} = 0 \end{aligned} \tag{2.55}$$

$$\begin{aligned} \Rightarrow \quad &\vec{\nabla} \cdot \left(k^{eff} \vec{\nabla} T \right) + D_{O_2,N_2}^{eff} c_{tot} \vec{\nabla} x_{O_2} \cdot (\vec{\nabla} \bar{H}_{O_2} - \vec{\nabla} \bar{H}_{N_2}) \\ &+ D_{H_2O,N_2}^{eff} c_{tot} \vec{\nabla} x_{H_2O} \cdot (\vec{\nabla} \bar{H}_{H_2O} - \vec{\nabla} \bar{H}_{N_2}) - \vec{\nabla} \cdot \left(\vec{N}_\lambda \bar{H}_\lambda \right) + \sigma_m^{eff} \left(\vec{\nabla} \phi_m \cdot \vec{\nabla} \phi_m \right) \\ &+ \sigma_s^{eff} \left(\vec{\nabla} \phi_s \cdot \vec{\nabla} \phi_s \right) + S_{irrev} + \frac{j}{2F} \left(-T \Delta \bar{S}_{ORR} \right) + \frac{k_t \rho_{dry}}{EW} (\lambda_{eq} - \lambda) \bar{H}_{H_2O} = 0 \end{aligned} \tag{2.56}$$

Now on expanding the enthalpy transport term corresponding to sorbed water transport:

$$-\vec{\nabla}\cdot\left(\vec{N_\lambda}\bar{H}_\lambda\right) = -\vec{N_\lambda}\cdot\vec{\nabla}\bar{H}_\lambda - \bar{H}_\lambda\vec{\nabla}\cdot\vec{N_\lambda} \tag{2.57}$$

Since the membrane in consideration is in equilibrium with water vapour, there is an equilibrium value for the membrane water content, λ_{eq} corresponding to water vapour content inside the layer. So the sorbed water also has a source/sink corresponding to sorption/desorption in the catalyst layer. This is given as follows (detailed in the Section 2.3.4.2):

$$\vec{\nabla}\cdot\vec{N_\lambda} = \frac{k_t\rho_{dry}}{EW}\left(\lambda_{eq}-\lambda\right) \tag{2.58}$$

On using the definition for molar enthalpy of sorbed water, $\bar{H}_\lambda$, given in Equation (2.38) and combining with the source term definitions above, Equation (2.57) is simplified as follows:

$$-\vec{\nabla}\cdot\left(\vec{N_\lambda}\bar{H}_\lambda\right) = -\vec{N_\lambda}\cdot\vec{\nabla}\bar{H}_\lambda - \frac{k_t\rho_{dry}}{EW}\left(\lambda_{eq}-\lambda\right)\bar{H}_\lambda \tag{2.59}$$

Combining this into the Equation (2.56) and using Equation (2.38):

$$\begin{aligned}
&\vec{\nabla}\cdot\left(k^{eff}\vec{\nabla}T\right) + D^{eff}_{O_2,N_2}c_{tot}\vec{\nabla}x_{O_2}\cdot\left(\vec{\nabla}\bar{H}_{O_2}-\vec{\nabla}\bar{H}_{N_2}\right)\\
&+ D^{eff}_{H_2O,N_2}c_{tot}\vec{\nabla}x_{H_2O}\cdot\left(\vec{\nabla}\bar{H}_{H_2O}-\vec{\nabla}\bar{H}_{N_2}\right) - \vec{N_\lambda}\cdot\vec{\nabla}\bar{H}_\lambda + \sigma_m^{eff}\left(\vec{\nabla}\phi_m\cdot\vec{\nabla}\phi_m\right)\\
&+ \sigma_s^{eff}\left(\vec{\nabla}\phi_s\cdot\vec{\nabla}\phi_s\right) + S_{heat,irrev} + \frac{j}{2F}\left(-T\Delta\bar{S}_{ORR}\right) + \frac{k_t\rho_{dry}}{EW}\left(\lambda_{eq}-\lambda\right)\bar{H}_{sorption} = 0
\end{aligned} \tag{2.60}$$

The rightmost term in the above equation corresponds to heat release due to sorption of water inside the catalyst layer. It is noteworthy that during the process of desorption, source term in the Equation (2.58) will automatically become negative and hence heat will be removed during that process. As discussed before, molar enthalpies of gaseous species and sorbed water are function of temperature alone. Thus considering the sorbed water transport due to electro-osmotic drag, water diffusion and thermo-osmotic diffusion, the thermal transport equation inside the cathode catalyst layer can finally be expressed as:

$$\begin{aligned}
&\vec{\nabla}\cdot\left(k^{eff}\vec{\nabla}T\right) + D^{eff}_{O_2,N_2}c_{tot}\left(\frac{\partial\bar{H}_{O_2}}{\partial T}-\frac{\partial\bar{H}_{N_2}}{\partial T}\right)\vec{\nabla}T\cdot\vec{\nabla}x_{O_2}\\
&+ D^{eff}_{H_2O,N_2}c_{tot}\left(\frac{\partial\bar{H}_{H_2O}}{\partial T}-\frac{\partial\bar{H}_{N_2}}{\partial T}\right)\vec{\nabla}T\cdot\vec{\nabla}x_{H_2O} + \frac{n_d\ \sigma_m^{eff}}{F}\frac{\partial\bar{H}_\lambda}{\partial T}\vec{\nabla}T\cdot\vec{\nabla}\phi_m
\end{aligned}$$

$$+\frac{\rho_{dry}}{EW}D_{\lambda}^{eff}\frac{\partial \bar{H}_{\lambda}}{\partial T}\vec{\nabla}T\cdot\vec{\nabla}\lambda+\frac{1}{M_{H_2O}}D_{T}^{eff}\frac{\partial \bar{H}_{\lambda}}{\partial T}\vec{\nabla}T\cdot\vec{\nabla}T+S_{heat}=0 \tag{2.61}$$

where, S_{heat} includes:

1. Irreversible heat generation inside the electrochemical reaction is formulated as:

$$S_{irrev,ORR}=-j\eta=-j\left(\phi_s-\phi_m-E_{ORR}\right) \tag{2.62}$$

   where E_{ORR} is the equilibrium potential for the ORR determined by the Nernst equation [43, 110]. The over-potential, η, for a cathodic reaction is negative, hence a negative sign is used in the formulation above.

2. Reversible heat release due to half-cell reaction of ORR. As discussed in Section 1.3.1, the entropy change corresponding to the overall reaction (hence reversible heat release) is well defined. However the distribution of reversible heat release in individual half cell reactions is ambiguous. A factor, f_{ORR}, is used to consider the fraction of reversible heat released in the ORR and given as:

$$S_{rev,ORR}=\frac{j}{2F}\left(-T\Delta\bar{S}_{ORR}\right)=\frac{j}{2F}\left(-Tf_{ORR}\Delta\bar{S}_{overall}\right) \tag{2.63}$$

   where $\bar{S}_{overall}$ is the overall entropy change per mole of fuel (H_2), which is given in the Equation (1.8).

3. For consistency with the single-phase model, an additional heat sink term corresponding to complete vaporization of liquid water produced during the ORR is considered. It is formulated as:

$$S_{vap,ORR}=-\frac{j}{2F}\bar{H}_{lv} \tag{2.64}$$

   where $\bar{H}_{lv}$ is the molar latent heat of vaporization of water, which is a function of temperature and is given as [111]:

$$\begin{aligned}\bar{H}_{lv}=\ & 2500.304-2.252\ (T-273.15)-0.0215\ (T-273.15)^{1.5}\\ & +3.175\times10^{-4}\ (T-273.15)^{2.5}-2.861\times10^{-5}\ (T-273.15)^{3}\end{aligned} \tag{2.65}$$

4. Irreversible Ohmic heating due to electron and proton movement inside the catalyst layer is given as:

$$S_{ohmic,CL}=\sigma_m^{eff}\left(\vec{\nabla}\phi_m\cdot\vec{\nabla}\phi_m\right)+\sigma_s^{eff}\left(\vec{\nabla}\phi_s\cdot\vec{\nabla}\phi_s\right) \tag{2.66}$$

5. Heat release/absorption due to sorption/desorption process of water vapour inside the catalyst layer is given as:

$$S_{sorption,CL} = \frac{k_t \rho_{dry}}{EW} \left(\lambda_{eq} - \lambda\right) \bar{H}_{sorption} \tag{2.67}$$

Similarly inside the anode catalyst layer, the transporting species are water vapour, hydrogen, protons, electrons and sorbed water. Similar to the discussion above, the thermal transport equation for the anode catalyst layer can be expressed as:

$$\begin{aligned}
&\vec{\nabla} \cdot \left(k^{eff} \vec{\nabla} T\right) + D^{eff}_{H_2O,H_2} c_{tot} \left(\frac{\partial \bar{H}_{H_2O}}{\partial T} - \frac{\partial \bar{H}_{H_2}}{\partial T}\right) \vec{\nabla} T \cdot \vec{\nabla} x_{H_2O} \\
&+ \frac{n_d \, \sigma^{eff}_m}{F} \frac{\partial \bar{H}_\lambda}{\partial T} \vec{\nabla} T \cdot \vec{\nabla} \lambda + \frac{\rho_{dry}}{EW} D^{eff}_\lambda \frac{\partial \bar{H}_\lambda}{\partial T} \vec{\nabla} T \cdot \vec{\nabla} \lambda + \frac{1}{M_{H_2O}} D^{eff}_T \frac{\partial \bar{H}_\lambda}{\partial T} \vec{\nabla} T \cdot \vec{\nabla} T \\
&+ S_{heat} = 0
\end{aligned} \tag{2.68}$$

where S_{heat} includes:

1. Irreversible heat generation inside the electrochemical reaction. It is formulated as:

$$S_{irrev,HOR} = j\eta = j\left(\phi_s - \phi_m - E_{HOR}\right) \tag{2.69}$$

   where E_{HOR} is the equilibrium potential for HOR, determined by the Nernst equation [43, 110]. The over-potential, η, for a anodic reaction is positive, hence no negative sign is used in the formulation above.

2. Reversible heat release due to half-cell reaction of HOR and is given as:

$$S_{rev,HOR} = \frac{j}{2F}\left(-T\Delta\bar{S}_{HOR}\right) = \frac{j}{2F}\left(-T(1 - f_{ORR})\Delta\bar{S}_{overall}\right) \tag{2.70}$$

3. Irreversible Ohmic heating due to electron and proton movement inside the catalyst layer, formulated similar to the Equation (2.66).

4. Heat release/absorption due to sorption/desorption process of water vapour inside the catalyst layer, formulated similar to the Equation (2.67).

Finally it is noteworthy that the energy of dissolution of H_2/O_2 in the polymer electrolyte is neglected here. Details of the membrane electrode assembly model are discussed in the next section.

2.3 Membrane Electrode Assembly Model

The membrane electrode assembly (MEA) model considered in this work is based upon the single-phase, isothermal model by Secanell [41], later improved upon by Dobson [42] and Moore [43]. It is an across-the-channel unit cell model, as shown in Figure 2.1. It is assumed that the fuel cell is operating under equilibriated conditions, *i.e.*, steady-state behaviour is modelled. The two-dimensional model is comprised of seven layers, *viz.*, anode gas diffusion layer (AGDL), anode microporous layer (AMPL), anode catalyst layer (ACL), membrane layer (ML), cathode catalyst layer (CCL), cathode microporous layer (CMPL) and cathode gas diffusion layer (CGDL). Hydrogen gas (fuel) flows into the MEA from the AGDL-Gas channel boundary (top half of the left side). The other reactant gas (oxygen) flows in from the CGDL-Gas channel boundary (top half of the right side). Electrons flow in and out from the CGDL-Bipolar plate boundary (bottom half of the right side) and AGDL-Bipolar plate boundary (bottom half of the left side) respectively. The model solves for transport of gaseous species, ionic (charged) species, sorbed water and heat (incorporated in this work).

Reactant gases, *viz.*, hydrogen and oxygen, travel through the GDL, MPL and react inside the CL on the anode and cathode electrodes respectively. A mixture of oxygen, nitrogen and water vapour is supplied in the cathode gas channel. Moreover water is produced during the ORR. Since the model is single-phase, water produced

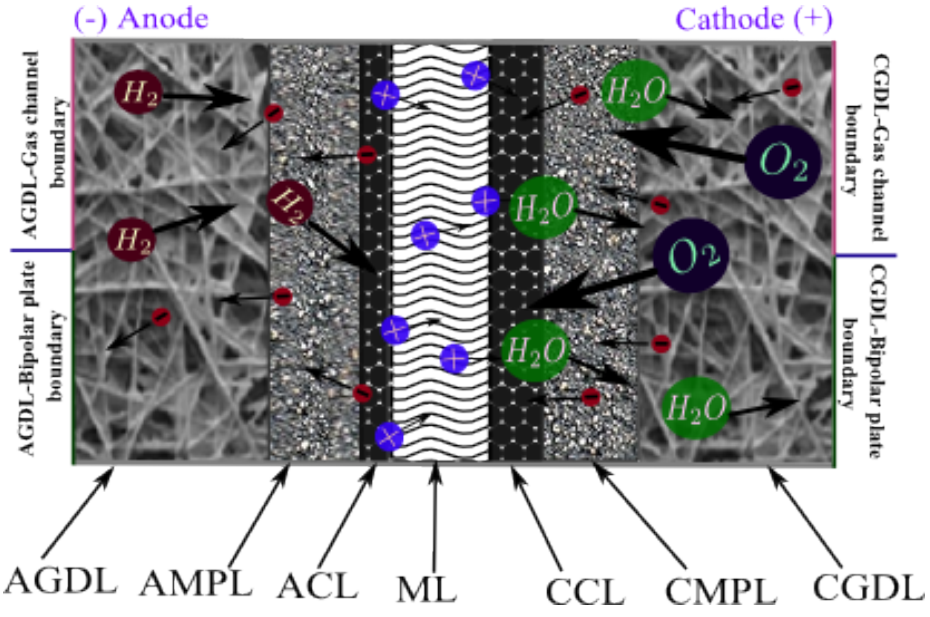

Figure 2.1 – Schematics of the MEA model showing the transport of species.

due to ORR is assumed to be in vapour phase as well as presence of liquid water and condensation/evaporation effects are neglected in this part of the work. The gaseous mixture on the cathode side is assumed to be a dilute mixture of nitrogen (more than 60 %), containing small amounts of oxygen and water vapour. Hence there is no need to solve for the transport of nitrogen gas. A binary mixture of hydrogen and water vapour is supplied at the anode side. The amount of gases inside a mixture can be determined by their respective mole fractions. A mole fraction is defined as the amount (in moles) of a constituent divided by the total amount of all constituents (in moles) in a mixture. Summation of the mole fractions of all gases present inside the mixture should be equal to one. So there is no need to solve for the hydrogen transport as its amount can be determined from the water molar fraction at the anode side. So the model solves for the transport of oxygen mole fraction, x_{O_2}, through the CGDL, CMPL and CCL (cathode side). It also solves for the transport of water mole fraction, x_{H_2O}, through all porous layers in the MEA, *viz.*, CGDL, CMPL, CCL, ACL, AGDL and AMPL.

Electrons are produced and consumed inside the HOR and ORR reactions respectively. Transport of electrons is essential for the electric current to flow. All the porous layers, *viz.*, CGDL, CMPL, CCL, ACL, AGDL and AMPL, are electronically conductive due to the presence of carbon in them. Transport of protons is also very essential for the overall reaction to proceed. Protons are produced inside the ACL due to HOR. They travel through the ML reaching the reactions sites inside the CCL, where they are consumed. Protons travel through the electrolyte phase present in the catalyst layers and the membrane. Transport of the ionic species (protons and electrons) is governed by the Ohm's law, driven by the potential differences. So the model solves for two more variables, *viz.*, solid potential, ϕ_s, and electrolyte potential, ϕ_m, through the respective conductive layers as discussed above.

Water exists as sorbed form (other than liquid and vapour phase) inside the electrolyte. Electrolyte inside the catalyst layers adsorb/desorb water vapour, which in turn increases/decreases the water content inside the electrolyte. Sorbed water can transport under the effect of concentration gradients, temperature gradients and drag due to proton transport. Membrane and ionomer inside the CL should be adequately humidified for better proton transport. Dried out membrane leads to large ohmic drop causing significant performance losses. Thus water exists as sorbed form also inside the CLs and ML. So the model solves for the transport of membrane water content, λ, through the electrolyte phase in the CL and ML.

Mass balance over an infinitesimal control volume can be performed to derive the governing equation for the transport of any species i. It can be expressed as [41]:

$$\frac{\partial c_i}{\partial t} + \vec{\nabla} \cdot \vec{N}_i = S_i \tag{2.71}$$

where c_i is the molar concentration of the species i, S_i is the volumetric source term expressed as number of moles of species i produced in a unit volume per unit time, and $\vec{N}_i$ is the molar flux of expressed as number of moles of species i leaving the control volume through a unit area in unit time. Under the steady-state conditions, there is no accumulation of the species, so $\partial c_i/\partial t = 0$. Thus the governing equations for the remaining five variables take the form as shown in Equation (2.72). Transport details of the remaining five species and their layer specific effective transport properties are incorporated into the Equation (2.72) and discussed in the subsequent sections.

$$\begin{aligned}
\vec{\nabla} \cdot \vec{N}_{O_2} &= S_{O_2} \\
\vec{\nabla} \cdot \vec{N}_{H_2O} &= S_{H_2O} \\
\vec{\nabla} \cdot \vec{N}_{H^+} &= S_{H^+} \\
\vec{\nabla} \cdot \vec{N}_{e^-} &= S_{e^-} \\
\vec{\nabla} \cdot \vec{N}_{\lambda} &= S_{\lambda}
\end{aligned} \tag{2.72}$$

2.3.1 Gaseous species transport

The MEA model is based on a straight-channel PEMFC configuration as shown in Figure 1.1. In a straight-channel configuration, reactant gases are largely transported to the catalyst layers by diffusion [41]. There is negligible pressure drop inside the MEA. So the MEA model is assumed to be isobaric and convective transport of the gases is neglected in this work. The cathode electrode is supplied with the humidified air, *i.e.*, mainly oxygen, nitrogen and water vapour. Similarly the anode side is supplied with a binary mixture of hydrogen and water vapour. These are multicomponent mixtures, hence the diffusion of individual gaseous species is governed by the Maxwell-Stefan diffusion model [100]. However in this work, air is assumed to be an infinitely dilute mixture which contains mainly nitrogen and small quantities of oxygen and water vapour. So the gas diffusion in the cathode side is solved using the Fick's law. As a simplifying assumption, water vapour transport in the anode side is also solved using the Ficks's law. As discussed previously that the transport of hydrogen mole fraction is not solved for. Since the anode gas mixture is a binary mixture, the hydrogen mole fraction can be determined using, $x_{H_2} = 1 - x_{H_2O}$.

According to Fick's law, the molar flux of gas i can be expressed as [100, 112]:

$$\vec{N}_i = -D_{i,j}^{eff} \vec{\nabla} c_i \tag{2.73}$$

where $D_{i,j}^{eff}$ is the effective diffusion coefficient of the gas i with respect to the gas j, obtained by correcting the bulk diffusion coefficient, in order to account for micro-structure (tortuosity and porosity) of the porous layer.

Using the ideal gas law, the concentration of individual gases can be expressed as:

$$c_i = c_T \times x_i = \frac{p_T}{RT} \times x_i \tag{2.74}$$

where x_i is the mole fraction of the gas i and c_T is the molar concentration of the total gaseous mixture and p_T is the total pressure on the either anode or cathode side of the cell.

In the cathode side, oxygen and water vapour diffuse with respect to the nitrogen, so the molar fluxes can be expressed as:

$$\vec{N}_{O_2} = -\frac{p_T}{RT} D_{O_2,N_2}^{eff} \vec{\nabla} x_{O_2} \tag{2.75}$$

and

$$\vec{N}_{H_2O} = -\frac{p_T}{RT} D_{H_2O,N_2}^{eff} \vec{\nabla} x_{H_2O} \tag{2.76}$$

In the anode side, water vapour diffuse with respect to the hydrogen, so the molar flux can be expressed as:

$$\vec{N}_{H_2O} = -\frac{p_T}{RT} D_{H_2O,H_2}^{eff} \vec{\nabla} x_{H_2O} \tag{2.77}$$

The focus of this work is to incorporate multi-phase, non-isothermal effects into a macro-homogeneous MEA model [41–43]. In a macro-homogenous layer model, effective transport properties are determined by averaged quantities across the layer. It is noteworthy that the structure of the porous layers in both the anode and cathode sides are similar in nature. Hence in order to determine the effective transport properties of particular layer, say GDL, same correction factors will be applied to the bulk transport properties for AGDL and CGDL.

The most common correlation used for determining the effective transport properties is the Bruggemann correlation [113]. For instance, the effective gas diffusion coefficient determined using Bruggemann correlation is given as:

$$D_{i,j}^{eff} = D_{i,j}\ \epsilon^{1.5} \tag{2.78}$$

It is observed that there is always a threshold porosity below which gas transport cannot occur. The Bruggemann correlation will account for the species transport even at low volume fractions. Porous media structure (porosity and tortuosity) can also be accounted using the percolation theory [114]. According to percolation theory, the species transport will not occur below a particular volume fraction of the transporting phase (for instance, void phase for the gas transport). The effective gas diffusion coefficient determined using the percolation theory is given as [41]:

$$D_{i,j}^{eff} = D_{i,j}\ \left(\frac{\epsilon - \epsilon^{th}}{1 - \epsilon^{th}}\right)^{\mu} \Theta\left(\epsilon - \epsilon^{th}\right) \tag{2.79}$$

where ϵ^{th} is the threshold volume fraction below which transport will not occur and μ is the network constant which depends on the fibre orientation. Both of these values are determined by fitting to the experimental data. No species transport below the threshold volume fraction is ensured by using the the Heaviside function, which is given as:

$$\Theta(\epsilon - \epsilon^{th}) = \begin{cases} 0 \text{ for } (\epsilon - \epsilon^{th}) < 0 \\ 1 \text{ for } (\epsilon - \epsilon^{th}) \geq 0 \end{cases} \tag{2.80}$$

GDLs have random, anisotropic stacking arrangement of the fibres. Tomadakis et al. [115, 116] performed Monte-Carlo simulations on randomly oriented fibrous structures and proposed the following relation:

$$D_{g,i}^{eff} = D_g\ \epsilon \left(\frac{\epsilon - \epsilon^{th}}{1 - \epsilon^{th}}\right)^{\mu^i} \Theta(\epsilon - \epsilon^{th}) \tag{2.81}$$

where $D_{g,i}^{eff}$ and D_g are the effective and bulk diffusion coefficients of the gas g, and μ^i is the network constant, in the i^{th} direction (either in-plane or through-plane). Tomadakis et al.'s correlation is considered for the GDL.

MPLs and CLs are isotropic in nature, so in-plane and through-plane values are not required separately. percolation model given in the Equation (2.79) is considered for the MPL and the CL in this work. The CL also contains the electrolyte which

allows for the proton transport to the reaction sites. Hence three phases exist inside the CL, *viz.*, void (empty space) phase, electrolyte phase and solid (carbon particles) phase. So three volume fractions, *viz.*, solid phase (ϵ_S), void phase (ϵ_V) and electrolyte phase (ϵ_N), are required to be computed for determining effective transport properties. Relations to compute the individual volume fractions are given in [43, 117] and not discussed further.

2.3.2 Charged species transport

Charged species whose transport is considered in this model are electrons, e^-, and protons, H^+. The proton flux in the solid polymer electrolyte (Nafion®) takes the form of Ohm's law and is given as [110]:

$$\vec{N}_{H^+} = -\frac{\sigma_m^{eff}}{z_{H^+}F}\vec{\nabla}\phi_m = -\frac{\sigma_m^{eff}}{F}\vec{\nabla}\phi_m \tag{2.82}$$

where σ_m^{eff} is the effective proton conductivity of the layer (in order to account for porous structure).

Electron transport is also governed by the Ohm's law and the electron flux is given as [41]:

$$\vec{N}_{e^-} = -\frac{\sigma_s^{eff}}{z_{e^-}F}\vec{\nabla}\phi_s = \frac{\sigma_s^{eff}}{F}\vec{\nabla}\phi_s \tag{2.83}$$

where z_{e^-} is the elementary charge of an electron, *i.e*, -1, σ_s^{eff} is the effective electron conductivity of the layer and ϕ_s is the solid electrical potential. Electrons travel through the fibres (solid phase) of the gas diffusion layer. The percolation theory is used to determine the anisotropic effective electron conductivity in the GDL. In the MPL and the CL, electrons travel through the isotropically packed carbon particles (solid phase). The percolation theory (same as the GDL) is also used to determine the effective electron conductivity in the MPL and the CL.

In the CL, protons are transported through the electrolyte phase. Proton conductivity is generally dependent on the membrane water content (λ) and the temperature (T) [103]. Iden et al. [118, 119] measured effective proton conductivity values for a pseudo-catalyst layer (created using a unique process). These pseudo-catalyst layers did not contain platinum hence electrochemically inactive, but possessed the same structure and composition of an actual catalyst layer. They reported effective proton conductivity values at different RH conditions. Moore [43] fitted the experimental

data from Iden et al.'s first paper [118] and used a third order polynomial expression in his work. However he reported that the expression is suitable for the ionomer volume fraction, ϵ_N, value of 0.19. Domican et al. [120] observed that the expression by Moore is accurate only for the Nafion (electrolyte) loading value of 40%. He reported that the data reported by Iden et al. in their second paper [119], is more suitable for a range of Nafion loadings. It is also observed that the new data matches well to the experimental data [120]. By fitting to the experimental data, Domican et al. reported a third order polynomial expression. The expression is considered in this work for the CLs and is given as [120]:

$$\sigma_m^{eff} = \epsilon_N^{1.6} \left(1.931 \times 10^{-7} a_w^3 - 6.735 \times 10^{-6} a_w^2 + 0.00075 a_w - 0.008\right) e^{751.5412\left(\frac{1}{353} - \frac{1}{T}\right)} \tag{2.84}$$

where ϵ_N is the electrolyte volume fraction, σ_m^{eff} is the effective proton conductivity in the catalyst layer and a_w is the water activity [120]:

$$a_w = \begin{cases} 100 \left(0.000094\lambda^3 - 0.00865\lambda^2 + 0.1832\lambda - 0.1254\right) & \text{for } \lambda < 13 \\ 100 & \text{otherwise} \end{cases} \tag{2.85}$$

The membrane is a bulk media, so bulk proton conductivity values are used for the membrane layer. Experimental results for Nafion® NRE-211 membranes are presented in the literature [121, 122]. Dobson et al. [123] reported a polynomial expression determined by fitting to the experimental data by BekkTech LLC for NRE-211 membranes [122], considered in this work for the ML:

$$\sigma_m = \left(-1.0125 \times 10^{-4} \lambda^2 + 0.01052\lambda - 0.020634\right) e^{751.5412\left(\frac{1}{303} - \frac{1}{T}\right)} \tag{2.86}$$

2.3.3 Sorbed Water Transport

Water is transported in sorbed form inside the electrolyte. Secanell [41] reviewed various sorbed water transport models available in the literature. The most used semi-empirical model presented by Springer et al. [103] is considered in this work. It accounts for water transport by electro-osmotic drag and back diffusion.

The sorbed water flux due to electro-osmotic drag, $\vec{N}_{\lambda,\text{drag}}$, is directly proportional to the proton flux in the membrane and is given as [103]:

$$\vec{N}_{\lambda,\text{drag}} = -n_d \frac{\sigma_m^{eff}}{F} \vec{\nabla} \phi_m \tag{2.87}$$

where n_d is the electro-osmotic drag coefficient and denotes the number of water molecules dragged by a proton. Springer et al. experimentally observed a maximum

λ value of 22 for a liquid water-equilibriated membrane at 100℃. So by assuming that that the number of water molecules dragged by a proton to be linearly proportional to λ values in the membrane, the n_d is expressed as [103]:

$$n_d = \frac{2.5\lambda}{22} \tag{2.88}$$

However recent experimental observations suggest that the value of n_d is constant and is equal to 1, which is considered in this work.

The sorbed water flux due to back diffusion, $\vec{N}_{\lambda,\text{diffusion}}$, is given as [103]:

$$\vec{N}_{\lambda,\text{diffusion}} = -\frac{\rho_{dry}}{EW} D_{\lambda}^{eff} \vec{\nabla}\lambda \tag{2.89}$$

where D_{λ}^{eff} is the effective water diffusion coefficient and is a function of λ and T, ρ_{dry} is the dry membrane density and EW is the equivalent weight. Motupally et al. [124] experimentally measured the water flux across the Nafion® 115 membrane. The bulk diffusion coefficient of the sorbed water, used in the membrane, as a function of λ and T is given as [124]:

$$D_{\lambda} = \begin{cases} 3.10 \times 10^{-3}\lambda(-1 + e^{0.28\lambda})\exp\left(\dfrac{-2436.0}{T}\right) & \text{if} \quad 0 < \lambda \leq 3 \\ 4.17 \times 10^{-4}\lambda(1 + 161e^{-\lambda})\exp\left(\dfrac{-2436.0}{T}\right) & \text{if} \quad 3 < \lambda \leq 17 \end{cases} \tag{2.90}$$

So the effective water diffusion coefficient, D_{λ}^{eff}, used in the CLs is given as:

$$D_{\lambda}^{eff} = \begin{cases} \epsilon_N^{1.6}\ 3.10 \times 10^{-3}\lambda(-1 + e^{0.28\lambda})\exp\left(\dfrac{-2436.0}{T}\right) & \text{if} \quad 0 < \lambda \leq 3 \\ \epsilon_N^{1.6}\ 4.17 \times 10^{-4}\lambda(1 + 161e^{-\lambda})\exp\left(\dfrac{-2436.0}{T}\right) & \text{if} \quad 3 < \lambda \leq 17 \end{cases} \tag{2.91}$$

Under non-isothermal conditions, a third mode of water transport is observed inside the membrane, known as thermal osmosis. Tasaka et al. [104, 105] observed that the sorbed water is transported through a hydrophillic/hydrophobic membrane under the effect of a temperature gradient. Based on non-equilibrium thermodynamics, they inferred that the water is in a ordered state inside the hydrophillic membranes (charged membranes), hence by second law of thermodynamics, water moves from the cold side to the hot side in order to increase the entropy. The reverse transport behaviour is observed for hydrophobic membranes. Tasaka et al. confirmed this behaviour by performing experiments on a number of different membrane types. For

instance, Nafion® 417 membrane showed the thermo-osmotic flux from the cold side to the hot side. Water flux was found to be linearly dependent on the temperature difference applied on the membrane. It was also shown that the thermo-osmotic flux increased strongly with fluidity of the solvent.

Villaluenga et al. [125] measured the thermo-osmotic fluxes by varying compositions of water-methanol mixtures through a Nafion® 117 membrane. They analyzed the effect of solution composition on the thermo-osmotic flux. They also confirmed that the flux is from cold to hot side (positive flux by convention). The overall flux is found to increase with the mean temperatures. Zaffou et al. [126] measured the net water flow due to the temperature gradients inside an assembly of the porous transport layers and membrane (with and without catalyst coating). They observed that the water flows from the hot side to the cold side. This contrary phenomenon is explained by Kim and Mench [107]. Zaffou et al.'s observation included all effects such as the evaporation/condensation of water, phase-change induced flow and back diffusion of water. Kim and Mench [107] performed an order of magnitude analysis for two important temperature driven water flows. First, the phase-change induced flow where water moves from the high temperature (high saturation concentration) to the low temperature (low saturation concentration). Second, thermal osmosis inside the membrane where water moves from cold to hot conditions. It is found that at normal operating conditions, vapour diffusion is more significant than the thermal osmosis, hence the observations by Zaffou et al. [126]. Kim and Mench visually confirmed these trends using neutron radiography. It is also shown that the thermo-osmotic water flow becomes more significant at high current densities and during the cell shutdown (forcing lots of water from anode to cathode, hence blocking pores for the next start-up of the cell).

Kim and Mench [106] directly measured the thermo-osmotic fluxes on non - reinforced Nafion® membranes and reinforced Gore-Select® and Flemion® membranes. They observed that the water flux is from cold to hot side. It was observed that with a reduction in the equivalent weight, the thermo-osmotic flux increased significantly and was comparable to water flux due to back diffusion. Lower equivalent weight leads to better connected pathways hence increased water flux.

The sorbed water flux due to thermal-osmosis, $\vec{N}_{\lambda,thermo-osmosis}$, is expressed as:

$$\vec{N}_{\lambda,thermo-osmosis} = -\frac{D_T^{eff}}{M_{H_2O}}\vec{\nabla}T \tag{2.92}$$

where M_{H_2O} is the molar mass of water and D_T^{eff} is the effective thermo-osmotic diffusion coefficient.

Thermo-osmotic diffusion coefficients values for different membrane materials have been reported in the literature [105, 106, 125]. Kim and Mench [106] have provided relations for the thermo-osmotic diffusion coefficient. They characterized the membrane surface temperatures using a two-dimensional model. Utilizing this information, they gave an Arrhenius-like expression for the bulk thermo-osmotic diffusion coefficient, D_T, of Nafion® 112 membrane, considered in this work:

$$D_T = -\left(1.04 \pm 0.08\right) \times 10^{-5} \exp\left(-\frac{2362 \pm 106}{T}\right) \qquad \left[kg \cdot m^{-1} \cdot s^{-1} \cdot K^{-1}\right] \quad (2.93)$$

Effective thermo-osmotic diffusion coefficient for the CL, D_T^{eff}, is given as:

$$D_T^{eff} = -\epsilon_N^{1.6}\left(1.04 \pm 0.08\right) \times 10^{-5} \exp\left(-\frac{2362 \pm 106}{T}\right) \quad (2.94)$$

So the sorbed water flux considering all the three modes of transport inside the electrolyte is given as:

$$\vec{N}_\lambda = -n_d \frac{\sigma_m^{eff}}{F} \vec{\nabla}\phi_m - \frac{\rho_{dry}}{EW} D_\lambda^{eff} \vec{\nabla}\lambda - \frac{D_T^{eff}}{M_{H_2O}} \vec{\nabla}T \quad (2.95)$$

2.3.4 Source Terms

Various species have source/sink terms corresponding to current production and sorption/desorption of water in the catalyst layers. Details of these source/sink terms are discussed in this section. It is noteworthy that the details of various heat source/sink terms are already discussed in the Section 2.2 and will not be discussed further. Finally, incorporating the flux terms for various species, the governing equations for the

single-phase non-isothermal MEA model can be expressed as:

$$\begin{aligned}
-\vec{\nabla}\cdot\left(\frac{p_T}{RT}\, D^{eff}_{O_2,N_2}\vec{\nabla}x_{O_2}\right) &= S_{O_2}\\
-\vec{\nabla}\cdot\left(\frac{p_T}{RT}\, D^{eff}_{H_2O,N_2 \text{ or } H_2}\vec{\nabla}x_{H_2O}\right) &= S_{H_2O}\\
-\vec{\nabla}\cdot\left(\frac{\sigma^{eff}_m}{F}\vec{\nabla}\phi_m\right) &= S_{H^+}\\
\vec{\nabla}\cdot\left(\frac{\sigma^{eff}_s}{F}\vec{\nabla}\phi_s\right) &= S_{e^-}\\
-\vec{\nabla}\cdot\left(n_d\frac{\sigma^{eff}_m}{F}\vec{\nabla}\phi_m + \frac{\rho_{dry}}{EW}D^{eff}_{\lambda}\vec{\nabla}\lambda + \frac{D^{eff}_T}{M_{H_2O}}\vec{\nabla}T\right) &= S_{\lambda}\\
-\vec{\nabla}\cdot\left(k^{eff}\vec{\nabla}T\right) + \sum_{\text{gases},\lambda}\left(\vec{N}_i\cdot\vec{\nabla}\bar{H}_i\right) &= S_T
\end{aligned} \tag{2.96}$$

2.3.4.1 Current Production

According to the Equation (1.2), a relationship can be obtained between the source terms for different species. Two moles of protons and electrons, and a half mole of oxygen are consumed in producing a mole of water vapour in the ORR. For the CCL:

$$-S_{O_2} = -\frac{1}{4}S_{H^+} = -\frac{1}{4}S_{e^-} = \frac{1}{2}S_{H_2O} \tag{2.97}$$

Consumption of electrons during the ORR can be expressed in terms of the volumetric current density, j, *i.e.*, amount of charge produced per unit volume in a unit time. So the consumption of electrons in the CCL can be expressed as:

$$S_{e^-} = -\frac{j}{F} \tag{2.98}$$

Using the Equation (2.97), source terms for various species inside the CCL, can be expressed as:

$$\begin{aligned}
S_{O_2} &= -\frac{j}{4F}\\
S_{H_2O} &= \frac{j}{2F}\\
S_{H^+} &= -\frac{j}{F}\\
S_{e^-} &= -\frac{j}{F}
\end{aligned} \tag{2.99}$$

The production of electrons and protons in the ACL, can be expressed as:

$$\begin{aligned} S_{H^+} &= \frac{j}{F} \\ S_{e^-} &= \frac{j}{F} \end{aligned} \tag{2.100}$$

Electrochemical reactions taking place inside the catalyst layers can be characterized using kinetics models. Kinetics models are used to compute the current per cm^2 of catalyst (platinum) surface. In a three-dimensional porous catalyst layer, the volumetric current density, j, is obtained by multiplying the current per cm^2 of Pt with the active area, A_v. The active area describes available surface area $[cm^2]$ of catalytic sites in a unit volume $[cm^3]$ of the layer and has the units of $\left[\frac{cm^2\ Pt}{cm^3\ CL}\right]$. The active area can be expressed as a function of the platinum loading and platinum to carbon ratio used in preparing the catalyst layer [41, 127, 128]. In this work however, experimentally determined values are used for the active area [42].

The ORR is a slow reaction, so the volumetric current density, j, in the CCL is typically computed using the Tafel kinetics model [41]. However the Tafel model is derived for single electron transfer reactions. Wang et al. [129] proposed the double-trap intrinsic kinetics model for the oxygen reduction reaction using platinum as catalyst. It accounted for four intermediate steps and the coverage of two intermediate species. The model could predict the experimentally observed doubling of the Tafel slope. Moore et al. [130] further improved the model by accounting for the backward reaction which was neglected by Wang et al. [129]. A multi-variable parameter estimation was employed by Moore in order to obtain the kinetic parameters [43]. The improved double-trap kinetics model can accurately predict the experimental Tafel slopes and coverage profiles of the intermediate species [120]. Oxygen must dissolve in the electrolyte before reaching the reaction site. The cathodic volumetric current density, j, using the improved double-trap kinetics model, can be expressed as [43, 130]:

$$j = A_v \left(2j^* e^{-\Delta G^*_{RD}/kT} \theta_{OH} - 2j^* e^{-\Delta G^*_{-RD}/kT} (1 - \theta_O - \theta_{OH}) \right) \tag{2.101}$$

Details of the various kinetics terms given in the Equation (2.101) can be found in references [43, 130] and are not discussed further.

The HOR is a fast reaction and is commonly modelled using Butler-Volmer kinetics [41]. However a more accurate multi-step dual-pathway kinetics model developed by Wang et al. [131] is considered in this work. The model considers three intermediate steps which leads to two potential paths for the reaction to proceed, and an

intermediate adsorbed specie in the reaction. The anodic volumetric current density, using the dual-path kinetics model, can be expressed as [131]:

$$j = A_v \frac{c_{H_2}}{c_{H_2}^{ref}} \left[j_{0T}(1 - e^{-2F\eta/\gamma RT}) + j_{0H}(e^{F\eta/\gamma RT} - e^{-F\eta/\gamma RT} e^{-F\eta/2RT}) \right] \tag{2.102}$$

Details of the various kinetics terms given in the Equation (2.101) can be found in references [41, 43] and are not discussed further.

Overpotential, η, is expressed as:

$$\eta = (\phi_s - \phi_m) - E_{eq} \tag{2.103}$$

where the E_{eq} is the equilibrium potential for the half-cell reaction (ORR or HOR), and is computed using the Nernst equation [43, 110].

Reactant gases must dissolve and diffuse through the electrolyte (Nafion®), before reaching the reaction sites. So the concentration of the reactant gases (either hydrogen or oxygen), c_g, at the reaction sites, is computed using the Henry's law. So the c_g used in the respective kinetics models, is computed as:

$$c_g = \frac{p_T x_g}{H_{g,N}} \tag{2.104}$$

where p_T is the total pressure, x_g is the mole fraction of the gas g, and $H_{g,N}$ is the Henry's constant for the dissolution of the gas g in the Nafion®. The values of $H_{H_2,N}$ and $H_{O_2,N}$ are taken as $6.69 \times 10^{10} \left[\frac{Pa \cdot cm^3}{mol}\right]$ [132] and $3.1664 \times 10^{10} \left[\frac{Pa \cdot cm^3}{mol}\right]$ [133] respectively.

2.3.4.2 Membrane Water Sorption

In a vapour-equilibriated membrane, the equilibrium value of λ in the electrolyte, is determined by a sorption isotherm [134]. The equilibrium value, λ_{eq} is a function of the equivalent weight of the membrane, water vapour mole fraction and temperature. So in a steady state model, a coupling term accounting for sorption/desorption, is added to the water vapour and sorbed water transport equations. This term will ensure that the membrane water content and water vapour in the CL are in equilibrium. Depending on the local humidity conditions and temperature values, water vapour will either be desorbed from the electrolyte to the pore space, or sorbed into the electrolyte from the pore space. This coupling term, S_λ, is given as [41]:

$$S_\lambda = k_t \frac{\rho_{dry}}{EW}(\lambda_{eq} - \lambda) \tag{2.105}$$

where k_t is a time constant and is set to $10000\,[s^{-1}]$, to ensure a strong coupling between the membrane and the CL [41]. If $\lambda_{eq} > \lambda$, the coupling term will be a driving force (source term) for the sorbed water equation, and the sorption phenomena is modelled such that the membrane reaches to the equilibrium conditions. So the coupling term, S_λ, is used as a source term for the sorbed water transport equation. At the same time, water vapour will be removed from the pore space, so a negative of the coupling term, $-S_\lambda$, is used for the water vapour equation (acting as a sink term). In the case of $\lambda_{eq} < \lambda$, reverse phenomenon (desorption of water inside the CL) is also captured by same usage of the coupling term.

The equilibrium membrane water content value, λ_{eq}, is determined by the sorption isotherm given by Liu et al. [135]:

$$\lambda_{eq} = \left[1 + 0.2352 a_w^2 \left(\frac{T - 303.15}{30}\right)\right] (14.22 a_w^3 - 18.92 a_w^2 + 13.41 a_w) \tag{2.106}$$

where a_w is the water vapour activity in the CL and is expressed as:

$$a_w = \frac{p_T \; x_{H_2O}}{p_{sat}(T)} \tag{2.107}$$

where p_{sat} is the water saturation pressure and a temperature dependent expression is used for p_{sat} here [103]:

$$\begin{aligned} log_{10}\,(p_{sat}) = &- 2.1794 + 0.02953\,(T - 273.15) - 9.1837 \times 10^{-5}\,(T - 273.15)^2 \\ &+ 1.4454 \times 10^{-7}\,(T - 273.15)^3 \end{aligned} \tag{2.108}$$

As discussed in the previous section of this chapter, the model under development is non-isothermal. So the model solves for the temperature, T, in all the layers of the MEA model under consideration. Therefore six variable will be solved in the MEA model being developed in current part of this work. A summary of the solution variables considered for a single-phase, non-isothermal MEA model is given in Table 2.2. The layers in which transport of a particular species is considered are depicted by ✓ symbol in the Table 2.2. The details of the thermal transport equation are already discussed in the previous section.

The final system of equations solved in the single-phase, non-isothermal MEA

model can be written as:

$$\begin{aligned}
-\vec{\nabla}\cdot\left(\frac{p_T}{RT}\, D^{eff}_{O_2,N_2}\vec{\nabla}x_{O_2}\right) &= S_{O_2}\\
-\vec{\nabla}\cdot\left(\frac{p_T}{RT}\, D^{eff}_{H_2O,N_2 \text{ or } H_2}\vec{\nabla}x_{H_2O}\right) &= S_{H_2O}\\
-\vec{\nabla}\cdot\left(\sigma_m^{eff}\vec{\nabla}\phi_m\right) &= S_{H^+}\\
\vec{\nabla}\cdot\left(\sigma_s^{eff}\vec{\nabla}\phi_s\right) &= S_{e^-}\\
-\vec{\nabla}\cdot\left(n_d\frac{\sigma_m^{eff}}{F}\vec{\nabla}\phi_m + \frac{\rho_{dry}}{EW}D_\lambda^{eff}\vec{\nabla}\lambda + \frac{D_T^{eff}}{M_{H_2O}}\vec{\nabla}T\right) &= S_\lambda\\
-\vec{\nabla}\cdot\left(k^{eff}\vec{\nabla}T\right) + \sum_{\text{gases},\lambda}\left(\vec{N}_i\cdot\vec{\nabla}\bar{H}_i\right) &= S_T
\end{aligned} \tag{2.109}$$

where the source terms corresponding to each equation are given as:

$$S_{O_2} = \begin{cases} \frac{-j}{4F} & \text{in CCL} \\ 0 & \text{otherwise} \end{cases} \tag{2.110}$$

$$S_{H_2O} = \begin{cases} \frac{j}{2F} - k_t\frac{\rho_{dry}}{EW}(\lambda_{eq}-\lambda) & \text{in CCL} \\ -k_t\frac{\rho_{dry}}{EW}(\lambda_{eq}-\lambda) & \text{in ACL} \\ 0 & \text{otherwise} \end{cases} \tag{2.111}$$

$$S_{H^+} = \begin{cases} -j & \text{in CCL} \\ j & \text{in ACL} \\ 0 & \text{otherwise} \end{cases} \tag{2.112}$$

$$S_{e^-} = \begin{cases} -j & \text{in CCL} \\ j & \text{in ACL} \\ 0 & \text{otherwise} \end{cases} \tag{2.113}$$

Table 2.2 – Table of solution variables considered in the single-phase, non-isothermal MEA model.

Solution variable	AGDL	AMPL	ACL	ML	CCL	CMPL	CGDL
Oxygen molar fraction, x_{O_2}					✓	✓	✓
Water molar fraction, x_{H_2O}	✓	✓	✓		✓	✓	✓
Solid potential, ϕ_s	✓	✓	✓		✓	✓	✓
Electrolyte potential, ϕ_m			✓	✓	✓		
Membrane water content, λ			✓	✓	✓		
Temperature, T	✓	✓	✓	✓	✓	✓	✓

$$S_\lambda = \begin{cases} k_t \frac{\rho_{dry}}{EW}(\lambda_{eq} - \lambda) & \text{in CLs} \\ 0 & \text{otherwise} \end{cases} \tag{2.114}$$

$$S_T = \begin{cases} \sigma_s^{eff}(\vec{\nabla}\phi_s \cdot \vec{\nabla}\phi_s) & \text{in GDL and MPL} \\ \sigma_m^{eff}(\vec{\nabla}\phi_m \cdot \vec{\nabla}\phi_m) & \text{in Membrane} \\ -j\eta + \frac{j}{2F}(-T f_{ORR}\Delta\bar{S}_{overall} - \bar{H}_{lv}) + \sigma_m^{eff}(\vec{\nabla}\phi_m \cdot \vec{\nabla}\phi_m) & \\ \quad +\sigma_s^{eff}(\vec{\nabla}\phi_s \cdot \vec{\nabla}\phi_s) + k_t \frac{\rho_{dry}}{EW}(\lambda_{eq} - \lambda)\bar{H}_{sorption} & \text{in CCL} \\ j\eta + \frac{j}{2F}(-T(1 - f_{ORR})\Delta\bar{S}_{overall}) + \sigma_m^{eff}(\vec{\nabla}\phi_m \cdot \vec{\nabla}\phi_m) & \\ \quad +\sigma_s^{eff}(\vec{\nabla}\phi_s \cdot \vec{\nabla}\phi_s) + k_t \frac{\rho_{dry}}{EW}(\lambda_{eq} - \lambda)\bar{H}_{sorption} & \text{in ACL} \end{cases} \tag{2.115}$$

2.4 Computational domain and parameters

The two-dimensional computational domain consisting of seven layers, considered in this work is given in the Figure 2.2. Symmetric boundary conditions (no species flux) are used on the top and bottom boundary of the geometry. It has the advantages of considering only half of the gas channel and half of the current collector, from the PEMFC configuration. Contact resistances between the layers are neglected in this work, *i.e.*, solution is assumed to continuous across the complete domain. There are five types of boundaries:

- AGDL - Gas channel boundary at $(x, y) = \{x = 0, y = [l_{Rib}, l_{Rib} + l_{Channel}]\}$.
- AGDL - Bipolar plate boundary at $(x, y) = \{x = 0, y = [0, l_{Rib}]\}$.
- CGDL - Bipolar plate boundary at $(x, y) = \{x = 2\ l_{GDL} + 2\ l_{MPL} + l_{ACL} + l_{CCL} + l_{ML}, y = [0, l_{Rib}]\}$.
- CGDL - Gas channel boundary at $(x, y) = \{x = 2\ l_{GDL} + 2\ l_{MPL} + l_{ACL} + l_{CCL} + l_{ML}, y = [l_{Rib}, l_{Rib} + l_{Channel}]\}$.
- Top and bottom boundaries at $(x, y) = \{\forall x, y = 0 \text{ and } l_{Rib} + l_{Channel}\}$.

where l_{GDL}, l_{MPL}, l_{CCL}, l_{ACL}, l_{ML} represent the GDL, MPL, ACL, CCL and membrane thicknesses respectively. l_{Rib} and $l_{Channel}$ represent the half-width of the gas channel and current collector of a PEMFC, as shown in the Figure 2.2. Thicknesses of the MPL and GDL are considered to be same for both electrodes.

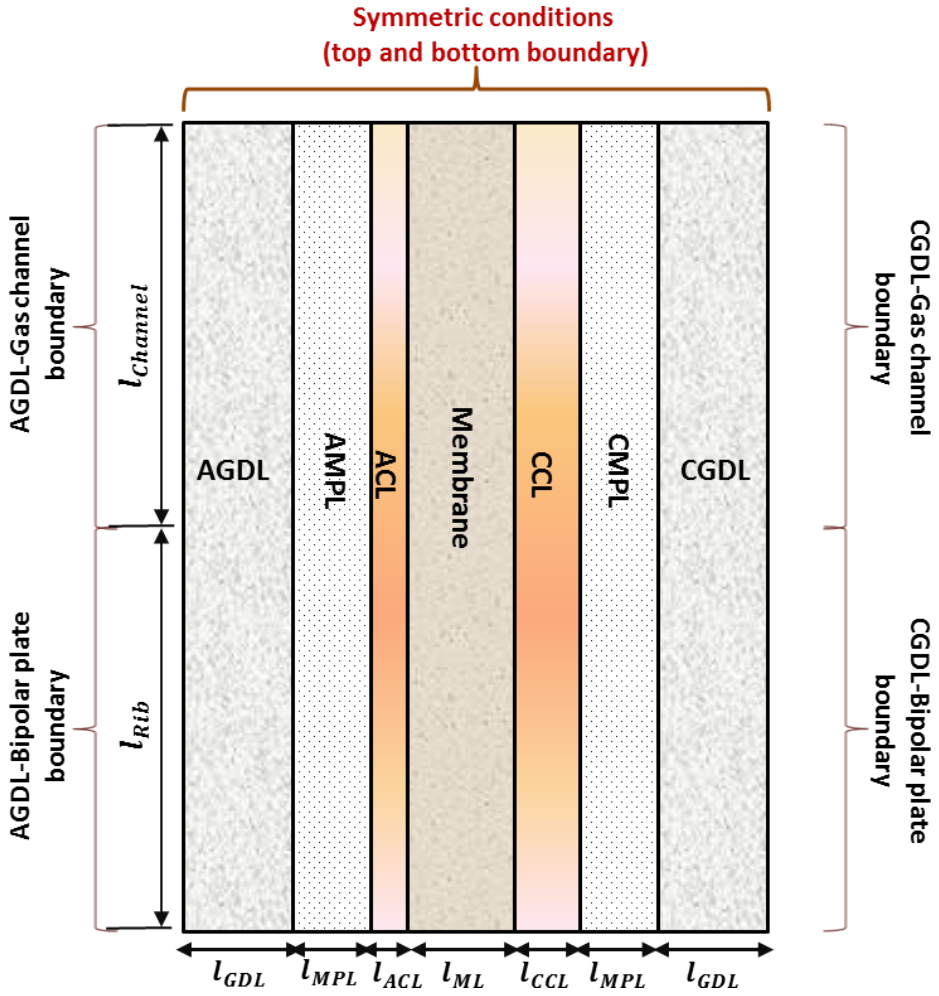

Figure 2.2 – Description of the computational domain.

Mathematical details of the boundary conditions used for transport of the species other than the temperature are discussed in detail by Secanell [41]. Oxygen mole fraction is supplied as Dirichlet conditions at the cathode gas channel. Water mole fraction is supplied at the cathode and anode gas channel boundaries (Dirichlet conditions). These mole fractions are determined based on the operating conditions, *viz.*, cell temperature, relative humidity and total pressure of the feed gas mixtures on the anode and cathode electrodes, and cell voltage. Oxygen mole fraction is computed using the assumption that air is supplied at the cathode gas channel, which contains 21% oxygen. The cell voltage is applied as an electron potential (Dirichlet) at the cathode current collector, while zero electron potential (Dirichlet) is applied at the anode current collector. This applied cell voltage is used to compute the current produced in the cell and assess the cell performance. Besides these discussed boundaries, no flux conditions (Neumann) are used at other boundaries for all species (except tem-

perature). The cell temperature, T_{cell}, is applied at the anode and cathode current collectors (Dirichlet conditions), while no heat flux conditions (Neumann) are used at the other boundaries. The boundary conditions applied for the thermal equation are mathematically expressed as:

$$T = T_{cell} \qquad \textbf{anode/cathode current collector} \tag{2.116}$$

$$\hat{n} \cdot \left(k^{eff} \vec{\nabla} T \right) = 0 \qquad \textbf{anode/cathode gas channel} \tag{2.117}$$

$$\hat{n} \cdot \left(k^{eff} \vec{\nabla} T \right) = 0 \qquad \textbf{top/bottom symmetric boundaries} \tag{2.118}$$

The geometric properties (dimensions) of the computational domain (MEA) considered in this work (Figure 2.2) are tabulated below:

Table 2.3 – Geometric dimensions of the computational domain

Parameters	Value, $[cm]$
l_{GDL}	2.5×10^{-2}
l_{MPL}	5×10^{-3}
l_{ACL}	3.33×10^{-3}
l_{CCL}	1×10^{-3}
l_{ML}	2.5×10^{-3}
l_{Rib}	5×10^{-2}
$l_{Channel}$	1×10^{-2}

Other parameters such as electron transport properties, which are not discussed in detail are summarized in tables. The composition and transport properties of the GDL and MPL, considered to be same for both electrodes, are given in the Table 2.4 and Table 2.5 respectively [41, 46, 47, 77, 136]. The composition and transport properties of the CCL and the ACL are given in the Table 2.6 and Table 2.7 respectively [41, 42, 137]. Bulk properties of the materials that the layers are composed from, *viz.*, carbon and Nafion®, are given in the Table 2.8 [41, 120, 138].

2.5 Numerical Solution Procedure

The system of partial differential equations given in the equation (2.109) are discretized and solved using the Galerkin finite element method (FEM). However the system of equations is non-linear, due to various factors such as current source terms and variable-dependent effective transport properties. An initial guess is assumed

Table 2.4 – Composition and transport properties of the GDL

Parameters	Value
Composition	
Porosity, ϵ	0.6
Gas transport properties	
Porosity threshold, ϵ^{th}	0.118
Porosity network constant X, μ^X	0.785
Porosity network constant Y, μ^Y	0.521
Electron transport properties	
Solid network threshold, ϵ_s^{th}	0.0
Solid network constant X, μ_s^X	1.5
Solid network constant Y, μ_s^Y	1.0
Thermal transport properties	
Effective thermal conductivity X, k_X^{eff}	Equation (2.31)
Effective thermal conductivity Y, k_Y^{eff}	Equation (2.33)

Table 2.5 – Composition and transport properties of the MPL

Parameters	Value
Composition	
Porosity, ϵ	0.4
Gas transport properties	
Porosity threshold, ϵ^{th}	0.118
Porosity network constant, μ	2.0
Electron transport properties	
Solid network threshold, ϵ_s^{th}	0.118
Solid network constant, μ_s	2.0
Thermal transport properties	
Effective thermal conductivity X, k_X^{eff} $[W \cdot cm^{-1} \cdot K^{-1}]$	0.003 [45]
Effective thermal conductivity Y, k_Y^{eff} $[W \cdot cm^{-1} \cdot K^{-1}]$	0.0387 [50]

Table 2.6 – Composition and transport properties of the CCL

Parameters	Value
Composition	
Platinum loading on support $[\%wt]$	0.46
Platinum loading per unit volume $[mg \cdot cm^{-3}]$	400
Electrolyte loading $[\%wt]$	0.3
Active area $[cm^2 \cdot cm^{-3}]$	2.0×10^5
Gas transport properties	
Porosity threshold, ϵ^{th}	0.25884
Porosity network constant, μ	2.0
Electron transport properties	
Solid network threshold, ϵ_s^{th}	0.118
Solid network constant, μ_s	2.0
Thermal transport properties	
Effective thermal conductivity, k^{eff} $[W \cdot cm^{-1} \cdot K^{-1}]$	0.015

Table 2.7 – Composition and transport properties of the ACL

Parameters	Value
Composition	
Platinum loading on support $[\%wt]$	0.46
Platinum loading per unit volume $[mg \cdot cm^{-3}]$	300
Electrolyte loading $[\%wt]$	0.3
Active area $[cm^2 \cdot cm^{-3}]$	1.2×10^5
Gas transport properties	
Porosity threshold, ϵ^{th}	0.25884
Porosity network constant, μ	2.0
Electron transport properties	
Solid network threshold, ϵ_s^{th}	0.118
Solid network constant, μ_s	2.0
Thermal transport properties	
Effective thermal conductivity, k^{eff} $[W \cdot cm^{-1} \cdot K^{-1}]$	0.015

Table 2.8 – Bulk properties of the materials

Parameters	Value
Nafion®	
Equivalent weight, EW $[g \cdot mol^{-1}]$	1100
Dry membrane density, ρ_{dry} $[g \cdot cm^{-3}]$	2.0
Thermal conductivity, k $[W \cdot cm^{-1} \cdot K^{-1}]$	0.0013
Carbon	
Density, $\rho[g \cdot cm^{-3}]$	1.25
Particle electron conductivity, σ_s $[S \cdot cm^{-1}]$	88.84
Fibre electron conductivity X, σ_s^X $[S \cdot cm^{-1}]$	16.03
Fibre electron conductivity Y, σ_s^Y $[S \cdot cm^{-1}]$	272.78

and governing equations are linearized and solved iteratively. There are two common method to solve non-linear FEM problems, *viz.*, Picard's and Newton's method. The method considered in this work is Newton's method. In this method, solution variables are perturbed and a linearized equation is obtained. Any governing equation can be expressed in the the residual form such that:

$$R(u) = 0 \tag{2.119}$$

On perturbing the solution variable, and using a Taylor series:

$$R(u) = R(u\Big|_n + \delta T) = R(u)\Big|_n + \frac{\partial R}{\partial u}\Big|_n (\delta u) + \mathcal{O}(\delta u^2) \tag{2.120}$$

Since $R(u) = R(u\Big|_n + \delta T) = 0$, and neglecting the second order terms, the linearized form for the governing equation is written as [41]:

$$-\frac{\partial R}{\partial u}\Big|_n (-\delta u) = -R\left(u\right)\Big|_n \tag{2.121}$$

where u is the solution variable, δu is the perturbed solution variable and $u\Big|_n$ refers to the solution variable u being evaluated at the previous iteration step, n. This linearized form is implemented for all governing equations in the open-source code, openFCST. As an example, the linearized form corresponding to the thermal transport equation in the CGDL is derived here. The expanded form of the thermal transport equation in the CGDL can be expressed in the residual form as follows:

$$R = \vec{\nabla} \cdot \left(k^{eff} \vec{\nabla} T\right) + D^{eff}_{O_2,N_2} \frac{p_T}{RT} \left(\frac{\partial \bar{H}_{O_2}}{\partial T} - \frac{\partial \bar{H}_{N_2}}{\partial T}\right) \vec{\nabla} T \cdot \vec{\nabla} x_{O_2}$$

$$+ D^{eff}_{H_2O,N_2} \frac{p_T}{RT} \left(\frac{\partial \bar{H}_{H_2O}}{\partial T} - \frac{\partial \bar{H}_{N_2}}{\partial T} \right) \vec{\nabla} T \cdot \vec{\nabla} x_{H_2O} + \sigma_s^{eff} \left(\vec{\nabla} \phi_s \cdot \vec{\nabla} \phi_s \right) \quad (2.122)$$

Effective transport properties such as k^{eff}, $D^{eff}_{O_2,N_2}$ and $D^{eff}_{H_2O,N_2}$ are functions of temperature. Enthalpy values such as $\bar{H}_{O_2}$, $\bar{H}_{H_2O}$ and $\bar{H}_{N_2}$ are also functions of temperature. Using the rules of variation:

$$\begin{aligned}
-\frac{\partial R}{\partial u}\Big|_n (\delta u) = &- \left(\frac{\partial k^{eff}}{\partial T}\Big|_n (\vec{\nabla} T)\Big|_n \vec{\nabla} \delta T \right) - \left(k^{eff}\Big|_n \vec{\nabla} \cdot (\vec{\nabla} \delta T) \right) \\
&- \left((\vec{\nabla} T)\Big|_n \cdot (\vec{\nabla} x_{O_2})\Big|_n \frac{\partial (D^{eff}_{O_2,N_2} \frac{p_T}{RT} (\frac{\partial \bar{H}_{O_2}}{\partial T} - \frac{\partial \bar{H}_{N_2}}{\partial T}))}{\partial T}\Big|_n \delta T \right) \\
&- \left((D^{eff}_{O_2,N_2} \frac{p_T}{RT} (\frac{\partial \bar{H}_{O_2}}{\partial T} - \frac{\partial \bar{H}_{N_2}}{\partial T}))\Big|_n (\vec{\nabla} T)\Big|_n \cdot (\vec{\nabla} \delta x_{O_2}) \right) \\
&- \left((D^{eff}_{O_2,N_2} \frac{p_T}{RT} (\frac{\partial \bar{H}_{O_2}}{\partial T} - \frac{\partial \bar{H}_{N_2}}{\partial T}))\Big|_n (\vec{\nabla} x_{O_2})\Big|_n \cdot (\vec{\nabla} \delta T) \right) \\
&- \left((\vec{\nabla} T)\Big|_n \cdot (\vec{\nabla} x_{H_2O})\Big|_n \frac{\partial (D^{eff}_{H_2O,N_2} \frac{p_T}{RT} (\frac{\partial \bar{H}_{H_2O}}{\partial T} - \frac{\partial \bar{H}_{N_2}}{\partial T}))}{\partial T}\Big|_n \delta T \right) \\
&- \left((D^{eff}_{H_2O,N_2} \frac{p_T}{RT} (\frac{\partial \bar{H}_{H_2O}}{\partial T} - \frac{\partial \bar{H}_{N_2}}{\partial T}))\Big|_n (\vec{\nabla} T)\Big|_n \cdot (\vec{\nabla} \delta x_{H_2O}) \right) \\
&- \left((D^{eff}_{H_2O,N_2} \frac{p_T}{RT} (\frac{\partial \bar{H}_{H_2O}}{\partial T} - \frac{\partial \bar{H}_{N_2}}{\partial T}))\Big|_n (\vec{\nabla} x_{H_2O})\Big|_n \cdot (\vec{\nabla} \delta T) \right) \\
&- \left(2(\sigma_s^{eff})\Big|_n (\vec{\nabla} \phi_s)\Big|_n \cdot (\vec{\nabla} \delta \phi_s) \right)
\end{aligned} \quad (2.123)$$

The third and sixth terms in the right hand side of equation (2.123) are further expanded using the product rule (not discussed here). The right hand side for the linearized equation is expressed as:

$$\begin{aligned}
-R(u)\Big|_n = &- \vec{\nabla} \cdot \left(k^{eff}\Big|_n \vec{\nabla} T\Big|_n \right) - D^{eff}_{O_2,N_2}\Big|_n \frac{p_T}{RT}\Big|_n \left(\frac{\partial \bar{H}_{O_2}}{\partial T} - \frac{\partial \bar{H}_{N_2}}{\partial T} \right) \Big|_n \vec{\nabla} T\Big|_n \cdot \vec{\nabla} x_{O_2}\Big|_n \\
&- D^{eff}_{H_2O,N_2}\Big|_n \frac{p_T}{RT}\Big|_n \left(\frac{\partial \bar{H}_{H_2O}}{\partial T} - \frac{\partial \bar{H}_{N_2}}{\partial T} \right) \Big|_n \vec{\nabla} T\Big|_n \cdot \vec{\nabla} x_{H_2O}\Big|_n \\
&- \sigma_s^{eff}\Big|_n \left(\vec{\nabla} \phi_s \cdot \vec{\nabla} \phi_s \right) \Big|_n
\end{aligned} \quad (2.124)$$

Using the same principles of variation, linearized form of other equations are obtained and coded into openFCST. The system of equations is weakened using the Bubanov-Galerkin FEM. In the Bubanov-Galerkin method, the linearized equation

is multiplied by a test function, v, on both the sides and integrated over the computational domain. Mathematical derivation of the weak form is discussed in detail by Secanell [41]. However mathematical details corresponding to the weak form involving non-zero flux boundary conditions (BC) are not found in the literature. So the weak form implementation of the Neumann and Robin boundary conditions is discussed here. A boundary term is obtained after weakening and integrating by-parts the second term on the right hand side of equation (2.123):

$$-\int_{\Omega} v\left[k^{eff}\Big|_n \vec{\nabla}\cdot(\vec{\nabla}\delta T)\right]d\Omega = -\int_{\Gamma} v\left[\hat{n}\cdot(k^{eff}\Big|_n \vec{\nabla}\delta T)\right]d\Gamma + \int_{\Omega}\left[k^{eff}\Big|_n \vec{\nabla}v\cdot\vec{\nabla}\delta T\right]d\Omega \tag{2.125}$$

where Ω and Γ are the domain and boundary respectively and $\hat{n}$ is the unit normal vector to the boundary Γ.

In the case of no-flux boundary conditions, the first term on the right hand side of equation (2.125) is zero. However the term is non-zero, when a heat flux is applied to a particular boundary and is not explicitly determined. The boundary condition corresponding to a constant heat flux, can be mathematically expressed as:

$$-\hat{n}\cdot\left(k^{eff}\ \vec{\nabla}T\right) = C \qquad \text{at boundary } \Gamma \tag{2.126}$$

where C is the constant heat flux. On taking the variation of equation (2.126) and considering that the effective thermal conductivity can be a function of T (for GDL) :

$$-\hat{n}\cdot\delta\left(k^{eff}\ \vec{\nabla}T\right) = \delta C = 0 \tag{2.127}$$

$$\Rightarrow -\hat{n}\cdot\left((\vec{\nabla}T)\Big|_n \frac{\partial k^{eff}}{\partial T}\Big|_n \delta T\ +\ k^{eff}\Big|_n \vec{\nabla}\delta T\right) = 0 \tag{2.128}$$

$$\Rightarrow -\hat{n}\cdot\left(k^{eff}\Big|_n \vec{\nabla}\delta T\right) = \hat{n}\cdot\left((\vec{\nabla}T)\Big|_n \frac{\partial k^{eff}}{\partial T}\Big|_n \delta T\right) \tag{2.129}$$

In a heat transfer problem, the most common example of a Robin boundary condition is convective cooling at the boundary. It is mathematically expressed as:

$$-\hat{n}\cdot\left(k^{eff}\ \vec{\nabla}T\right) = h\,(T - T_{\infty}) \qquad \text{at boundary } \Gamma \tag{2.130}$$

where h is the convective heat transfer coefficient and T_{∞} is the ambient temperature. On taking variation of equation (2.130):

$$-\hat{n}\cdot\delta\left(k^{eff}\ \vec{\nabla}T\right) = \delta\left[h\,(T - T_{\infty})\right] \tag{2.131}$$

$$\Rightarrow -\hat{n} \cdot \left((\vec{\nabla} T)\Big|_n \frac{\partial k^{eff}}{\partial T}\Big|_n \delta T \; + \; k^{eff}\Big|_n \vec{\nabla}\delta T \right) = h\delta T - 0 \tag{2.132}$$

$$\Rightarrow -\hat{n} \cdot \left(k^{eff}\Big|_n \vec{\nabla}\delta T \right) = h\delta T + \hat{n} \cdot \left((\vec{\nabla} T)\Big|_n \frac{\partial k^{eff}}{\partial T}\Big|_n \delta T \right) \tag{2.133}$$

Equations (2.129) and (2.133) depend on δT, the unknown variable in our problem, and they can be used to suitably modify the weak form, in order to account for constant heat flux BC and convective cooling BC respectively. So for constant heat flux case, the first term on the right hand side of equation (2.125) is modified and the weak form is therefore expressed as:

$$\begin{aligned} -\int_\Omega v \left[k^{eff}\Big|_n \vec{\nabla} \cdot (\vec{\nabla}\delta T) \right] d\Omega = & \int_\Gamma v \left[\hat{n} \cdot \left((\vec{\nabla} T)\Big|_n \frac{\partial k^{eff}}{\partial T}\Big|_n \delta T \right) \right] d\Gamma \\ & + \int_\Omega \left[k^{eff}\Big|_n \vec{\nabla} v \cdot \vec{\nabla}\delta T \right] d\Omega \end{aligned} \tag{2.134}$$

Similarly, on integrating by-parts the first term on the right hand side of the equation (2.124):

$$\begin{aligned} -\int_\Omega v \left[\vec{\nabla} \cdot \left(k^{eff}\Big|_n \vec{\nabla} T\Big|_n \right) \right] d\Omega = & -\int_\Gamma v \left[\hat{n} \cdot (k^{eff}\Big|_n \vec{\nabla} T\Big|_n) \right] d\Gamma \\ & + \int_\Omega \left[k^{eff}\Big|_n \vec{\nabla} v \cdot \vec{\nabla} T\Big|_n \right] d\Omega \end{aligned} \tag{2.135}$$

Equations (2.126) and (2.130) can be used to suitably modify the weak form on the right hand side of the linearized equation (residual), in order to account for constant heat flux BC and convective cooling BC respectively. So for constant heat flux case, the first term on the right hand side of equation (2.135) and weak form of the residual is expressed as:

$$-\int_\Omega v \left[\vec{\nabla} \cdot \left(k^{eff}\Big|_n \vec{\nabla} T\Big|_n \right) \right] d\Omega = \int_\Gamma v \; C \; d\Gamma + \int_\Omega \left[k^{eff}\Big|_n \vec{\nabla} v \cdot \vec{\nabla} T\Big|_n \right] d\Omega \tag{2.136}$$

The linearized equations are then discretized using continuous second order Galerkin elements for test function and solution variables. On numerically integrating the linearized weak forms using the Gauss-Legendre quadrature, a system of linear algebraic equations in $(-\delta u)$ is obtained. The domain of interest, for instance, MEA geometry, is broken down into a structure grid. The global system matrix and the right

hand side vectors, corresponding to the algebraic equations, are then assembled. A direct solver, namely UMFPACK [139] is utilized since the system matrix is non-symmetric. Moreover, in this case, the direct solver is 20 to 50 times faster than the iterative solvers [41]. Starting with an initial solution u^0, these algebraic equations are solved to determine $(-\delta u)$. The solution is then updated as:

$$u^{n+1} = u^n - (-\delta u) \tag{2.137}$$

This process is repeated until the desired convergence is achieved.

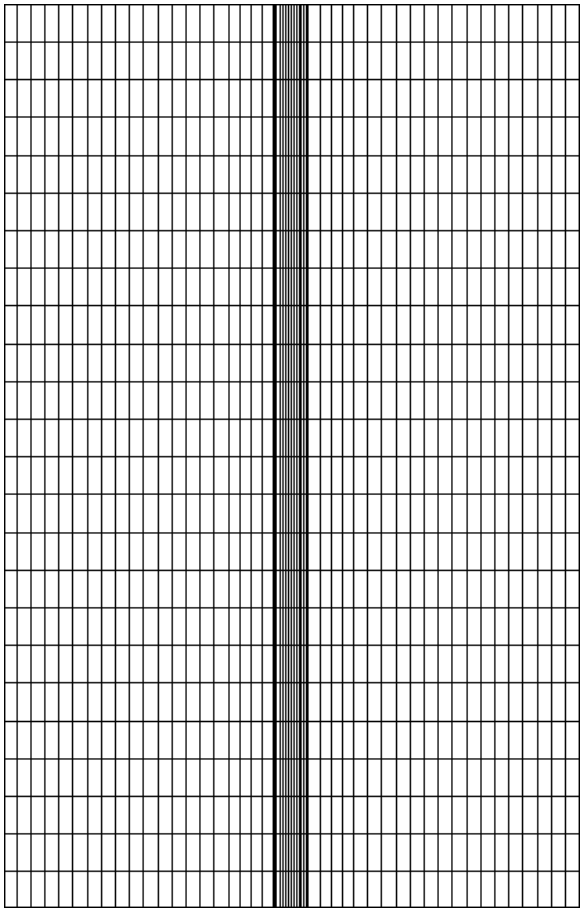

Figure 2.3 – Initial grid (first step of the adaptive refinement) of the MEA model.

The initial grid used for simulating the MEA model is shown in Figure 2.3. Once the convergence is achieved, the mesh is adaptively refined to obtain a grid-independent solution. In contrast to the global refining methods, only the cells with largest error are refined. In a single refinement, 30 % of the cells that have the highest error are refined. During the refinement, a single cell is split into four smaller cells. At the same time, 3 % of the cells that have the smallest error are coarsened by merging

four neighbouring cells. Error in the cells is estimated using the method by Kelly et al. [140]. Numerical implementation of the grid handling, discretization (finite element shape functions), linear solvers and adaptive refinement algorithms are provided by the deal.II (Differential Equations Analysis Library) [141, 142]. These libraries are integrated into the openFCST, which provides the physical properties and linearized governing equations of the fuel cell. Before performing non-isothermal simulations on the MEA model, it is important to validate the the implementation of the thermal equation. Validation studies and results of the single-phase, non-isothermal MEA model are discussed in the subsequent sections.

2.6 Validation of the code

The implementation of new physical phenomenon in the openFCST code is done in a modular fashion. openFCST has the flexibility of solving individual equations separately on any problem (including non fuel cell ones). As discussed in the Section 2.2, the thermal equation for a PEMFC is comprised of various terms such as heat conduction (Fourier term), enthalpy transport due to diffusion, heating due to electrochemical reaction and ohmic heating. However depending on the requirement, these individual terms can be easily switched ON/OFF during a particular simulation. A simple heat conduction problem on a plate with no source terms, can therefore be simulated. Two cases are validated with different set of boundary conditions, *i.e.*, Dirichlet and Neumann BC, on a two-dimensional rectangular geometry. The comparison of analytical results of the Fourier (heat conduction) equation against numerical results obtained from the code are presented here.

2.6.1 Case 1

The governing equation corresponding to a two-dimensional isotropic heat conduction problem can be expressed as:

$$k\frac{\partial^2 T}{\partial x^2} + k\frac{\partial^2 T}{\partial y^2} = 0 \tag{2.138}$$

As a first study case, a rectangular geometry with Dirichlet BC imposed on all four boundaries is considered. The length and the width of the rectangular domain are 5 cm and 1 cm respectively. Details about the problem and computational domain are shown in the Figure 2.4. Details about the Dirichlet conditions on all four boundaries in the problem can be expressed as:

- Left boundary at $\{x = 0, y \in [0, 1]\}$: $T = T_1 = 50$ [℃]
- Bottom boundary at $\{x \in [0, 5], y = 0\}$: $T = T_1 = 50$ [℃]
- Right boundary at $\{x = 5, y \in [0, 1]\}$: $T = T_1 = 50$ [℃]
- Top boundary at $\{x \in [0, 5], y = 5\}$: $T = T_2 = 30 \sin(\frac{\pi x}{5}) + 50$ [℃]

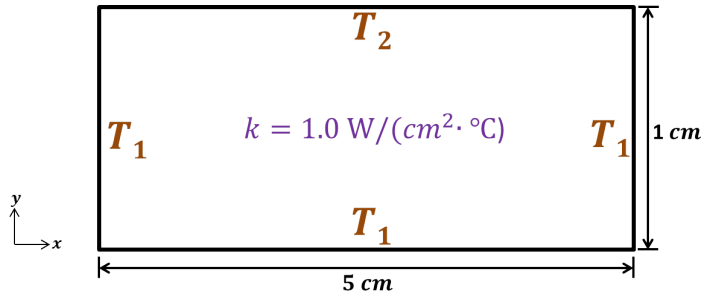

Figure 2.4 – Details about the problem and computation domain for the thermal equation test case 1.

For this problem, a temperature profile can be analytically determined [143]:

$$T(x, y) = 30 \, \frac{\sinh(\frac{\pi y}{5})}{\sinh(\frac{\pi}{5})} \sin\left(\frac{\pi x}{5}\right) + 50 \quad [℃] \tag{2.139}$$

Figure 2.5 shows the grid containing 256 cells, used in solving the problem. Second order Galerkin elements are used to discretize the problem; solving the problem on 1089 degrees of freedom (DOF). The temperature profile obtained from the numerical simulation is shown in Figure 2.6. On post-processing, the numerically-predicted temperature values are determined for five random points in the domain. These are then compared against the analytical results on those points (computed using equation (2.139)). Results match well within 0.01 %, as shown in the Table 2.9. This validates the numerical implementation of the thermal equation in openFCST.

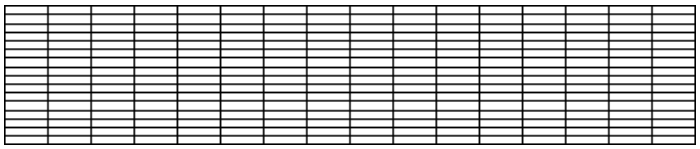

Figure 2.5 – Mesh used in solving the thermal equation test case 1.

Figure 2.7 shows the temperature (analytical and numerical) values on a line in the domain. Line spans from Point 1 (1, 0.75) to Point 2 (3.5, 0.25). It further validates the implementation of the equation with Dirichlet BC. This however does

Table 2.9 – Comparison of numerical against analytical predictions for thermal equation test case 1, at five points in the domain.

x [cm]	y [cm]	Analytical [°C]	Numerical [°C]
0.46875	0.1875	51.5337	51.5337
0.9375	0.21875	53.4274	53.4274
1.71875	0.125	53.1024	53.1024
2.96875	0.46875	62.7938	66.7938
2.8125	0.71875	70.49876	70.4988

not validate the numerical implementation of Neumann boundary conditions for the thermal transport equation. A problem with Neumann BC (constant heat flux) is considered in the next case.

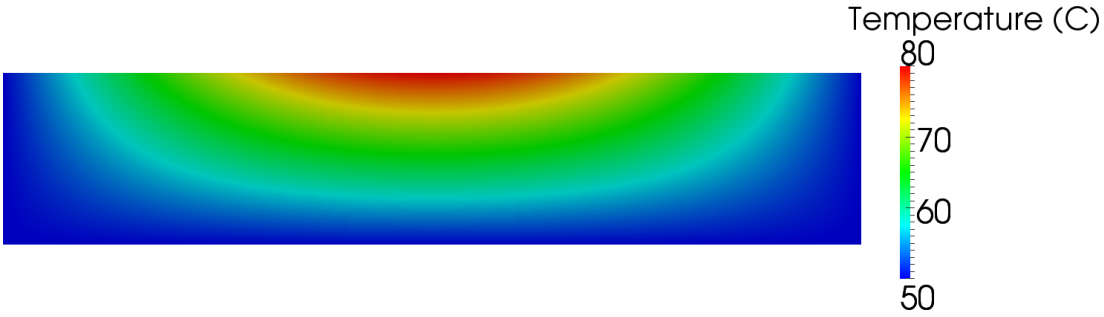

Figure 2.6 – Temperature profiles over the whole domain for the thermal equation test case 1.

2.6.2 Case 2

Analytical solutions for a one-dimensional heat conduction problem can easily be determined. So heat conduction on a line of length 5 cm is considered, with Neumann and Dirichlet boundary conditions applied at the alternate boundaries. The problem is formulated as:

$$k\frac{d^2T}{dx^2} = 0 \qquad \text{where } 0 \leq x \leq 5 \ [cm] \tag{2.140}$$

where the thermal conductivity, k, is equal to 1 W/(cm-°C). The boundary conditions are given as:

- Left boundary at $\{x = 0\}$: $\quad \hat{n} \cdot (-k\frac{dT}{dx}) = k\frac{dT}{dx} = -5 \quad$ [W/cm^2]
- Right boundary at $\{x = 5\}$: $\quad T = 50 \quad$ [°C]

openFCST can easily switch from performing a two-dimensional simulation to a three-dimensional one (due to advantages of template programming in `C++`). However

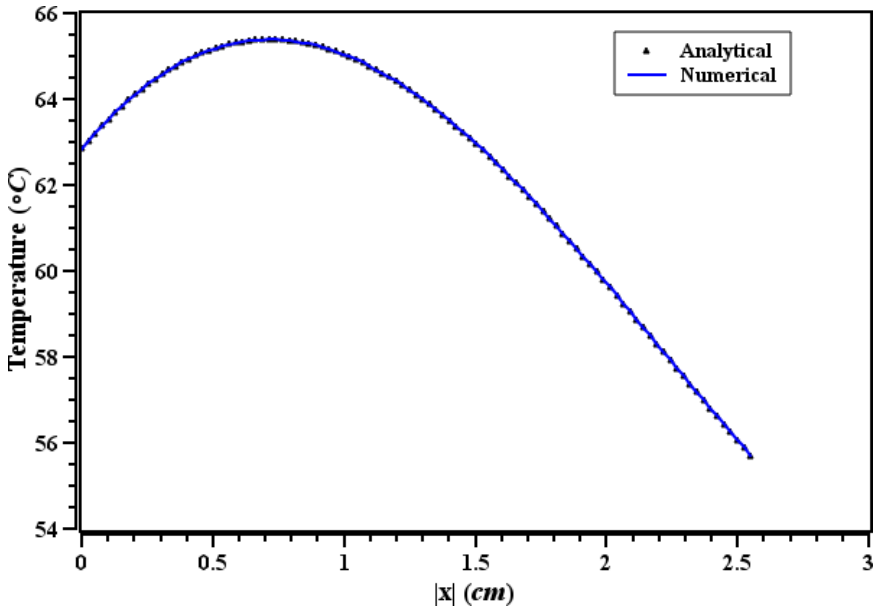

Figure 2.7 – Plot of temperature versus arc length on a line from (1,0.75) to (3.5,0.25) for the thermal equation test case 1.

the same is not true for performing a switch to a one-dimensional problem. A one-dimensional (line) problem can be solved as a two-dimensional (rectangular) problem by putting symmetric boundary conditions on the top and bottom boundary. The mesh given in Figure 2.5, is therefore considered for this case. Boundary conditions on the two-dimensional computational domain can be written as:

- Left boundary at $\{x = 0, y \in [0, 1]\}$: $\hat{n} \cdot (-k\frac{dT}{dx}) = k\frac{dT}{dx} = -5$ [W/cm^2]
- Bottom boundary at $\{x \in [0, 5], y = 0\}$: $\hat{n} \cdot (-k\frac{dT}{dx}) = 0$ (Symmetric BC)
- Right boundary at $\{x = 5, y \in [0, 1]\}$: $T = 50$ [℃]
- Top boundary at $\{x \in [0, 5], y = 5\}$: $\hat{n} \cdot (-k\frac{dT}{dx}) = 0$ (Symmetric BC)

Analytical solution to this problem is determined as:

$$T(x, y) = 75 - 5x \quad [℃] \tag{2.141}$$

Second order Galerkin elements are used to discretize the problem; solving the problem on 1089 degrees of freedom (DOF). The temperature profile obtained from the numerical simulation is shown in the Figure 2.8. On post-processing, numerically-predicted temperature values are determined for five random points in the x-direction. These are then compared against the analytical results on those points (computed

Table 2.10 – Comparison of analytical against numerical predictions (for $y = 0$, 0.5 and 1) for thermal equation test case 2, at five x values in the domain.

x [cm]	Analytical [°C]	Numerical [°C] (at y = 0)	Numerical [°C] (at y = 0.5)	Numerical [°C] (at y = 1)
0.0	75.0	75.0	75.0	75.0
1.0	70.0	70.0	70.0	70.0
2.0	65.0	65.0	65.0	65.0
3.0	60.0	60.0	60.0	60.0
4.0	55.0	55.0	55.0	55.0

using equation (2.141)). In order to ensure that the simulation performed is a one-dimensional problem (in true sense), temperature values should match for different y values at a particular x. Temperature values are also therefore compared at three y values, *viz.*, 0, 0.5 and 1.0, for each x. Analytical and numerical predictions match exactly, as shown in the Table 2.10. Table 2.10 also confirms that the temperature values at a particular x are independent of y value. This validates the numerical implementation of the thermal equation for Neumann BC in openFCST and hence complete implementation of the thermal equation in openFCST. Simulations on overall MEA model will therefore be performed and discussed in the subsequent sections.

Figure 2.8 – Temperature profiles over the whole domain for the thermal equation test case 2.

2.7 Results and Discussion

This section presents the results on an MEA model under different operating conditions. Non-isothermal model predictions are validated against experimental data. They are also compared against the isothermal model predictions, highlighting the importance of non-isothermal effects. Parametric studies are performed on various thermal parameters, in order to assess their impact on fuel cell performance.

2.7.1 Low humidity operation - Base case

In order to assess the impact of non-isothermal model predictions over the isothermal simulations, cell performance at low humidity conditions is evaluated. Operating conditions parameters for the base case are tabulated in Table 2.11. Two simulations, *viz.*, non-isothermal and isothermal, are run employing exactly the same parameters such as transport properties, kinetics and layer composition (given in the Section 2.4). Temperature is not solved for in the case of isothermal simulations. For the isothermal runs, the cell temperature is maintained at 80℃, while the same temperature is applied as a Dirichlet BC on the bipolar plates in the non-isothermal simulation.

Table 2.11 – Operating conditions for the base case

Parameters	Value
Anode relative humidity	50 %
Anode pressure	101325.0 $[Pa]$
Cathode relative humidity	50 %
Cathode pressure	101325.0 $[Pa]$
Cell temperature	353.15 $[K]$

Figure 2.9 shows the polarization curve (i-V curve) for both simulations. Model predictions are also validated against the experimental data, as shown in the Figure 2.9. The experimental data was published previously by our research group in collaboration with the National Research Council Canada - Institute for Fuel Cell Innovation (NRC-IFCI) [42]. So the MEA parameters such as computational geometry, transport properties and kinetics parameters (given in the Section 2.4), are in line with the tested PEMFC configuration [42, 43, 123]. The experimental data is available as polarization curves obtained under different operating conditions by varying humidification levels, operating temperatures and pressures. Under the operating conditions specified in Table 2.11, using the Nernst equation, the open cell voltage is determined to be 1.162 V. Simulations are performed by varying the cell voltage from 1.0 V to 0.1 V. The current density is computed as an integral in the CCL (refer Secanell [41] for details). As discussed previously, the polarization curve of a PEMFC can be divided into three regions, kinetics losses, ohmic losses and mass transport limitations. Simulations match quite well with the experimental predictions in the kinetics regime. No difference is observed between the isothermal and non-isothermal results in this regime. At currents higher than 500 mA/cm^2, the isothermal model out-performs the experimental data significantly. It is experimentally observed that mass transport limitations occur at high current densities. The current density is

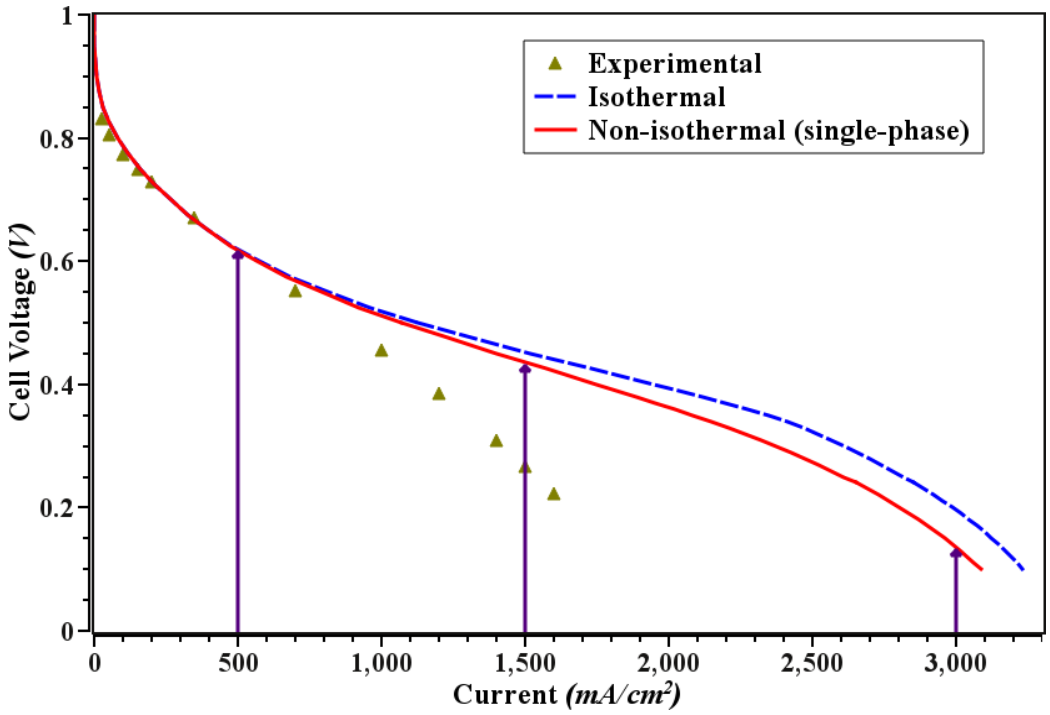

Figure 2.9 – Polarization curve for the base case where *solid red* line represents the non-isothermal case, *dashed blue* line represents the isothermal case, and *dark yellow triangle* point represents the experimental results [42].

over-predicted roughly two times at 0.1 V. This difference can be explained on the basis that the model does not account for the micro-structure of the catalyst layers [123], and the presence of liquid water impeding gas transport. It is interesting to note that the non-isothermal model predictions significantly under-perform the isothermal model at higher current densities. Differences of upto 150 mA/cm^2 are observed at 0.1 V. The non-isothermal model predictions are closer to the experimental data. Three current densities marked with arrows in the Figure 2.9, *viz.*, 500 mA/cm^2 (low), 1500 mA/cm^2 (moderate), and 3000 mA/cm^2 (high), are chosen to understand the non-isothermal effects inside the MEA. Various phenomenon such as heat distribution, current distribution and water management inside the cell at these current densities are discussed in the subsequent sections.

2.7.1.1 Temperature distribution

The temperature distribution in the MEA at three current densities is shown in Figure 2.10. It is observed that the maximum temperature in the MEA increases significantly from 353.9 K (80.75℃) to 361.6 k (88.4℃) as higher current densities are obtained. Figure 2.11 plots the maximum temperature in the MEA versus the current density. An increase of up to 3-4℃ and 9℃ is observed at the medium and the high

current densities respectively, negating the isothermal assumption generally used in the PEMFC modelling literature. The lowest temperature in all three cases is 353.15 K (80℃). This temperature is observed at the Dirichlet boundaries (bipolar plates), implying that there is a net heat release in the MEA. So the current production is associated with temperature rise in the cell. Red hot regions in the middle of the MEA imply that the highest temperatures are observed in the regions where electrochemical reactions take place (catalyst layers). At 3000 mA/cm^2, as shown in the Figure 2.10(c), the hot regions in the middle of the MEA are narrower in bottom portion (in front of the bipolar plates).

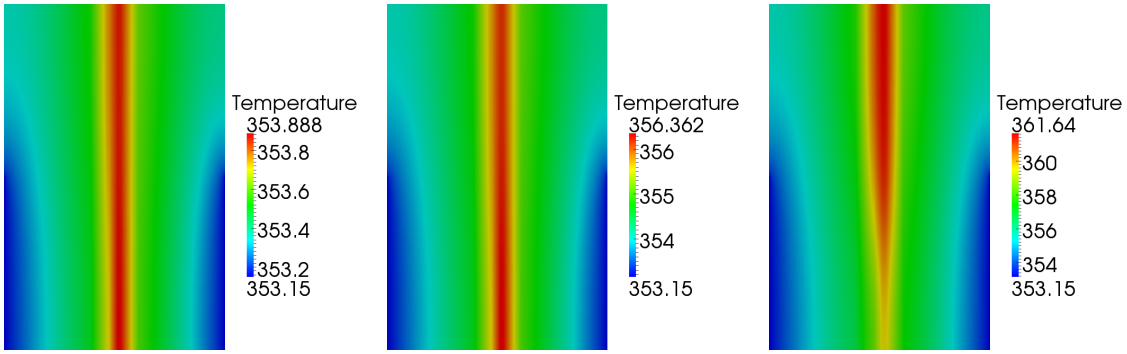

Figure 2.10 – Base case temperature distribution plots in the MEA, for the non-isothermal case at: (a) 500 mA/cm^2, (b) 1500 mA/cm^2, and (c) 3000 mA/cm^2.

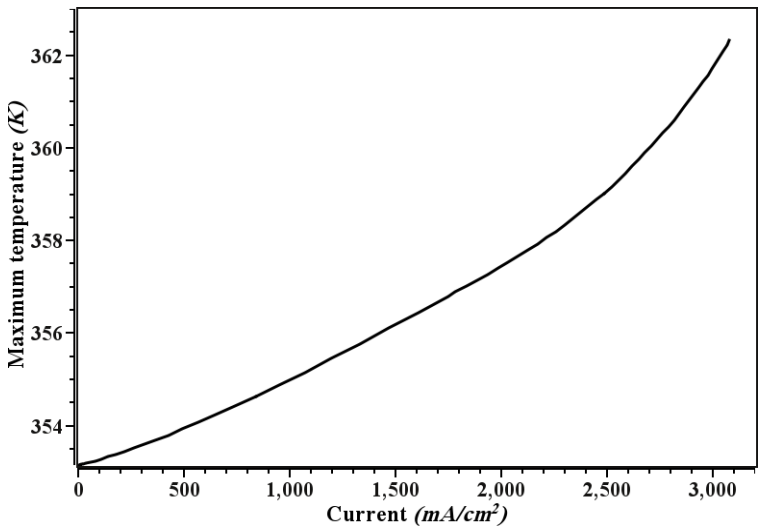

Figure 2.11 – Plot of maximum temperature in the MEA versus the current for the base case.

In the base case, the fraction of the total reversible heat release in the cathode during the ORR, f_{ORR}, is considered to be 1. Figure 2.12 further zooms into these red hot zones (ACL + ML + CCL) in the MEA. Although the temperature profiles are continuous at interfaces between the layers, sharp gradient changes can be observed at the interfaces. It is observed that the CCL (right side) is generally hotter than the ACL (left side), since there are a number of significant heat sources in the CCL, such as, irreversible, reversible and protonic ohmic heating. ACL is generally observed to be hotter in the top portion (in front of the gas channels). At the low current density, the CCL is uniformly hot in the in-plane direction (y-direction). The CCL is hotter in the under-the-rib region at the medium current density. Then, there is complete reversal of temperature distribution in the CCL at high current density conditions. Since PEMFCs are generally operated at medium current densities, strategic cooling of the rib can be performed to increase the cell performance. In order to understand the reversal of temperature distribution in the CCL at high current density, the heat source/sink distribution in the MEA is studied. The magnitudes of individual heat terms in the MEA per unit thickness in the along-the-channel direction (z-direction), are plotted in Figure 2.13, as the current density is varied. It is observed that the irreversible heating due to over-potentials in the CCL dominates the bulk of heat release in the cell, while the irreversible heating in the ACL and electronic ohmic heating in the overall MEA are generally negligible. It can easily be shown that the heat generated due to irreversible heating is in the same order of magnitude as the power due to current generated in the cell.

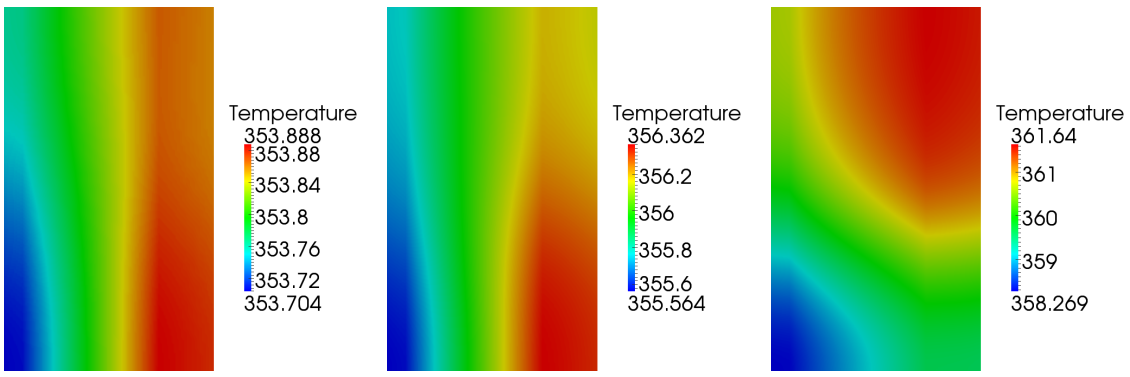

Figure 2.12 – Base case temperature (T) distribution plots in the ACL + ML + CL, for the non-isothermal case at: (a) 500 mA/cm^2, (b) 1500 mA/cm^2, and (c) 3000 mA/cm^2.

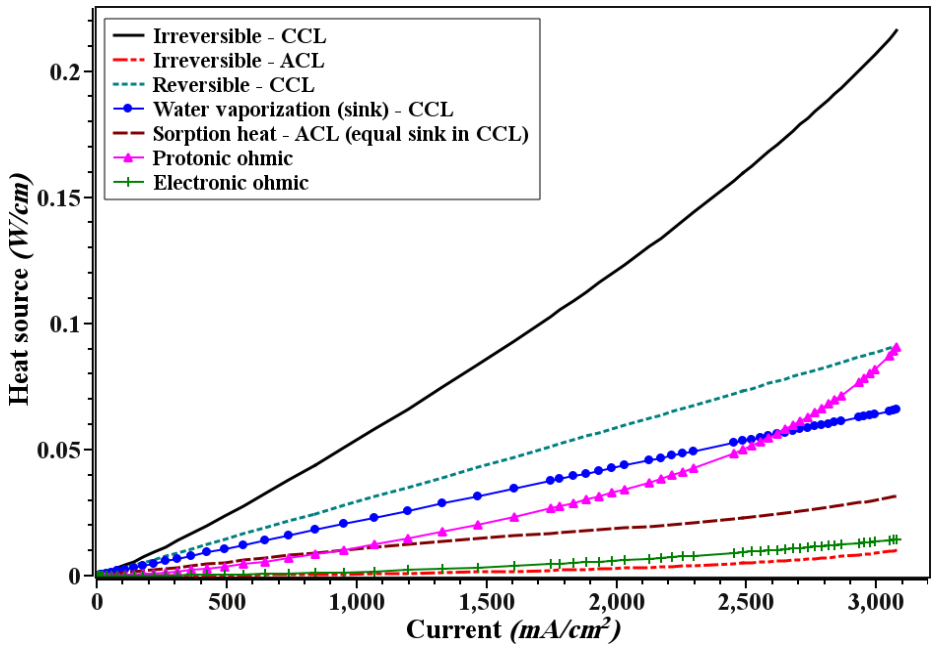

Figure 2.13 – Plot of magnitudes of individual heat terms in the MEA per unit thickness in the z-direction versus the current for the base case.

Figure 2.14 zooms in the heat distribution plot for low to medium current densities (up to 1200 mA/cm^2). It is interesting to note that up to 1000 mA/cm^2, the heat released/absorbed due to sorption/desorption of water in the catalyst layers is higher than the protonic ohmic heat source. Even at high current densities as shown in the Figure 2.13, the heat of sorption/desorption reach up to 10 % of the total heat released/absorbed in the cell. Water in sorbed form moves from the ACL to the CCL due to electro-osmotic drag and thermo-osmosis. So the water is absorbed at the ACL releasing heat. This explains the higher temperatures in the under-the-channel region than the under-the-rib region of the ACL, since there is no reversible heat release in the ACL. For the water balance, equal amounts of water are desorbed at the CCL, which causes heat absorption (sink) in the CCL. It will be seen that the under-the-channel region of the CCL is drier (lower water content in the electrolyte) than the under-the-rib region (Figure 2.20). So higher desorption of water hence more heat is absorbed at the under-the-channel region of the CCL, explaining the observation that the CCL is hotter in the under-the-rib region at medium current density (Figure 2.12(b)). A simulation is run using the same parameters with heat of sorption turned OFF. Temperature distribution in the ACL + ML + CCL, for this simulation are plotted in the Figure 2.15 at low and medium currents. It is observed that the ACL is colder when the heat of sorption is not included in the model. Moreover the temperature distribution is uniform in the in-plane direction which is not observed when

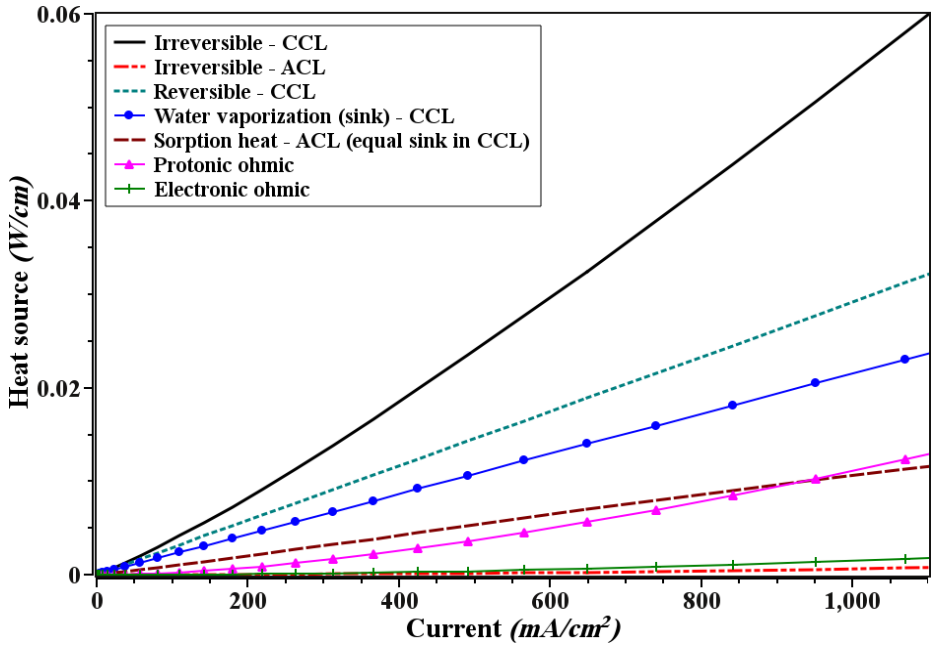

Figure 2.14 – Plot of magnitudes of individual heat terms in the MEA per unit thickness in the z-direction versus the current, upto 1200 mA/cm^2, for the base case.

the heat of sorption is included. Hence the sorption/desorption heat term, neglected in the PEMFC modelling literature (except in Ref. [27]), should be considered for proper assessment of the thermal management in the PEMFC.

Ohmic heating due to proton current overtakes the heat of sorption/desorption at 1000 mA/cm^2, and increases significantly (up to 30 %) at higher current densities. In order to be consistent with the single phase formulation, reversible heat release is computed assuming the entropy of water vapour in this work. This is in contrast to various single-phase models in the literature such as Ju et al. [22, 30], that use the liquid water entropy instead. It is noteworthy that the reversible heat released due to ORR is mostly counterbalanced (roughly 80 %) due to complete evaporation of water produced during the ORR. Finally at higher current densities, irreversible heat production in the CCL dominates all other heat terms. It will also be seen that the current production in the under-the-rib region is severely limited at high current density, thus explaining the complete reversal of temperature distribution in the CCL (Figure 2.12(c)).

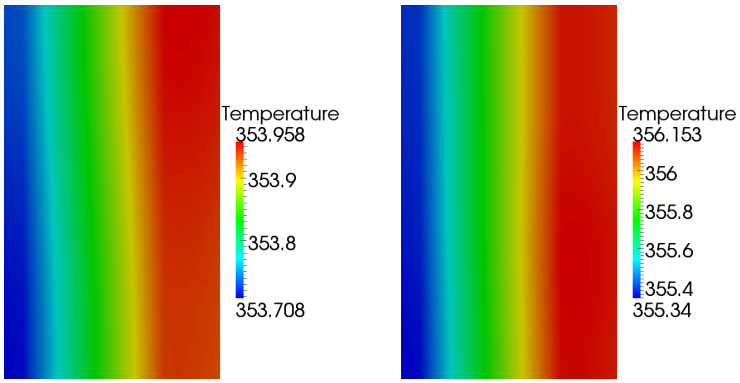

(a) (b)

Figure 2.15 – Temperature (T) distribution plots in the ACL + ML + CL, for the non-isothermal case without heat of sorption at: (a) 500 mA/cm^2, and (b) 1500 mA/cm^2.

2.7.1.2 Non-isothermal effects on current distribution

Figure 2.16 compares the current production in the CCL for the isothermal (first row) and the non-isothermal (second row) case at different current densities. No difference is observed in the low current density case (Figures 2.16(a) and 2.16(b)). The highest current is observed at the CCL-membrane interface suggesting high oxygen gas availability. As current is increased to 1500 mA/cm^2, current production is reduced in the region near the CMPL (right side of the Figure 2.16(e)), for the non-isothermal case due to reduced proton transport and increases slightly at the membrane-CCL interface due to increased kinetic activity and temperature. At high current density, a significant portion of the under-the-rib area is producing no current in the cell. Higher maximum current densities are observed in the CCL due to higher overpotentials (low cell voltage) being applied. The non-isothermal case has a larger inactive region in the under-the-rib region near the membrane (bottom left side of the Figure 2.16(f)). Interestingly for the isothermal model, the under-the-rib region near the CMPL (bottom right side of the Figure 2.16(c)) has slightly better current production than the non-isothermal case, due to better oxygen availability. It is interesting to note that the maximum current density value in the case of the non-isothermal model is higher at the medium current case, while it is lower at the high current case, than the isothermal results. This observation at the high current case is contrary to the expectation that the maximum current values must increase due to better kinetics at high temperatures.

Limitations in current production occur either due to mass transport limitations (availability of oxygen), and due to ohmic overpotentials (charge transport limita-

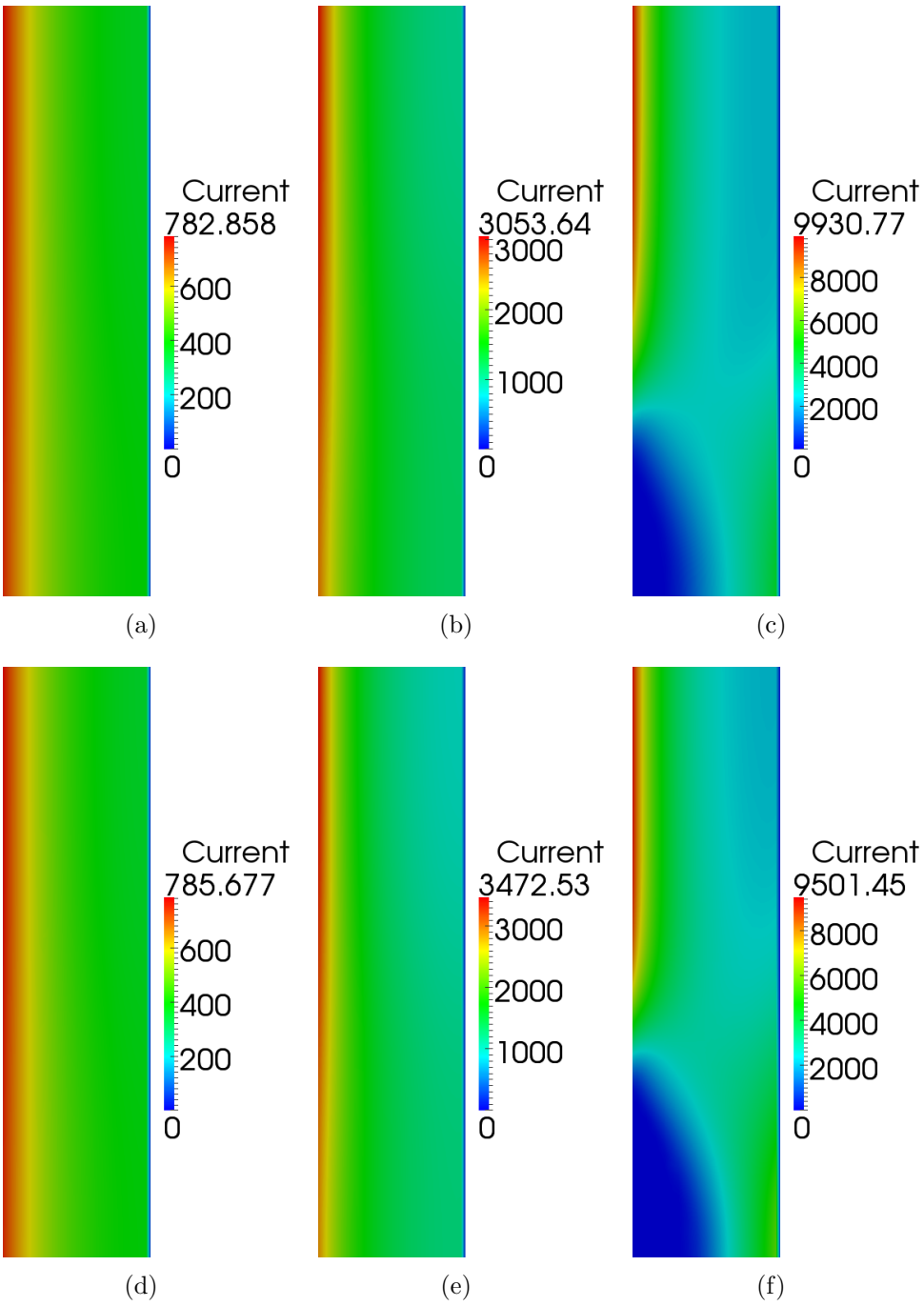

Figure 2.16 – Base case current production plots in the CCL, for the isothermal case at: (a) 500 mA/cm^2, (b) 1500 mA/cm^2, and (c) 3000 mA/cm^2; and for the non-isothermal case at: (d) 500 mA/cm^2, (e) 1500 mA/cm^2, and (f) 3000 mA/cm^2.

tions). Figure 2.17 compares the oxygen availability in the CCL for the isothermal (first row) and the non-isothermal (second row) case at different current densities. It can be seen that the oxygen is available everywhere in the CCL at low and medium current densities for both the cases. The consumption rate of oxygen increases with the current as ascertained by reduction in the x_{O_2} values from low to high current. At high current density, there is zero oxygen availability in the under-the-rib region of the CCL. This explains the blackened out (zero current production) region in under-the-rib area of the CCL at high current density for both cases. It is interesting to note that the non-isothermal case has higher oxygen availability near the membrane in the under-the-channel region (top left side of the Figure 2.17(f)). This behaviour is due to the oxygen diffusion increase with temperature. So the oxygen availability is therefore not the reason behind the reduced performance of the non-isothermal model compared to the isothermal model.

Figure 2.18 compares the electronic potential distribution in the CCL for the isothermal (first row) and the non-isothermal (second row) case at different current densities. It can be seen that the ohmic losses due to electron transport are negligible inside the catalyst layer. However due to under-performance of the non-isothermal model, lower electron potential values (lower cell voltages) are observed compared to the isothermal case at the same current densities. Figure 2.19 compares the protonic potential distribution in the CCL for the isothermal (first row) and the non-isothermal (second row) case at different current densities. It can be seen that proton potentials are decreasing from left to right side (membrane boundary to CGDL boundary) as the proton travels in the direction of decreasing potentials. Although the trends between the isothermal and non-isothermal simulations look the same, the difference between minimum and maximum potential values is different. At medium current density, the differences observed in the case of isothermal and non-isothermal simulations are 0.09 V and 0.11 V respectively. At high current density, the differences observed in the case of isothermal and non-isothermal simulations are 0.23 V and 0.28 V respectively. So the ohmic losses due to proton transport increase with current and are higher for the non-isothermal case than the isothermal case. The lower maximum current density previously discussed, can be explained using the difference, $(\phi_s - \phi_m)$, *i.e.*, potential jump required at a reaction site. This jump has increased considerably in the non-isothermal case due to protonic ohmic losses. Moreover the theoretical equilibrium potential (E_{eq}) decreases with temperature. This results in lower overpotentials (mathematically higher since the values are negative), which offset the effect of higher temperatures resulting in lower maximum current values.

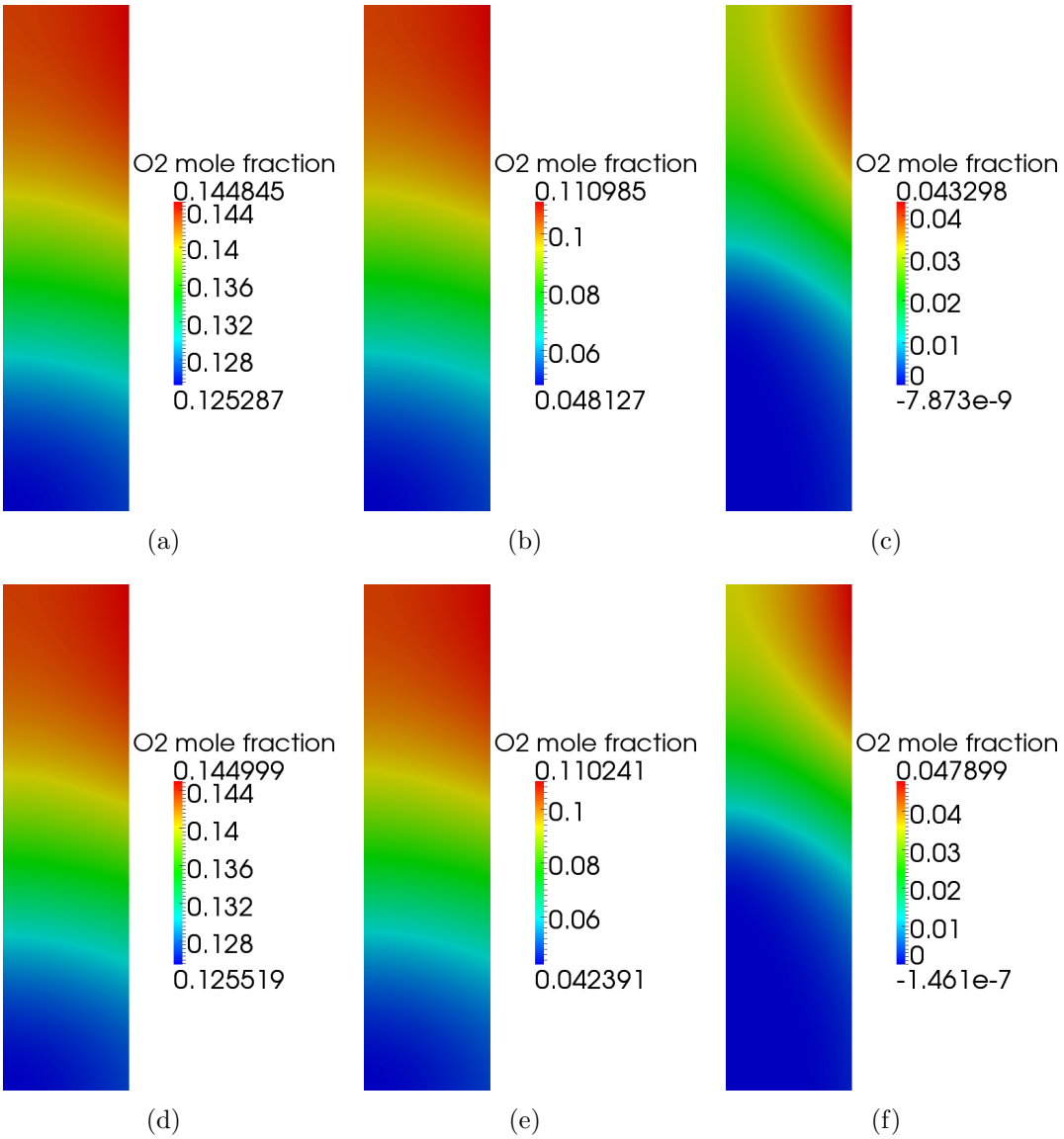

Figure 2.17 – Base case oxygen mole fraction (x_{O_2}) plots in the CCL, for the isothermal case at: (a) 500 mA/cm^2, (b) 1500 mA/cm^2, and (c) 3000 mA/cm^2; and for the non-isothermal case at: (d) 500 mA/cm^2, (e) 1500 mA/cm^2, and (f) 3000 mA/cm^2.

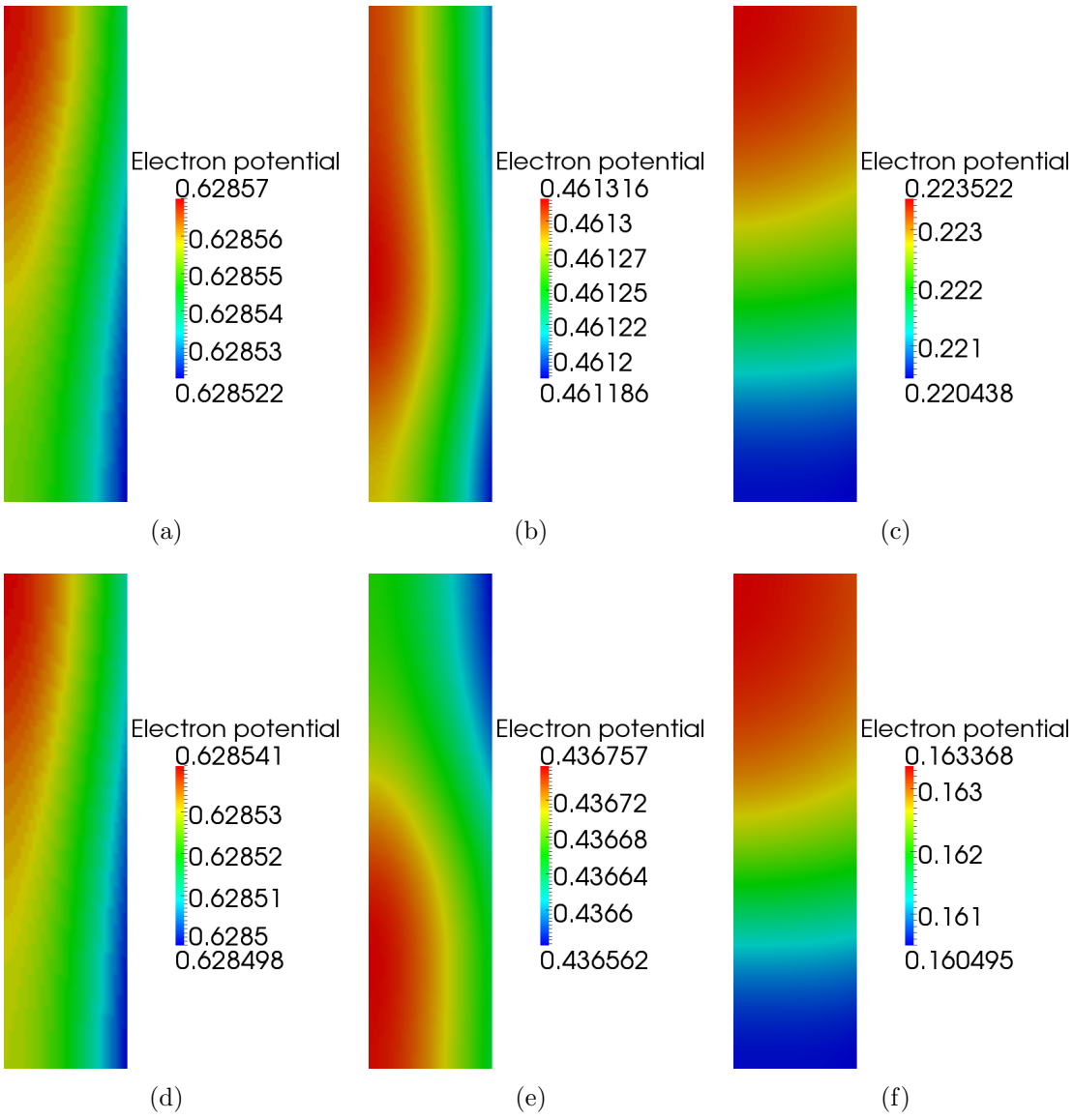

Figure 2.18 – Base case electron potential (phi_s), plots in the CCL, for the isothermal case at: (a) 500 mA/cm^2, (b) 1500 mA/cm^2, and (c) 3000 mA/cm^2; and for the non-isothermal case at: (d) 500 mA/cm^2, (e) 1500 mA/cm^2, and (f) 3000 mA/cm^2.

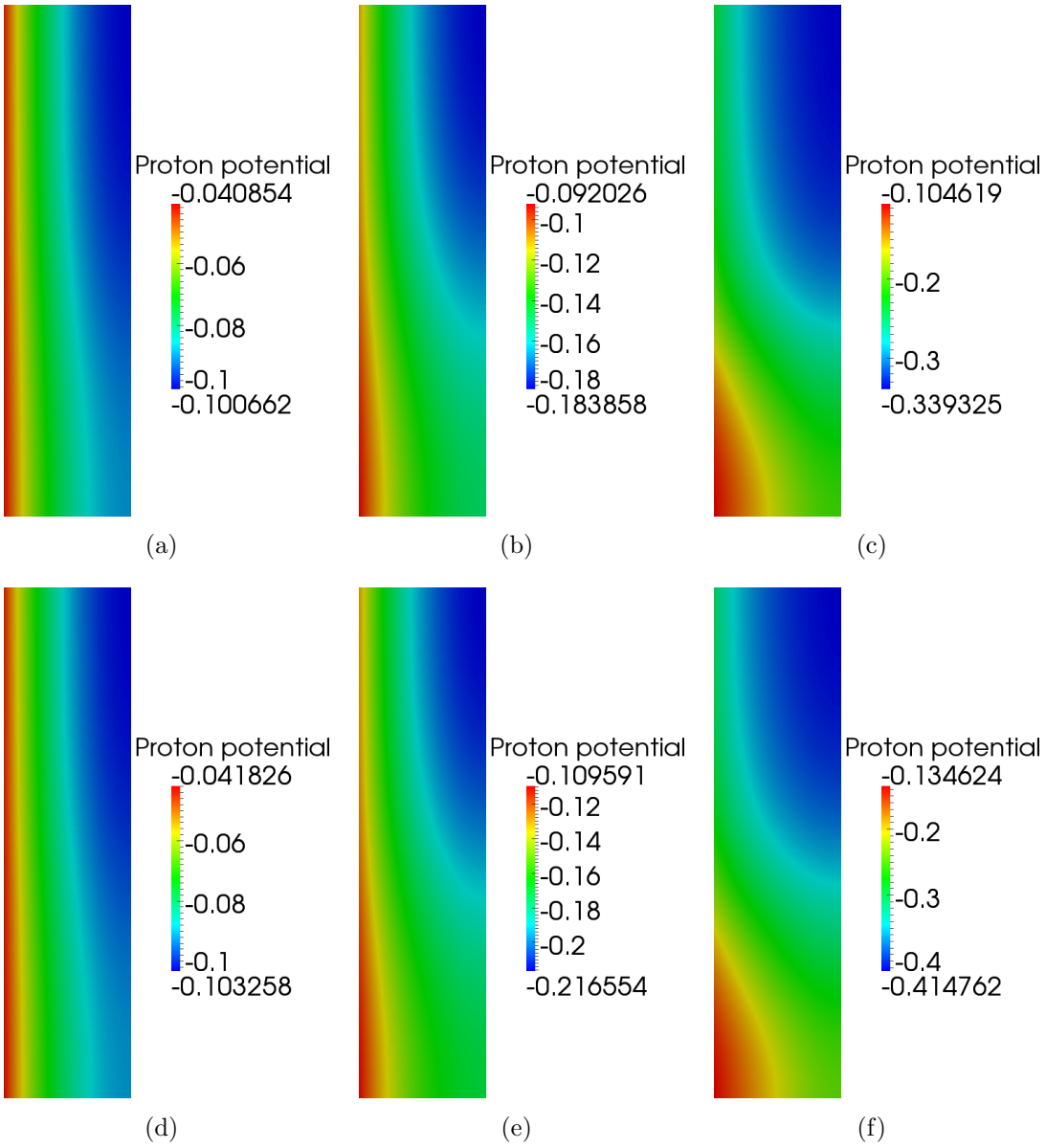

Figure 2.19 – Base case proton potential (ϕ_m) plots in the CCL, for the isothermal case at: (a) 500 mA/cm^2, (b) 1500 mA/cm^2, and (c) 3000 mA/cm^2; and for the non-isothermal case at: (d) 500 mA/cm^2, (e) 1500 mA/cm^2, and (f) 3000 mA/cm^2.

2.7.1.3 Non-isothermal effects on water management

In the base case, the lower performance of the non-isothermal model is attributed due to proton transport limitations. Proton conductivity in the electrolyte (Nafion®) increases with membrane water content (λ) and temperature (T). In a vapour-equilibriated membrane, λ values in the CLs are determined based on the local RH values. The production rate of water vapour increases with current density, leading to higher x_{H_2O} values (hence higher RH). This can be observed by the increasing λ values in the CCL as the current density increases, as shown in the Figure 2.20. Water vapour saturation pressure is constant for the isothermal model (due to constant temperature). At high current density, this leads to non-physical RH values (more than 100 %) in the CCL for the isothermal model. This results in a nearly constant high λ value in the CCL in Figure 2.20(c). In the non-isothermal model, RH values decrease with temperature (saturation pressure). The membrane is therefore not fully humidified as observed Figure 2.20(f). The increase in protonic ohmic losses are therefore corroborated by this observation.

Figure 2.21 compares the membrane water content distribution in the ACL + ML + CL at high current density, for the isothermal and non-isothermal case. It can be seen that all the layers (ACL + ML + CCL) have much lower water content in the non-isothermal case due to high temperature values. Temperatures in the ACL increase due to heat released by sorption of water. RH values in the ACL are therefore decreased leading to even lower λ values as observed in the Figure 2.21(b). Water in the sorbed form travels from the ACL to the CCL due to electro-osmotic drag, counterbalanced by the back diffusion. However due to temperature gradients, thermal osmosis is observed from the low temperature region (ACL) to the high temperature region (CCL). In order to assess the impact of thermal osmosis on the non-isothermal model, a simulation is run with the thermal osmosis term switched OFF. The impact of thermal osmosis on the λ distribution in the CCL, at the 3000 mA/cm^2 current density is assessed in the Figure 2.22. It can be clearly seen that the CCL has lower λ value when the thermal osmosis is turned OFF in the model (Figure 2.22(b)), hence higher ohmic losses and further lower performance. Since lower temperatures (higher RH values) are observed in the under-the-rib region, higher λ values are observed in the under-the-rib region when the thermal osmosis is turned ON (Figure 2.22(a)).

Figure 2.23 plots the sorbed water flux from the ACL to the CCL as the current is increased, for the three cases, *viz.*, isothermal model (pink double dashed line),

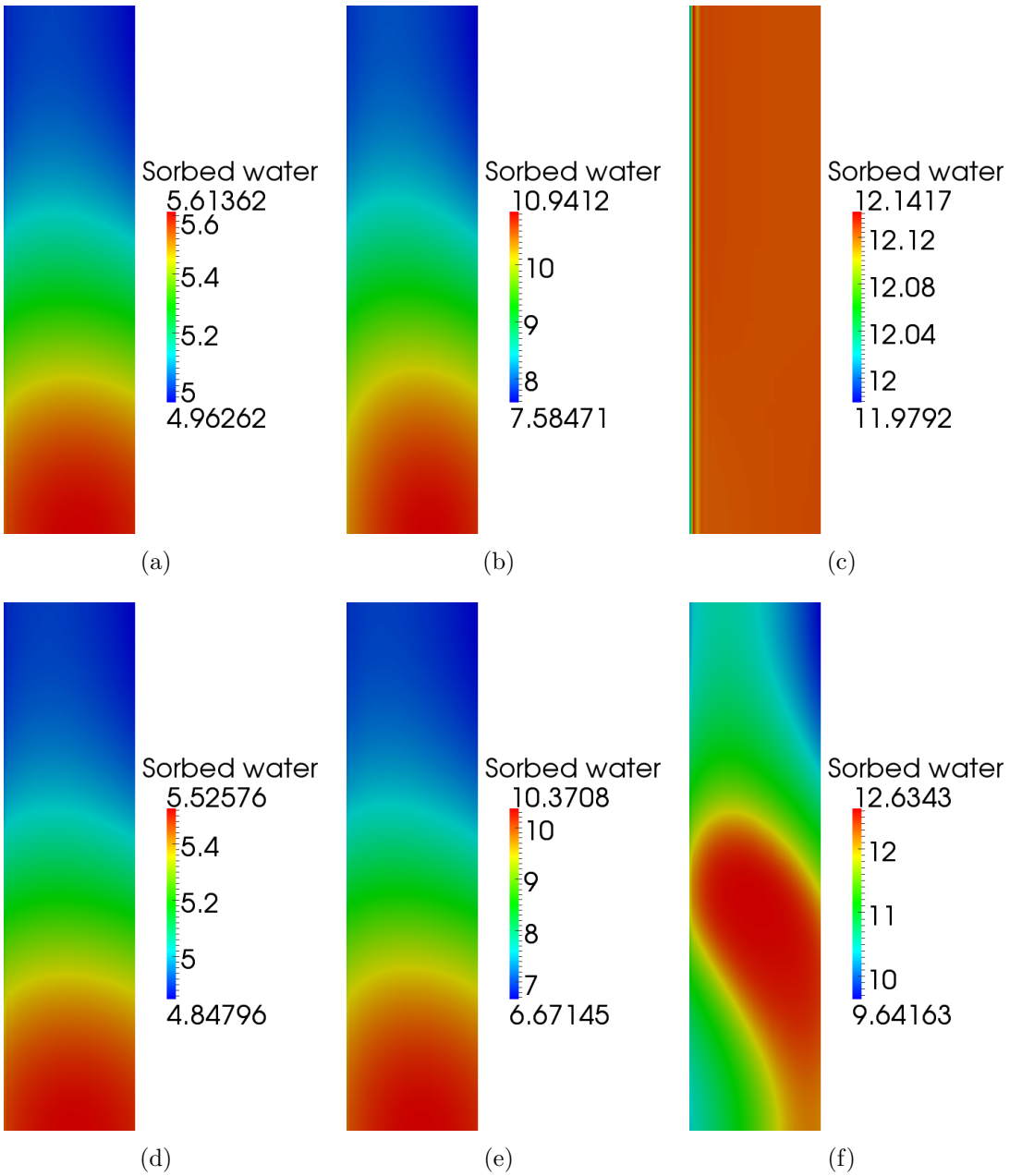

Figure 2.20 – Base case sorbed water content (λ) plots in the CCL, for the isothermal case at: (a) 500 mA/cm^2, (b) 1500 mA/cm^2, and (c) 3000 mA/cm^2; and for the non-isothermal case at: (d) 500 mA/cm^2, (e) 1500 mA/cm^2, and (f) 3000 mA/cm^2.

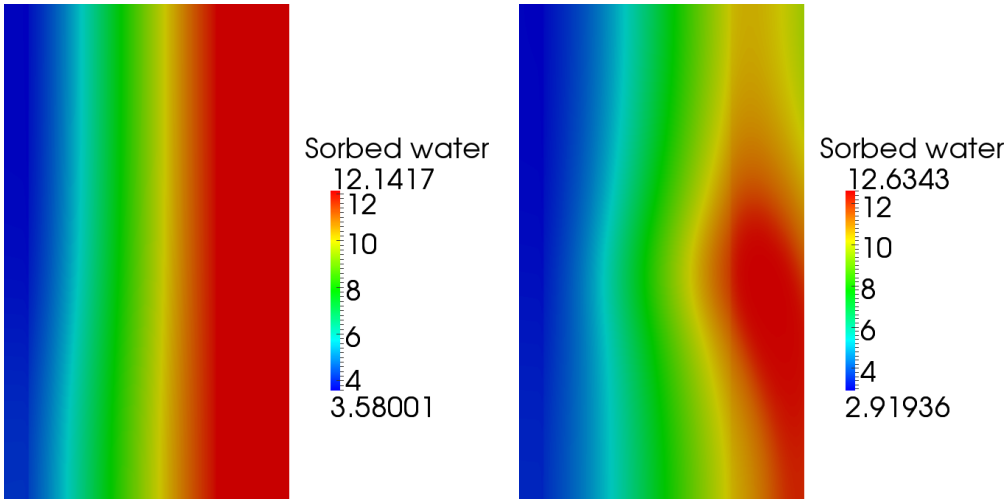

(a) (b)

Figure 2.21 – Base case sorbed water content (λ) plots in the ACL + ML + CCL, for the isothermal case at: (a) 3000 mA/cm^2; and for the non-isothermal case at: (b) 3000 mA/cm^2.

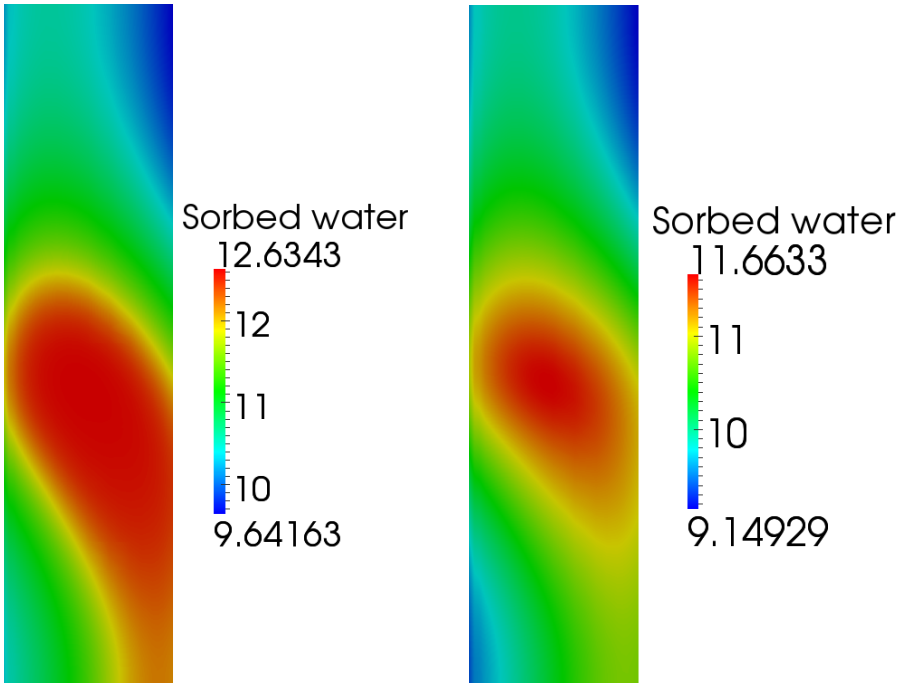

(a) (b)

Figure 2.22 – Membrane water content (λ) distribution plots in the CCL at 3000 mA/cm^2 for the: (a) non-isothermal model with thermal osmosis, and (b) non-isothermal model without thermal osmosis.

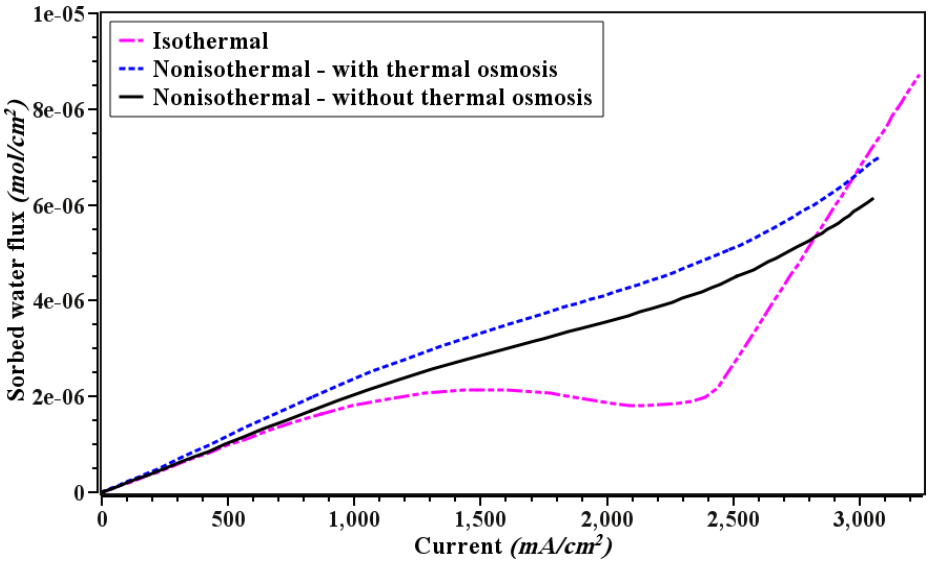

Figure 2.23 – Comparison of the sorbed water flux (from the ACL to the CCL) versus the current, where *pink double dashed* line represents the isothermal model, *solid black* line represents the non-isothermal model without thermal osmosis, and *blue dashed* line represents the non-isothermal model with thermal osmosis.

non-isothermal model without thermal osmosis (black solid line), and non-isothermal model with thermal osmosis (blue dashed line). The water flux increases as the current is increased from low to medium values (1000 mA/cm^2). Water flux increases more rapidly in the case of thermal osmosis due to lower temperatures in the ACL as discussed before. However in the isothermal model, due to water buildup in the CCL, the back diffusion counterbalances the electro-osmotic drag and water flux increment rate is reduced. The water flux drops from 1500 mA/cm^2 to 2000 mA/cm^2, as back diffusion counteracts the electro-osmosis effects. λ values in the CCL cannot increase beyond 100 % RH value. At very high current densities ($>$ 2200 mA/cm^2), back diffusion reaches its maximum value while the electro-osmotic drag continues to increase resulting in a rapid rise in water flux. The non-isothermal model sees a steady rise in water flux from the ACL to the CCL. This is due to the fact that the CCL is drier (due to increase in temperature), hence back diffusion does not counterbalance the electro-osmotic drag. The water flux is further increased by roughly 15 % due to the thermal osmosis, corroborating the observation of higher λ values in the CCL.

The non-isothermal model also affects the water transport in the vapour phase. Figure 2.24 shows the relative humidity values in the cathode electode (CCL + CMPL + CGDL) for the isothermal and non-isothermal models at different current densities.

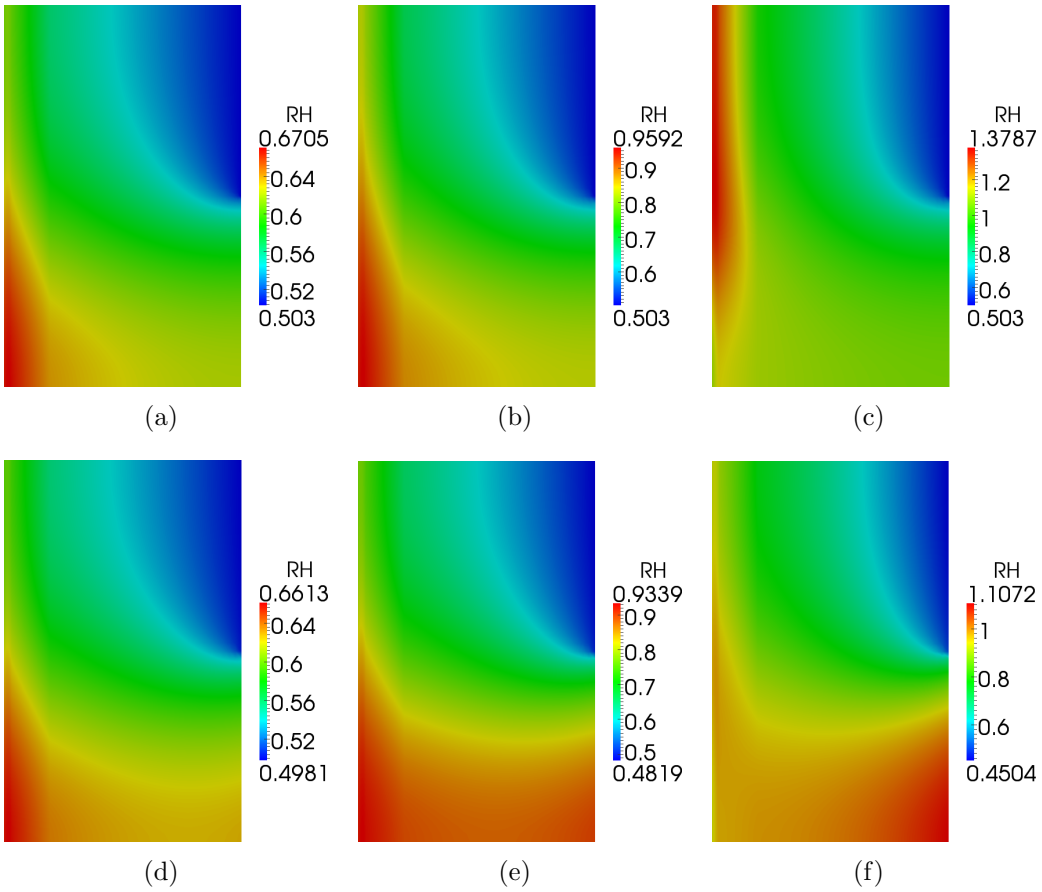

Figure 2.24 – Base case relative humidity plots in the cathode electrode (CCL + CMPL + CGDL), for the isothermal case at: (a) 500 mA/cm^2, (b) 1500 mA/cm^2, and (c) 3000 mA/cm^2; and for the non-isothermal case at: (d) 500 mA/cm^2, (e) 1500 mA/cm^2, and (f) 3000 mA/cm^2.

No significant differences are observed for the low current case. However as the current density increases, water vapour under-the-rib area is very different for the two cases. Figure 2.24(e) and 2.24(f) show higher relative humidity values under-the-rib for the non-isothermal case. Non-physical RH values (more than 100 %) can be observed for both the cases at high current densities (more for the isothermal case). Hence liquid water condensation will take place. It is interesting to note that the isothermal model predicts liquid water condensation in the CCL, while in the case of non-isothermal model, liquid water condensation will take place near the rib in the CGDL. It also asserts the need for a two-phase model to be solved alongside the non-isothermal model.

2.7.1.4 Impact of reversible heat distribution

The overall reaction of hydrogen and oxygen producing water is exothermic. The non-isothermal models in the literature assume that the total reversible heat due to overall reaction is generated during the half-reaction of ORR while no reversible heat is generated during the half-reaction of HOR. In contrast to this, Ramousse et al. [19] calculated that the HOR is highly exothermic while the ORR is endothermic. Based on their calculations, the f_{ORR} is determined to be -0.385. In order to assess the impact of the reversible heat distribution, a simulation is run employing the f_{ORR} to be -0.385. Figure 2.25 compares the performance from this simulation to the base case ($f_{ORR} = 1.0$). A reduction in performance is predicted in the case of endothermic ORR reaction.

Figure 2.26 compares the temperature distribution inside the ACL + ML + CL for values of f_{ORR} to be 1.0 (first row) and -0.385 (second row), at medium and high current density. The ACL is observed to be hotter than the CCL in the case of exothermic HOR reaction. It is interesting to note that the heat of sorption alongside the reversible heat release makes the under-the-channel region of the ACL the hottest. A complete reversal of temperature profiles in the in-plane and through-plane direction is observed at medium current density for $f_{ORR} = -0.385$ (Figure 2.26(c)). The under-the-rib area is observed to be the coldest of all three layers at high current conditions (Figure 2.26(d)). Figure 2.27 plots the variation of reversible,

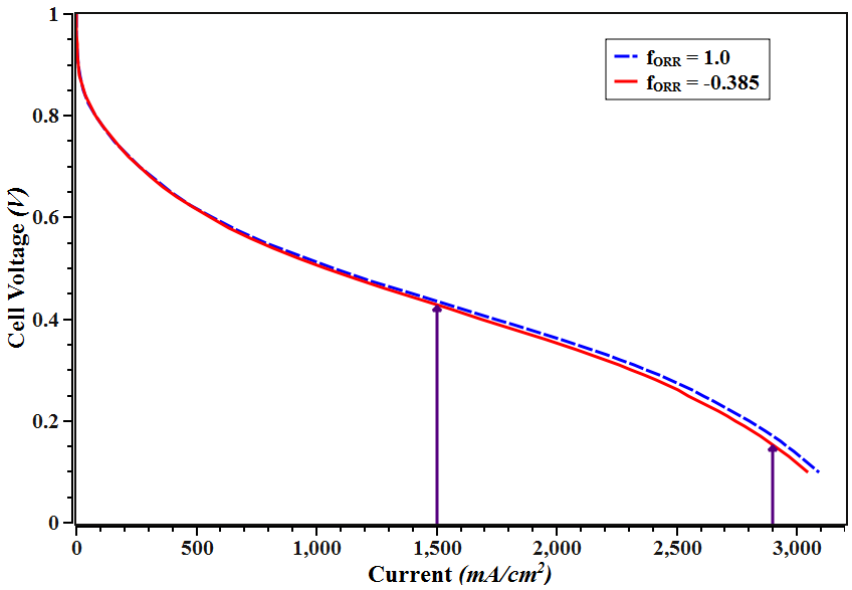

Figure 2.25 – Polarization curve for the base case, where *blue dashed* line represents the case of $f_{ORR} = 1.0$, and *solid red* line represents the case of $f_{ORR} = -0.385$.

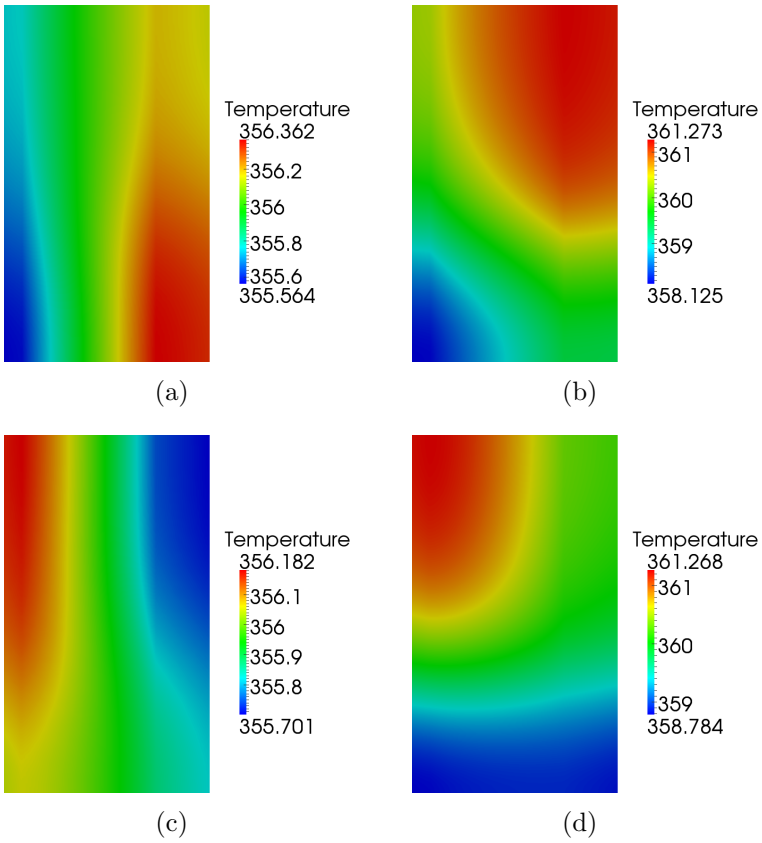

Figure 2.26 – Base case temperature distribution in the ACL + ML + CL, for $f_{ORR} = 1.0$ at: (a) 1500 mA/cm^2, and (b) 3000 mA/cm^2; and for $f_{ORR} = -0.385$ at: (c) 1500 mA/cm^2, and (d) 3000 mA/cm^2.

irreversible and water vaporization heat terms in the CLs with current density. The irreversible heating in the CCL is observed to be the dominating heat source (solid black line). However it is counterbalanced by the heat sinks corresponding to the ORR and complete vaporization of water such that the net heat source due to these three effects in the CCL (red line with ellipse symbols) is significantly smaller than the reversible heat produced due to the HOR in the ACL (dashed blue line). Figure 2.28 compares the sorbed water distribution inside the CCL at high current value. Less water is sorbed at the ACL due to the higher temperatures. This eventually results in a smaller amount of water movement to the CCL, hence the CCL is drier (Figure 2.28(b)). Moreover thermal osmosis occurs from the CCL (low temperature) to the ACL (high temperature). All these factors combine to increase the protonic ohmic losses and hence reduce the performance for the exothermic HOR case. It is therefore important to characterize the reversible heat distribution inside the MEA for realistic assessment of the fuel cell performance.

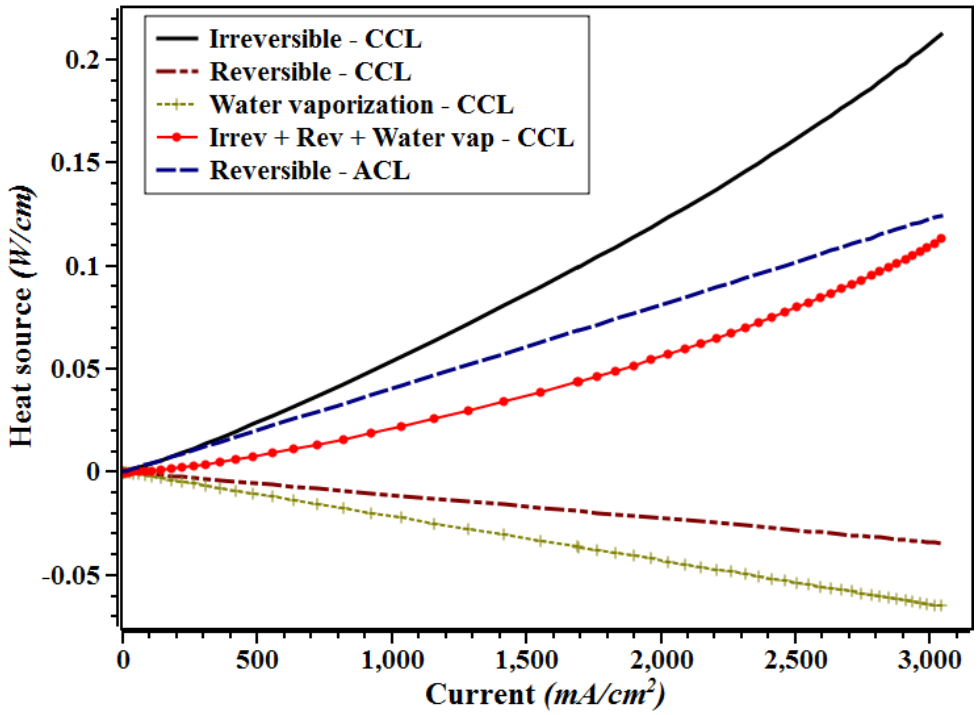

Figure 2.27 – Variation of reversible, irreversible and water vaporization heat terms in the CLs with current for $f_{ORR} = -0.385$.

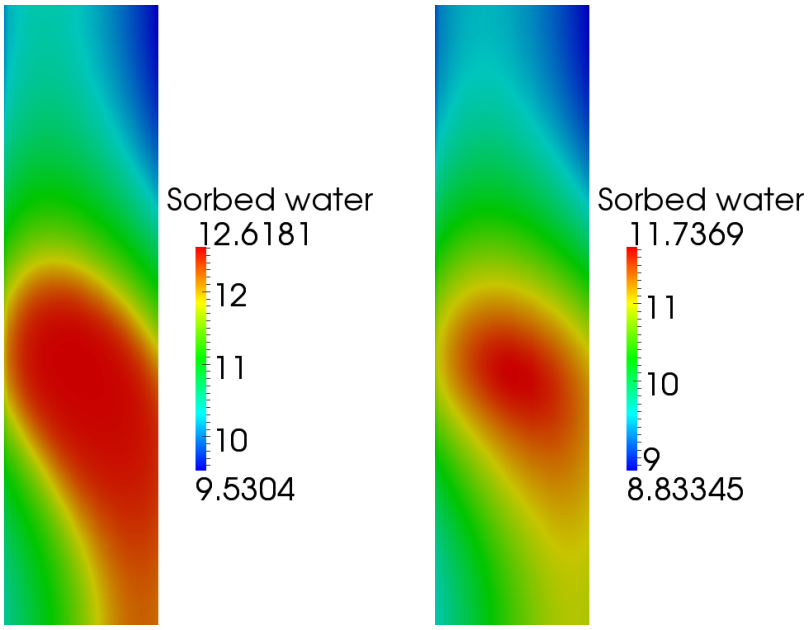

(a) (b)

Figure 2.28 – Base case λ distribution in the CCL, for $f_{ORR} = 1.0$ at: (a) 3000 mA/cm^2; and for $f_{ORR} = -0.385$ at: (b) 3000 mA/cm^2.

2.7.1.5 Impact of MPL thermal conductivity

As discussed before, the majority of the heat is produced inside the CCL. Temperature rises of upto 10℃ are observed inside the CCL leading to performance losses (due to drier membrane). For effective thermal management, the heat produced in the cell has to be effectively rejected. The CMPL thermal conductivity plays an important role in effective heat conduction out of the CCL. In the base case, the CMPL thermal conductivity is considered to be anisotropic such that it is ten times more thermally conductive in the in-plane direction than the through-plane direction (based on the data by Ref. [45, 50]). The observation for the in-plane thermal conductivity by Teertstra et al. [50] might be due to penetration of the MPL ink in the GDL. Nevertheless it is the only data reported in the literature for the in-plane thermal conductivity of the MPL.

The MPL transport properties are generally considered to be isotropic due to its homogeneous nature. Wide variations in the through-plane thermal conductivity of the MPL are reported in the literature with values in the range of 0.0005 to 0.0012 W/(cm-K) [144]. Simulations are run considering four sets of isotropic thermal conductivity values for the MPL, *viz.*, 0.1, 0.01, 0.001, 0.0005 and 0.0001 W/(cm-K). Figure 2.29 compares the performance of these simulations to the base case (non-isothermal model) and the experimental data [42]. In the base case, anisotropic values are considered for the MPL thermal conductivity, with the in-plane value one order of magnitude higher than the through-plane value. Significant improvements in the performance (double dashed blue line) are observed when the MPL is made more thermally conductive, *i.e.*, $k_{MPL} = 0.01$ W/(cm-K). However the improvement is marginal when the k_{MPL} is further increased to 0.1 W/(cm-K). As the thermal conductivity of the MPL is reduced further from the base case, the simulation predictions deviate more significantly from the isothermal results and are closer to the experimental data. It is therefore fair to say that if the in-plane thermal conductivity of the MPL is considered to be of the same order as the through-plane value, same as the $k_{MPL} = 0.001$ W/(cm-K) case, then the non-isothermal model predictions would deviate even more significantly from the isothermal results. The phenomenon of membrane dry-out [145] is observed in the case of $k_{MPL} = 0.0001$ W/(cm-K). The membrane water content decreased significantly resulting in severe protonic ohmic losses. This further increases the amount of heat generated and causes self-heating (despite very low current). At the cell voltage of 0.1 V, the maximum temperature observed in the cell is 378.85 K (105.7℃), *i.e.*, a rise of 25.7℃. There is a rapid decline

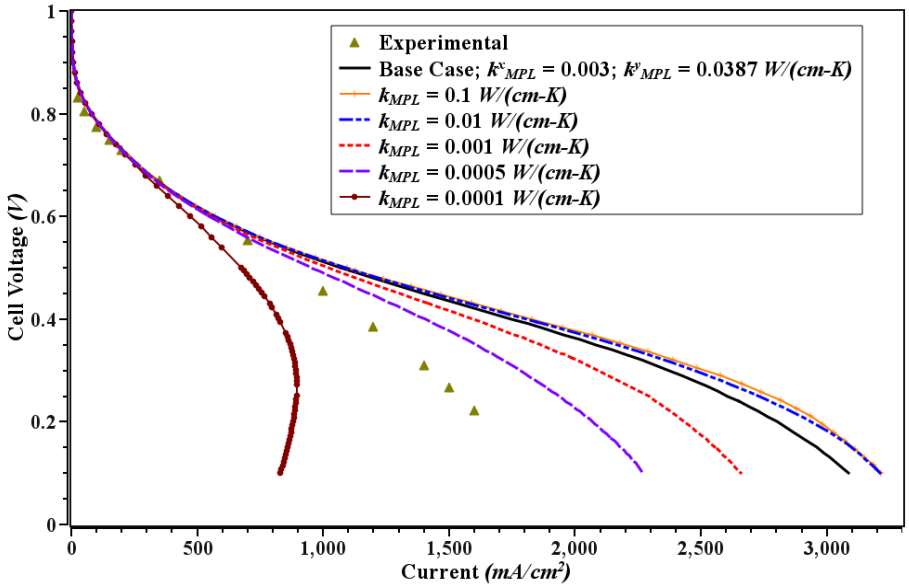

Figure 2.29 – Comparison of performance for various MPL thermal conductivity values to the base case and the experimental data.

in the cell voltage and the model under-predicts the performance significantly. It can be seen that despite the cell voltage being further reduced from roughly 0.3 V, a reduction in current is observed. The MPL thermal conductivity therefore significantly affects the cell performance and is required to be reliably assessed.

2.7.2 Low humidity and high temperature conditions

The cell performance is assessed for the same humidity conditions, but at higher temperatures. T_{cell} is considered to be 368.15 K (95℃). Figure 2.30 compares the performance of the non-isothermal and isothermal model predictions with the experimental data. Figure 2.30 also plots the maximum temperature observed in the cell (right y-axis) as the current is varied. A rise of upto 8℃ is observed that is lower than the base case. This is due to lower current production when the cell is run under these conditions. Predictions of the isothermal and non-isothermal models are the same in the low current density ranges (up to 500 mA/cm^2). Both model predictions overestimate the experimental data. At high temperature conditions fuel-crossover is high, which is not considered in this model. This could be the possible reason for the over-estimation.

As the current density increases, both model predictions deviate significantly from the experimental data. This might be due to a lack of consideration of the micro-

structure (agglomerate formation) of the catalyst layers. The non-isothermal model under-predicts performance significantly compared to the isothermal model for current densities higher than 1000 mA/cm^2. The non-isothermal model predictions are closer to the experimental data again. It is interesting to observe that the mass transport knee (limited oxygen availability) is observed for the isothermal model at 2500 mA/cm^2; however the same is not observed for the non-isothermal case. Figure 2.31 compares the current, x_{O_2} and λ distribution plots in the CCL for the isothermal (first row) and non-isothermal (second row) models, at high current density of 2500 mA/cm^2 (arrow-marked in the Figure 2.30). Large inactive regions (negligible current) are observed for the non-isothermal model in the under-the-rib region (Figure 2.31(d)). The current production in the under-the-channel region near to the CMPL is significantly reduced in the case of non-isothermal model (top right side of the Figure 2.31(d)). It is interesting to note that the maximum current value in the non-isothermal case (Figure 2.31(d)) is much higher than the isothermal case (Figure 2.31(a)). It is observed that the overpotential is nearly the same in the high current area for both the isothermal and non-isothermal models. This is in contrast to the observation made for the low temperature conditions. So the higher temperatures in the non-isothermal model results in better kinetics hence higher maximum current values. Oxygen availability is higher in the case of non-isothermal model as diffusion

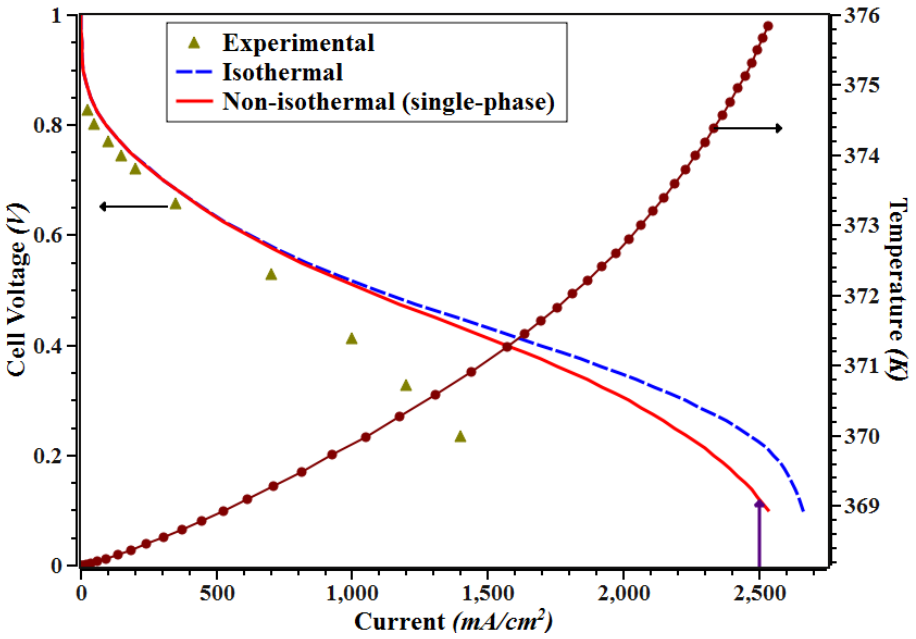

Figure 2.30 – Polarization curves (isothermal, non-isothermal and experimental) and maximum temperature versus current plot (wine red line with ellipse symbols) for the 50 % RH and 95℃ conditions.

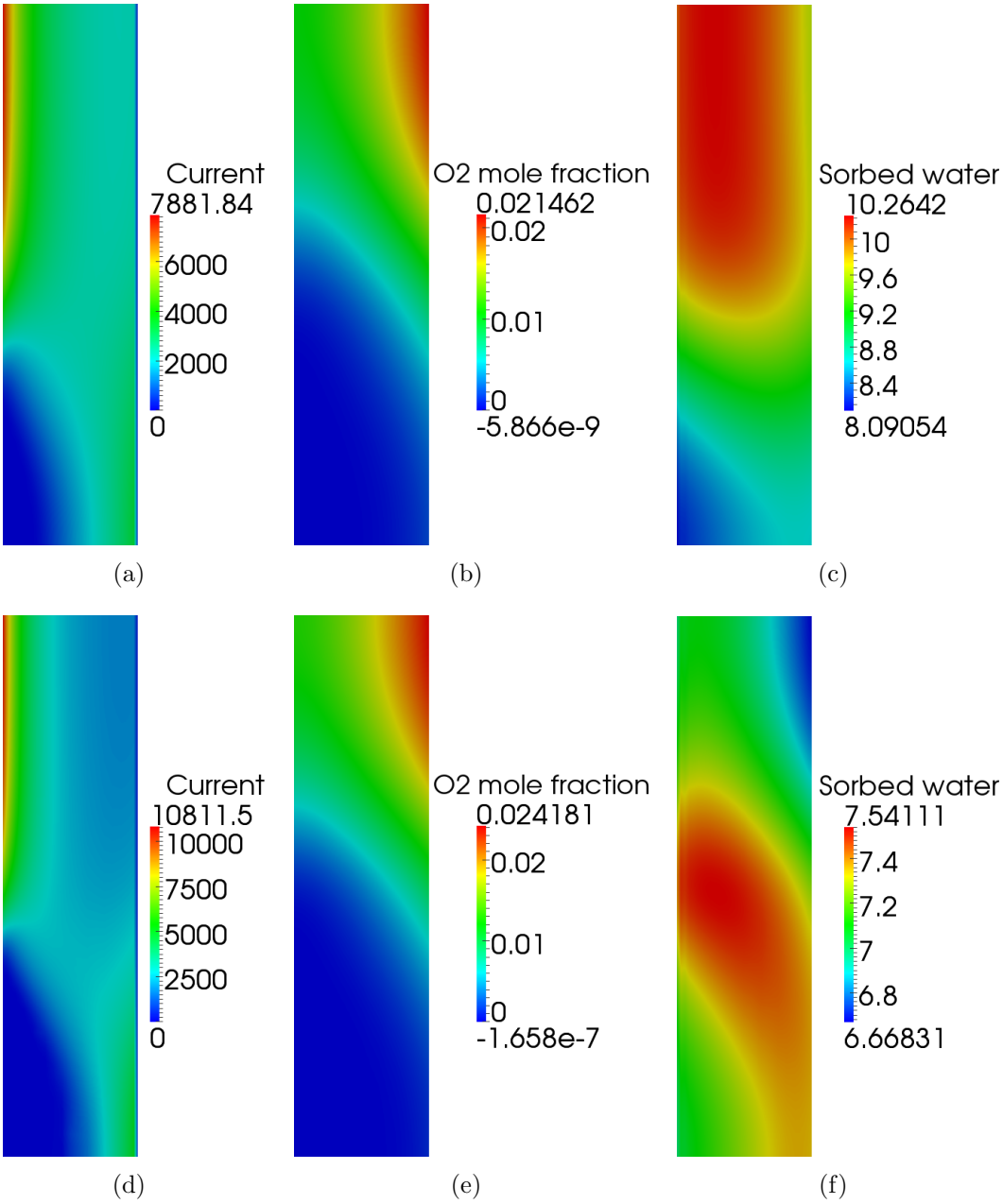

Figure 2.31 – Distribution of various species inside the CCL for 50% RH and 95°Cat 2500 mA/cm^2, for the isothermal case: (a) current, (b) x_{O_2}, and (c) λ; and for the non-isothermal case: (d) current, (e) x_{O_2}, and (f) λ.

increases with temperature. The ionomer in the CCL is severely dried out because of the very high temperatures observed in the cell (more than 100℃). The difference in maximum λ values for the two cases is more than in the case of the base case (low temperature operation). The under-performance predicted by the non-isothermal model is therefore more severe at high temperature. Higher oxygen availability also confirms that mass transport limitations in the case of non-isothermal model are less severe. However, the performance is severely proton transport limited.

2.7.3 High humidity and low temperature conditions

The cell performance at high humidity conditions is evaluated by considering the anode and cathode RH values to be 70 %. The cell temperature is considered as 353.15 K (80℃). Figure 2.32 compares the performance predictions of the non-isothermal model to the isothermal model and the experimental data [42]. The isothermal and non-isothermal model predictions significantly deviate from the experimental data from 700 mA/cm^2 onwards (due to lack of consideration of the micro-structure). However there is negligible difference observed between the isothermal and non-isothermal model predictions under these conditions. Despite this, a temperature rise of up to 9-10℃ is observed in the cell (red line with ellipse symbols in the Figure 2.32).

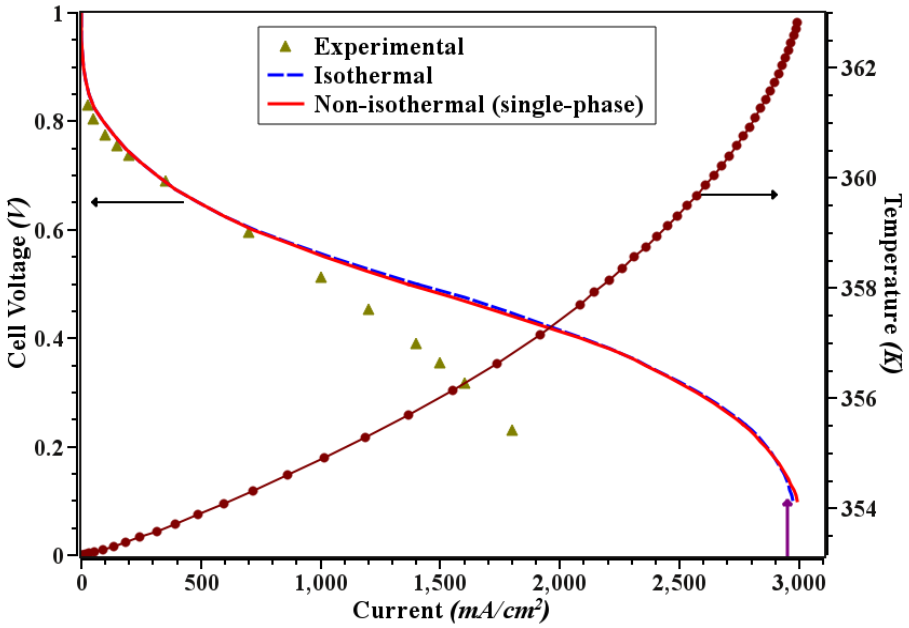

Figure 2.32 – Polarization curves (isothermal, non-isothermal and experimental) and maximum temperature versus current plot (wine red line with ellipse symbols) for the 70 % RH and 80℃ conditions.

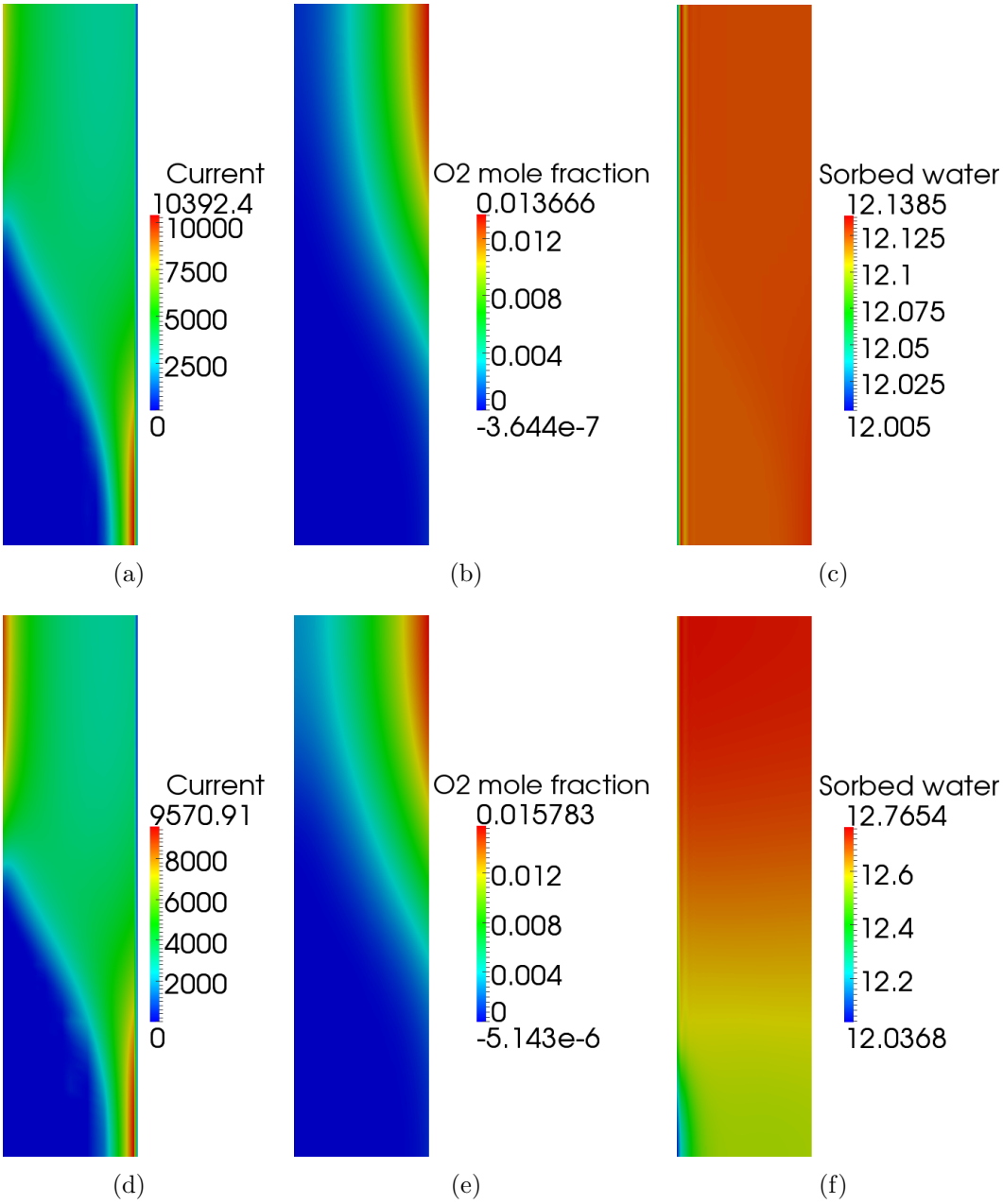

Figure 2.33 – Distribution of various species inside the CCL for 70% RH and 80°Cat 2950 mA/cm^2, for the isothermal case: (a) current, (b) x_{O_2}, and (c) λ; and for the non-isothermal case: (d) current, (e) x_{O_2}, and (f) λ.

Figure 2.33 compares the current, x_{O_2} and λ distribution plots in the CCL for the isothermal (first row) and non-isothermal (second row) models, at a current density of 2950 mA/cm^2 (arrow-marked in the Figure 2.32). Large inactive regions (negligible current) are observed in the under-the-rib regions for both the isothermal and non-isothermal models. An additional maximum current spot is observed in the under-the channel region of the membrane-CCL interface for the non-isothermal model (top left side of the Figure 2.33(d)). This is observed due to increased oxygen availability under the non-isothermal conditions (Figure 2.33(e)). This explains the observation of a slight over-performance in the non-isothermal model at high current densities. It is noteworthy that the maximum current value in the non-isothermal case (Figure 2.33(d)) is lower than the isothermal case (Figure 2.33(a)). This observation is similar to the low humidity conditions (potential jumps counterbalancing the effects of temperature increase). Slight reductions in the λ values can be observed for the non-isothermal model in the under-the-channel region (Figure 2.33(f)). The ionomer in the CCL is flooded for both the cases (minimum value of λ is more than 12). So the cell performance is not proton transport limited under high humidity and low temperature conditions. It is noteworthy that the maximum RH value observed in the non-isothermal model at the high current density is 1.221. This asserts the need for a two-phase (and non-isothermal) model.

2.7.4 High humidity and high temperature conditions

Under the same high humidity conditions, the cell temperature is increased to 368.15 K (95℃). Figure 2.34 compares the performance predictions of the non-isothermal model to the isothermal model and the experimental data [42]. A temperature rise of up to 6-7℃ is observed due to lower current production when the cell is run under these conditions. Predictions of the isothermal and non-isothermal models are the same in the low current ranges (up to 700 mA/cm^2). Both model predictions slightly over-estimate the experimental data at low current density due to lack of consideration of the fuel cross-over. The non-isothermal model under-performs the isothermal results from 700 mA/cm^2 onwards. It can be observed that the maximum deviations between the isothermal and non-isothermal results are observed as the oxygen transport becomes limited (mass-transport knee). This deviation is observed due to reduced proton transport in the case of non-isothermal model, as shown by drier ionomer in the CCL at the current density of 1850 mA/cm^2 (Figure 2.35).

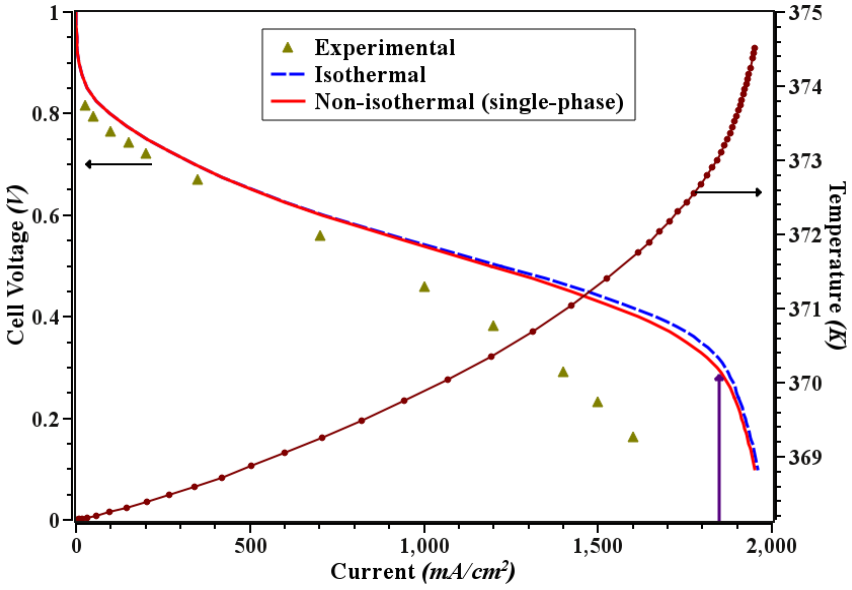

Figure 2.34 – Polarization curves (isothermal, non-isothermal and experimental) and maximum temperature versus current plot (wine red line with ellipse symbols) for the 70 % RH and 95℃ conditions.

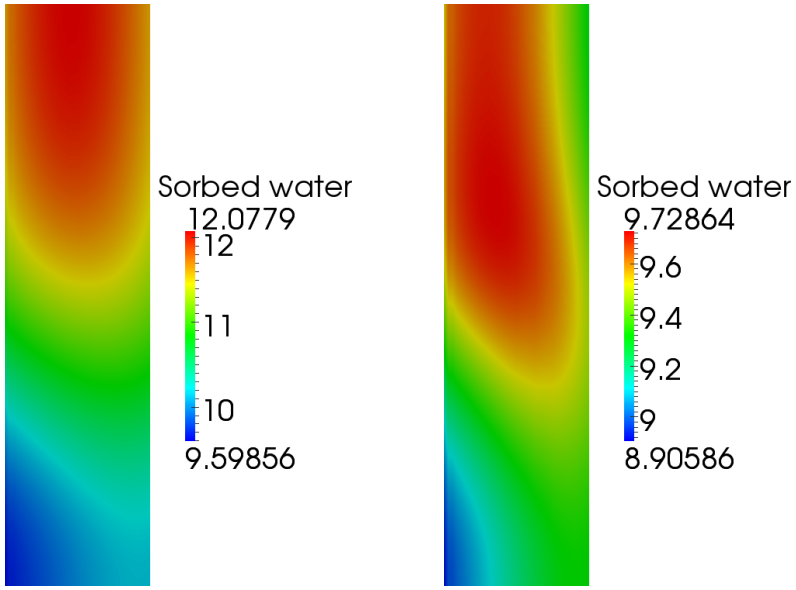

(a) (b)

Figure 2.35 – Distribution of membrane water content inside the CCL for 70% RH and 95℃at 1850 mA/cm^2, for the: (a) isothermal, and (b) non-isothermal models.

In conclusion, the non-isothermal model predictions are found closer to the experimental data and significant deviations from the isothermal model are observed in the case of low humidity operations. The importance of neglected phenomenon such as heat of sorption and thermal osmosis are asserted. Parametric studies are performed on various thermal parameters such as reversible heat distribution and the MPL thermal conductivity and their impact on the cell performance is assessed. Non-physical RH values are observed even in the non-isothermal model, hence a two-phase model is discussed and developed in the next chapter.

Chapter 3

Two-phase non-isothermal model

3.1 Introduction

In the previous chapter, a single phase nonisothermal MEA model is presented. Various physical phenomena such as oxygen transport, water vapour transport, electron transport, proton transport, sorbed water transport and heat transport, are solved for inside a two-dimensional, through the channel MEA configuration. Very high temperatures are observed at high current densities, inside the cathode catalyst layer (mass transport limiting region). The membrane is shown to dry out significantly under these conditions, hence increasing the ohmic losses due to proton transport. Non-physical relative humidity values greater than 100 % are also observed inside the MEA, due to the inherent limitations of using the single phase model. Under these conditions, water vapour will condense giving rise to two-phase flow inside the PEMFC. Water vapour saturation pressures are also observed to fluctuate significantly in the operating temperature ranges of the PEMFC (80-100 ℃) [103]. Hence in a PEMFC, water management and thermal management are critically linked to each other [17, 53].

In this chapter, a two-phase, non-isothermal MEA model is presented and implemented in openFCST [9, 10]. Based on the literature review presented in Chapter 1, a single capillary diffusion equation for liquid water saturation transport inside the PEMFC is considered in this work. Various physical relations/parameters such as capillary pressure-saturation relationships, relative permeability and effective gas diffusivity correlations reported in the literature are also discussed in detail. Simulation results comparing single-phase and two-phase model predictions are presented here, by varying operating conditions, *viz.*, pressure, temperature and humidification. This chapter is divided into three sections. The first section will present the liquid

water transport equation and various constitutive relations necessary to characterize the two-phase flow inside the PEMFC. Corresponding changes to the other transport equations due to the presence of liquid water are formulated and their numerical implementation details are discussed in the subsequent section. Simulations results are validated and discussed in the final section.

3.2 Liquid Water Transport Equation

PEMFC layers are porous composite materials, composed of various phases, such as solid phase, fluid phase in the pore (empty) spaces and electrolyte phase in the CL and membrane. Water exists in sorbed form in the electrolyte phase and in gas (water vapour) and liquid forms inside the pore networks of the PEMFC. Void spaces inside the porous media are characterized using porosity, ϵ, which represents the fraction of the overall volume of the porous media available as empty pore volume and tortuosity, τ, which represents the increased transport characteristic length due to the tortuous flow paths in the porous media. In the single phase model formulation, the pore space is assumed to contain a dilute multi-component gas mixture. However, in physical situations, the pore space is also occupied by the liquid phase, hence restricting the path available to gas transport. Due to extremely low condensation temperatures for gases such as oxygen and hydrogen, only water is commonly assumed to exist in the liquid form inside the PEMFC [56]. Presence of liquid water inside the PEMFC porous media is accounted for by using an additional variable, namely, liquid water saturation, s, which represents the fraction of the pore volume available to liquid water. Then,

$$s = \frac{V_l}{V_{pore}} \tag{3.1}$$

where, V_l is the volume occupied by the liquid water and V_{pore} is the overall pore (void space) volume inside the porous media.

The conservation equation for the liquid water can be written as follows [56, 146]:

$$\frac{\partial \left(\epsilon s \rho_l\right)}{\partial t} + \vec{\nabla} \cdot \left(\rho_l \vec{v}_l\right) = S_l \tag{3.2}$$

where, ρ_l is liquid water density, $\vec{v}_l$ is the interstitial liquid water velocity and S_l is a source term averaged over the REV representing the mass of the liquid water produced per unit volume of the layer.

Liquid water movement inside the porous media is governed by various mechanisms, *viz.*, capillary pressure driven flow due to surface tension effects, viscous drag due to movement of the surrounding gas phase, inertial effects and the effect of body forces such as gravity. Capillary driven flow is found to be the most domination mechanism for liquid water transport inside the PEMFC porous layers [56, 66, 85]. It can also be shown using various non-dimensional numbers. Firstly, the capillary number, Ca, provides the ratio between the viscous forces and the interfacial tension forces [56, 147]:

$$Ca = \frac{\vec{v}_g \mu_g}{\gamma} \tag{3.3}$$

where $\vec{v}_g$ is the interstitial gas velocity, μ_g is the viscosity of the surrounding gas (mixture) phase and γ is the surface tension between the liquid and the gas phase at fuel cell operating conditions. $\vec{v}_g$ is of the order of $10^{-4}\,[m \cdot s^{-1}]$ [17], μ_g is of the order of $10^{-5}\,[kg \cdot m^{-1} \cdot s^{-1}]$ and γ is of the order of $10^{-2}\,[N \cdot m^{-1}]$. So inside the PEMFC layers, $Ca \sim 10^{-7} <<< 1$. Hence liquid water flow due to viscous drag is neglected in this work.

The Bond number, Bo, represents the ratio between the gravitational forces and the interfacial tension forces. For the PEMFC porous media, it can be represented as [148, 149]:

$$Bo = \frac{(\rho_l - \rho_g)\, g d_{pore}^2}{\gamma} \tag{3.4}$$

where, ρ_l is the liquid water density, ρ_g is the gas mixture density, g is the acceleration due to gravity and and d_{pore} is the pore diameter. ρ_l is of the order of $10^3\,[kg \cdot m^{-3}]$, ρ_g is of the order of $1\,[kg \cdot m^{-3}]$, g is of the order of $10^1\,[m \cdot s^{-2}]$ and d_{pore} is the characteristic length for flow in the porous media and has an order of $10^{-5}\,[m]$ for a PEMFC porous media [98, 150]. So inside the PEMFC layers, $Bo \sim 10^{-3} << 1$. Hence the gravity effect in considering liquid water flow inside the PEMFC layers is neglected in this work.

The Weber number, We, represents the ratio between the inertia forces and the interfacial tension forces. For the PEMFC porous media, it can be represented as [149]:

$$We = \frac{\rho_l \vec{v}_l^2 d_{pore}}{\gamma} \tag{3.5}$$

where, $\vec{v}_l$, is the interstitial liquid water velocity. $\vec{v}_l$ is of the order of $10^{-5}\,[m \cdot s^{-1}]$ [149]. So inside the PEMFC layers, $We \sim 10^{-10} <<< 1$. Hence inertial effect in

considering liquid water flow inside the PEMFC layers is neglected in this work.

Since viscous, inertial and gravitational effects are negligible, the liquid water flows primarily due to the interfacial pressure difference between the wetting phase and the non-wetting phase inside the porous media. This pressure difference arises due to interfacial tension which is defined as the tendency of the fluid to reduce its surface area. In a capillary tube, the surface tension causes the liquid to form a curved meniscus which can be convex-shaped or concave-shaped, depending on the wettability of the liquid towards the solid surface. A pressure difference is developed across the interface due to the surface tension, leading to the phenomena of capillary rise/decline. A hydrostatic explanation to this phenomenon is given in the Figure 3.1 and paragraph below.

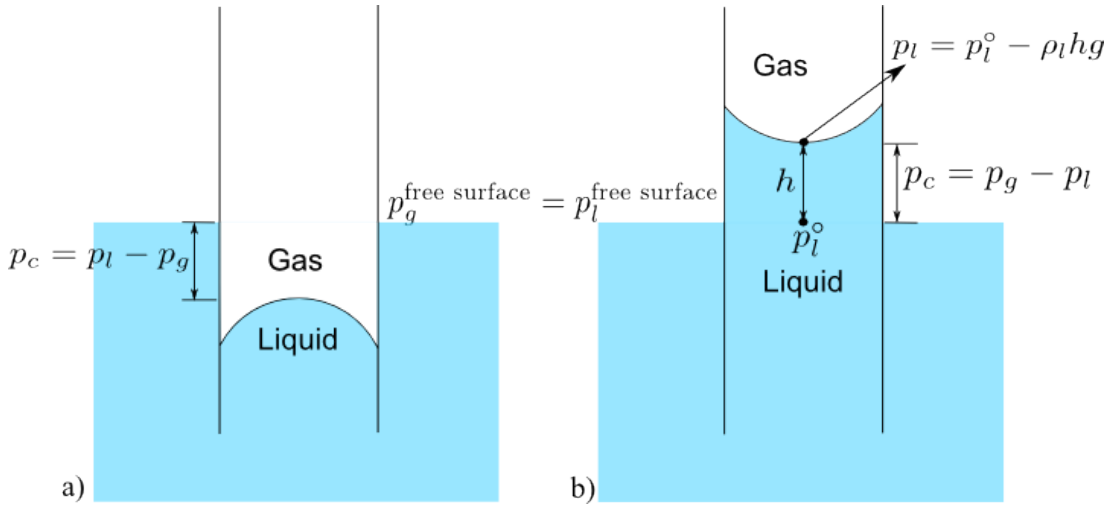

Figure 3.1 – a) Liquid pressure is higher than the gas pressure when the gas is the wetting phase. b) Gas pressure is higher than the liquid pressure when the liquid is the wetting phase.

Different immiscible fluids present inside the porous media compete for the occupancy of the pore space. Depending on the wettability of the porous medium, one of the fluids has a preferred tendency to occupy the pores and wet the pore surfaces. For instance in a hydrophobic pore, the gas mixture is preferred over the liquid water in filling the pore (Figure 3.1(a)). This preference is reversed in the case of hydrophillic pores inside the porous media (Figure 3.1(b)). Thus in this competition of pore occupancy, the preferred fluid pushes the less preferred fluid out which leads to an increase in the pressure of the less preferred fluid. These immiscible fluids inside the porous media form curved interfaces, across which a pressure difference between the two fluids is developed. This pressure difference is known as the capillary pressure,

p_c, and is generally defined as [151]:

$$p_c = p_{\text{non-wetting phase}} - p_{\text{wetting phase}} \tag{3.6}$$

where under equilibrium conditions, non-wetting phase pressure is always higher than the wetting phase pressure, *i.e.*, $p_{\text{non-wetting phase}} > p_{\text{wetting phase}}$.

In PEMFC diffusion media, the hydrophilic porous carbon matrix is treated with hydrophobic Teflon. Hydrophillic cracks are formed in the porous media due to imperfections in the material development process. Thus PEMFC diffusion media is rendered as a mixed wettability media with varying pore sizes and highly anisotropic nature. Due to this liquid water can sometimes be the wetting phase in certain sections while non-wetting phase in the remaining sections of the porous media. It leads to separate flow networks being formed for the liquid water in the hydrophobic pores and in the hydrophillic pores of the PEMFC diffusion media [54, 77, 152]. Since the PEMFC diffusion media is mostly hydrophobic in nature, it is common in the PEMFC literature to consider liquid water as the non-wetting phase in the PEMFC diffusion media. Thus, the capillary pressure defined in equation (3.6) is defined as:

$$p_c = p_l - p_g \tag{3.7}$$

where p_l and p_g are the liquid water and the gas mixture pressures respectively.

Under the assumptions of laminar, incompressible and Newtonian flow, the liquid water flow inside the porous media can be characterized using Darcy's law [153]:

$$\vec{v_l} = -\frac{\kappa_l}{\mu_l}\vec{\nabla} p_l \tag{3.8}$$

where κ_l is the liquid permeability of the porous medium and μ_l is the viscosity of the liquid water. From equation (3.7), the liquid water pressure, p_l, can be expressed as follows:

$$p_l = p_c + p_g \tag{3.9}$$

Taking gradients on equation (3.9):

$$\vec{\nabla} p_l = \vec{\nabla} p_c + \vec{\nabla} p_g \tag{3.10}$$

Under the assumption of negligible gas pressure gradients, which is generally valid inside the MEA for a straight channel PEMFC configuration [41], equation (3.10) is simplified to:

$$\vec{\nabla} p_l = \vec{\nabla} p_c \tag{3.11}$$

Hence considering only capillary driven flow, Darcy equation (3.8) is simplified to:

$$\vec{v}_l = -\frac{\kappa_l}{\mu_l} \vec{\nabla} p_c \tag{3.12}$$

Thus under steady state conditions, the conservation equation for the liquid water flow inside the PEMFC layers can be written as:

$$-\vec{\nabla} \cdot \left(\frac{\rho_l \kappa_l}{\mu_l} \vec{\nabla} p_c \right) = S_l \tag{3.13}$$

For a liquid droplet lying on a plane surface, the capillary pressure is directly proportional to the surface tension and indirectly proportional to the radius of the droplet and can be determined using Young-Laplace equation [154]. However in a porous medium, the capillary pressure depends on various factors such as saturation, wettability, surface tension, pore sizes and porosity of the medium. Increasing the porosity (hence larger pore sizes) leads to better reactant transport but it also results in lower capillary pressures. This makes it a complicated phenomenon causing more retention of excessive liquid water hence blocking the flow path of reactant gases. It is therefore common to use semi-empirical functions defining capillary pressure-saturation relationships inside the porous media. This method was first proposed by Leverett [68]. These relationships inherently account for the other factors discussed above. Hence a single governing equation based on the liquid water saturation, s, is obtained for characterizing liquid water flow inside the PEMFC layers:

$$-\vec{\nabla} \cdot \left(\frac{\rho_l \kappa_l}{\mu_l} \left(\frac{\partial p_c}{\partial s} \right) \vec{\nabla} s \right) = S_l \tag{3.14}$$

where the liquid water viscosity, μ_l, varies significantly with temperature and can be expressed empirically as follows [155]:

$$\mu_l = \left(2.414 \times 10^{-4}\right) \times 10^{\frac{247.8}{T-140}} \quad \left[g \cdot cm^{-1} \cdot s^{-1}\right] \tag{3.15}$$

Constitutive expressions for capillary pressure-saturation relationships are discussed in the next sections. Also the liquid water permeability, κ_l, is related to the

absolute permeability, κ, of the porous medium. As the liquid water content in the pores increases, the resistance to liquid water flow decreases. The liquid water permeability is non-linearly dependent on the local liquid water saturation values and details of these expressions are discussed in the next sections. Source terms due to phase change involving vaporization/condensation of water are also detailed in the subsequent sections.

3.2.1 Capillary pressure - saturation relationships

3.2.1.1 Literature review

Leverett [68] performed dimensional analysis on the experimental data available on reservoir rocks for petroleum engineering. He proposed a semi-empirical expression for the capillary pressure - saturation relationship. The expression accounts for the surface tension and absolute permeability of the porous medium as follows:

$$J(s) = \frac{p_c}{\sigma}\left(\frac{\kappa}{\epsilon}\right)^{\frac{1}{2}} \tag{3.16}$$

Udell [69] used the data by Leverett [68], and presented the following J-function, $J(s)$, for the porous media:

$$J(s) = 1.417(1-s) - 2.120(1-s)^2 + 1.263(1-s)^3 \tag{3.17}$$

Scheidegger [156] proposed the following J-function for packed soil beds:

$$J(s) = 0.364(1 - e^{-40(1-s)}) + 0.221(1-s) + \frac{0.005}{s - 0.08} \tag{3.18}$$

In the PEMFC modelling literature, Udell's function (3.17) is most commonly used by replacing $(1-s)$ with s, since it is empirically derived from data obtained for isotropic soil beds which are hydrophillic in nature. In order to account for mixed wettability porous medium, Nam and Kaviany [77] and Pasaogullari and Wang [86] incorporated a factor of contact angle, θ, in the traditional Leverett function (3.16):

$$J(s) = \frac{p_c}{\sigma|cos(\theta)|}\left(\frac{\kappa}{\epsilon}\right)^{\frac{1}{2}} \tag{3.19}$$

Nam and Kaviany [77] improvised further by using apparent contact angle values in their model. The apparent contact angle was used to account for roughness of the PTFE surfaces. This approach is valid only for a uniform wettability media and the external contact angle values used are not accurate in characterizing flow inside

a highly anisotropic, fibrous porous media [75]. Thus as discussed in the literature review of Chapter 1, this approach is ineffective for assessing the liquid water flow inside the PEMFC [56, 90].

Characterization of the liquid water flow inside the PEMFC can thus be more accurately predicted using recent experimental data obtained on the PEMFC materials. Acosta et al. [70] determined a capillary pressure - saturation relationship experimentally for commercially available ELAT GDL(s) from E-TEK®, Inc, using mercury intrusion porosimetry (MIP). Capillary pressure curves are obtained for mercury and are later converted into water-air curves by using a contact angle correction factor. They observed hysteresis by determining both imbibition and drainage curves. They later showed that the drainage curves represented a much better fit with the experimental data. The expression for the drainage curve they reported is as follows [70]:

$$p_c = -600 \exp(25s - 16) - 3300(1 - s) + \frac{800}{s} \quad [Pa] \tag{3.20}$$

However it is also observed that the results of MIP experiments are limited by difficulties in pore accessibility and sample deformation, especially drainage curves [157].

Koido et al. [88] measured a capillary pressure - saturation relationship during imbibition for commercially available Toray® TGP-H-060 GDL having 5% PTFE content, by forcing liquid water into the sample and measuring the change in liquid water pressure. The experimentally obtained relationships are later validated against a pore network model prediction, and are given as follows:

$$p_c = \begin{cases} 2.4 \times 10^6 s^2 - 2.5 \times 10^5 s, & 0 \leq s < 0.05 \\ -10^4 s - 6 \times 10^3, & 0.05 \leq s < 1 \end{cases} \quad [Pa] \tag{3.21}$$

Ye and Van Nguyen [75] utilized an improved volume displacement technique [158] to measure a capillary pressure - saturation relationship for commercially available Toray® TGP-H-060 having 10% PTFE content. The expression for the drainage curve is reported as follows:

$$p_c = -35.6 + 2.09 \left(e^{44.9(s-0.321)} - e^{-22.2(s-0.321)}\right) \quad [Pa] \tag{3.22}$$

They also reported expressions for a thickened catalyst layer measured using the Neutron Radiography technique [158]:

$$p_c = 2395 + 2431 \left(e^{92.36(s-0.567)} - e^{-0.0088(s-0.567)}\right) \quad [Pa] \tag{3.23}$$

Hao and Cheng [159] measured capillary pressure curves of Toray® TGP-090 GDL(s) with varying PTFE content during imbibition and drainage. They used the approach employed first by Fairweather et al. [160], in which a microfluidic device is used to control the saturation and measure the capillary pressure values. Hao and Cheng further validated their experimental results with simulations performed using Lattice-Boltzmann method. The J-function corresponding to the drainage curve in accordance with the Leverett approach given in equation (3.16) is reported as follows:

$$J(s) = 0.13363 + 0.00498e^{9.404(s-0.5)} + 0.00397e^{-11.19(s-0.5)} \tag{3.24}$$

Gostick et al. [54] experimentally measured the hydrophillic and overall porosity values of numerous commercially available GDL(s). Using the method of standard porosimetry (MSP), they determined the capillary pressure - saturation relationships for wide range of GDL(s) such as Sigracet®, E-TEK®, Toray® and Lyflex®. Experimentally measured data is fitted to various models available in the literature, *viz.*, Brooks-Corey model [154] and Van Genuchten model [161], as well as to the standard Leverett function (3.16). They reported numerous expressions for various GDL(s) but it is also observed that all of the capillary pressure - saturation curves obtained for various GDL(s) are nearly the same. However it is noted that the data reported is applicable only at room temperature conditions (25 ℃), and does not account for the temperature dependence. Kumbur et al. [90] fitted Gostick et al.'s data and reported an expression which represents all of the curves fairly well:

$$p_c = -4854.1s^2 + 12958s \quad [Pa] \qquad \text{for} \;\; 0 < s < 0.8 \tag{3.25}$$

Kumbur et al. [72–74] proposed a generalized Leverett function, which is validated against the experimental data obtained using MSP. They observed the effects of variation in PTFE loading (from 5% to 20%) on capillary pressure curves and found it to be a dominating factor at moderate saturation values ($s < 0.5$) [72]. Later the effects of compression during fuel cell assembly are studied for the compression pressure range of 0 - 1.4 MPa [73]. It is observed that there is a reduction in pore size and porosity due to compression which eventually leads to higher capillary pressure enhancing the water removal rate. Based on the stress-strain measurements, new effective porosity values are determined and calibrated into the generalized function. Finally it is observed that hydrophobicity of the diffusion media (PTFE effect) is

reduced with increase in temperature. This leads to more flooding in the layers. Changes in surface tension values due to temperature variations are included in the generalized function. Hence by including all these effects, an elaborate, validated capillary pressure - saturation function is proposed for Sigracet® 24 series diffusion media (GDL with MPL) [74]:

$$p_c = \left(\frac{293}{T}\right)^6 \gamma(T)\ 2^{0.4C}\sqrt{\frac{\epsilon_c}{\kappa}}\ \mathbf{K}(s) \tag{3.26}$$

where C is the compaction pressure used during the fuel cell assembly in MPa and ϵ_c is the new porosity after compression and it is given as [73]:

$$\epsilon_c = \left(\frac{0.9}{1+s_{TR}} + 0.1\right)\epsilon \tag{3.27}$$

where ϵ is the uncompressed porosity and s_{TR} is the experimentally measured compressive strain given as [73]:

$$s_{TR} = \begin{cases} -0.0083C^2 + 0.0911C & \text{SGL 24 series} \\ -0.0046C^2 + 0.0843C & \text{SGL 10BB} \end{cases} \tag{3.28}$$

Surface tension of the water-air system as a function of temperature, $\gamma(T)$, is given as [74]:

$$\gamma(T) = \left(-1.78 \times 10^{-4}\right) T + 0.1247 \tag{3.29}$$

The effects of PTFE content in the diffusion media are incorporated into equation (3.26), using the empirical function $\mathbf{K}(s)$ given as [72]:

$$\mathbf{K}(s) = \begin{cases} w_{\%}\left(0.0469 - 0.00152w_{\%} - 0.0406s^2 + 0.143s^3\right) + 0.0561\ln(s), & 0 < s < 0.5 \\ w_{\%}\left(1.534 - 0.0293w_{\%} - 12.68s^2 + 18.824s^3\right) + 3.416\ln(s), & 0.5 \le s \le 0.65 \\ w_{\%}\left(1.7 - 0.0324w_{\%} - 14.1s^2 + 20.9s^3\right) + 3.79\ln(s), & 0.65 < s < 1 \end{cases} \tag{3.30}$$

where $w_{\%}$ is weight percent of PTFE in the porous layer.

3.2.1.2 Capillary pressure - saturation relationships used in this work

The capillary pressure function measured by Ye and Van Nguyen [75] is considered for the catalyst layers in this work, since it is the only reported capillary function for the CLs in the literature, to the best of my knowledge. Capillary pressure - saturation curves for GDL-MPL based on Kumbur et al.'s data [72–74] are compared against the curves for CL based on Ye and Nguyen's equation (3.23) in Figure 3.2. The parameters used in plotting GDL-MPL saturation curve by employing Kumbur

et al.'s equation (3.26) are: $\epsilon = 0.6$, $\kappa = 1.8 \times 10^{-11}\,[m^2]$, $C = 1\,[\text{MPa}]$, $T = 353\,[K]$ and PTFE loading of 5 %. It is observed that in the low to moderate saturation ranges, *i.e.*, $s < 0.5$, the capillary pressures reported by Ye and Nguyen are negative and one to two orders smaller than Kumbur et al.'s data. This is attributed to the fact that the catalyst layers are mostly hydrophillic in nature. It will cause liquid water to remain in the catalyst layer and block the reaction sites. However due to the exponential nature of equation (3.23), Ye and Nguyen's capillary pressures are significantly higher (more than 10 orders of magnitude) than Kumbur et al.'s data in the high saturation ranges, *i.e.*, $s > 0.6$. Both pressure values cross each other at $s \approx 0.59$, hence liquid water will be pushed out of the CL at high saturation levels avoiding complete blocking of the reaction sites in the layer.

For PEMFC diffusion media, there are a number of experimentally measured capillary pressure - saturation correlations reported in the literature as discussed above. However it is observed that these correlations are restricted to the particular type of GDL-MPL on which experiments are performed. As discussed in Chapter 2, the model predictions are validated against experimental results obtained for a MEA using Sigracet® SGL diffusion media [42]. Thus the generalized equation (3.26) pro-

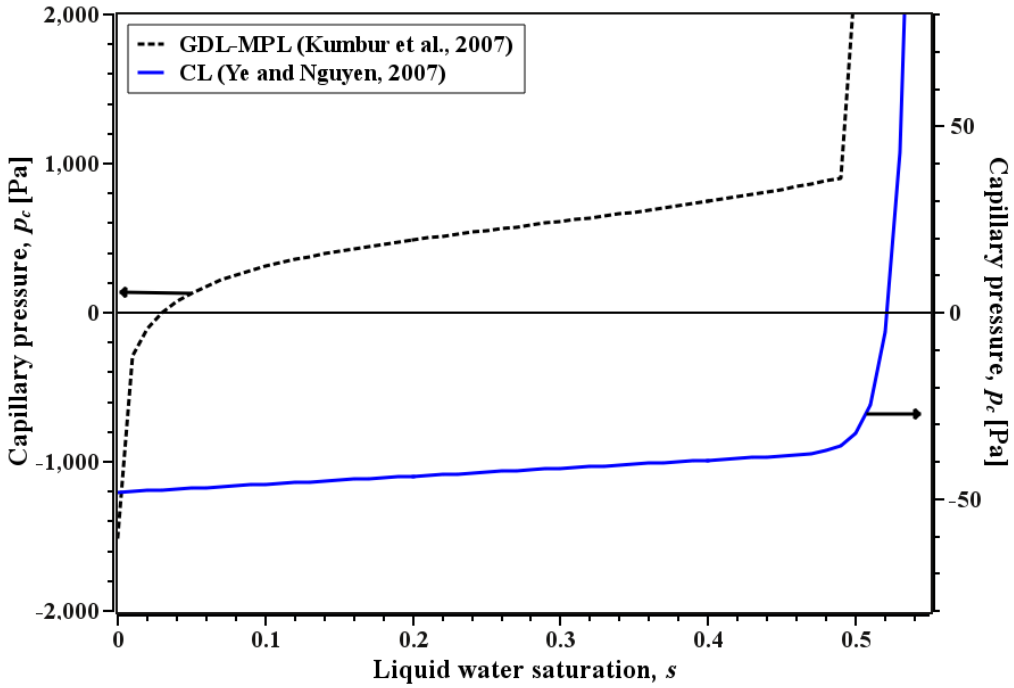

Figure 3.2 – Comparison of capillary pressure - saturation curves for CL based on the data by Ye and Nguyen [75] (solid line, right Y-axis) and for GDL-MPL based on the data by Kumbur et al. [72–74] (dashed line, left Y-axis).

posed by Kumbur et al. [72–74] for SGL 24-series diffusion media is considered in this work. This approach has the advantage of inherent inclusion of the contact angle values, thus accounting for mixed wettability and highly anisotropic nature of the PEMFC diffusion media. It is noteworthy that equation (3.26) is derived for composite diffusion media, consisting of MPL coated on a GDL. However up to moderate saturation levels, *i.e.*, $s < 0.5$, there is no difference observed on comparing GDL(s), with and without MPL, for instance SGL 24BC and SGL 24BA respectively. At high saturation levels, *i.e.*, $s > 0.65$, a drastic jump in capillary pressure is observed for GDL with MPL. This pressure rise is attributed to the presence of a microporous layer in the diffusion media. The MPL is observed to be hydrophobic and compact in nature based on the experimentally measured pore size distributions. Gostick et al. [54] has reported that individual correlations for MPL and GDL can hence be extracted from the experimental data.

The saturation, s, used in equation (3.30) is computed for the overall diffusion media (GDL with MPL). However the actual saturation value in the GDL/MPL alone would be different from the overall saturation value. Since GDLs and MPLs are treated as separate layers in this work, Kumbur et al.'s expressions are re-devised based on the actual saturation values in the individual GDL/MPL. Saturation of the GDL with MPL sample, s_{sample}, can be expressed as:

$$s_{sample} = \frac{V_{l,sample}}{V_{pore,sample}} \tag{3.31}$$

where $V_{l,sample}$ is the volume of liquid water inside the sample and $V_{pore,sample}$ is the pore (empty) volume of the sample.

Kumbur et al. has assumed the same values of the porosity in GDL and MPL, in determining the semi-empirical equations (3.26) and (3.30). Hence using the same assumption, pore volume of the sample can be expressed as:

$$V_{pore,sample} = A_{sample}\,(t_{GDL} + t_{MPL})\,\epsilon \tag{3.32}$$

where A_{sample} is the cross section area of the sample used in the experiment, t_{GDL} and t_{MPL} are the individual thicknesses of the GDL and MPL respectively, and ϵ is the porosity of the sample.

Then, saturation of the GDL, s_{GDL}, can be written as:

$$s_{GDL} = \frac{V_{l,GDL}}{V_{pore,GDL}} \tag{3.33}$$

where $V_{l,GDL}$ is volume of liquid water inside the GDL and $V_{pore,GDL}$ is the pore (empty) volume of the GDL alone and it can be expressed as:

$$V_{pore,GDL} = A_{sample}\ t_{GDL}\ \epsilon \tag{3.34}$$

Kumbur et al. [72] observed that liquid water starts penetrating into the MPL at an overall saturation value of 0.65. Hence for $s_{sample} \leq 0.65$, the volume of liquid water inside the GDL is the same as the volume of liquid water inside the overall sample.

$$V_{l,GDL} = V_{l,sample} \qquad \text{for } s_{sample} \leq 0.65 \tag{3.35}$$

Combining equations (3.31) to (3.35) we can write:

$$s_{GDL} = \frac{(t_{GDL} + t_{MPL})}{t_{GDL}}\ s_{sample} \qquad \text{for } s_{sample} \leq 0.65 \tag{3.36}$$

Individual thickness values for SGL 24-series diffusion media, *i.e.*, $t_{GDL} = 190\mu m$ and $t_{MPL} = 45\mu m$, are adapted from the manufacturer technical specification sheets [162]. Hence actual saturation value in the GDL can be expressed as:

$$s_{GDL} = 1.2368\ s_{sample} \qquad \text{for } s_{sample} \leq 0.65 \tag{3.37}$$

Under the assumptions of equal porosity values for both GDL and MPL, only $\mathbf{K}(s)$ function in equation (3.26) is required to be reassessed for the actual saturation value in the GDL. Kumbur et al. [72] has stated that $\mathbf{K}(s_{sample})$ represents the best fit to the experimental data in the saturation range, $0 < s_{sample} \leq 0.5$. It is also stated that GDL capillary pressure - saturation behaviour can also be determined by extending $\mathbf{K}(s_{sample})$ function in this saturation range to the whole range, *i.e.*, $0 < s_{sample} < 1$. Therefore, a new semi-empirical function, $\hat{\mathbf{K}}(s_{GDL})$, which corresponds to actual saturation values in the GDL alone, is assumed to be of the following form:

$$\hat{\mathbf{K}}(s_{GDL}) = w_{\%}\left[\hat{a} + \hat{b}\ w_{\%} + \hat{c}\ s_{GDL}^2 + \hat{d}\ s_{GDL}^3\right] + \hat{e}\ln\left(s_{GDL}\right) \tag{3.38}$$

where $\hat{a}$, $\hat{b}$, $\hat{c}$, $\hat{d}$ and $\hat{e}$ are empirical constants.

These empirical constants are determined by least squares minimization, *i.e.*, $min\sum\left[\hat{\mathbf{K}}(s_{GDL}) - \mathbf{K}(s_{sample})\right]^2$. A multi-point regression analysis is performed for different saturation values at PTFE loadings of 5%, 10% and 15%. The regression is performed for more than 150 points in the saturation range, $0 < s_{sample} \leq 0.5$, using

DEPS Evolutionary algorithm provided in LibreOffice® Calc software. $\hat{\mathbf{K}}(s_{GDL})$ is obtained as follows :

$$\hat{\mathbf{K}}(s_{GDL}) = w_{\%}\left(0.0444 - 0.0014 w_{\%} - 0.0275\ s_{GDL}^{2} + 0.0769\ s_{GDL}^{3}\right) + 0.0564 \ln\left(s_{GDL}\right) \tag{3.39}$$

As previously discussed, liquid water starts penetrating into the MPL for $s_{sample} > 0.65$. Using equation (3.37), the actual saturation in the GDL, s_{GDL}, at $s_{sample} = 0.65$, is calculated as 0.80392. This implies that the GDL is not completely flooded at the point when liquid water starts filling the MPL as well. Hence from this point onwards, *i.e.*, $s_{sample} > 0.65$, it is assumed that the liquid water will fill both layers simultaneously. The volume of liquid water, $V_{l,GDL+MPL}$, which will fill both layers, can be expressed as:

$$V_{l,GDL+MPL} = A_{sample}\ \left(t_{GDL} + t_{MPL}\right)\epsilon \times \left(s_{sample} - 0.65\right) \qquad \text{for } s_{sample} > 0.65 \tag{3.40}$$

Further individual volumes of liquid water being filled in GDL and MPL respectively can be expressed as:

$$V_{l,GDL} = V_{l,GDL+MPL} \times (\varphi) \qquad \text{for } s_{sample} > 0.65 \tag{3.41}$$

$$V_{l,MPL} = V_{l,GDL+MPL} \times (1 - \varphi) \qquad \text{for } s_{sample} > 0.65 \tag{3.42}$$

where φ is the fraction of volume of liquid water filling the GDL pores to overall volume of liquid water which is filling simultaneously both layers.

Hence individual saturation values in the GDL and MPL can be expressed as:

$$s_{GDL} = 0.80392 + \frac{\varphi A_{sample}\left(t_{GDL} + t_{MPL}\right)\epsilon \times \left(s_{sample} - 0.65\right)}{A_{sample}\ t_{GDL}\ \epsilon} \quad \text{for } s_{sample} > 0.65 \tag{3.43}$$

$$s_{MPL} = \frac{(1 - \varphi)\, A_{sample}\left(t_{GDL} + t_{MPL}\right)\epsilon \times \left(s_{sample} - 0.65\right)}{A_{sample}\ t_{MPL}\ \epsilon} \qquad \text{for } s_{sample} > 0.65 \tag{3.44}$$

Using individual length values of the layers from manufacturer's technical specification sheet [162], equations (3.43) and (3.44) can further be simplified to:

$$s_{GDL} = 0.80392 + 1.2368\ \varphi\left(s_{sample} - 0.65\right) \quad \text{for } s_{sample} > 0.65 \tag{3.45}$$

$$s_{MPL} = 5.222\left(1 - \varphi\right)\left(s_{sample} - 0.65\right) \qquad \text{for } s_{sample} > 0.65 \tag{3.46}$$

Now when the sample is completely saturated, *i.e.*, $s_{sample} = 1$, individual saturation values of the GDL and MPL should also be unity, *i.e.*, $s_{GDL} = 1$ and $s_{MPL} = 1$. Using $s_{GDL} = 1$ at $s_{sample} = 1$ in equation (3.45), we get $\varphi = 0.4529$. It can be easily verified that by using the same analogy for the MPL in equation (3.46), we get the same value for φ. Thus individual saturation values of the GDL and MPL for the complete saturation range of the sample can be expressed as:

$$s_{GDL} = \begin{cases} 1.2368 \times s_{sample} & \text{for } 0 \leq s_{sample} \leq 0.65 \\ 0.80392 + 0.56015\,(s_{sample} - 0.65) & \text{for } 0.65 < s_{sample} \leq 1 \end{cases} \tag{3.47}$$

$$s_{MPL} = \begin{cases} 0 & \text{for } 0 \leq s_{sample} \leq 0.65 \\ 2.8569\,(s_{sample} - 0.65) & \text{for } 0.65 < s_{sample} \leq 1 \end{cases} \tag{3.48}$$

Similar to the discussions above, only the $\mathbf{K}(s)$ function in equation (3.26) is required to be reassessed for the actual saturation value in the MPL. Hence a new semi-empirical function, $\bar{\mathbf{K}}(s_{MPL})$, which corresponds to actual saturation values in the MPL alone, is assumed to be of the following form:

$$\bar{\mathbf{K}}(s_{MPL}) = w_{\%}\left[\bar{a} + \bar{b}\; w_{\%} + \bar{c}\; s_{MPL}^2 + \bar{d}\; s_{MPL}^3\right] + \bar{e}\ln\left(s_{MPL}\right) \tag{3.49}$$

where $\bar{a}$, $\bar{b}$, $\bar{c}$, $\bar{d}$ and $\bar{e}$ are empirical constants.

These empirical constants are also determined by least squares minimization, *i.e.*, $min\sum\left[\bar{\mathbf{K}}(s_{MPL}) - \mathbf{K}(s_{sample})\right]^2$. A multi-point regression analysis is performed for different saturation values at PTFE loadings of 5%, 10% and 15%. It is noteworthy that PTFE content in MPL is generally different from the PTFE content in the GDL. However PTFE content in MPL for the commercially available Sigracet® diffusion media is not available in public domain. Kumbur et al. [72] has determined the $\mathbf{K}(s_{sample})$ function by using the PTFE content of GDL only. Hence the same value for PTFE content in the MPL, *i.e.*, 5%, 10% and 15%, are assumed for performing regression in this work. The MPL effects, *i.e.*, a sudden rise in capillary pressure, is observed only for $s_{sample} > 0.65$. Hence the regression is performed for more than 100 points in the saturation range, $0.65 < s_{sample} \leq 1$, using DEPS Evolutionary algorithm provided in LibreOffice® Calc software. $\bar{\mathbf{K}}(s_{MPL})$ is obtained as follows :

$$\bar{\mathbf{K}}(s_{MPL}) = w_{\%}\left(1.8158 - 0.0328 w_{\%} + 9.1235 s_{MPL}^2 - 2.5089 s_{MPL}^3\right) + 0.7126\ln\left(s_{MPL}\right) \tag{3.50}$$

Capillary pressures in GDL and MPL computed using corrected functions of saturation, are plotted in Figure 3.3. The parameters used in plotting Figure 3.3 using equation (3.26) are: $C = 1\,[\text{MPa}]$, $T = 353\,[K]$, $\epsilon_{GDL} = 0.6$, $\epsilon_{MPL} = 0.4$, $\kappa_{GDL} = 1.8 \times 10^{-11}\,[m^2]$, $\kappa_{MPL} = 1.5 \times 10^{-13}\,[m^2]$ and PTFE loading of 5%. Visible differences in order of magnitude between individual capillary pressures in GDL and MPL are observed in Figure 3.3. Capillary pressures in the MPL are observed to be two to three orders higher than in the GDL, because of the smaller pore radii and hydrophobic nature of the MPL. MPL will therefore push the liquid water towards the GDL thereby blocking the gas transport. Gostick et al. [54] has reported a capillary pressure - saturation relationship for an MPL by comparing experimental results for commercially available Sigracet® SGL 10 BA and SGL 10BC diffusion media. Capillary pressures for MPL determined in this work are compared against the MPL capillary pressures reported by Gostick et al. in Figure 3.3. They are found to be of the same order, hence qualitatively validating the corrected expressions computed in this work. Thus the corrected saturation functions, $\hat{\mathbf{K}}(s)$ and $\bar{\mathbf{K}}(s)$, given in equations (3.39) and (3.50) are considered for GDL and MPL respectively in this work.

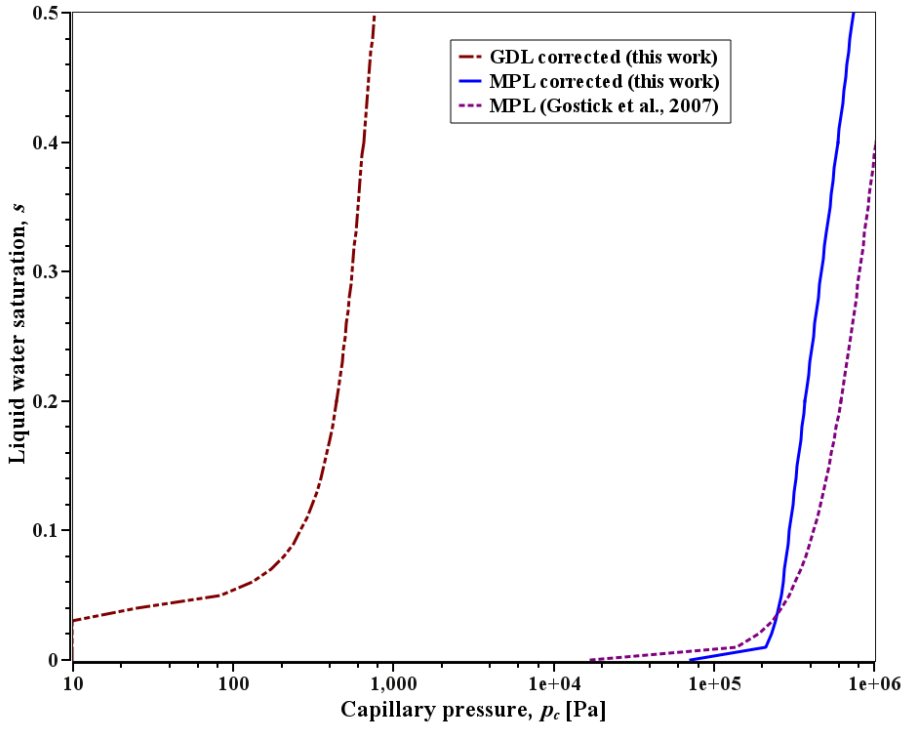

Figure 3.3 – Comparison of order of magnitudes of individual capillary pressures for GDL and MPL based on corrected functions and data by Gostick et al. [54].

3.2.2 Relative liquid permeability

Relative liquid permeability, κ_{rl}, is another important parameter for defining the liquid water flow inside the PEMFC layers. In case of both liquid and gas occupying an REV, the flow path of one of the phases is restricted due to the presence of the another phase. Thus in order to adjust for this restriction to the flow, the relative permeability factor is used to correct the absolute permeability, κ, of the medium. Liquid permeability, κ_l, is then given as:

$$\kappa_l = \kappa_{rl} \times \kappa \tag{3.51}$$

Numerous semi-empirical correlations either based on experimental data or using physical models such as capillary models, statistical models, pore network models are reported in the literature [90]. As discussed in the literature review of Chapter 1, the liquid water remains stagnant inside the pores until a minimum saturation value (threshold), namely irreducible saturation, s_{irr}, is attained inside the pores. Hence in order to account for irreducible saturation, the effective saturation, $\hat{s}$, is introduced and it is defined as follows:

$$\hat{s} = \frac{s - s_{irr}}{1 - s_{irr}} \tag{3.52}$$

Nam and Kaviany [77] utilized the following relation for the relative liquid permeability and is conventionally used in the PEMFC models in the literature [56]:

$$\kappa_{rl} = \hat{s}^3 \tag{3.53}$$

Ye and Van Nguyen [75] assumed zero irreducible saturation and suggested the following expression:

$$\kappa_{rl} = \hat{s}^{4.5} \tag{3.54}$$

Acosta et al. [70] stated that equation (3.53) is suited well to a hydrophillic medium since at lower saturation levels only small pores are filled and therefore permeability would be less while it will increase rapidly at higher saturation levels as the larger pores fill. However in the case of a hydrophobic medium, the liquid water fills the larger pores first thus increasing liquid permeability significantly even at lower saturation levels. Kumbur et al. [90] has analyzed various semi-empirical models available in the literature and based on the data by Gostick et al. [54] has proposed the following semi-empirical correlation, which is being considered in this work:

$$\kappa_{rl} = \hat{s}^{2.16} \tag{3.55}$$

The irreducible saturation, s_{irr} is considered as zero in this work.

3.2.3 Phase change source term

A source term for the phase change between liquid water and water vapour is required in the model to couple both phases. Depending on the local properties, either the liquid water is evaporated or the water vapour is condensed inside the pores. Phase change inside the porous media is not very well defined yet. A detailed review of various approaches used in the PEMFC modelling literature is discussed by Litster and Djilali [56]. Two major approaches used in the literature are: a) using kinetic theory to approximate a mass transfer rate [71, 77], and; b) assuming spherical liquid droplets and determining mass diffusion rate using dimensionless numbers such as Nusselt number and Schmidt number [67]. However both of these approaches require many assumptions for various parameters such as droplet radius and liquid-gas interfacial area. Hence these approaches are not considered in this work.

Some other noteworthy approaches used in the literature separately account for both condensation and evaporation [75, 80, 163]. An approach used by Villanueva [98] which employs a single equation to account for both condensation and evaporation. If the water vapour pressure is higher than the saturation pressure, then the source term becomes positive hence accounting for condensation. Alternately if the water vapour pressure is lower than the saturation pressure, then the source term becomes negative hence accounting for evaporation. The phase change source term for liquid water considered in this work is thus given as [98]:

$$S_l = K_{e/c}\ a_{lv}\ M_{H_2O}\,(p_v - p_{sat}(T)) \qquad \left[g \cdot cm^{-3} \cdot s^{-1}\right] \tag{3.56}$$

where the saturation pressure of water, $p_{sat}(T)$, is a function of temperature and is given in the equation (2.108), and $K_{e/c}$ is rate constant for evaporation/condensation. It is an unknown parameter and a parametric study shall be performed on it assessing its impact on cell performance. a_{lv} is the liquid water - vapour interfacial surface area per unit volume. It is a function of the local saturation values and must be zero when there is no liquid water, *i.e*, $s = 0$, or under completely flooded conditions, *i.e*, $s = 1$. Villanueva [98] developed an improved mixed wettability PSD model and determined a_{lv} as a function of s. It is also dependent on the distribution of the hydrophillic and hydrophobic pores and their sizes in the porous media and hence numerous trends are given for $a_{lv}(s)$ [98]. An empirical fit is determined which approximates the trends for various porous layers of PEMFC. The empirical expression for GDL (50 % hydrophillic and 50 % hydrophobic pores) is determined as:

$$a_{lv} = 140\ s^{1.15}\,(1-s)^{1.75} \qquad \left[cm^2 \cdot cm^{-3}\right] \tag{3.57}$$

The empirical expression for MPL (100 % hydrophobic pores) is determined as:

$$a_{lv} = 9 \times 10^4 \; s^5 \, (1-s)^{1.25} \qquad \left[cm^2 \cdot cm^{-3}\right] \tag{3.58}$$

The empirical expression for CL (50 % hydrophillic and 50 % hydrophobic pores) is determined as:

$$a_{lv} = 4.4 \times 10^4 \; s^{1.25} \, (1-s)^{2.5} \qquad \left[cm^2 \cdot cm^{-3}\right] \tag{3.59}$$

Figures 3.4 and 3.5 plot the variation of interfacial surface area per unit volume with saturation for the GDL and MPL/CL respectively. Hydrophillic pores are immediately filled leading to a rapid spike in the interfacial surface area, as observed for the GDL and CL. The reverse is observed for the completely hydrophobic MPL. Hydrophobic pores are characterized by obtuse contact angles, *i.e.*, surrounding gas phase pushes liquid water to large pores, minimizing its interfacial area. For all cases, saturation is increased past a certain value, too many pores start to flood and a decrease is observed in the interfacial surface areas. One distinct observation is that the GDL interfacial surface area is two orders smaller than for the case of the MPL and CL. This is due to the larger pores in the GDL, hence lower interfacial surface area.

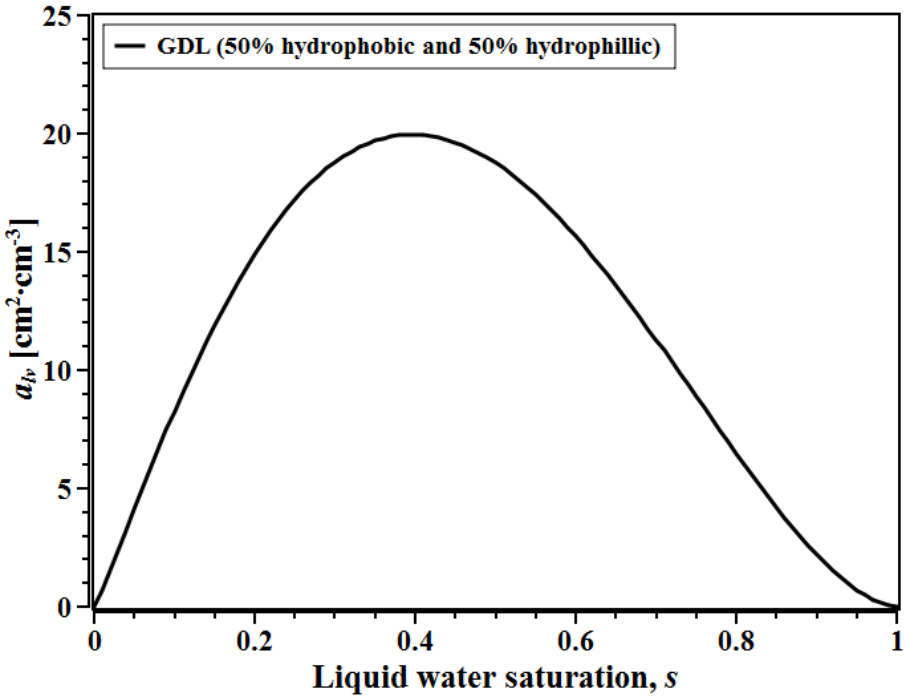

Figure 3.4 – Variation of liquid water - vapour interfacial surface area per unit volume against saturation for the GDL.

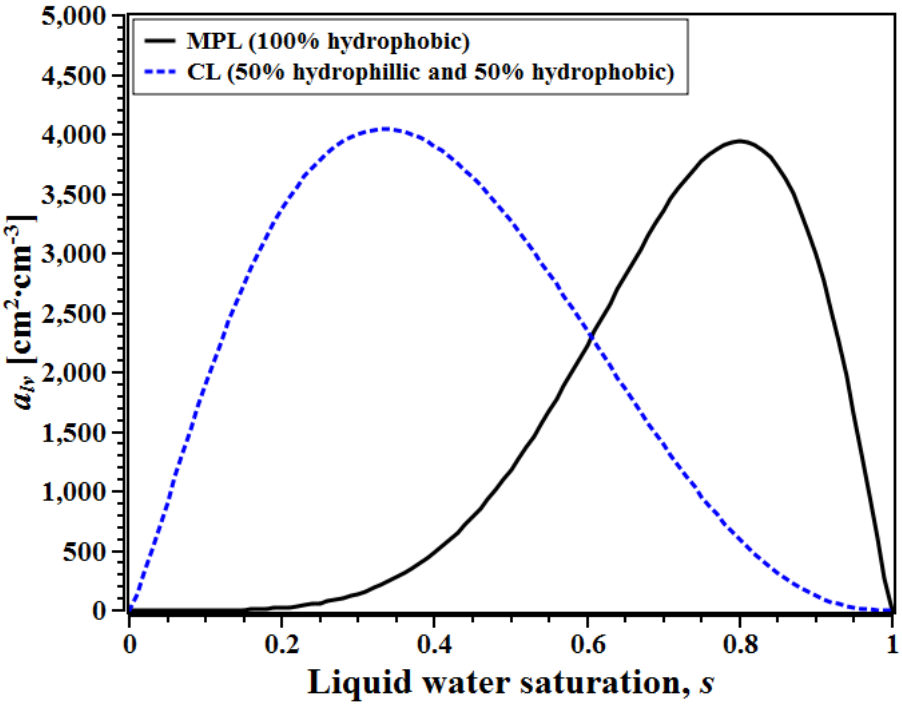

Figure 3.5 – Variation of liquid water - vapour interfacial surface area per unit volume against saturation for the MPL and CL.

Equation (3.14) defining the liquid water transport inside the PEMFC porous layers, *viz.*, GDL, MPL and CL, in this work is defined as:

$$-\vec{\nabla}\cdot\left(\frac{\rho_l\kappa_l}{\mu_l}\left(\frac{\partial p_c}{\partial s}\right)\vec{\nabla}s\right) = K_{e/c}\; a_{lv}\; M_{H_2O}\,(p_v - p_{sat}(T)) \tag{3.60}$$

Water produced during the ORR is assumed in liquid phase. The source term considered for the water vapour (corresponding to ORR), in case of the single-phase model in Chapter 2 is removed. Additional heat sink term corresponding to complete vaporization of water produced during ORR is also removed in the two-phase model. An additional liquid water source term is therefore added to the equation (2.3.1) in the cathode catalyst layer and is given as:

$$S_l = \frac{j}{2F}M_{H_2O} \tag{3.61}$$

It is noteworthy that liquid water block the transport of other gaseous species such as oxygen. It also covers the reaction sites inside the catalyst layer thus causing performance losses. Heat is released when condensation of water vapour occurs and the reverse phenomenon is observed when liquid water is evaporated. Hence the two phase model requires suitable modifications to transport equations of other species presented in the Chapter 2. Details of these changes are given in the next section.

3.3 Changes in other Transport Equations

3.3.1 Effective gas diffusivity

As discussed in Chapter 2, gas transport inside the PEMFC layers is modelled using Fick's law of diffusion. Since the PEMFC layers are porous in nature, the diffusion equation is averaged over a REV. Hence diffusion coefficients are corrected using a semi-empirical factor of porosity and tortuosity. Presence of liquid water inside the porous layers of PEMFC reduce the available empty (void) space for gas diffusion. Bruggeman equation [113] is the most common correlation used in the PEMFC modelling literature for predicting effective gas diffusion coefficients. So porosity, ϵ, is corrected using a factor of $(1-s)$. The saturation-corrected effective gas diffusivity commonly used in the literature is given by [86]:

$$D_g^{eff} = D_g \left[\epsilon \left(1-s\right)\right]^{1.5} \tag{3.62}$$

where D_g^{eff} and D_g are the effective diffusivity and bulk diffusion coefficient for gas $'g'$ respectively.

The Brugemann equation is derived for packed bad of spheres and is found to over-predict gas diffusivity for the cylindrical fibrous media used in PEMFC [164]. Tomadakis and Sotirchos [115, 116] developed a correlation for random fibrous porous media based on percolation theory. For a single phase medium, it is given as follows:

$$D_g^{eff} = D_g\, \epsilon \left(\frac{\epsilon - \epsilon^{th}}{1-\epsilon^{th}}\right)^{\mu} \Theta(\epsilon - \epsilon^{th}) \tag{3.63}$$

where ϵ^{th} is the percolation threshold of porosity and μ is the network constant.

Nam and Kaviany [77] simulated a model of randomly arranged intersecting/overlapping cylindrical fibres and results are found to have a close match with model by Tomadakis and Sotirchos. Liquid water effects are simulated by using randomly distributed and connected water droplets. They proposed the following correlation which works well in the porosity ranges of PEMFC layers and hence are considered for the fibrous GDLs in this work:

$$D_g^{eff} = D_g\, \epsilon \left(\frac{\epsilon - 0.11}{1-0.11}\right)^{0.785} (1-s)^2\, \Theta(\epsilon - \epsilon^{th}) \tag{3.64}$$

As discussed in Section 2.3.1, effective gas diffusivity in the MPL and CL is computed using percolation theory. In order to account for liquid water presence, porosity

is corrected using a factor of $(1-s)$, and the effective diffusivity for the MPL and CL is therefore given as:

$$D_g^{eff} = D_g \left(\frac{\epsilon(1-s)-\epsilon^{th}}{1-\epsilon^{th}}\right)^{\mu} \Theta\left(\epsilon(1-s)-\epsilon^{th}\right) \tag{3.65}$$

where the same values for ϵ^{th} and μ are considered for the respective layers (MPL and CL), as discussed in the Section 2.3.1.

3.3.2 Phase change source term for water vapour

An additional source term in the water vapour transport equation is incorporated in order to account for condensation/evaporation. Liquid water is being converted into water vapour and vice-versa during phase change and hence, by reversing (multiplying with -1) the liquid water source term, S_l, the phase change source term for water vapour is obtained. It is noteworthy that the source term for liquid water is in terms of mass units, however the water vapour transport equation is expressed in terms of moles. So the molar mass factor used in equation (3.56) is removed and source term for water vapour, S_v, considered in this work is given as follows:

$$S_v = K_{e/c}\ a_{lv}\left(p_{sat}(T) - p_v\right) \qquad \left[mol \cdot cm^{-3} \cdot s^{-1}\right] \tag{3.66}$$

3.3.3 Condensation/Evaporation heat source/sink

Heat is released when water vapour is condensed, or absorbed when liquid water is evaporated inside the PEMFC layers. Hence an additional heat source/sink terms is added to the thermal transport equation, which is given as:

$$S_{heat} = K_{e/c}\ a_{lv}\left(p_v - p_{sat}(T)\right) \times \bar{H}_{lv} \tag{3.67}$$

where $\bar{H}_{lv}$ is the molar latent heat of vaporization of water and is given in equation (2.65). During condensation, this source term becomes positive accounting for heat release and the opposite happens during evaporation.

The assumption of vapour-equilibriated membranes is still considered valid (λ_{eq} values are determined based on the local RH values). Finally liquid water transport through the electrolyte (Nafion®) is neglected in this work.

The final system of equations solved in the two-phase, non-isothermal MEA model can be written as:

$$\begin{aligned}
-\vec{\nabla}\cdot\left(\frac{p_T}{RT}\ D^{eff}_{O_2,N_2}\vec{\nabla}x_{O_2}\right) &= S_{O_2}\\
-\vec{\nabla}\cdot\left(\frac{p_T}{RT}\ D^{eff}_{H_2O,N_2\ \text{or}\ H_2}\vec{\nabla}x_{H_2O}\right) &= S_{H_2O}\\
-\vec{\nabla}\cdot\left(\sigma^{eff}_m\vec{\nabla}\phi_m\right) &= S_{H^+}\\
\vec{\nabla}\cdot\left(\sigma^{eff}_s\vec{\nabla}\phi_s\right) &= S_{e^-}\\
-\vec{\nabla}\cdot\left(n_d\frac{\sigma^{eff}_m}{F}\vec{\nabla}\phi_m+\frac{\rho_{dry}}{EW}D^{eff}_\lambda\vec{\nabla}\lambda+\frac{D^{eff}_T}{M_{H_2O}}\vec{\nabla}T\right) &= S_\lambda\\
-\vec{\nabla}\cdot\left(k^{eff}\vec{\nabla}T\right)+\sum_{\text{gases},\lambda}\left(\vec{N}_i\cdot\vec{\nabla}\bar{H}_i\right) &= S_T\\
-\vec{\nabla}\cdot\left(\frac{\rho_l\kappa_l}{\mu_l}\left(\frac{\partial p_c}{\partial s}\right)\vec{\nabla}s\right) &= S_l
\end{aligned} \tag{3.68}$$

where the source terms corresponding to each equation are given as:

$$S_{O_2}=\begin{cases}\frac{-j}{4F} & \text{in CCL}\\ 0 & \text{otherwise}\end{cases} \tag{3.69}$$

$$S_{H_2O}=\begin{cases}K_{e/c}\ a_{lv}(p_{sat}-p_v)-k_t\frac{\rho_{dry}}{EW}(\lambda_{eq}-\lambda) & \text{in CLs}\\ 0 & \text{in Membrane}\\ K_{e/c}\ a_{lv}(p_{sat}-p_v) & \text{otherwise}\end{cases} \tag{3.70}$$

$$S_{H^+}=\begin{cases}-j & \text{in CCL}\\ j & \text{in ACL}\\ 0 & \text{otherwise}\end{cases} \tag{3.71}$$

$$S_{e^-}=\begin{cases}-j & \text{in CCL}\\ j & \text{in ACL}\\ 0 & \text{otherwise}\end{cases} \tag{3.72}$$

$$S_\lambda=\begin{cases}k_t\frac{\rho_{dry}}{EW}(\lambda_{eq}-\lambda) & \text{in CLs}\\ 0 & \text{otherwise}\end{cases} \tag{3.73}$$

$$S_T = \begin{cases} \sigma_s^{eff}(\vec{\nabla}\phi_s \cdot \vec{\nabla}\phi_s) + K_{e/c}\ a_{lv}(p_v - p_{sat})\bar{H}_{lv} & \text{in GDLs and MPLs} \\ \\ \sigma_m^{eff}(\vec{\nabla}\phi_m \cdot \vec{\nabla}\phi_m) & \text{in Membrane} \\ \\ -j\eta + \frac{j}{2F}(-T f_{ORR}\Delta\bar{S}_{overall}) + \sigma_m^{eff}(\vec{\nabla}\phi_m \cdot \vec{\nabla}\phi_m) & \\ \quad +\sigma_s^{eff}(\vec{\nabla}\phi_s \cdot \vec{\nabla}\phi_s) + k_t\frac{\rho_{dry}}{EW}(\lambda_{eq} - \lambda)\bar{H}_{sorption} & \\ \quad +K_{e/c}\ a_{lv}(p_v - p_{sat})\bar{H}_{lv} & \text{in CCL} \\ \\ j\eta + \frac{j}{2F}(-T(1 - f_{ORR})\Delta\bar{S}_{overall}) + \sigma_m^{eff}(\vec{\nabla}\phi_m \cdot \vec{\nabla}\phi_m) & \\ \quad +\sigma_s^{eff}(\vec{\nabla}\phi_s \cdot \vec{\nabla}\phi_s) + k_t\frac{\rho_{dry}}{EW}(\lambda_{eq} - \lambda)\bar{H}_{sorption} & \\ \quad +K_{e/c}\ a_{lv}(p_v - p_{sat})\bar{H}_{lv} & \text{in ACL} \end{cases} \tag{3.74}$$

$$S_l = \begin{cases} \frac{j}{2F}M_{H_2O} + K_{e/c}\ a_{lv}\ M_{H_2O}(p_v - p_{sat}) & \text{in CCLs} \\ 0 & \text{in Membrane} \\ K_{e/c}\ a_{lv}\ M_{H_2O}(p_v - p_{sat}) & \text{otherwise} \end{cases} \tag{3.75}$$

3.4 Computation domain and parameters

The two-dimensional computational domain is the same as given in the Figure 2.2. The boundary conditions and parameters for the transport equations except the liquid saturation transport equation are considered the same as discussed in Chapter 2. Saturation values are specified at the gas channel boundaries (Dirichlet conditions) and no liquid water flux conditions are used at the bipolar plate boundaries (Neumann conditions). It is observed that a minimum saturation value of 0.1 is required to be applied at the gas channel boundary. This is due to very low liquid permeability values at $s < 0.1$, hence the liquid water transport is not sufficient for the model to converge. The boundary conditions applied for the saturation transport equation are mathematically expressed as:

$$s = 0.1 \qquad \textbf{anode/cathode gas channel} \tag{3.76}$$

$$\hat{n} \cdot \left(\frac{\rho_l k_l}{\mu_l}\left(\frac{\partial p_c}{\partial s}\right)\vec{\nabla}s\right) = 0 \qquad \textbf{anode/cathode current collector} \tag{3.77}$$

$$\hat{n} \cdot \left(\frac{\rho_l k_l}{\mu_l}\left(\frac{\partial p_c}{\partial s}\right)\vec{\nabla}s\right) = 0 \qquad \textbf{top/bottom symmetric boundaries} \tag{3.78}$$

Due to non-availability of the data for phase change rate constants in a porous media, the values for condensation and evaporation rate constants are assumed in this work. The condensation rate constant is considered several orders higher than the evaporation rate constant. The condensation rate constant is determined such that immediate condensation of water takes place in the case of RH values becoming more than 100%. Studies are performed by increasing the condensation rate constant to the point when the maximum RH value in the MEA, predicted by the simulation is nearly 100%. The model predictions do not change on further increasing the condensation rate constant value. The condensation rate constant is therefore taken as 1×10^{-4} mol/(Pa-cm^2-s). For the base case, the evaporation rate constant is assumed to be 1×10^{-10} mol/(Pa-cm^2-s). Such low evaporation rate constant is considered because the other quantities in the phase change source term are of high orders such as pressure (10^5 Pa) and interfacial area (10^3 cm^2/cm^3). The choice of this evaporation rate constant value allows the overall phase change term to be of the same order of magnitude as the phase change terms used in other models in the literature [75, 80, 163]. The transport parameters for the GDL and MPL correspond to the Sigracet® SGL 24BC (5% PTFE loading) porous transport layers used in the experimental data. The PTFE loading for the MPL ink used in preparing the Sigracet® SGL 24BC diffusion media is not available in the literature. Moreover in re-formulating the capillary pressure - saturation correlation given in equation (3.50), it is assumed that the PTFE loading in the MPL is same as the GDL. So the same loading of 5% is considered in this work. The compaction pressure is assumed to be zero because the porosity values used in the model (Tables 2.4 and 2.5) already account for the reduced porosity due to compression in the cell [42]. Due to non-availability of data for the CL permeability, it is assumed to be of same value as the MPL permeability (due to their similar structure). The liquid saturation transport parameters of the PEMFC porous layers considered in this work are tabulated in Table 3.1.

The numerical implementation details are the same as in the Section 2.5 and are not discussed further. Results for the two-phase non-isothermal MEA model are discussed in the next section.

Table 3.1 – Liquid saturation transport parameters of the PEMFC porous layers

Parameters	Value
GDL	
Absolute permeability, κ $[cm^2]$	1.8×10^{-7} [162]
Irreducible liquid saturation, s_{irr}	0.0
Capillary pressure - saturation function	Equation (3.39)
Compaction pressure, $C[MPa]$	0.0
PTFE loading, $[\%wt]$	5.0 [162]
MPL	
Absolute permeability, κ $[cm^2]$	1.5×10^{-9} [165]
Irreducible liquid saturation, s_{irr}	0.0
Capillary pressure - saturation function	Equation (3.50)
Compaction pressure, $C[MPa]$	0.0
PTFE loading, $[\%wt]$	5.0
CL	
Absolute permeability, κ $[cm^2]$	1.5×10^{-9}
Irreducible liquid saturation, s_{irr}	0.0
Capillary pressure - saturation function	Equation (3.23)

3.5 Results and Discussion

3.5.1 Low humidity conditions - Base case

The two-phase non-isothermal model is run for the base case operating conditions tabulated in Table 2.11. Figure 3.6 compares the cell performance for the isothermal, single-phase non-isothermal and two-phase non-isothermal against the experimental data [42]. No difference is observed between various model predictions in low current densities upto 700 mA/cm^2. As the current densities are increased further, two-phase model predictions are significantly lower than the single-phase and isothermal model results. Differences of upto 700 mA/cm^2 (between single-phase and two-phase models) are observed at 0.1 V. The two-phase model predictions are much closer to the experimental data. Two current densities marked with arrows in the Figure 3.6, *viz.*, 1000 mA/cm^2, and 2300 mA/cm^2, are chosen to understand the two-phase effects inside the MEA. Various phenomenon such as current distribution, water management and temperature distribution inside the cell are compared against the single-phase non-isothermal model predictions in the subsequent sections.

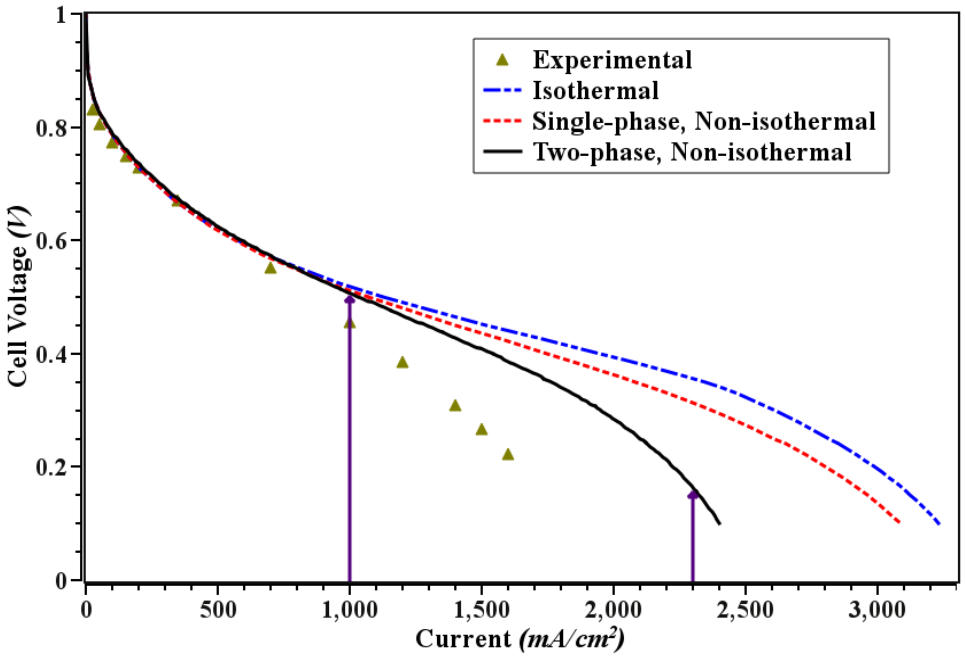

Figure 3.6 – Polarization curve for the base case where *solid black* line represents the two-phase non-isothermal, *dashed red* line represents the single-phase non-isothermal, *double dashed blue* line represents the isothermal, and *dark yellow triangle* point represents the experimental results [42].

3.5.1.1 Saturation distribution

Figure 3.7 plots the liquid water saturation profiles inside the CCL at different current densities. At 100 mA/cm^2 (Figure 3.7(a)), the saturation values are found to be lower than 0.1 (boundary condition at the gas channel). This is observed due to evaporation being faster than the liquid water production due to current. Since the simulations are being run at low humidity conditions, the driving force for evaporation is higher at low cell voltages. As the current is increased to 1000 mA/cm^2 (Figure 3.7(b)), the saturation values in the CCL are now higher than 0.1 value. The liquid water production rate has increased significantly and water accumulation is observed near the membrane. At moderate current density (1000 mA/cm^2), the current production is uniformly distributed in the in-plane direction (Figure 3.10(c)). However the evaporation in under-the-channel region is higher due to lower water vapour mole fractions (hence lower partial water vapour pressures), as shown in Figure 3.8(a). As the current is increased further to 2300 mA/cm^2, higher saturation values are observed in the CCL. However the liquid water accumulation is more in the under-the-channel region. This is due to current production being limited to the under-the-channel region (Figure 3.10(d)). The saturation pressures are much higher (due to higher tempera-

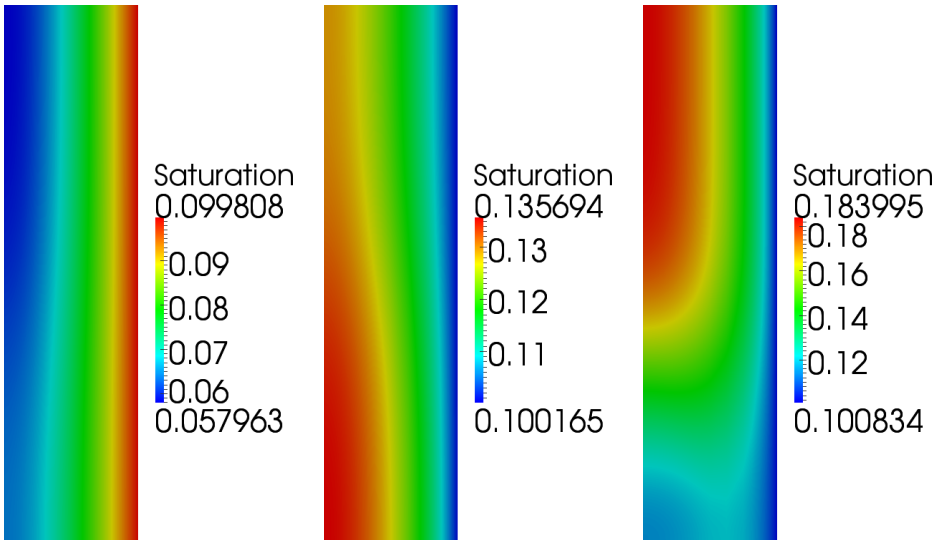

(a) (b) (c)

Figure 3.7 – Base case liquid water saturation distribution profiles in the CCL at: (a) 100 mA/cm^2, (b) 1000 mA/cm^2, and (c) 2300 mA/cm^2.

tures) in the under-the-channel region, hence higher evaporation rates lead to higher water mole fraction values in the under-the-channel region (Figure 3.8(b)). However the evaporation rates are high everywhere in the CCL which results in lower saturation values (roughly 0.1) in the under-the-rib region (lower part of the Figure 3.7(c)).

It is observed that the saturation values at the CCL-CMPL interface are around 0.1 in all the three current densities. Saturation values are inherently continuous across the interface due to FEM formulation. Figure 3.9 plots the liquid water saturation distribution in the CMPL and CGDL at 2300 mA/cm^2. Negligible variations are observed in both the layers. This is because the term $k_l \frac{\partial p_c}{\partial s}$ is roughly 4 to 5 order of magnitudes higher for the GDL and MPL than the CL. Moreover due to the GDL and MPL being thicker than the CL, evaporation of water in significant amounts take place inside the GDL and MPL. So the model can therefore predict the water buildup in the CCL but the saturation values higher than 0.25 are not observed inside the CCL, even at high current densities. In reality, the liquid water will not enter the MPL until the breakthrough pressures (capillary pressures) of roughly 10^4 Pa are not observed inside the CCL, *i.e.*, at $s \approx 0.55$, in the CCL (refer Figures 3.2 and 3.3). Moreover the local rise in liquid water saturation due to condensation inside the GDL does not cause significant saturation gradients due to the reasons discussed above. It is therefore observed that the single saturation equation can not sufficiently capture the actual liquid water profiles in a network of layers of different wettabilities.

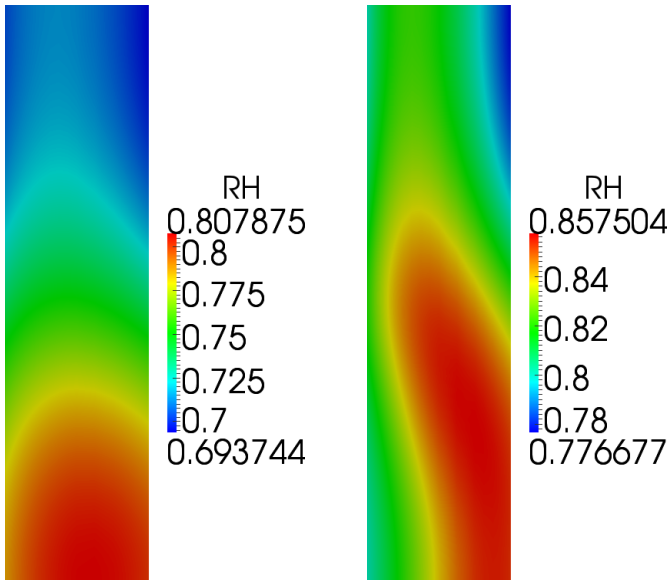

(a) (b)

Figure 3.8 – Base case relative humidity profiles in the CCL for the two-phase model at: (a) 1000 mA/cm^2, and (b) 2300 mA/cm^2.

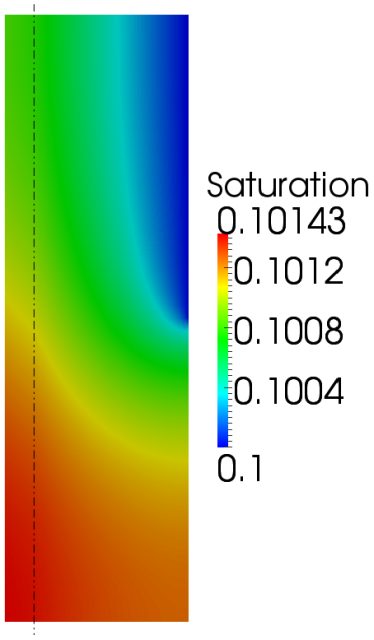

Figure 3.9 – Liquid water saturation distribution in the CMPL (left side of the double dashed line) and CGDL (right side).

3.5.1.2 Two-phase effects on current distribution

Figure 3.10 compares the current production in the CCL for the single-phase non-isothermal (first row) and the two-phase non-isothermal (second row) case at different current densities. No difference is observed in the 1000 mA/cm^2 case (Figures 3.10(a) and 3.10(c)). The highest current is observed at the CCL-membrane interface suggesting high oxygen gas availability. At 2300 mA/cm^2, current production in the single-phase model is reduced in the region near the CMPL (right side of the Figure 3.10(d)). Due to reduced proton transport, it increases slightly at the membrane-CCL interface due to increased temperature and as a result, kinetic activity. There are no inactive regions observed in the CCL. On the other hand, a significant portion of the under-the-rib area (Figure 3.10(d)) is inactive for the two-phase model at 2300 mA/cm^2 current density. In the two-phase model, higher maximum current densities are observed in the CCL due to higher overpotentials (low cell voltage) being applied and the temperatures observed in the CCL (Figure 3.12).

Figure 3.11 compares ϕ_s, ϕ_m, and x_{O_2} distributions in the CCL at 2300 mA/cm^2 for the single-phase (first row) and two-phase (second row) non-isothermal models. The two-phase model has much lower cell voltages of roughly 0.18 V (Figure 3.11(a)). The difference between maximum and minimum proton potential values for the single-phase (Figure 3.11(b)) and two-phase (Figure 3.11(b)) models are roughly 0.15 V and 0.27 V respectively. These higher protonic ohmic overpotentials in the case of two-phase model are due to drier ionomer (Figure 3.16(d)). This explains the lower current production in the under-the-channel region close to the CMPL in the two-phase model (Figure 3.10(d)). In the case of single-phase model, oxygen is available everywhere (minimum value greater than zero in Figure 3.11(c)) hence no inactive regions are observed in the CCL. However the oxygen availability is severely limited in the two-phase model with more than 50% of the CCL (mainly under-the-rib region) without oxygen available (Figure 3.11(f)). Moreover the maximum x_{O_2} value in the two-phase model is much lower (roughly half) than in the single-phase model. The lower performance is therefore attributed to severe mass transport limitations and ohmic losses inside the cell.

3.5.1.3 Two-phase effects on temperature distribution

Figure 3.12 compares the maximum temperature inside the cell as the current is increased for the single-phase (red dashed line) and two-phase (black solid line) models. It is observed for the two-phase model that up to roughly 200 mA/cm^2, the

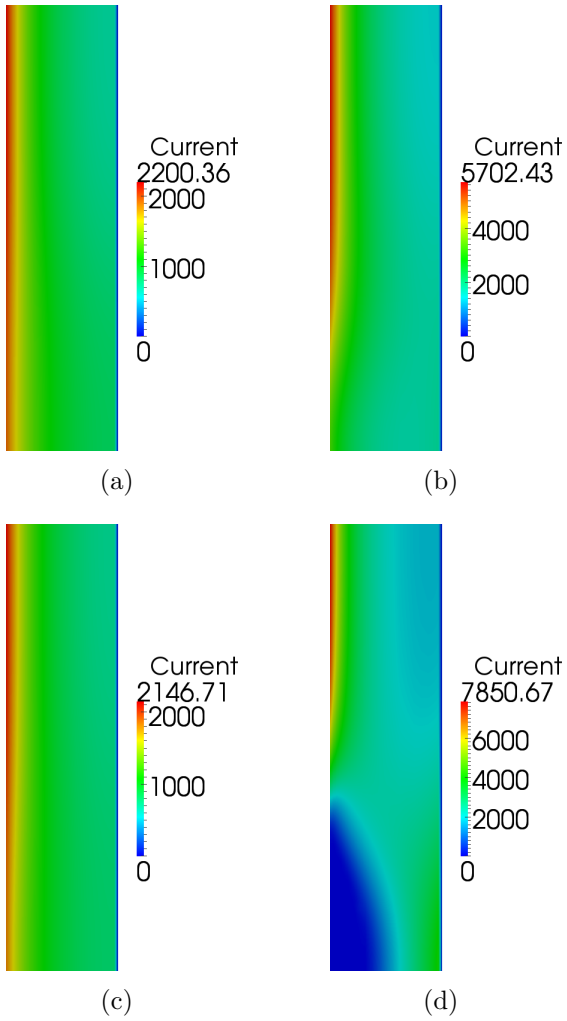

Figure 3.10 – Base case current production plots in the CCL, for the single-phase non-isothermal case at: (a) 1000 mA/cm^2, and (b) 2300 mA/cm^2; and for the two-phase non-isothermal case at: (c) 1000 mA/cm^2, and (d) 2300 mA/cm^2.

maximum temperature in the cell does not increase and remains at 353.15 K (plate temperature). Figure 3.13(a) plots the temperature distribution inside the MEA for the two-phase model at 100 mA/cm^2. It can be seen that temperatures inside the cell are lower than 353.15 K at 100 mA/cm^2. This is due to higher heat sink corresponding to evaporation of water inside the cell (saturation values lower than 0.1 in the cell as shown in Figure 3.7(a)). It can be seen that the cold regions near the CCL are wider than the regions near the ACL. Temperatures inside the CCL are found to be lower than in the ACL. This is because the ACL is three times thinner than the CCL, so larger amounts of heat is absorbed (due to evaporation) inside the CCL. The current phase change model results in evaporation of water more than the amount

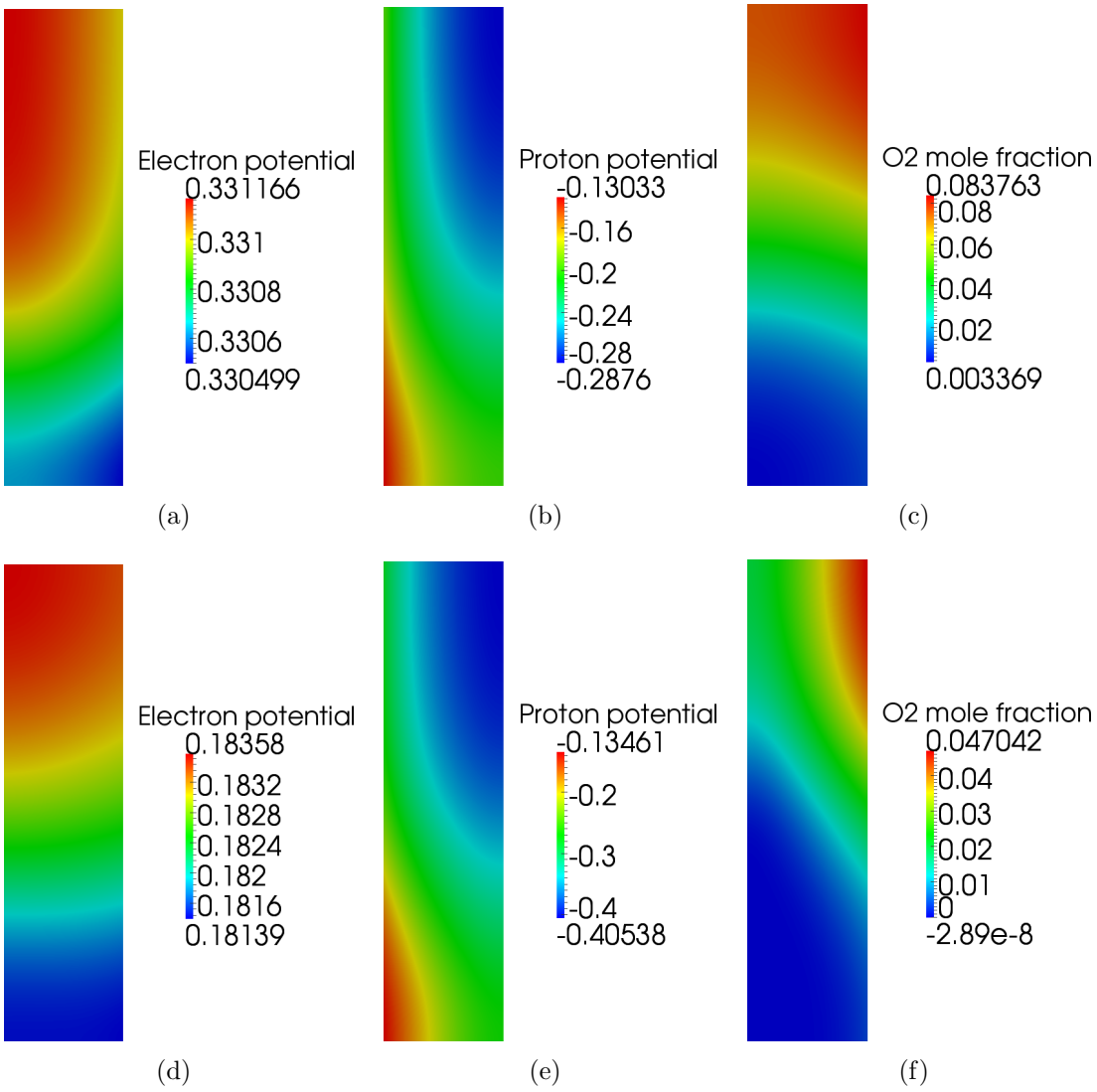

Figure 3.11 – Distribution of various species inside the CCL for the base case at 2300 mA/cm^2, for the single-phase non-isothermal case: (a) ϕ_s, (b) ϕ_m, and (c) x_{O_2}; and for the two-phase non-isothermal case: (d) ϕ_s, (e) ϕ_m, and (f) x_{O_2}.

produced during the ORR, corresponding to a constant supply of liquid water at the gas channel boundary (Dirichlet conditions). Hence the model predicts cooling down of the cell at low current densities.

As currents are increased beyond 200 mA/cm^2, temperatures rise significantly for the two-phase model. In the two-phase model, water production due to current is in liquid phase. So the heat sink corresponding to complete evaporation of the produced water (considered in the single-phase model) is not present. Due to this, the maximum temperature in the cell rises more rapidly for the two-phase model than the single-phase model, as shown in Figure 3.12. Figure 3.13 plots the temperature distribution inside the MEA for the two-phase model at different current densities. At 2300 mA/cm^2, the maximum temperature in the case of two-phase model is 2-3°C higher than the single-phase model. Figure 3.14 compares the temperature distribution inside the ACL + ML + CCL for the single-phase and two-phase models at 2300 mA/cm^2. It can be seen that the CCL is uniformly hot in the case of single-phase model (Figure 3.14(a)). On the other hand in the two-phase case, current is limited to the under-the-channel region. Irreversible heat generation is higher due to overpotential losses, hence the under-the-channel region is significantly hotter than the under-the-rib region in the two-phase model (Figure 3.14(b)). This can also be seen by narrowing down of the hot zones in the MEA as the current is increased in the two-phase model (Figures 3.13(b) and 3.13(c)).

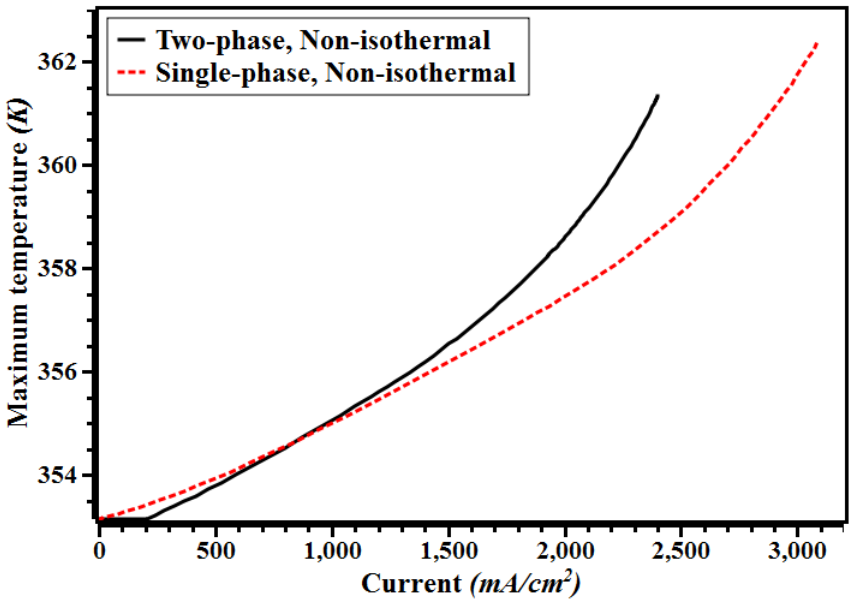

Figure 3.12 – Plot of maximum temperature in the MEA versus the current for the base case.

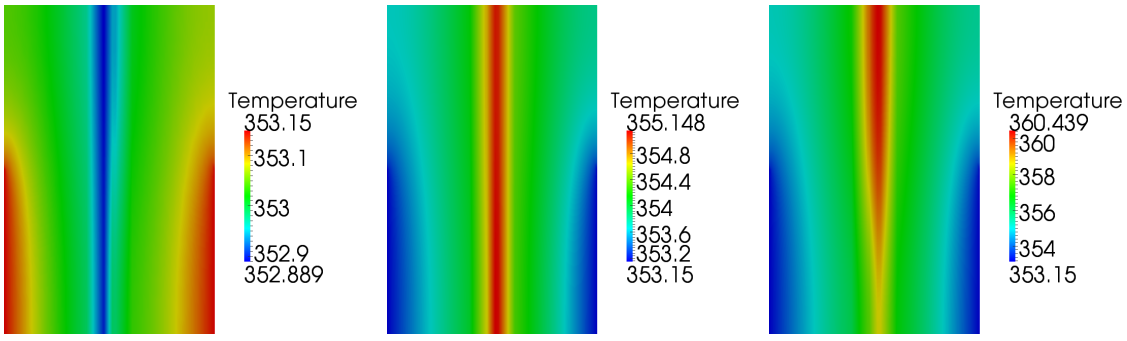

(a) (b) (c)

Figure 3.13 – Base case temperature distribution plots in the MEA, for the two-phase model at: (a) 100 mA/cm^2, (b) 1000 mA/cm^2, and (c) 2300 mA/cm^2.

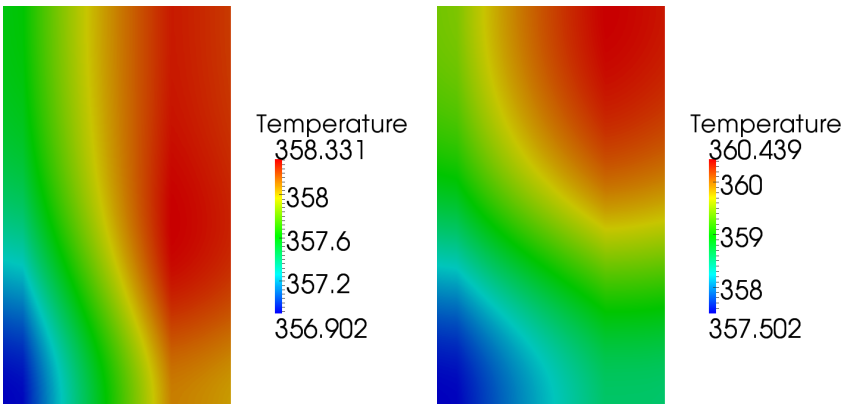

(a) (b)

Figure 3.14 – Base case temperature (T) distribution plots in the ACL + ML + CL at 2300 mA/cm^2 for: (a) single-phase non-isothermal, and (b) two-phase non-isothermal model.

3.5.1.4 Two-phase effects on water management

Figure 3.15 compares the variation of sorbed water flux with current for the two-phase model against the single-phase and isothermal model. At very low current densities (up to 300 mA/cm^2), temperatures are lower inside the CCL compared to the ACL. This will lead to lower saturation pressures inside the CCL. Moreover higher amount of water is evaporated inside the CCL (3 times thicker than the ACL). So the RH values inside the CCL will be higher than in the ACL under these low current densities. Figure 3.17 plots the λ values in the ACL + ML + CL at 100 mA/cm^2 for the two-phase model. λ values are significantly higher in the CCL under these current densities. The back-diffusion dominates the electro-osmotic drag at these low current

densities, hence the net water movement is from the CCL to the ACL.

As the current density is increased, water vapour mole fraction values are lower in the case of the two-phase model as compared to single-phase model. It is because water produced due to ORR is in the liquid phase. Moreover temperatures in the CCL are higher since the heat sink corresponding to vaporization of water is now dependent on a rate constant in the two-phase model, and complete evaporation is not achieved. So at higher currents, the RH values in the CCL are lower as compared to the single-phase non-isothermal model. This leads to lower λ_{eq} values hence drier ionomer in the CCL (vapour-equilibriated membranes). Hence lower cell voltage was observed in the two-phase model at 1000 mA/cm^2 (Figure 3.6), due to slightly higher protonic ohmic overpotentials (drier ionomer). Figure 3.16 compares the sorbed water content in the CCL at 2300 mA/cm^2 for the single-phase and two-phase model. So the back-diffusion is significantly less in the case of two-phase model, hence the water flux from the ACL to the CCL is much higher in the case of two-phase model. This also explains higher ohmic overpotentials observed in the two-phase model, besides severe mass transport limitations.

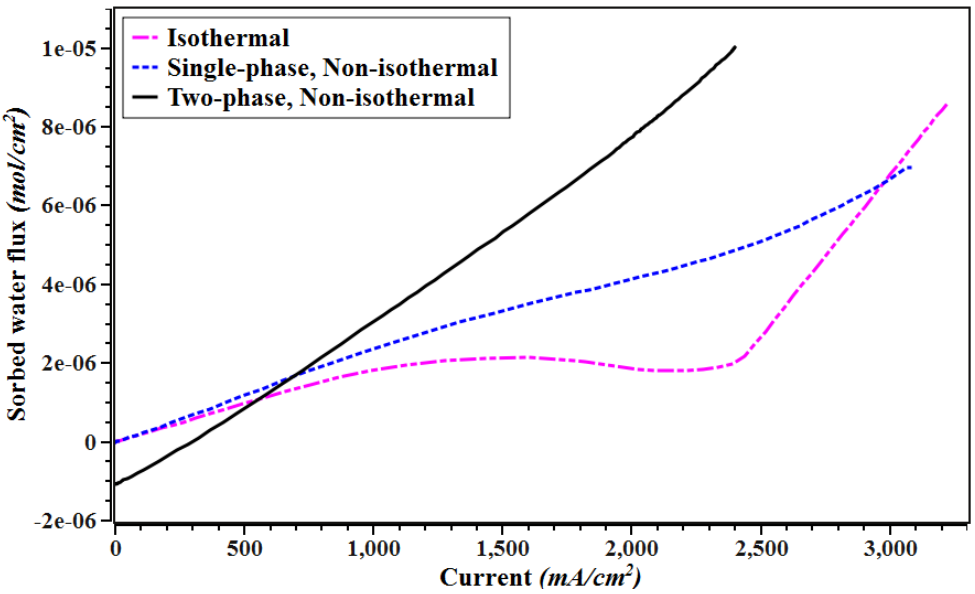

Figure 3.15 – Variation of sorbed water flux with current for the two-phase model (solid black line), single-phase model (dashed blue line) and isothermal model (double dashed magenta line).

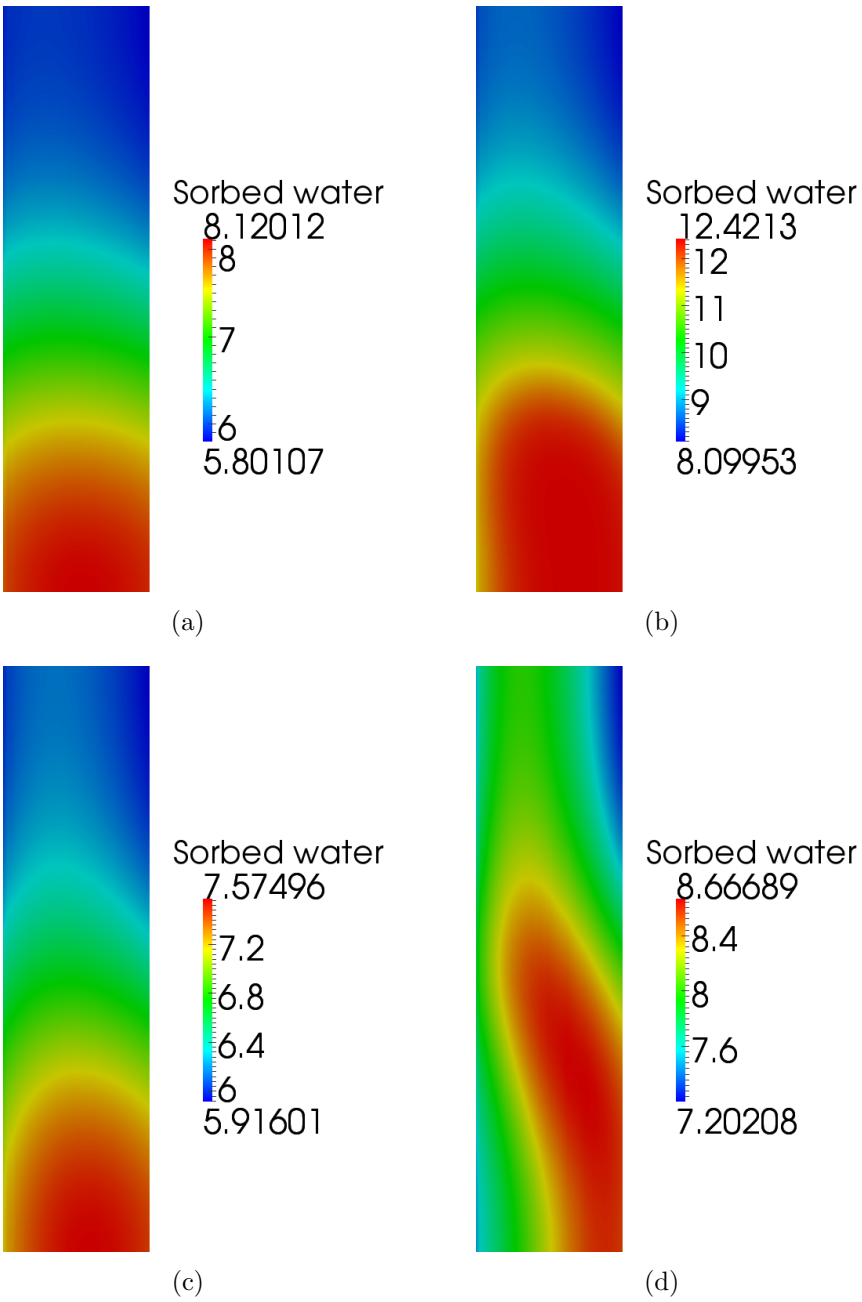

Figure 3.16 – Base case sorbed water content (λ) plots in the CCL, for the single-phase non-isothermal case: (a) 1000 mA/cm^2, and (b) 2300 mA/cm^2; and for the two-phase non-isothermal case: (c) 1000 mA/cm^2, and (d) 2300 mA/cm^2.

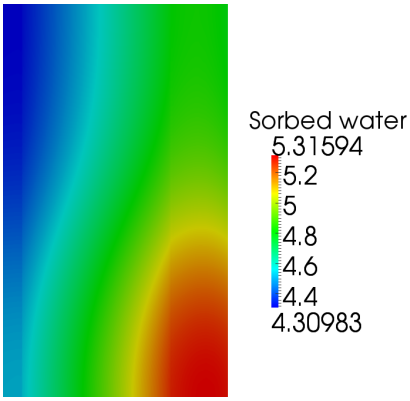

Figure 3.17 – Variation of sorbed water flux with current for the two-phase model (solid black line), single-phase model (dashed blue line) and isothermal model (double dashed magenta line).

3.5.1.5 Effect of evaporation rate constant

Simulations are run for different evaporation rate constants, *viz.*, 1×10^{-11}, 5×10^{-11}, 1×10^{-10}, and 5×10^{-10} mol/(Pa-cm^2-s). The model fails to converge at low overpotentials (high cell voltages) when the evaporation rate constant is increased further. This is due to the evaporation term being severely high leading to non-physical negative saturation values in the model. Even in the case of evaporation rate constant value of 5×10^{-10} mol/(Pa-cm^2-s), the model does not converge in the cell voltage range of 1.0-0.9 V. So higher evaporation rate constants are not considered here. Figure 3.18 compares the variation of cell performance with evaporation rate constants against the single-phase non-isothermal, isothermal and experimental results. The cell performance is reduced and closer to the experimental data as the evaporation rate constant is reduced further from 1×10^{-10} mol/(Pa-cm^2-s). As the evaporation rate is reduced, the saturation levels in the CCL increase leading to higher mass transport losses and ohmic overpotentials (lower x_{H_2O} production hence lower RH values).

Figure 3.19 plots maximum temperature in the MEA versus current for different evaporation rate constants. It is observed that maximum temperature in the MEA remains at 353.15K (plate temperature) upto 500 mA/cm^2 for high evaporation rate constant (double dashed black line in Figure 3.19). Maximum temperature in the MEA increases as the evaporation rate is reduced from 1×10^{-10} mol/(Pa-cm^2-s) due to lower heat sink corresponding to water evaporation. For the evaporation rate constant value of 5×10^{-10} mol/(Pa-cm^2-s), the two-phase model over-performs the isothermal model upto 1500 mA/cm^2. Since the evaporation rate is so high, the MEA has higher heat sink due to evaporation than heat production due to various other

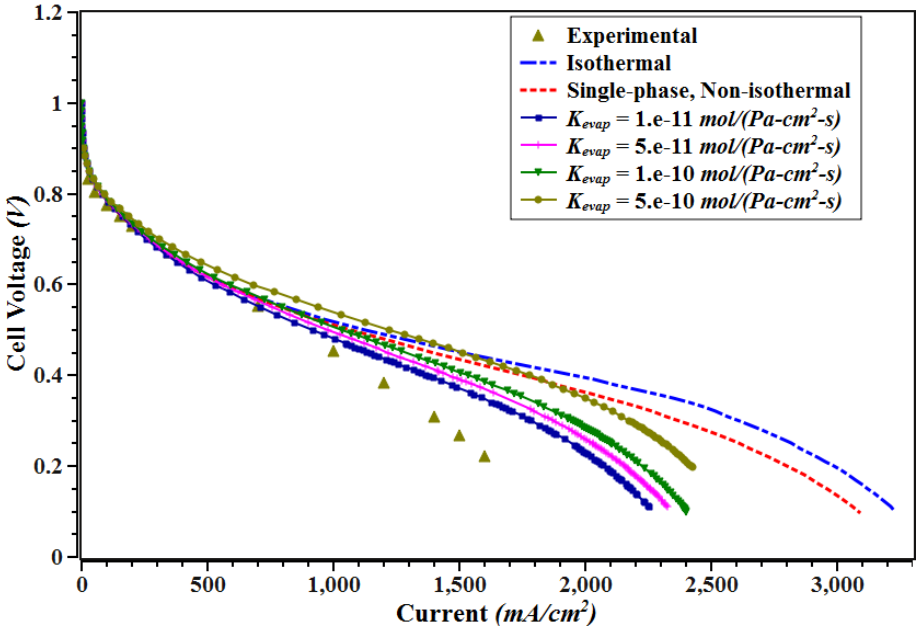

Figure 3.18 – Variation of cell performance with evaporation rate constants for the two-phase model.

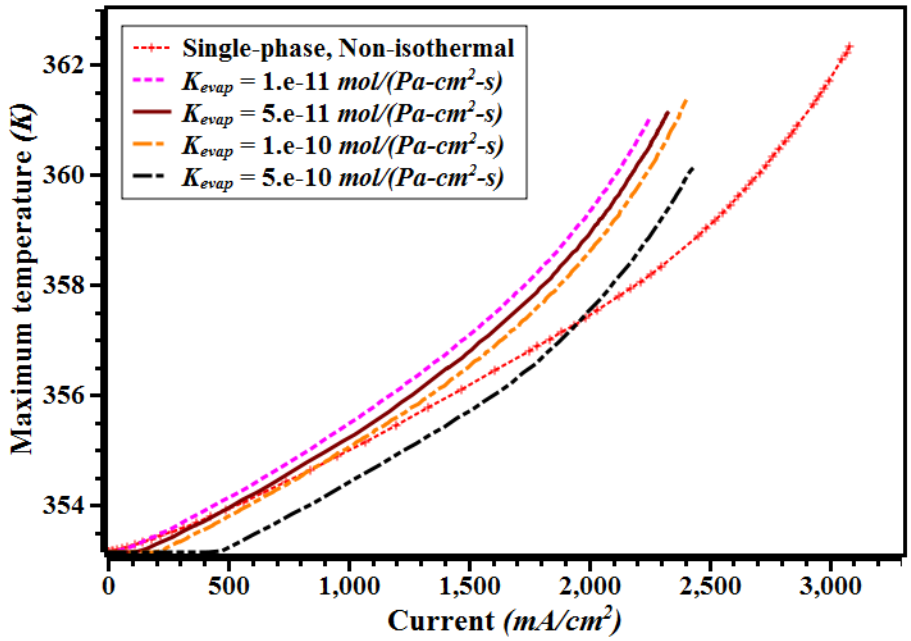

Figure 3.19 – Variation of maximum temperature in the MEA with evaporation rate constants for the two-phase model.

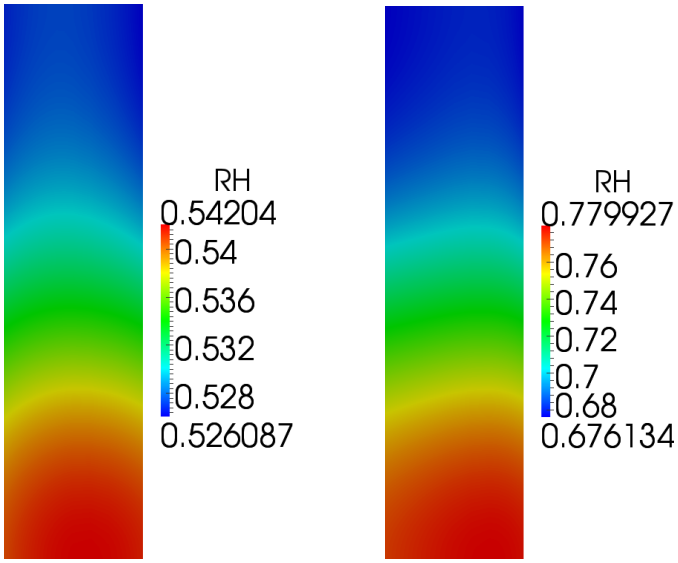

(a) (b)

Figure 3.20 – Base case RH profiles in the CCL at 100 mA/cm^2, for: (a) single-phase, and (b) two-phase with $k_{evap} = 5 \times 10^{-10}$ mol/(Pa-cm^2-s) models.

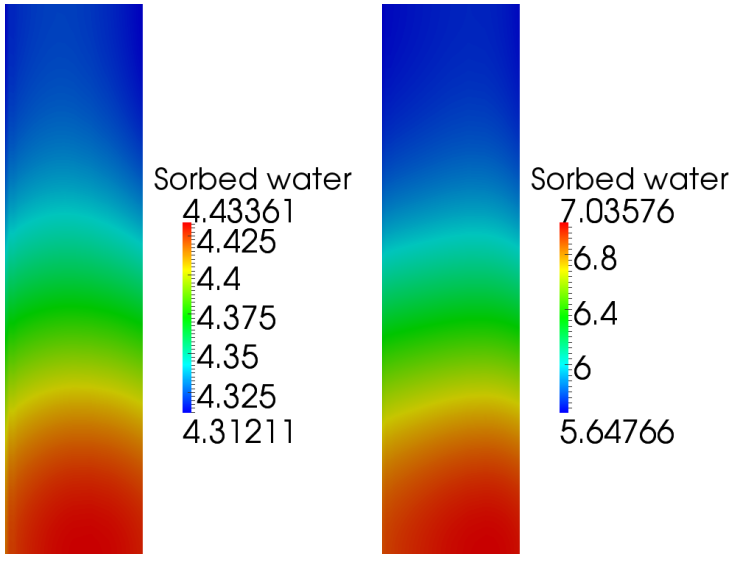

(a) (b)

Figure 3.21 – Base case sorbed water content plots (λ) profiles in the CCL at 1000 mA/cm^2, for: (a) single-phase, and (b) two-phase with $k_{evap} = 5 \times 10^{-10}$ mol/(Pa-cm^2-s) models.

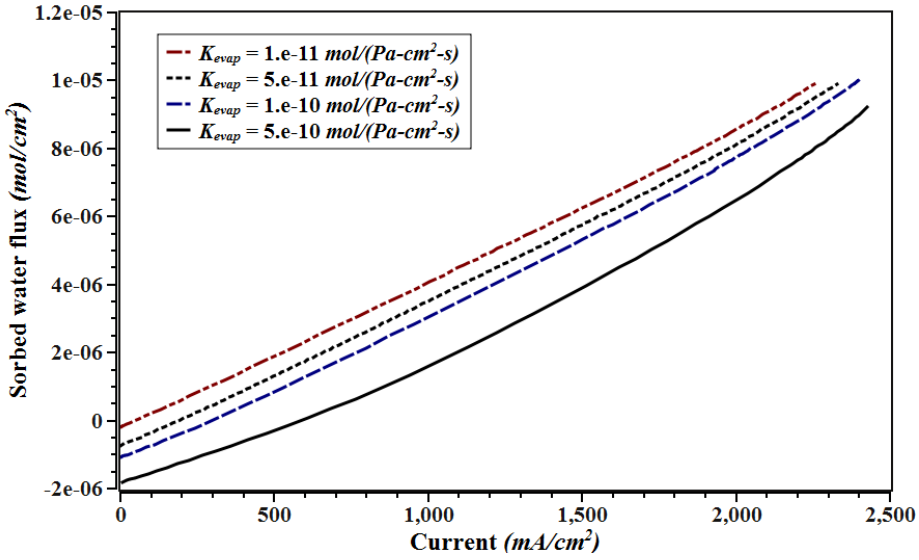

Figure 3.22 – Variation of sorbed water flux with evaporation rate constants for the two-phase model.

terms. The water vapour production due to evaporation is much higher in this case. This leads to higher λ values in the CCL as discussed before. So the ohmic losses are lesser which are confirmed by reduced slopes of cell voltage versus current (green line with ellipse symbols in Figure 3.18). Figures 3.20 and 3.21 compare the RH and λ profiles inside the CCL respectively, at 100 mA/cm^2 for the single-phase and two-phase model with evaporation rate constant value of 5×10^{-10} mol/(Pa-cm^2-s). It can be clearly seen that ionomer has higher water content in the latter case leading to better cell performance.

Figure 3.22 plots the sorbed water flux from the ACL to the CCL as evaporation rate constants are varied. The water flux increases when the evaporation rate constant is reduced. This is due to drier ionomer (for higher evaporation rate constant values) in the CCL hence the back diffusion is reduced further. In the case of evaporation rate constant value of 5×10^{-10} mol/(Pa-cm^2-s), the water flux is from the CCL to the ACL upto 500 mA/cm^2 due to higher back-diffusion as the ionomer in the CCL has higher water content (Figure 3.21).

3.5.2 High humidity and low temperature conditions

The cell performance at high humidity conditions is evaluated by considering the anode and cathode RH values to be 70 %. The cell temperature is considered as 353.15 K (80℃). Figure 3.23 compares the performance predictions of the two-phase

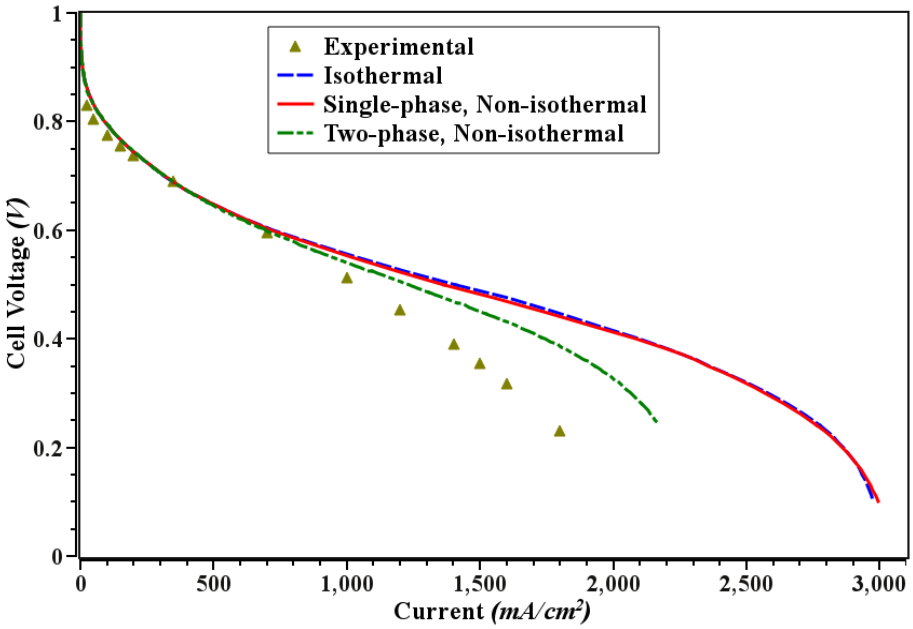

Figure 3.23 – Polarization curves for the isothermal, single-phase non-isothermal, two-phase non-isothermal models and experimental data for the 70 % RH and 80℃ conditions.

model to the single-phase non-isothermal, isothermal model and the experimental data. Negligible difference was observed between the isothermal and non-isothermal model predictions under these conditions. The two-phase model under-performs significantly (roughly 800 mA/cm^2 at 0.2 V) than the single-phase model. The observed loss of performance for the two-phase model is due to mass transport limitations corresponding to presence of liquid water. The model predictions are now closer to the experimental data thereby highlighting the utility of the two-phase model.

In conclusion, a two-phase non-isothermal model is developed and integrated into the openFCST. The model predictions are much closer to the experimental data than the isothermal model. A single saturation equation is developed and re-formulated capillary pressure-saturation correlations [72–74] are accounted for in the two-phase model. The cell performance is studied for the low and high humidity conditions. The model can assess the mass transport limitations due to presence of liquid water in the MEA. However the single saturation equation is found to be insufficient for correct prediction of saturation profiles in layers of mixed wettability. Effects of different evaporation rate constants on the cell performance are also studied.

Chapter 4

Conclusion and Future Work

4.1 Conclusion

A comprehensive two-phase, non-isothermal model employing accurate multi-step reaction kinetics for oxygen reduction reaction (ORR) and hydrogen oxidation reaction (HOR) is developed for the first time. The governing equations describing the transport of heat and liquid water inside the MEA were developed, taking into account all the relevant effects occurring inside the MEA. The model was integrated with an accurate MEA model including an MPL and an accurate catalyst layer model. It resulted in the expansion of an open-source FEM based fuel cell simulation framework, namely openFCST [9, 10], with two new modules, one for thermal analysis and one for two-phase flow. The dependence of various quantities such as constitutive relations, kinetics parameters and material properties on the temperature are rigorously considered in the model.

The single-phase non-isothermal model was developed first. Based on a literature review, it was observed that a detailed non-isothermal PEMFC model did not exist that considered all relevant non-isothermal effects such as anisotropic heat transport, reversible and irreversible heating, ohmic heating, phase change terms and heat of sorption. A detailed energy transport equation was considered, that accounted for heat transport via three modes, *viz.*, conduction, convection and inter-species diffusion. An order of magnitude analysis was performed and the convective heat transport was found to be insignificant inside a PEMFC. Considering the other two significant effects, detailed layer-specific thermal equations were derived. The ohmic heating due to ionic transport was derived from the term considering diffusive enthalpy transport of ions (protons and electrons). The electronic ohmic heating was found to be generally neglected in the literature. Similarly, another neglected phenomena was the heat

released/absorbed due to desorption/sorption of water in the ionomer. This term was derived considering diffusive enthalpy transport of sorbed water. The other significant reversible and irreversible heat terms due to the electrochemical reactions taking place inside the CL were also considered. For consistency of a single-phase model, the water produced at the ORR was evaporated completely and a corresponding heat sink was introduced. An additional phenomena of thermal osmosis [104–107] was introduced into the sorbed water transport model [41, 103]. To the best of author's information, it is considered for the first time in the PEMFC modelling literature. Anisotropic transport properties were extensively used in the MEA model.

In order to assess the importance of non-isothermal models, the model predictions were compared against the isothermal results and experimental data [42]. The non-isothermal model predicts lower fuel cell performance compared to the isothermal model, at low humidity and low temperature conditions (50% RH and 80℃ operating conditions). A temperature rise of up to 9-10℃ is observed at high current densities inside the cell. Difference of up to 150 mA/cm^2 were observed at 0.1 V cell voltage. The non-isothermal model predictions were closer to the experimental data than the isothermal results. It was observed that the heat of sorption (neglected in the literature) is significant (higher than the protonic ohmic heating) at low to medium current densities. Due to this, the under-the-rib region of the CCL is hotter than the under-the-channel region at these current densities. On the other hand, if the heat of sorption is not considered, the temperatures are found to be nearly uniform in the in-plane direction of the CCL. At high current densities, irreversible heating accounts for roughly 70% of the heat generated in the cell and is of the same order as the power density due to current generated in the cell. The under-the-rib region of the CCL is the hottest region at high current densities. The protonic ohmic heating and heat of sorption are the other major heat terms at high current densities. The reversible heating is counterbalanced by the heat needed for evaporation of water.

The isothermal model predicted a fully humidified ionomer in the CCL and RH values of more than 100% in the cell. The non-isothermal model could predict the drying out of the ionomer due to large amounts of heat generated (of the same order as the power density) in the cell. Despite the increased oxygen transport due to higher temperatures, the model could predict higher ohmic overpotentials and thus a significant drop in cell performance. In the isothermal model, the sorbed water movement from the ACL to the CCL could be divided into three regimes, electro-osmotic drag dominated, back-diffusion counterbalancing the electro-osmosis, and fully humidified

ionomer hence higher electro-osmosis with constant back-diffusion. On the other hand, due to drying out of the ionomer in the non-isothermal model, electro-osmosis always dominated the back-diffusion and the net water movement always increased with the current density. The water movement further increased by 10-15% when accounting for thermo-osmosis in the model.

The impact of reversible heat distribution in the individual half-cell reactions of the ORR and HOR was studied. It was observed that the temperature profiles reversed when considering the HOR to be highly exothermic and the ORR to be endothermic reactions, based on the data by Ramousse et al. [19]. The cell performance dropped further in this case due to lower sorbed water content in the CCL because of thermal osmosis.

It was also observed that the cell performance varied significantly with the MPL thermal conductivity. In the base model, the in-plane thermal conductivity of the MPL was considered to be anisotropic and one order of magnitude higher than the through-plane value. On considering the in-plane thermal conductivity of the same order as that of the through-plane, *i.e.*, 0.001 W/(cm-K), the cell performance dropped significantly and was closer to the experimental data. In the case of even lower values for the MPL thermal conductivity, *i.e.*, 0.0001 W/(cm-K), a massive drop in the cell performance and the phenomenon of membrane dry-out was observed. At low humidity and high temperature conditions (50% RH and 95℃), the performance drop for the non-isothermal model was even more due to even drier membrane.

At high humidity and low temperature conditions (70% RH and 80℃), there were negligible differences in the performance predictions of the isothermal and non-isothermal models. This is observed due to well humidified ionomer in this case. Moreover the non-isothermal model performed slightly better at high current densities due to better oxygen transport. However a temperature rise of about 9-10℃ is still observed in these conditions. At high humidity and high temperature conditions (70% RH and 95℃), the non-isothermal model under-performs slightly due to drier ionomer in the CCL. In the high humidity operations, non-physical RH values of more than 100% were observed at high current densities, highlighting the need of a two-phase non-isothermal MEA model. Hence a non-isothermal model was found to be necessary for proper assessment of the fuel cell performance.

In the second part of the thesis, a two-phase model considering liquid water trans-

port is integrated into the existing single-phase non-isothermal MEA model. Based on the analysis of various important dimensionless numbers in Fluid Mechanics, it was concluded that capillary driven transport is the only significant mechanism in PEMFC porous media. A single transport equation for the saturation considering capillary diffusion was developed in this work. The majority of PEMFC modelling literature was found to be employing empirical Leverett correlations for the capillary pressure-saturation relationship[68, 69]. These approaches are however suited only to hydrophillic media such as packed soil beds. The modified Leverett approach [77, 86] employing external contact angle values has been shown to be ineffective for the mixed wettability, highly anisotropic, fibrous diffusion media of the PEMFC [90]. In this work, the experimental data by Kumbur et al. [72–74] for the commercially available Sigracet® porous diffusion media is considered. These correlations were obtained by Kumbur et al. for the composite diffusion media (GDL + MPL). In this work, the correlations by Kumbur et al. are revised and separate correlations for the GDL and MPL are developed. The correlations obtained for the MPL are qualitatively validated against the data by Gostick et al. [54]. The phase change term corresponding to evaporation/condensation was considered by adapting the data by Villanueva [98] (based on a pore size distribution model). The presence of liquid water was accounted for by correcting the effective gas diffusivity in the porous layers.

At low humidity conditions, a significant performance drop (up to 700 mA/cm^2 at 0.1 V) was observed for the two-phase model bringing the cell performance predictions much closer to experimental data. The liquid water accumulated in the under-the-rib region of the CCL at medium current densities, while the accumulation shifted to the under-the-channel region at high current densities. The saturation gradients inside the GDL and MPL were negligible as compared to the CCL. This is due to the fact that the term $k_l \frac{\partial p_c}{\partial s}$ is much more significant in the case of the GDL and MPL. The temperature rise in the cell was more rapid in the case of two-phase model due to the incomplete evaporation of water produced during the ORR. The mass transfer losses increased significantly due to the presence of liquid water in the layers. Moreover, due to lower water vapour mole fraction values and higher temperatures, the ionomer in the CCL was found to be further dried up. The impact of increased mass transport losses and protonic ohmic losses resulted in a significant performance drop.

Evaporation and condensation rate constants are unknown in a porous media. Therefore, a sensitivity analysis on these parameters was performed. On reducing the evaporation rate constant, the cell performance dropped due to higher amounts

of liquid water in the MEA. However, in the case of evaporation rate constant value of 5×10^{-10} mol/(Pa-cm^2-s), the two-phase model over-performed significantly than isothermal model up to medium current densities. In this case, the evaporation rate increased and due to a constant supply of liquid water at the channel boundary (Dirichlet conditions). This resulted in increased RH values (hence λ values) in the CCL. The ohmic losses therefore reduced causing a rise in the cell performance. However this situation is caused due to non-physical extra evaporation of water other than the water produced during the reaction. A significant performance drop was observed in the case of high humidity operations also using the two-phase model. Even though the two-phase model can predict water buildup in the CL but the single equation for saturation is found to be insufficient for accurately predicting the saturation jumps across the layers of mixed wettabilities. This is due to inherent continuous nature of the solution variables in a FEM formulation.

In summary, a detailed open-source two-phase non-isothermal MEA model is developed in this work. The model results demonstrate the importance of presence of liquid water and non-isothermal effects in MEA operation. The importance of various neglected phenomena such as thermal osmosis and heat of sorption were assessed in this work. More accurate capillary pressure-saturation correlations were re-developed and used. This detailed model can be used to accurately and reliably assess the fuel cell performance at high current densities.

4.2 Future Work

This work has created several avenues of future research. In this thesis, the liquid water transport was solved using a single saturation transport equation. However it was found to be insufficient for predicting the saturation jumps across the layers of mixed wettabilities. In reality, in a liquid water flow through a porous media, liquid water pressure (hence capillary pressure) instead of saturation, is continuous across the interfaces. The liquid water transport can therefore be improved by developing an equation solving for the capillary pressures. The capillary pressure - saturation correlations developed in this work will need to be reformulated by expressing saturation as a function of capillary pressures. The former will be required to determine various parameters such as liquid permeability and effective gas diffusivity.

The phase change rate constants were assumed in this work due to non-availability of the data for a porous media. The cell performance was observed to vary signifi-

cantly based on a sensitivity analysis performed over these constants. A more accurate kinetics based phase change model can therefore be developed in order to accurately assess the cell performance. In the current phase change model, it was also observed that non-physical evaporation takes place at low current densities. This resulted in over-prediction of cell performance. As a starting point, the current model will need to be suitably corrected using a factor of irreducible saturation.

In this work, we developed models for heat and liquid water transport inside the MEA. The model considered a macro-homogeneous catalyst layer structure. However multi-scale catalyst layer models [42, 123] available in openFCST were not included and they might bring the model results closer to the experimental data.

Multi-step reaction kinetics models were considered in this work. The effect of temperature on the coverage profiles on the intermediate species produced during the ORR should be studied.

A new class of pore-size distribution based models have emerged that can be used to reliably characterize a porous media [93, 98]. Various properties such as permeability, diffusivity, capillary pressure correlations and interfacial liquid-vapour area can be determined using these models. They can also be used to design and optimize a porous media. The model by Villanueva [98] can be integrated into the existing fuel cell simulation framework and analyzed in tandem with various other models present.

Besides the thermal resistance in the layer, it is likely that there is a contact resistance at the layer interfaces. These contact resistance values such as thermal contact resistance vary considerably with compaction pressure [51]. In the existing continuous Galerkin FEM framework, solution variables are assumed continuous at the interface. The possibility of coupling a discontinuous Galerkin FEM with the continuous approach can be explored and integrated into the framework.

References

[1] Papageorgopoulos D. DOE fuel cell technology program overview and introduction to the 2010 fuel cell pre-solicitation workshop in DOE fuel cell pre-solicitation workshop. Technical report, Department of Energy, Lakewood, Colorado, 2010.

[2] Friedrich K, Kallo J, and Schirmer J. Fuel cells for aircraft application. Number PART B, pages 1231–1240, 2009.

[3] Tüber K, Zobel M, Schmidt H, and Hebling C. A polymer electrolyte membrane fuel cell system for powering portable computers. *Journal of Power Sources*, 122(1):1–8, 2003.

[4] Wang Y, Chen K, Mishler J, Cho S, and Adroher X. A review of polymer electrolyte membrane fuel cells: Technology, applications, and needs on fundamental research. *Applied Energy*, 88(4):981–1007, 2011.

[5] Secanell M, Karan K, Suleman A, and Djilali N. Multi-variable optimization of PEMFC cathodes using an agglomerate model. *Electrochimica Acta*, 52(22): 6318–6337, 2007.

[6] Secanell M, Carnes B, Suleman A, and Djilali N. Numerical optimization of proton exchange membrane fuel cell cathodes. *Electrochimica Acta*, 52(7):2668–2682, 2007.

[7] Secanell M, Wishart J, and Dobson P. Computational design and optimization of fuel cells and fuel cell systems: A review. *Journal of Power Sources*, 196(8): 3690–3704, 2011.

[8] Weber A and Newman J. Modeling transport in polymer-electrolyte fuel cells. *Chemical Reviews*, 104(10):4679–4726, 2004.

[9] URL `http://www.openfcst.mece.ualberta.ca`.

[10] Secanell M, Putz A, Zingan V, Bhaiya M, Moore M, Dobson P, Wardlaw P, and Domican K. Open-source Fuel Cell Simulation Toolbox (OpenFCST): User and Developer's Reference Guide, September 2013. URL `http://www.openfcst.mece.ualberta.ca/pdfs/Reference_for_developers.pdf`. Taken on November 05, 2013.

[11] Larminie J and Dicks A. *Fuel Cell Systems Explained*. Wiley, West Sussex, England, 2 edition, 2003.

[12] Inaba M, Kinumoto T, Kiriake M, Umebayashi R, Tasaka A, and Ogumi Z. Gas crossover and membrane degradation in polymer electrolyte fuel cells. *Electrochimica Acta*, 51(26):5746–5753, 2006.

[13] Hayre R. O, Cha S. W, Colella W, and Prinz F. B. *Fuel Cell Fundamentals*. Wiley, New York, USA, 2 edition, 2008.

[14] Pilatowsky I, Romero R, Isaza C, Gamboa S, Sebastian P, and Rivera W. Thermodynamics of Fuel Cells. In *Cogeneration Fuel Cell-Sorption Air Conditioning Systems*, pages 25–36. Springer London, 2011.

[15] Lewis G and Randall M. *International Critical Tables*, volume 7. McGraw Hill, New York, 1930.

[16] Newman J and Thomas-Alyea K. *Electrochemical Systems*. John Wiley & Sons, New York, 3rd edition, 2004.

[17] Weber A and Newman J. Coupled thermal and water management in polymer electrolyte fuel cells. *Journal of the Electrochemical Society*, 153(12):A2205–A2214, 2006.

[18] Lampinen M. J and Fomino M. Analysis of free energy and entropy changes for half-cell reactions. *Journal of the Electrochemical Society*, 140(12):3537–3546, 1993.

[19] Ramousse J, Lottin O, Didierjean S, and Maillet D. Heat sources in proton exchange membrane (PEM) fuel cells. *Journal of Power Sources*, 192(2):435–441, 2009.

[20] Burheim O, Kjelstrup S, Pharoah J, Vie P, and Mller-Holst S. Calculation of reversible electrode heats in the proton exchange membrane fuel cell from calorimetric measurements. *Electrochimica Acta*, 56(9):3248–3257, 2011.

[21] Kjelstrup S, Vie P, Akyalcin L, Zefaniya P, Pharoah J, and Burheim O. The Seebeck coefficient and the Peltier effect in a polymer electrolyte membrane cell with two hydrogen electrodes. *Electrochimica Acta*, 99:166–175, 2013.

[22] Ju H, Meng H, and Wang C.-Y. A single-phase, non-isothermal model for PEM fuel cells. *International Journal of Heat and Mass Transfer*, 48(7):1303–1315, 2005.

[23] Nguyen T. V and White R. E. Water and heat management model for proton-exchange-membrane fuel cells. *Journal of the Electrochemical Society*, 140(8): 2178–2186, 1993.

[24] Lange K, Sui P.-C, and Djilali N. Pore scale modeling of a proton exchange membrane fuel cell catalyst layer: Effects of water vapor and temperature. *Journal of Power Sources*, 196(6):3195–3203, 2011.

[25] Shimpalee S and Dutta S. Numerical prediction of temperature distribution in PEM fuel cells. *Numerical Heat Transfer; Part A: Applications*, 38(2):111–128, 2000.

[26] Rowe A and Li X. Mathematical modeling of proton exchange membrane fuel cells. *Journal of Power Sources*, 102(1-2):82–96, 2001.

[27] Ramousse J, Deseure J, Lottin O, Didierjean S, and Maillet D. Modelling of heat, mass and charge transfer in a PEMFC single cell. *Journal of Power Sources*, 145(2):416–427, 2005.

[28] Wang L, Husar A, Zhou T, and Liu H. A parametric study of PEM fuel cell performances. *International Journal of Hydrogen Energy*, 28(11):1263–1272, 2003.

[29] Mazumder S and Cole J. Rigorous 3-D mathematical modeling of PEM fuel cells II. Model predictions with liquid water transport. *Journal of the Electrochemical Society*, 150(11):A1510–A1517, 2003.

[30] Ju H, Wang C.-Y, Cleghorn S, and Beuscher U. Nonisothermal modeling of polymer electrolyte fuel cells I. Experimental validation. *Journal of the Electrochemical Society*, 152(8):A1645–A1653, 2005.

[31] Wang Y and Wang C.-Y. A nonisothermal, two-phase model for polymer electrolyte fuel cells. *Journal of the Electrochemical Society*, 153(6):A1193–A1200, 2006.

[32] Pasaogullari U, Mukherjee P, Wang C.-Y, and Chen K. Anisotropic heat and water transport in a PEFC cathode gas diffusion layer. *Journal of the Electrochemical Society*, 154(8):B823–B834, 2007.

[33] Bapat C and Thynell S. Anisotropic heat conduction effects in proton-exchange membrane fuel cells. *Journal of Heat Transfer*, 129(9):1109–1118, 2007.

[34] Birgersson E, Noponen M, and Vynnycky M. Analysis of a two-phase non-isothermal model for a PEFC. *Journal of the Electrochemical Society*, 152(5): A1021–A1034, 2005.

[35] Zamel N and Li X. Non-isothermal multi-phase modeling of PEM fuel cell cathode. *International Journal of Energy Research*, 34(7):568–584, 2010.

[36] Berning T, Lu D, and Djilali N. Three-dimensional computational analysis of transport phenomena in a PEM fuel cell. *Journal of Power Sources*, 106(1-2): 284–294, 2002.

[37] Hwang J and Chen P. Heat/mass transfer in porous electrodes of fuel cells. *International Journal of Heat and Mass Transfer*, 49(13-14):2315–2327, 2006.

[38] Hwang J, Chao C, and Wu W. Thermal-fluid transports in a five-layer membrane-electrode assembly of a PEM fuel cell. *Journal of Power Sources*, 163(1 SPEC. ISS.):450–459, 2006.

[39] Hwang J, Chao C, Chang C, Ho W, and Wang D. Modeling of two-phase temperatures in a two-layer porous cathode of polymer electrolyte fuel cells. *International Journal of Hydrogen Energy*, 32(3):405–414, 2007.

[40] Kjelstrup S and Røsjorde A. Local and total entropy production and heat and water fluxes in a one-dimensional polymer electrolyte fuel cell. *Journal of Physical Chemistry B*, 109(18):9020–9033, 2005. cited By (since 1996)22.

[41] Secanell M. *Computational modeling and optimization of proton exchange membrane fuel cells*. PhD thesis, University of Victoria, November 2007.

[42] Dobson P. Investigation of the Polymer Electrolyte Membrane Fuel Cell Catalyst Layer Microstructure. Master's thesis, University of Alberta, September 2011.

[43] Moore M. Investigation of the Double-Trap Intrinsic Kinetic Equation for the Oxygen Reduction Reaction and its implementation into a Membrane Electrode Assembly model. Master's thesis, University of Alberta, 2012.

[44] Burheim O, Vie P, Pharoah J, and Kjelstrup S. Ex situ measurements of through-plane thermal conductivities in a polymer electrolyte fuel cell. *Journal of Power Sources*, 195(1):249–256, 2010.

[45] Karimi G, Li X, and Teertstra P. Measurement of through-plane effective thermal conductivity and contact resistance in PEM fuel cell diffusion media. *Electrochimica Acta*, 55(5):1619–1625, 2010.

[46] Zamel N, Litovsky E, Shakhshir S, Li X, and Kleiman J. Measurement of in-plane thermal conductivity of carbon paper diffusion media in the temperature range of -20C to +120C. *Applied Energy*, 88(9):3042–3050, 2011.

[47] Zamel N, Litovsky E, Li X, and Kleiman J. Measurement of the through-plane thermal conductivity of carbon paper diffusion media for the temperature range from -50 to +120 c. *International Journal of Hydrogen Energy*, 36(19):12618–12625, 2011.

[48] Unsworth G, Zamel N, and Li X. Through-plane thermal conductivity of the microporous layer in a polymer electrolyte membrane fuel cell. *International Journal of Hydrogen Energy*, 37(6):5161–5169, 2012.

[49] Sadeghifar H, Djilali N, and Bahrami M. Effect of Polytetrafluoroethylene (PTFE) and micro porous layer (MPL) on thermal conductivity of fuel cell gas diffusion layers: Modeling and experiments. *Journal of Power Sources*, 248: 632–641, 2014.

[50] Teertstra P, Karimi G, and Li X. Measurement of in-plane effective thermal conductivity in PEM fuel cell diffusion media. *Electrochimica Acta*, 56(3):1670–1675, 2011.

[51] Zamel N and Li X. Effective transport properties for polymer electrolyte membrane fuel cells - With a focus on the gas diffusion layer. *Progress in Energy and Combustion Science*, 39(1):111–146, 2013.

[52] Dai W, Wang H, Yuan X.-Z, Martin J, Yang D, Qiao J, and Ma J. A review on water balance in the membrane electrode assembly of proton exchange membrane fuel cells. *International Journal of Hydrogen Energy*, 34(23):9461–9478, 2009.

[53] Fuller T. F and Newman J. Water and thermal management in solid-polymer-electrolyte fuel cells. *Journal of the Electrochemical Society*, 140(5):1218–1225, 1993.

[54] Gostick J, Fowler M, Ioannidis M, Pritzker M, Volfkovich Y, and Sakars A. Capillary pressure and hydrophilic porosity in gas diffusion layers for polymer electrolyte fuel cells. *Journal of Power Sources*, 156(2):375–387, 2006.

[55] Hatzell M, Turhan A, Kim S, Hussey D, Jacobson D, and Mench M. Quantification of temperature driven flow in a polymer electrolyte fuel cell using high-resolution neutron radiography. *Journal of the Electrochemical Society*, 158(6):B717–B726, 2011.

[56] Litster S and Djilali . *Transport Phenomena in Fuel Cells*, chapter 5. WIT Press, Ashurst, U.K., 1st edition, 2006.

[57] Mukherjee P, Wang C.-Y, and Kang Q. Mesoscopic modeling of two-phase behavior and flooding phenomena in polymer electrolyte fuel cells. *Electrochimica Acta*, 54(27):6861–6875, 2009.

[58] Schulz V, Becker J, Wiegmann A, Mukherjee P, and Wang C.-Y. Modeling of two-phase behavior in the gas diffusion medium of PEFCs via full morphology approach. *Journal of the Electrochemical Society*, 154(4):B419–B426, 2007.

[59] Markicevic B and Djilali N. Analysis of liquid water transport in fuel cell gas diffusion media using two-mobile phase pore network simulations. *Journal of Power Sources*, 196(5):2725–2734, 2011.

[60] Lee K.-J, Nam J, and Kim C.-J. Pore-network analysis of two-phase water transport in gas diffusion layers of polymer electrolyte membrane fuel cells. *Electrochimica Acta*, 54(4):1166–1176, 2009.

[61] Bernardi D. M. Water-balance calculations for solid-polymer-electrolyte fuel cells. *Journal of the Electrochemical Society*, 137(11):3344–3350, 1990.

[62] Bernardi D. M and Verbrugge M. W. Mathematical model of a gas diffusion electrode bonded to a polymer electrolyte. *AIChE Journal*, 37(8):1151–1163, 1991.

[63] Bernardi D. M and Verbrugge M. W. Mathematical model of the solid-polymer-electrolyte fuel cell. *Journal of the Electrochemical Society*, 139(9):2477–2491, 1992.

[64] Janssen G. A Phenomenological Model of Water Transport in a Proton Exchange Membrane Fuel Cell. *Journal of the Electrochemical Society*, 148(12): a1313–a1323, 2001.

[65] Baschuk J and Li X. Modelling of polymer electrolyte membrane fuel cells with variable degrees of water flooding. *Journal of Power Sources*, 86(1):181–196, 2000.

[66] Pasaogullari U and Wang C. Liquid Water Transport in Gas Diffusion Layer of Polymer Electrolyte Fuel Cells. *Journal of the Electrochemical Society*, 151 (3):A399–A406, 2004.

[67] Berning T and Djilali N. A 3D, multiphase, multicomponent model of the cathode and anode of a PEM fuel cell. *Journal of the Electrochemical Society*, 150(12):A1589–A1598, 2003.

[68] Leverett M. Capillary behavior in porous solids. *AIME Trans.*, 142:152–169, 1940.

[69] Udell K. Heat transfer in porous media considering phase change and capillarity-the heat pipe effect. *International Journal of Heat and Mass Transfer*, 28(2): 485–495, 1985.

[70] Acosta M, Merten C, Eigenberger G, Class H, Helmig R, Thoben B, and Mller-Steinhagen H. Modeling non-isothermal two-phase multicomponent flow in the cathode of PEM fuel cells. *Journal of Power Sources*, 159(2):1123–1141, 2006.

[71] Wu H, Li X, and Berg P. On the modeling of water transport in polymer electrolyte membrane fuel cells. *Electrochimica Acta*, 54(27):6913–6927, 2009.

[72] Kumbur E, Sharp K, and Mench M. Validated Leverett approach for multiphase flow in PEFC diffusion media: I. Hydrophobicity effect. *Journal of the Electrochemical Society*, 154(12):B1295–B1304, 2007.

[73] Kumbur E, Sharp K, and Mench M. Validated Leverett approach for multiphase flow in PEFC diffusion media: II. Compression effect. *Journal of the Electrochemical Society*, 154(12):B1305–B1314, 2007.

[74] Kumbur E, Sharp K, and Mench M. Validated Leverett approach for multiphase flow in PEFC diffusion media: III. Temperature effect and unified approach. *Journal of the Electrochemical Society*, 154(12):B1315–B1324, 2007.

[75] Ye Q and Van Nguyen T. Three-dimensional simulation of liquid water distribution in a PEMFC with experimentally measured capillary functions. *Journal of the Electrochemical Society*, 154(12):B1242–B1251, 2007.

[76] Luikov A. Systems of differential equations of heat and mass transfer in capillary-porous bodies (review). *International Journal of Heat and Mass Transfer*, 18(1):1–14, 1975.

[77] Nam J and Kaviany M. Effective diffusivity and water-saturation distribution in single- and two-layer PEMFC diffusion medium. *International Journal of Heat and Mass Transfer*, 46(24):4595–4611, 2003.

[78] Natarajan D and Van Nguyen T. Three-dimensional effects of liquid water flooding in the cathode of a PEM fuel cell. *Journal of Power Sources*, 115(1): 66–80, 2003.

[79] Natarajan D and Van Nguyen T. A Two-Dimensional, Two-Phase, Multicomponent, Transient Model for the Cathode of a Proton Exchange Membrane Fuel Cell Using Conventional Gas Distributors. *Journal of the Electrochemical Society*, 148(12):a1324–a1335, 2001.

[80] Shah A, Kim G.-S, Sui P, and Harvey D. Transient non-isothermal model of a polymer electrolyte fuel cell. *Journal of Power Sources*, 163(2):793–806, 2007.

[81] Wang X and Van Nguyen T. Modeling the effects of capillary property of porous media on the performance of the cathode of a PEMFC. *Journal of the Electrochemical Society*, 155(11):B1085–B1092, 2008.

[82] Gerteisen D, Heilmann T, and Ziegler C. Modeling the phenomena of dehydration and flooding of a polymer electrolyte membrane fuel cell. *Journal of Power Sources*, 187(1):165–181, 2009.

[83] Wang C and Cheng P. Multiphase Flow and Heat Transfer in Porous Media. volume 30 of *Advances in Heat Transfer*, pages 93 – 196. Elsevier, 1997.

[84] Wang C and Cheng P. A multiphase mixture model for multiphase, multicomponent transport in capillary porous media - I. Model development. *International Journal of Heat and Mass Transfer*, 39(17):3607–3618, 1996.

[85] Wang Z, Wang C, and Chen K. Two-phase flow and transport in the air cathode of proton exchange membrane fuel cells. *Journal of Power Sources*, 94(1):40–50, 2001.

[86] Pasaogullari U and Wang C.-Y. Two-phase modeling and flooding prediction of polymer electrolyte fuel cells. *Journal of the Electrochemical Society*, 152(2): A380–A390, 2005.

[87] Ju H, Luo G, and Wang C.-Y. Probing liquid water saturation in diffusion media of polymer electrolyte fuel cells. *Journal of the Electrochemical Society*, 154(2):B218–B228, 2007.

[88] Koido T, Furusawa T, and Moriyama K. An approach to modeling two-phase transport in the gas diffusion layer of a proton exchange membrane fuel cell. *Journal of Power Sources*, 175(1):127–136, 2008.

[89] Gurau V, Bluemle M, De Castro E, Tsou Y.-M, Mann Jr. J, and Zawodzinski Jr. T. Characterization of transport properties in gas diffusion layers for proton exchange membrane fuel cells. 1. Wettability (internal contact angle to water and surface energy of GDL fibers). *Journal of Power Sources*, 160(2 SPEC. ISS.):1156–1162, 2006.

[90] Kumbur E, Sharp K, and Mench M. On the effectiveness of Leverett approach for describing the water transport in fuel cell diffusion media. *Journal of Power Sources*, 168(2):356–368, 2007.

[91] Kaviany M. *Principles of Heat Transfer in Porous Media*. Springer-Verlag, New York, 1991.

[92] Weber A, Darling R, and Newman J. Modeling Two-Phase behavior in PEFCs. *Journal of the Electrochemical Society*, 151(10):A1715–A1727, 2004.

[93] Weber A. Improved modeling and understanding of diffusion-media wettability on polymer-electrolyte-fuel-cell performance. *Journal of Power Sources*, 195 (16):5292–5304, 2010.

[94] Sinha P, Mukherjee P, and Wang C.-Y. Impact of GDL structure and wettability on water management in polymer electrolyte fuel cells. *Journal of Materials Chemistry*, 17(30):3089–3103, 2007.

[95] Cheung P, Fairweather J, and Schwartz D. Characterization of internal wetting in polymer electrolyte membrane gas diffusion layers. *Journal of Power Sources*, 187(2):487–492, 2009.

[96] Eikerling M. Water management in cathode catalyst layers of PEM fuel cells. *Journal of the Electrochemical Society*, 153(3):E58–E70, 2006.

[97] Mulone V and Karan K. Analysis of capillary flow driven model for water transport in PEFC cathode catalyst layer: Consideration of mixed wettability

and pore size distribution. *International Journal of Hydrogen Energy*, 38(1): 558–569, 2013.

[98] Villanueva P. A. M. A mixed wettability pore size distribution model for the Analysis of water transport in PEMFC materials. Master's thesis, University of Alberta, 2013.

[99] Gallagher K, Darling R, Patterson T, and Perry M. Capillary pressure saturation relations for PEM fuel cell gas diffusion layers. *Journal of the Electrochemical Society*, 155(11):B1225–B1231, 2008.

[100] Bird R. B, Stewart W. E, and Lightfoot E. N. *Transport Phenomena, Revised 2nd Edition*. John Wiley & Sons, Inc., 2nd edition, December 2006. ISBN 0470115394.

[101] Moran M. J and Shapiro H. N. *Fundamentals of Engineering Thermodynamics*. John Wiley & Sons, Inc., Chichester, England, fifth edition, 2006.

[102] Sonntag R, Borgnakke C, and Van Wylen G. *Fundamentals of Thermodynamics*. Wiley, 2003. ISBN 9780471152323.

[103] Springer T, Zawodzinski T, and Gottesfeld S. Polymer electrolyte fuel cell model. *Journal of the Electrochemical Society*, 138(8):2334–2342, 1991.

[104] Tasaka M, Mizuta T, and Sekiguchi O. Mass transfer through polymer membranes due to a temperature gradient. *Journal of Membrane Science*, 54(1-2): 191–204, 1990.

[105] Tasaka M, Hirai T, Kiyono R, and Aki Y. Solvent transport across cation-exchange membranes under a temperature difference and under an osmotic pressure difference. *Journal of Membrane Science*, 71(1-2):151–159, 1992.

[106] Kim S and Mench M. Investigation of temperature-driven water transport in polymer electrolyte fuel cell: Thermo-osmosis in membranes. *Journal of Membrane Science*, 328(1-2):113–120, 2009.

[107] Kim S and Mench M. Investigation of temperature-driven water transport in polymer electrolyte fuel cell: Phase-change-induced flow. *Journal of the Electrochemical Society*, 156(3):B353–B362, 2009.

[108] Ostrovskii V and Gostev B. Heat effects and rates and molecular mechanisms of water sorption by perfluorinated polymer materials bearing functional groups. *Journal of Thermal Analysis*, 46(2):397–416, 1996.

[109] Rowe A. M. Mathematical modeling of proton exchange membrane fuel cells. Master's thesis, University of Victoria, 1997.

[110] Bard A. J and Faulkner L. R. *Electrochemical Methods: Fundamentals and Applications*. John Wiley & Sons, Inc., second edition, 2001.

[111] Popiel C and Wojtkowiak J. Simple formulas for thermophysical properties of liquid water for heat transfer calculations (from 0 ℃to 150 ℃). *Heat Transfer Engineering*, 19(3):87–101, 1998.

[112] Fick A. Ueber Diffusion. *Annalen der Physik*, 170(1):59–86, 1855. ISSN 1521-3889.

[113] Bruggeman D. A. G. Berechnung Verschiedener Physikalischer Konstanten von Heterogenen Substanzen. I. Dielektrizitatskonstanten und Leitfahigkeiten der Mischkorper aus Isotropen Substanzen. *Annalen der Physik*, 24:636–679, 1935.

[114] Stauffer D and Aharony A. *Introduction to Percolation Theory*. Taylor & Francis, London, 2nd edition, 1992.

[115] Tomadakis M. M and Sotirchos S. V. Effective Knudsen diffusivities in structures of randomly overlapping fibers. *AIChE Journal*, 37(1):74–86, 1991.

[116] Tomadakis M. M and Sotirchos S. V. Ordinary and transition regime diffusion in random fiber structures. *AIChE Journal*, 39(3):397–412, 1993.

[117] Wang Q, Eikerling M, Song D, Liu Z, Navessin T, Xie Z, and Holdcroft S. Functionally Graded Cathode Catalyst Layers for Polymer Electrolyte Fuel Cells. I. Theoretical Modeling. *Journal of the Electrochemical Society*, 151(7): A950–A957, 2004.

[118] Iden H, Ohma A, and Shinohara K. Analysis of Proton Transport in Pseudo Catalyst Layers. *Journal of The Electrochemical Society*, 156(9):B1078–B1084, 2009.

[119] Iden H, Sato K, Ohma A, and Shinohara K. Relationship among Microstructure, Ionomer Property and Proton Transport in Pseudo Catalyst Layers. *Journal of The Electrochemical Society*, 158(8):B987–B994, 2011.

[120] Domican K, Shukla S, Wunder F, and Secanell M. Low Loading Cathode Catalyst Layer Mathematical Modelling & Experimental Validation. Presented at the Hydrogen + Fuel Cells Congerence 2013, Vancouver, June 16-19 2013.

[121] Peron J, Mani A, Zhao X, Edwards D, Adachi M, Soboleva T, Shi Z, Xie Z, Navessin T, and Holdcroft S. Properties of Nafion® NR-211 membranes for PEMFCs. *Journal of Membrane Science*, 356(1-2):44–51, 2010.

[122] BekkTech L. In-Plane Conductivity Testing Procedures & Results, 2007. Taken on August 10, 2010.

[123] Dobson P, Lei C, Navessin T, and Secanell M. Characterization of the PEM fuel cell catalyst layer microstructure by nonlinear least-squares parameter estimation. *Journal of the Electrochemical Society*, 159(5):B514–B523, 2012.

[124] Motupally S, Becker A. J, and W. Weidner john . Diffusion of Water in Nafion 115 Membranes. *Journal of the Electrochemical Society*, 147(9):3171–3177, 2000.

[125] Villaluenga J, Seoane B, Barragn V, and Ruiz-Bauz C. Thermo-osmosis of mixtures of water and methanol through a Nafion membrane. *Journal of Membrane Science*, 274(1-2):116–122, 2006.

[126] Zaffou R, Yi J, Kunz H, and Fenton J. Temperature-driven water transport through membrane electrode assembly of proton exchange membrane fuel cells. *Electrochemical and Solid-State Letters*, 9(9):A418–A422, 2006.

[127] Marr C and Li X. Composition and performance modelling of catalyst layer in a proton exchange membrane fuel cell. *Journal of Power Sources*, 77(1):17–27, 1999.

[128] E-TEK . Specifications for C-1: HP Platinum on Vulcan XC-72. *www.etek-inc.com*, Data accessed on February 2, 2007.

[129] Wang J, Zhang J, and Adzic R. Double-trap kinetic equation for the oxygen reduction reaction on pt(111) in acidic media. *Journal of Physical Chemistry A*, 111(49):12702–12710, 2007.

[130] Moore M, Putz A, and Secanell M. Investigation of the ORR using the double-trap intrinsic kinetic model. *Journal of the Electrochemical Society*, 160(6): F670–F681, 2013.

[131] Wang J. X, Springer T. E, and Adzic R. R. Dual-Pathway Kinetic Equation for the Hydrogen Oxidation Reaction on Pt Electrodes. *Journal of the Electrochemical Society*, 153(9):A1732–A1740, 2006.

[132] Bhaiya M, Moore M, and Secanell M. Development of a single-phase non-isothermal MEA model for multi-step Oxygen Reduction Reaction (ORR) kinetics. Presented at the Hydrogen + Fuel Cells Congerence 2013, Vancouver, June 16-19 2013.

[133] Sun W, Peppley B, and Karan K. An improved two-dimensional agglomerate cathode model to study the influence of catalyst layer structural parameters. *Electrochimica Acta*, 50(16-17):3359–3374, 2005.

[134] Hinatsu J. T, Mizuhata M, and Takenaka H. Water uptake of perfluorosulfonic acid membranes from liquid water and water vapor. *Journal of the Electrochemical Society*, 141(6):1493–1498, 1994.

[135] Liu Y, Murphy M, Baker D, Gu W, Ji C, Jorne J, and Gasteiger H. Proton conduction and oxygen reduction kinetics in PEM fuel cell cathodes: Effects of ionomer-to-carbon ratio and relative humidity. *Journal of the Electrochemical Society*, 156(8):B970–B980, 2009.

[136] Pharoah J, Karan K, and Sun W. On effective transport coefficients in PEM fuel cell electrodes: Anisotropy of the porous transport layers. *Journal of Power Sources*, 161(1):214–224, 2006.

[137] Yu Z and Carter R. N. Measurement of effective oxygen diffusivity in electrodes for proton exchange membrane fuel cells. *Journal of Power Sources*, 195(4):1079 – 1084, 2010. ISSN 0378-7753.

[138] Khandelwal M and Mench M. Direct measurement of through-plane thermal conductivity and contact resistance in fuel cell materials. *Journal of Power Sources*, 161(2):1106–1115, 2006.

[139] Davis T. A. Algorithm 832: UMFPACK, an unsymmetric-pattern multifrontal method. *ACM Transactions on Mathematical Software*, 30(2):196–199, June 2004.

[140] Kelly D, S. R. Gago de J, Zienkiewicz O, and Babuska I. A posteriori error analysis and adaptive processes in the finite element method: Part I - error analysis. *International Journal for Numerical Methods in Engineering*, 19(11): 1593–1619, 1983.

[141] Bangerth W, Hartmann R, and Kanschat G. `deal.II` *Differential Equations Analysis Library, Technical Reference*. URL `http://www.dealii.org`.

[142] Bangerth W, Hartmann R, and Kanschat G. deal.II - a General Purpose Object Oriented Finite Element Library. *ACM Trans. Math. Softw.*, 33(4):24/1–24/27, 2007.

[143] Holman J. *Heat Transfer*. McGraw Hill, New York, tenth edition, 2010.

[144] Burheim O, Su H, Pasupathi S, Pharoah J, and Pollet B. Thermal conductivity and temperature profiles of the micro porous layers used for the polymer electrolyte membrane fuel cell. *International Journal of Hydrogen Energy*, 38(20): 8437–8447, 2013.

[145] Fabian T, Posner J, O'Hayre R, Cha S.-W, Eaton J, Prinz F, and Santiago J. The role of ambient conditions on the performance of a planar, air-breathing hydrogen PEM fuel cell. *Journal of Power Sources*, 161(1):168–182, 2006.

[146] Dullien F. A. L. *Porous Media: Fluid Transport and Pore Structure*. Academic Press, Inc., second edition, 1992.

[147] Arabi A. J. Analysis of droplet dynamics on the GDL surface of a PEM fuel cell cathode. Master's thesis, Universitat Politecnica De Catalunya, June 2013.

[148] Culligan P and Barry D. Scaling Immiscible Flow in Porous Media. Technical report, Research Report ED 1207 PC, Centre for Water Research, University of Western Australia, Perth, Australia, 1996.

[149] Jiao K and Li X. Water transport in polymer electrolyte membrane fuel cells. *Progress in Energy and Combustion Science*, 37(3):221–291, 2011.

[150] Ihonen J, Mikkola M, and Lindbergh G. Flooding of gas diffusion backing in PEFCs: Physical and electrochemical characterization. *Journal of the Electrochemical Society*, 151(8):A1152–A1161, 2004.

[151] Dong M and Dullien F. A. L. *Porous Media Flows*, chapter 10, pages 10–1–10–55. Multiphase Flow Handbook. CRC Press, Taylor & Francis Group, September 2005.

[152] Litster S, Sinton D, and Djilali N. Ex situ visualization of liquid water transport in PEM fuel cell gas diffusion layers. *Journal of Power Sources*, 154(1):95–105, 2006.

[153] Darcy H. Les fontaines publiques de la ville de Dijon. *Dalmont, Paris*, 70, 1856.

[154] Bear J. *Dynamics of fluids in porous media*. Dover Publications Inc., New York, NY, 1972.

[155] Fox R. W and McDonald A. T. *Introduction to Fluid Mechanics*. John Wiley & Sons, Inc., New York, fifth edition, 1998.

[156] Scheidegger A. The physics of flow through porous media. *University of Toronto Press, Toronto*, 1974.

[157] Ioannidis M and Chatzis I. Network modelling of pore structure and transport properties of porous media. *Chemical Engineering Science*, 48(5):951–972, 1993.

[158] Nguyen T, Lin G, Ohn H, Wang X, Hussey D, Jacobson D, and Arif M. Measurements of two-phase flow properties of the porous media used in pem fuel cells. volume 3, pages 415–423, 2006.

[159] Hao L and Cheng P. Capillary pressures in carbon paper gas diffusion layers having hydrophilic and hydrophobic pores. *International Journal of Heat and Mass Transfer*, 55(1-3):133–139, 2012.

[160] Fairweather J, Cheung P, St-Pierre J, and Schwartz D. A microfluidic approach for measuring capillary pressure in PEMFC gas diffusion layers. *Electrochemistry Communications*, 9(9):2340–2345, 2007.

[161] Van Genuchten M. A closed-form equation for predicting the hydraulic conductivity of unsaturated soils. *Soil Science Society of America Journal*, 44(5): 892–898, 1980.

[162] *Sigracet® GDL 24 & 25 Series Gas Diffusion Layer*. SGL Technologies GmbH. URL `http://www.sglgroup.com/cms/_common/downloads/products/product-groups/su/fuel-cell-components/GDL_24_25_Series_Gas_Diffusion_Layer.pdf`. Taken on October 01, 2013.

[163] He W, Yi J, and Van Nguyen T. Two-phase flow model of the cathode of PEM fuel cells using interdigitated flow fields. *AIChE Journal*, 46(10):2053–2064, 2000.

[164] Pant L. M. Experimental and Theoretical Investigation of Mass Transport in Porous Media of a PEM Fuel Cell. Master's thesis, University of Alberta, Fall 2011.

[165] Pant L, Mitra S, and Secanell M. Absolute permeability and Knudsen diffusivity measurements in PEMFC gas diffusion layers and micro porous layers. *Journal of Power Sources*, 206:153–160, 2012.